



**Use of Perfusion PET/CT Imaging to Assess
Cardiac Function and Repair in Murine Diabetic
Cardiac Models and Subsequent Refinement and
Validation of Predictive in Silico Cardiac Models**

by

Aishah Alenezi

Thesis submitted on July 2022 at Cardiff University for the award of Doctor of
Philosophy

Wales Research & Diagnostic Positron Emission Tomography Imaging Centre
(PETIC)

School of Medicine, Cardiff University,
CF14 4XN Cardiff, United Kingdom

Supervisors:

Dr. Stephen Paisey, Dr. Anita Thomas, Professor Paolo Madeddu and

Christopher Marshall

In the name of God, most gracious, most Merciful

This work is dedicated to.

My late Father

My mother

My children Agab and Ahmad

My supervisors Dr. Stephen Paisey and Dr. Anita Thomas

and

all my beloved family and friends

Acknowledgements:

Thanks be to Almighty God, the most merciful, for giving me the strength to complete this research despite all difficulties. Thanks be to God, for giving me the privilege to be supervised by a great person like Dr. Stephen Paisey.

I am grateful to having received great support from my parents, Mubarak and Alhanoof Alenezi. Thank you for being the best parents a person could have.

I would like to express my special thanks of gratitude to my supervisor Dr. Stephen Paisey for his endless support throughout my PhD journey. The completion of this thesis could not have been possible without his guidance, patience, and enthusiasm.

A massive thanks to Kuwait University for giving me the opportunity to complete my postgraduate studies.

A special thanks to Dr. Anita Thomas for her support and advice during this research and till the last minute. Thank you for being such an amazingly true inspiration to me.

A big thanks to Professor Paolo Madeddu for allowing me to work with their great group in Bristol University by offering every piece of advice as well as allowing the smooth access to their facility during the covid crisis in order to complete my work.

Thanks to the director of Wales Research & Diagnostic Positron Emission Tomography Imaging Centre, Professor Christopher Marshall for offering all the support in using the preclinical imaging facility.

I must also thank Luiza Haberska in the production team of the Wales Research and Diagnostic PET Imaging Centre for facilitating the production and the delivery of the radiotracers.

Thanks go to all my lab colleagues and the entire academic team in Cardiff University.

Many thanks to my dearest friends Sadia Malik, Ahlam Abdelkader and Asma Bibtana for being true friends.

Finally, special thanks to my children (Agab & Ahmad), my sister Karema Alenezi, my brother Abdullah Alenezi, all my sisters and brothers, my nieces and nephews for their unconditional love, and encouragement.

Table of Contents

SUMMARY:	10
LIST OF FIGURES:	11
LIST OF TABLES:	22
CHAPTER 1: OVERVIEW	24
1.1 THESIS OVERVIEW:.....	24
1.2 THESIS HYPOTHESIS:.....	26
1.3 THESIS OBJECTIVES:	26
1.3.1 <i>Objectives outline:</i>	26
1.4 THESIS OUTLINE:	27
CHAPTER 2: GENERAL BACKGROUND	29
2.1 INTRODUCTION:.....	29
2.2 RISK FACTORS ASSOCIATED WITH CVDs:.....	30
2.3 OVERVIEW OF CARDIOVASCULAR SYSTEM (CVS):.....	30
2.4 THE METABOLIC AND GENETIC ADAPTATION DURING CVDs:.....	33
2.5 WAYS TO EVALUATE OR SCAN THE CVS:	34
2.6 PET BASIC PRINCIPLE:	40
2.7 PET SYSTEM COMPONENTS:.....	41
2.7.1 <i>Solid scintillation crystal (detectors):</i>	41
2.7.2 <i>Photomultiplier tubes (PMTs):</i>	44
2.7.3 <i>Preamplifier, amplifier, and pulse height analysers (PHA):</i>	45
2.7.4 <i>Annihilation coincidence detection (ACD) circuits:</i>	45
2.8 COMBINED PET/CT IMAGING:	47
2.9 APPLIED CORRECTION IN PET IMAGES:.....	48
2.9.1 <i>Attenuation correction:</i>	48
2.9.2 <i>Types of coincidence events, scatter, and random corrections:</i>	48
2.9.3 <i>Deadtime:</i>	50
2.9.4 <i>Normalization:</i>	51
2.10 TYPES OF IMAGE ACQUISITION IN PET SYSTEM:.....	51
2.10.1 <i>Static acquisition:</i>	51
2.10.2 <i>Dynamic acquisition:</i>	51
2.10.3 <i>Gated acquisition:</i>	52

2.10.4 Whole-body acquisition:	52
2.11 DATA RECONSTRUCTION:.....	53
2.11.1 Filtered back-projection (FBP):.....	53
2.11.2 Iterative reconstruction (IR) algorithm:	54
2.12 OVERVIEW OF PET QUANTIFICATION METHODS:.....	55
2.12.1 The standard uptake value (SUV):	55
2.12.2 Pharmacokinetic modelling (PKIN) or compartmental modelling:.....	56
2.13 COMMONLY USED COMPARTMENT MODELS:.....	58
2.13.1 One tissue compartment model (1TC):.....	58
2.13.2 Two tissue compartment model (2TC):.....	58
2.14 THE APPLICATION OF COMPARTMENTAL MODELLING:.....	60
2.15 THE USE OF THE MURINE MODEL:.....	60
2.16 EXAMPLES OF MURINE MODELS:	61
2.16.1 Diabetes mellitus:	61
2.16.2 Ageing:.....	62
2.16.3 The hindlimb ischemic model:.....	62
2.17 THE POTENTIAL UTILITY OF MBF, CFR, AND MGM IN CARDIAC PET IMAGING:	62
2.18 PET/CT AS A QUANTIFICATION TOOL FOR MBF AND CM:.....	64
2.19 MICRO-PET/CT IMAGING OF MURINE MODELS:	65
2.20 GENE THERAPY:	67
2.21 GAPS OF KNOWLEDGE:.....	68
2.22 CONCLUSION:	69
CHAPTER 3: METHODOLOGY	70
3.1 MATERIALS AND METHODS:	70
3.1.1 The PET/CT Scanner:	70
3.1.2 The used Cyclotron:.....	70
3.1.3 Radionuclides (radiotracers) used in this research:.....	70
3.2 ANIMAL MODELS:	72
3.3 THERAPEUTIC GENE NAME:	72
3.4 VARIANTS OF THE GENE:.....	72
3.5 GENE CLONING:	72
3.6 VECTOR PRODUCTION:.....	72
3.7 GENE DELIVERY METHOD:	73
3.8 HEALTHY MICE:	73

3.9 HINDLIMB MICE MODEL:	73
3.10 THE DIABETIC MICE MODEL:	73
3.10.1 Mice groups for the diabetic model:.....	73
3.11 AGEING MICE MODEL:.....	74
3.11.1 Mice groups for ageing model:.....	75
3.12 HINDLIMB MICE MODEL:	76
3.13 IMAGING PROTOCOLS:	76
3.13.1 Imaging protocols for diabetic model:.....	76
3.13.2 Imaging protocols for healthy, ageing and HLI models:.....	77
3.14 IMAGE RECONSTRUCTION:	78
3.15 THE DATA ANALYSIS SOFTWARE:	78
3.16 ECHOCARDIOGRAPHY:.....	79
3.17 LASER DOPPLER IMAGING:.....	80
3.18 HAIR RE-GROWTH GRID:.....	80
3.19 ORGAN HARVESTING:	80
3.20 IMMUNOHISTOCHEMISTRY STAINING:	81
3.21 FLUORESCENCE MICROSCOPY:	81
3.22 IMAGE J SOFTWARE:.....	82
3.23 STATISTICAL ANALYSIS:.....	82

CHAPTER 4: EVALUATION OF MICRO-PET/CT SYSTEM QUANTIFICATION ACCURACY WITH ¹⁸F-FDG AND ¹³N-NH₃ USING NEMA STANDARD TESTS 83

4.1 INTRODUCTION:.....	83
4.1.1 Spatial resolution (SR):.....	85
4.1.2 Sensitivity:	88
4.1.3 Scatter fractions (SF) and counting rate measurements:	89
4.1.4 Image quality (IQ):.....	90
4.2 OBJECTIVE:	96
4.3 MATERIALS AND METHODS:	96
4.3.1 PET/CT scanner:	96
4.3.2 Radionuclides (or radiotracers):.....	96
4.3.3 The IQ phantom:	97
4.3.4 The analysis software:	97
4.3.5 The IQ phantom test:	97
4.3.6 Data analysis of the IQ phantom:	98

4.4 RESULTS:.....	101
4.5 DISCUSSION:.....	104
4.5.1 RC% analysis:	105
4.5.2 Uniformity analysis:.....	109
4.5.3 SOR analysis:.....	110
4.6 CONCLUSION:.....	111
CHAPTER 5: ASSESSING THE ACCURACY AND REPEATABILITY IN THE PET/CT IMAGING PROTOCOL IN HEALTHY MURINE STUDIES	113
5.1 INTRODUCTION:.....	113
5.1.1 Previous studies to assess cardiac metabolism in mice:.....	114
5.1.2 Previous PET studies on MBF quantification:.....	116
5.2 TECHNICAL CHALLENGES IN MICE IMAGING:	117
5.2.1 Animal handling:.....	118
5.2.2 Compartmental modelling:.....	120
5.2.3 Available software for Compartmental modelling:	123
5.3 PHARMACOLOGICAL STRESS AGENT, DOBUTAMINE VERSUS ADENOSINE:	123
5.4 OBJECTIVES:	124
5.5 MATERIAL AND METHODS:.....	125
5.5.1 Animal and the sample size:	125
5.5.2 The micro-PET/CT Scanner:.....	125
5.5.3 Radiotracers:.....	125
5.5.4 Type of pharmacological stress agent:	125
5.5.5 Study design:.....	126
5.5.6 Reconstruction of PET images:.....	129
5.5.7 Data analysis and the used software:.....	129
5.5.8 Statistic:	134
5.6 RESULTS:.....	135
5.6.1 MBF analysis results:.....	135
5.6.2 MGM analysis results:.....	138
5.6.3 SUVs for ¹⁸ F-FDG and ¹³ N-NH ₃ rest scans:.....	138
5.7 DISCUSSION:	140
5.7.1 Standard protocol analysis:	140
5.7.2 MBF quantification:	142
5.7.3 MGM quantification:	146

5.8 CONCLUSION:.....	147
CHAPTER 6: THE ABILITY OF THE MICRO-PET/CT SYSTEM TO DETECT METABOLIC AND BLOOD FLOW CHANGES IN THE HLI MODEL.....	149
6.1 INTRODUCTION:.....	149
6.2 OBJECTIVES:	150
6.3 MATERIALS AND METHODS:	150
6.3.1 <i>The animals:</i>	151
6.3.2 <i>Animal preparation and surgical HLI induction:</i>	151
6.3.3 <i>The doppler imaging:</i>	152
6.3.4 <i>The micro-PET/CT scanner:</i>	152
6.3.5 <i>Radiotracers:</i>	152
6.3.6 <i>PET/CT imaging protocol:</i>	152
6.3.7 <i>Culling, tissue collection and histological analysis:</i>	153
6.3.8 <i>PET image reconstruction and analysis software:</i>	153
6.3.9 <i>Statistical analysis:</i>	154
6.4 RESULTS:.....	154
6.4.1 <i>Doppler imaging results:</i>	154
6.4.2 <i>PET Results:</i>	154
6.4.3 <i>Capillary and artery density results:</i>	160
6.4.4 <i>Comparison of PET results with the Doppler imaging and histology:</i>	162
6.5 DISCUSSION:.....	165
6.6 CONCLUSION:.....	167
CHAPTER 7: THE THERAPEUTIC EFFECT OF LONGEVITY-ASSOCIATED VARIANT (LAV)-BPIFB4 GENE THERAPY ON DIABETES MELLITUS (DM) MURINE MODELS.....	168
7.1 INTRODUCTION:.....	168
7.2 OBJECTIVE:	171
7.3 MATERIAL AND METHODS:.....	171
7.3.1 <i>Study design:</i>	171
7.3.2 <i>Animal groups:</i>	172
7.3.3 <i>Micro PET/CT scanner:</i>	173
7.3.4 <i>The used radiotracers:</i>	173
7.3.5 <i>Animal preparation:</i>	173
7.3.6 <i>Animal PET/CT imaging:</i>	173
7.3.7 <i>Reconstruction of PET images:</i>	173

7.3.8 Data analysis:.....	174
7.3.9 SUV measurements:.....	174
7.3.10 Myocardial glucose metabolism (MGM) measurements:	174
7.3.11 Echocardiography:	174
7.3.12 Histological analysis:.....	175
7.4 STATISTICS:	175
7.5 RESULTS:.....	175
7.5.1 SUV measurements:.....	177
7.5.2 MGM measurements through compartmental modelling:	179
7.5.3 Echocardiography:	180
7.5.4 Histological data:	184
7.5.5 PET comparison with echocardiography:	186
7.5.6 PET comparison with the histology data:	187
7.6 DISCUSSIONS:	188
7.7 CONCLUSION:.....	191

CHAPTER 8: THE THERAPEUTIC EFFECT OF LONGEVITY-ASSOCIATED VARIANT (LAV)-BPIFB4 GENE THERAPY

ON AGEING MODEL.....	193
8.1 INTRODUCTION:.....	193
8.1.1 Aging and Cellular Senescence:	193
8.2 OBJECTIVE:	195
8.3 MATERIALS AND METHODS:	195
8.3.1 Study design:.....	195
8.3.2 Animal groups:.....	197
8.3.3 Micro PET/CT Scanner:.....	197
8.3.4 The used radiotracers:	197
8.3.5 Animal preparation, scanning and tissue harvesting:	198
8.3.6 Image Reconstruction for the PET/CT scans:	199
8.3.7 Medical Image analysis software for PET/CT scans:	200
8.3.8 Echocardiography:	200
8.3.9 Histological analysis:.....	200
8.3.10 Statistical analysis:.....	200
8.4 RESULTS:.....	201
8.4.1 Rest perfusion imaging:	201
8.4.2 Stress perfusion imaging:.....	201

8.4.3 Echocardiography results:.....	205
8.4.4 Capillary and artery density results:	205
8.4.5 Comparison of the PET results with the echocardiography and histological data:.....	205
8.5 DISCUSSION:.....	216
8.6 CONCLUSION:.....	219
CHAPTER 9: FINAL DISCUSSION:.....	221
CHAPTER 10: CONCLUSION, LIMITATIONS, AND FUTURE WORK:.....	229
10.1 SUMMARY AND CONCLUSION:	229
10.2 NOVELTY OF THE RESEARCH:	230
10.3 RESEARCH LIMITATIONS:	230
10.4 FUTURE WORK:	231
APPENDICES:	232
10.1 APPENDIX A: THE GAIN IN BODY WEIGHT (IN GRAM) FOR ALL THE DIABETIC GROUPS AT WEEK 6,8,9 AND 13.	232
10.2 APPENDIX B: THE CHEST HAIR REGROWTH (# OF GRIDS) IN ALL THE DIABETIC GROUPS.....	234
10.3 APPENDIX C: IMAGE DEMONSTRATION FOR THE ¹³ N-NH ₃ DYNAMIC SCANS AT REST AND STRESS FOR ALL THE AGEING GROUPS DURING THE EARLY AND LATE TREATMENTS.....	235
10.4 APPENDIX D:	243
10.4.1 Publications:.....	243
10.4.2 Expected to be published:.....	243
10.4.3 Presentation:.....	243
10.4.4 Poster:.....	243
REFERENCES:	244
LIST OF ABBREVIATIONS:.....	275

Summary:

Micro-positron emission tomography (micro-PET) imaging is a powerful imaging modality in cardiovascular studies for the assessment of mice cardiac function in-vivo. This modality offers an insight into biochemical changes on a molecular level through quantifying myocardial blood flow (MBF), and glucose metabolism (MGM) as prognostic biomarkers in cardiovascular diseases (CVDs). In the past decade, the amount of cardiovascular research using micro-PET/CT has increased widely to understand human diseases, standardize imaging protocols, or to evaluate treatment interventions. Until recently, there has been a lack of a standard quantitative PET/CT protocols to quantify MBF and MGM due to the challenges associated with small animal imaging such as resolution, animal handling and the complexity of image analysis with the compartmental modelling method. The combination of a well performing micro-PET/CT scanner and accurate and repeatable imaging protocols could provide invaluable qualitative and quantitative data that might resolve questions about a potential gene therapy. Accordingly, we have gathered interesting data about the bactericidal/permeability-increasing fold-containing- family-B-member-4 longevity associated variant (LAV-BPIFB4) gene that has been identified by our collaborators and that has shown therapeutic effects in protecting against CVDs and age-related pathologies. This gene variant has been demonstrated to enhance revascularization and reduce endothelial dysfunction in mice. Therefore, this research aimed to first demonstrate the feasibility of our micro-PET/CT scanner to assess cardiac function in murine models through developing accurate and repeatable imaging protocol sets. Next, investigating the beneficial effects of the LAV-BPIFB4 gene in maintaining cardiac function using diabetic and elderly mice models. Our standardized imaging protocols produced accurate and repeatable quantitative PET data of both MBF and MGM using a compartmental modelling quantification method. Importantly, our results from both murine models demonstrated the therapeutic role of the gene in preserving cardiac function by enhancing its contractile function, improved blood flow and reduced capillary rarefaction. PET data were consistent with echocardiography and histological results. Our findings confirmed that our micro-PET/CT scanner allows the quantitative evaluation of cardiac perfusion and metabolism in mice models, as well as demonstrating the beneficial influence of the LAV-BPIFB4 gene treatment. This research has the potential to be extended for further refinement of the imaging methods or to investigate the duration of the effect of the gene and the metabolic mechanisms that have caused its therapeutical action.

List of Figures:

FIGURE 1.1: FLOW CHART FOR THE THESIS STRUCTURE..... 28

FIGURE 2.1: NORMAL AND ATHEROSCLEROTIC ARTERIAL WALLS. IN ATHEROSCLEROSIS EVENT, A BUILD-UP OF PLAQUE IN THE INTIMAL LAYER MAY CAUSE NARROWING OF THE ARTERY (BIORENDER 2017)..... 29

FIGURE 2.2: SCHEMATIC REPRESENTATION OF THE MAMMALIAN HEART. INCLUDED THE ANATOMY OF THE FOUR CHAMBERS, REPRESENTATION OF THE MYOCARDIAL HISTOLOGICAL LAYERS AND A CARTOON OF THE MAIN CELLULAR COMPONENT OF THE HEART WHICH IS THE CARDIOMYOCYTES (BIORENDER 2017)..... 32

FIGURE 2.3: SCHEMATIC REPRESENTATION OF THE VASCULAR WALL LAYERS IN THE ARTERY AND VEIN (BIORENDER 2017). 33

FIGURE 2.4: THE ECG TRACE. IN A TYPICAL ECG READING, PEAKS (R) AND VALLEYS CAN BE OBSERVED. THE DURATION BETWEEN SUBSEQUENT HEART BEATS IS REPRESENTED BY R-R INTERVAL (BIORENDER 2017). 35

FIGURE 2.5: THE DIFFERENT PARTS OF THE CARDIAC CYCLE. EACH PART REFLECTS A SPECIFIC FUNCTION IN THE MYOCARDIUM (BIORENDER 2017)..... 35

FIGURE 2.6: SCHEMATIC ECHOCARDIOGRAPHY CONCEPT. A. SIMPLE ILLUSTRATION OF THE ECHOCARDIOGRAPHY PHYSICAL CONCEPT IN WHICH HIGH PITCHED SOUND WAVES ARE USED TO CREATE THE IMAGE OF THE HEART AS WELL AS MEASURING OTHER VARIOUS CARDIAC DIMENSIONAL AND FUNCTIONAL PARAMETERS. B. STANDARD MOUSE ECHOCARDIOGRAPHY IMAGE USING VEVO 3100 PRECLINICAL ECHOCARDIOGRAPHY. IN THIS IMAGE, THE LV MEASUREMENTS WERE TAKEN FROM A B-MODE PARASTERNAL LONG AXIS IMAGE (FUJIFILM VISUALSONICS DESIGNS 1999). 37

FIGURE 2.7: THE PHYSICAL CONCEPT OF THE DOPPLER US IMAGING. DOPPLER US USES THE DOPPLER PRINCIPLE AND DOPPLER FREQUENCY SHIFT TO ESTIMATE THE BLOOD FLOW IN THE BLOOD VESSELS. THE ULTRASOUND PULSE REFLECTED FROM THE BLOOD CELLS, THAT ARE MOVING TOWARD THE TRANSDUCER, WILL HAVE A HIGHER FREQUENCY WAVE THAN THE ORIGINAL TRANSMITTED ULTRASOUND PULSE (UPPER PANELS). THE OPPOSITE CAN BE SEEN WITH BLOOD MOVING AWAY FROM THE TRANSDUCER (LOWER PANELS). DOPPLER ECHOCARDIOGRAPHY MODALITY USES THE SHIFT IN FREQUENCY, WHICH IS CALLED DOPPLER FREQUENCY SHIFT, TO DERIVE BLOOD FLOW VELOCITIES. THE DIRECTION OF BLOOD FLOW IS PRESENTED GRAPHICALLY AS A TIME-VELOCITY SPECTRUM ABOVE OR BELOW THE BASELINE OR AS COLOUR GRADIENT MAP OF THE BLOOD FLOW (SLIDESHARE SCRIBD COMPANY 2006). 37

FIGURE 2.8: SCHEMATIC OF MRI SCANNER AND BASIC PHYSICAL CONCEPT. MRI USES STRONG MAGNETS THAT GENERATE A STRONG MAGNETIC FIELD. THIS MAGNETIC FIELD FORCES PROTONS IN THE BODY TO ALIGN WITH IT. WHEN A RADIO-FREQUENCY CURRENT IS THEN PULSED THROUGH THE OBJECT, THE PROTONS ARE ACTIVATED, AND SPIN OUT OF EQUILIBRIUM STATE, STRAINING PERPENDICULAR TO THE MAGNETIC FIELD. AFTER TURNING OFF THE RADIO-FREQUENCY FIELD, THE MRI SENSORS CAN DETECT THE ENERGY RELEASED AS THE PROTONS REALIGN WITH THE MAGNETIC FIELD. DUE TO THE DIFFERENCES IN THE ENVIRONMENT AND THE CHEMICAL NATURE OF THE MOLECULES, THE TIME TAKEN BY THE PROTONS TO REALIGN WITH THE MAGNETIC FIELD AS WELL AS THE AMOUNT OF THEIR RELEASED ENERGY VARY. THE DIFFERENT IN TIME AND ENERGY RELEASED BY THE PROTONS ALLOW THE PHYSICIANS TO DIFFERENTIATE BETWEEN VARIOUS TYPES OF TISSUES (SLIDESHARE SCRIBD COMPANY 2006). 38

FIGURE 2.9: THE BASIC CONCEPT OF X-RAY IMAGING. IN X-RAY IMAGING, A BEAM OF X-RAYS IS GENERATED AND PASSED THROUGH THE OBJECT BODY. A PORTION OF THE X-RAYS ARE EITHER ABSORBED OR SCATTERED DEPENDING ON THE OBJECT STRUCTURES, AND THE

REMAINING X-RAYS PATTERN ARE TRANSMITTED TO A DETECTOR (SUCH AS A FILM OR A COMPUTER SCREEN) FOR RECORDING OR FURTHER IMAGE PROCESSING BY A COMPUTER (SLIDESHARE SCRIBD COMPANY 2006).	38
FIGURE 2.10: SCHEMATIC DIAGRAM OF THE CT SCANNER. CT USES A ROTATING X-RAY TUBE WITH A ROW OF DETECTORS PLACED IN THE GANTRY ARE USED. THE ROTATING X-RAY TUBE EMITS RADIATION AT MULTIPLE ANGLES ACROSS THE OBJECT BODY. THE X-RAY GETS ATTENUATED BY THE DIFFERENT TISSUES INSIDE THE OBJECT AND THEN DETECTED BY THE OPPOSING DETECTOR. THE DETECTED RADIATION IS THEN USED TO GENERATE A SERIES OF SLICES WHICH ARE THEN RECONSTRUCTED TO PRODUCE A 3D IMAGE OF THE SOFT TISSUES AND BONES (SLIDESHARE SCRIBD COMPANY 2006).	39
FIGURE 2.11: A SCHEMATIC REPRESENTATION OF THE ANNIHILATION EVENT THAT OCCUR WHEN THE POSITRON (β^+) COME AT REST AND COLLIDES WITH ITS ANTIPARTICLE, THE ELECTRON (e^-). THIS COLLISION RESULTS IN THE ANNIHILATION OF THE TWO PARTICLES AND THE EMISSION OF TWO GAMMA RAY PHOTONS WITH BOTH HAVING THE ENERGY OF 511 KeV AND EMITTED IN OPPOSITE DIRECTION OF EACH OTHER. THE EMITTED PHOTONS THEN CAN BE DETECTED BY PET SCANNER THROUGH CERTAIN TYPE OF DETECTORS (SLIDESHARE SCRIBD COMPANY 2006).	40
FIGURE 2.12: THE BLOCK DETECTOR DESIGN IN PET SYSTEMS. IN THIS DESIGN, EACH CRYSTAL DETECTOR BLOCK IS CONNECTED TO 2-4 PHOTOMULTIPLIER TUBES (PMTs). DEPENDING ON THE MANUFACTURER DESIGN, EACH CRYSTAL BLOCKS MAY HAVE DIFFERENT NUMBER OF ELEMENTS (FOR EXAMPLE SOME HAS 6x8, 7x8, OR 8x8 ELEMENTS) WITH A LENGTH OF 3 TO 6.5 MM AND A DEPTH OF APPROXIMATELY 3 CM (SLIDESHARE SCRIBD COMPANY 2006) (BIORENDER 2017).	42
FIGURE 2.13: A REPRESENTATION OF THE PHOTOELECTRIC EFFECT. THIS INTERACTION INVOLVES THE FORMATION OF AN AUGER ELECTRON (BIORENDER 2017).	43
FIGURE 2.14: A REPRESENTATION OF THE COMPTON SCATTERING INTERACTION. IN THIS INTERACTION, THE PHOTON COLLIDES WITH AN OUTER SHELL ELECTRON CAUSING THE EJECTION OF AN ELECTRON AND THE SCATTERING OF THE PHOTON (BIORENDER 2017).	44
FIGURE 2.15: A REPRESENTATION OF THE PAIR PRODUCTION INTERACTION. IN THIS INTERACTION, A HIGH ENERGY PHOTON (> 1.02 MeV) INTERACTS WITH THE NUCLEUS RESULTING IN THE EMISSION OF A POSITRON AND A NEGATIVE ELECTRON AT THE EXPENSE OF THE PHOTON (BIORENDER 2017).	44
FIGURE 2.16: A SCHEMATIC REPRESENTATION OF A PHOTOMULTIPLIER TUBE COUPLED WITH A SCINTILLATOR CRYSTAL (BIORENDER 2017).	45
FIGURE 2.17: SCHEMATIC DIAGRAM OF THE CROSS SECTION OF THE PET SCANNER ILLUSTRATING THE 2D AND 3D ACQUISITION MODES (SLIDESHARE SCRIBD COMPANY 2006).	46
FIGURE 2.18: A SCHEMATIC ILLUSTRATION OF THE COMBINED PET/CT SYSTEM (BIORENDER 2017).	47
FIGURE 2.19: TYPES OF VARIOUS COINCIDENCE EVENTS DETECTED BY THE PET SCANNER. THE BLACK DOTE INDICATES THE LOCATION OF THE ANNIHILATION EVENTS. THESE EVENTS CAN BE EITHER A TRUE, SCATTERED, RANDOM, MULTIPLE COINCIDENCES (SLIDESHARE SCRIBD COMPANY 2006).	48
FIGURE 2.20: A DIAGRAM OF THE STATIC (A) VERSUS THE DYNAMIC (B) PET ACQUISITIONS. IN STATIC ACQUISITION, THE RADIOACTIVITY OF THE TRACER IS MEASURED OVER A SINGLE FIXED PERIOD (A). IN CONTRAST, THE DYNAMIC ACQUISITION IS A SERIES OF FRAMES IN A CONTINUOUS ACQUISITION.	52

FIGURE 2.21: THE ECG-GATED PET ACQUISITION. IN ECG GATING, R-R INTERVALS OF THE HEART ARE DIVIDED INTO AN EQUAL NUMBER OF BINS ($N=8$) TO CREATE A MEAN R-R INTERVAL (BioRender 2017). 53

FIGURE 2.22: THE FBP RECONSTRUCTION PROCESS. EACH SET OF PROJECTION VIEWS, THAT WERE ACQUIRED AT DIFFERENT ANGLES, UNDERGOES FILTERING BEFORE ITS BACK PROJECTED. THIS PROCESS REMOVES THE BLURRING THAT WE WOULD SEE IN SIMPLE BACK PROJECTION (Cherry et al. 2012). 55

FIGURE 2.23: THE COMPARTMENTAL MODELLING USED IN QUANTIFYING GLUCOSE METABOLIC RATE WITH ^{18}F -FDG. 57

FIGURE 2.24: 1TC MODEL USED IN COMPARTMENTAL MODELLING. 59

FIGURE 2.25: THE 2TC MODEL. 59

FIGURE 3.1: THE EXPERIMENTAL DESIGN FOR THE DIABETIC MODEL GROUPS. 74

FIGURE 3.2: THE EXPERIMENTAL DESIGN FOR THE AGEING MODEL OF THE EARLY TREATMENT GROUP..... 75

FIGURE 3.3: THE EXPERIMENTAL DESIGN FOR THE AGEING MODEL OF THE LATE TREATMENT GROUP. 75

FIGURE 3.4: CHEST HAIRINESS GRID IN (NUMBER/GRID). REGROWTH USUALLY OBSERVED AS: 1-3 FIRST TO APPEAR, 4-6 MID, 7-9 LAST TO APPEAR, AND 10= COMPLETELY RE-GROWN (NO GAPS). 80

FIGURE 4.1: THE MEASUREMENT OF THE SYSTEM PSF. A SHOW A RADIOACTIVE POINT SOURCE PLACED IN THE MIDDLE OF THE IMAGING FIELD. B SHOWS THE CURVE OBTAINED AFTER DRAWING A LINE ACROSS ONE DIMENSION OF THE IMAGE TO PRODUCE AN INTENSITY CURVE. THIS IS A GAUSSIAN CURVE WITH A BRIGHT CENTER CALLED THE MAXIMUM AND A DARKER INTENSITY AT THE OUTER EDGES. 85

FIGURE 4.2: THE RESOLUTION LIMITATION DUE TO THE LIMITED OF THE PSF. A SHOW TWO-POINT SOURCES SEPARATED BY A DISTANCE SMALLER THAN THE PSF. B SHOWS THE FINAL BLURRED GAUSSIAN CURVE THAT WILL BE PRODUCED FOR THE TWO POINTS WHICH WILL APPEAR AS ONE OBJECT IN THE FINAL IMAGE. 86

FIGURE 4.3: THE DIFFERENCE IN THE PSF AT DIFFERENT DIRECTIONS. A SHOW THAT THE PSF IS LARGER IN THE AXIAL THAN THE LATERAL DIRECTION, RESULTING IN A BETTER SR IN THE LATERAL DIRECTION. IN A, THE FWHM ARE ALMOST EQUAL TO THE MINIMA DIAMETER OF THE GAUSSIAN CURVE IN THE LATERAL DIRECTION (XY PLANE), WHILE B VISUALIZES THE SAME CONCEPT IN THE AXIAL DIRECTION (Z PLANE) WHERE THE MINIMA DIAMETER IS EQUAL TO THE FWHM. 87

FIGURE 4.4: AN ARBITRARY CIRCULAR SOURCE (WITH A DIAMETER OF 10 MM) AND A UNIFORM ACTIVITY OF 100 ARBITRARY UNITS IN A NON-RADIOACTIVE BACKGROUND. THE GENERATED IMAGE HAS REDUCED SIGNALS OF 85 UNITS DUE TO THE SPILL-OUTS FROM THE ACTUAL SOURCE. 92

FIGURE 4.5: THE SPILL-OVER EFFECT ON THE ACTUAL OBJECT. A IS THE TRUE ARBITRARY BIODISTRIBUTION OBJECT. D REPRESENTS THE MEASURED IMAGE OF THE TRUE OBJECT A. THE GENERATED IMAGE IN D IS THE SUM OF THE SPILL-OUT EFFECT IN B AND SPILL-IN EFFECT SEEN IN (C)..... 93

FIGURE 4.6: THE PVE RESULTED FROM IMAGE SAMPLING. VOXELS (ALTHOUGH HERE ITS ONLY 2D) ON THE EDGES OF SOURCE REGION INCLUDE BOTH SOURCE AND BACKGROUND TISSUES. THE CONCENTRATION OR (SIGNAL INTENSITY) IN THESE VOXELS IS THE AVERAGE OF ALL SIGNAL INTENSITIES IN THE UNDERLYING TISSUES. PART OF THE SIGNAL IN THE SOURCE REGION EMANATES OUTSIDE THE TRUE OBJECT AND THUS IS DEFINED AS SPILLING-OUT..... 93

FIGURE 4.7: THE NEMA NU 4-2008 IQ PHANTOM FOR A SMALL PET SCANNER..... 95

FIGURE 4.8: A SCHEMATIC DIAGRAM OF THE NEMA NU 4-2008 IQ PHANTOM IN WHICH A IS THE CORONAL-SECTION VIEW AND B IS THE AXIAL-SECTION VIEW OF THE ROD REGION.....	96
FIGURE 4.9: THE RECONSTRUCTED SLICES COVERING THE CENTRAL 10 MM DEPTH OF REGION. A. REGION THAT WAS USED TO PRODUCE A SINGLE SLICE OF THE FIVE RODS. B. ILLUSTRATES THE ROIS AROUND THE FIVE SPHERES REPRESENTING THE DIFFERENT SIZES OF THE RODS.....	99
FIGURE 4.10: THE RECONSTRUCTED SLICES COVERING THE CENTRAL 10 MM DEPTH OF REGION (B) THAT WERE USED TO PRODUCE A SINGLE SLICE OF THE UNIFORM REGION (B). THIS CAN BE SEEN IN A, WHILE B ILLUSTRATES THE SINGLE SLICE OF THE UNIFORM REGION (B) IN THE IQ PHANTOM AND THE CIRCULAR ROI WHICH WAS GENERATED WITH AN ACTIVE DIAMETER COVERING 75% OF THE FIELD. C SHOWS THE PRODUCED SINGLE SLICE OF THE UNIFORM REGION (B) BUT WITH A DIFFERENT COLOR ALONG WITH THE LINE PROFILE ACROSS THE SLICE. D REVEALS THE LINE PROFILE ACROSS THE UNIFORM REGION.....	100
FIGURE 4.11: THE TRANSVERSE PLANE OF THE 2 NON-RADIOACTIVE COMPARTMENT REGIONS IN THE IMAGE OF THE IQ PHANTOM.	101
FIGURE 4.12: IMAGES A AND B OF THE CORONEL VIEW OF THE NEMA IQ PHANTOM AND A TRANS-AXIAL VIEW OF THE THREE REGIONS (A, B, AND C) WITH THEIR ROIS FOR ¹³ N (A) AND ¹⁸ F (B) RESPECTIVELY.	102
FIGURE 4.13: THE RC VALUES FOR ¹⁸ F AND ¹³ N. THE DATA ARE PRESENTED AS THE MEAN ± STD.	107
FIGURE 4.14: THE FOUR ATTEMPTS OF THE IQ TESTS USING ¹⁸ F. THE DATA ALONG EACH ROD SIZE WERE CLOSE REFLECTING HIGH REPEATABILITY.....	108
FIGURE 4.15: THE FOUR ATTEMPTS OF THE IQ TEST USING ¹³ N. THE DATA ALONG EACH ROD SIZE WERE CLOSE REFLECTING HIGH REPEATABILITY.....	108
FIGURE 4.16: SHOWS THE STD% FOR THE TWO RADIOTRACERS IN THE UNIFORM REGION. THEIR RESULTS WERE WITHIN THE ACCEPTABLE LIMITS OF THE NEMA STANDARD WHICH IS TO BE LESS THAN 15%.	109
FIGURE 4.17: COMPARES THE RESULTS OF THE SOR VALUES OBTAINED FROM ¹³ N AND ¹⁸ F IN THE AIR AND WATER COMPARTMENTS REGIONS. THE WATER COMPARTMENTS HAVE HIGHER SOR VALUES COMPARED TO THE AIR COMPARTMENT.....	111
FIGURE 5.1: THE IMAGING PROTOCOLS THAT WERE DEVELOPED TO ASSESS MGM AND MBF IN HEALTHY MICE, IN WHICH THE ADENOSINE WAS USED AS STRESS PHARMACOLOGICAL AGENT.....	128
FIGURE 5.2: THE IMAGING PROTOCOLS THAT WERE DEVELOPED TO ASSESS MGM AND MBF IN HEALTHY MICE, IN WHICH THE DOBUTAMINE WAS USED AS STRESS PHARMACOLOGICAL AGENT.....	128
FIGURE 5.3: CARDIAC PLANES DEFINITION AND DISPLAY FOR IN PET IMAGING.	131
FIGURE 5.4: SHOWS THE THREE LV AXES. A. IS THE SA OF THE MYOCARDIUM, B. IS THE VLA, AND C. IS THE HLA.	131
FIGURE 5.5: THE DYNAMIC RANGE STEP THAT NEED TO BE SPECIFIED IN DERIVING AND DRAWING THE VOIS FOR THE LV AND LVBP. A. SHOWS THE DYNAMIC RANGE FROM WHICH IDIF WAS DERIVED, WHILE B. SHOWS THE DYNAMIC RANGE OF THE LV VOIS, BUT GENERALLY IN MBF ANALYSIS, LV VOI WAS DERIVED FROM THE EARLY 2-3 MINUTES OF THE AMMONIA SCAN. IN MGM ANALYSIS, THE VOI WAS DERIVED FROM THE LAST 20 MINUTES OF FDG SCAN WHICH IS THE EQUILIBRIUM STATE. FINALLY, IN THE ASSESSMENT OF AMMONIA METABOLIC TRAPPING, LV VOI WAS DERIVED FROM THE LAST 15-20 MINUTES OF THE AMMONIA SCAN.....	132
FIGURE 5.6: THE MYOCARDIUM VOIS THAT WERE DRAWN IN ALL THE THREE PLANES. FOR CLARITY REASONS, ARROWS FOR EACH VOI WERE IDENTIFIED IN SEPARATE PLANE BUT THEY ARE ALL EXISTED IN ALL THREE PLANES IN WHICH, A. IS THE RV VOI, IN THE SA	

PLANE, TO CORRECT FOR SPILL-IN ACTIVITY FROM RV INTO LVBP FOR IDIF CALCULATION. BOTH B, WHICH REPRESENT THE EPICARDIUM VOI OR THE OUTER WALL, AND C, WHICH REPRESENT THE ENDOCARDIUM VOI OR THE INNER WALL OF THE MYOCARDIUM, ARE IN THE VLA PLANE. D. IS THE LVBP VOI IN THE HLA PLANE.	132
FIGURE 5.7: SHOWS THE 1TC (OR DeGRADO) MODEL THAT WAS USED FOR MBF ESTIMATION WITH ¹³ N-NH ₃ AS A RADIOTRACER.	133
IN WHICH THE:	133
FIGURE 5.8: THE 2TC MODEL THAT WAS USED FOR FDG UPTAKE ESTIMATION.	135
FIGURE 5.9: THE MBF VALUES IN REST AND FOLLOWING THE ADMINISTRATION OF ADENOSINE AS A PHARMACOLOGICAL STRESS DRUG. THE DATA ARE SHOWN IN MEAN, STD, SEM. THERE WAS NO STATISTICAL DIFFERENCE REPORTED AND THE P VALUE OF 0.0842 (>0.05) BETWEEN THE TWO PHYSICAL STATES. THE UNPAIRED T-TEST WAS USED FOR THE STATISTICAL ANALYSIS IN THE DATA PRESENTED.	137
FIGURE 5.10: SHOW THE MBF VALUES IN REST AND FOLLOWING THE ADMINISTRATION OF DOBUTAMINE AS A PHARMACOLOGICAL STRESS. THE DATA ARE SHOWN IN MEAN, STD, SEM. THERE WAS A STATISTICAL DIFFERENCE BETWEEN MBF IN THE TWO PHYSICAL STATES WITH A P VALUE OF 0.0001 (<0.05). THE UNPAIRED T-TEST WAS USED FOR THE STATISTICAL ANALYSIS IN THE DATA PRESENTED.	138
FIGURE 6.1: DEMONSTRATION OF DOPPLER REPEATED SCANS FOR THE FOUR MICE DURING DAY 0,3 AND 7. PERFUSION SIGNAL WHICH APPEARED IN RED COLOUR REPRESENTS GOOD BLOOD FLOW, WHILE THE BLUE COLOUR REPRESENTS THE POOR BLOOD FLOW. THE MOUSE IS PLACED IN DORSAL RECUMBENCY. IT VISIBLE THAT THE LIGATED (L) LEG IN ALL MICE HAD SIGNIFICANT DECREASE IN THE BLOOD FLOW FOLLOWING LIGATION AT D0. THE NORMAL (N) LEG SHOWED GOOD BLOOD FLOW PERFUSION WITH RED COLOUR IN ALL MICE.	156
FIGURE 6.2: THE DOPPLER BLOOD FLOW FOR THE LIGATED AND NORMAL LEGS AT DAY 7. THE DATA ARE PRESENTED AS THE MEAN ± STD, N=4/GROUP. THERE WAS A STATISTICAL DIFFERENCE IN BLOOD FLOW BETWEEN THE NORMAL LEG GROUP COMPARED TO THE LIGATED LEG. THE SYMBOL ** INDICATE STATISTICAL SIGNIFICANCE IN WHICH P ** < 0.005. THE UNPAIRED T-TEST WAS USED FOR THE STATISTICAL ANALYSIS IN THE DATA PRESENTED.	156
FIGURE 6.3: THE ¹³ N-NH ₃ RESTING BLOOD FLOW VALUES (ML/MIN/G) FOR THE LIGATED (L) AND NORMAL (N) LEG. THE DATA ARE PRESENTED AS THE MEAN ± STD, N=4/GROUP. THERE WAS A STATISTICAL DIFFERENCE IN BLOOD FLOW BETWEEN THE NORMAL LEG GROUP COMPARED TO THE LIGATED LEG. THE SYMBOL **** INDICATE STATISTICAL SIGNIFICANCE IN WHICH P ** < 0.0001. THE UNPAIRED T-TEST WAS USED FOR THE STATISTICAL ANALYSIS IN THE DATA PRESENTED.	157
FIGURE 6.4: THE ¹³ N-NH ₃ BLOOD FLOW VALUES (ML/MIN/G) FOR THE NORMAL LEGS DURING REST AND STRESS SCANS. THE DATA ARE PRESENTED AS THE MEAN ± STD, N=4/GROUP. THERE WAS A STATISTICAL DIFFERENCE IN BLOOD FLOW BETWEEN THE REST AND STRESS. THE SYMBOL *** INDICATE STATISTICAL SIGNIFICANCE IN WHICH P ** < 0.005. THE UNPAIRED T-TEST WAS USED FOR THE STATISTICAL ANALYSIS IN THE DATA PRESENTED.	158
FIGURE 6.5: THE ¹³ N-NH ₃ BLOOD FLOW VALUES (ML/MIN/G) FOR THE LIGATED LEGS DURING REST AND STRESS SCANS. THE DATA ARE PRESENTED AS THE MEAN ± STD, N=4/GROUP. THERE WAS NO STATISTICAL DIFFERENCE IN BLOOD FLOW BETWEEN THE REST AND STRESS. THE SYMBOL NS INDICATE NO STATISTICAL SIGNIFICANCE IN WHICH P > 0.05. THE UNPAIRED T-TEST WAS USED FOR THE STATISTICAL ANALYSIS IN THE DATA PRESENTED.	158

FIGURE 6.6: SCATTER PLOT OF THE BLOOD FLOW (ML/MIN/G) MEASURED WITH $^{13}\text{N-NH}_3$ VERSUS THE GLUCOSE UPTAKE MEASURED WITH $^{18}\text{F-FDG}$ IN THE NORMAL LEGS. THE REGRESSION LINE WAS FITTED USING THE LEAST SQUARE METHOD. THE $N=4$. PEARSON CORRELATION COEFFICIENT $R = 0.93$ SHOWS THAT THERE IS A STRONG CORRELATION BETWEEN THE BLOOD FLOW AND GLUCOSE UPTAKE IN THE NORMAL HINDLIMB..... 159

FIGURE 6.7: SCATTER PLOT OF THE BLOOD FLOW (ML/MIN/G) MEASURED WITH $^{13}\text{N-NH}_3$ VERSUS THE GLUCOSE UPTAKE MEASURED WITH $^{18}\text{F-FDG}$ IN THE LIGATED LEGS. THE REGRESSION LINE WAS FITTED USING THE LEAST SQUARE METHOD. THE $N=4$. PEARSON CORRELATION COEFFICIENT $R = 0.67$ SHOWS A GOOD CORRELATION BETWEEN THE BLOOD FLOW AND GLUCOSE UPTAKE IN THE LIGATED HINDLIMB..... 159

FIGURE 6.8: THE CAPILLARY DENSITY (N/MM²) IN BOTH THE NORMAL AND LIGATED LEGS. THE DATA ARE PRESENTED AS MEAN \pm STD, $N=4$. THE CAPILLARY DENSITY IN NORMAL LEGS WAS STATISTICALLY HIGHER THAN THE LIGATED LEGS. THE SYMBOL * REPRESENTS SIGNIFICANT DIFFERENCE WITH P VALUES $** < 0.005$. THE UNPAIRED T-TEST WAS USED FOR THE STATISTICAL ANALYSIS IN THE DATA PRESENTED. 160

FIGURE 6.9: THE ARTERY DENSITY (N/MM²) IN THE NORMAL AND THE LIGATED LEGS. THE DATA ARE PRESENTED AS MEAN \pm STD, $N=4$. THE ARTERY DENSITY IN NORMAL LEGS WAS STATISTICALLY HIGHER THAN THE LIGATED LEGS. THE SYMBOL *** REPRESENTS SIGNIFICANT DIFFERENCE WITH P VALUES $** < 0.0005$. THE UNPAIRED T-TEST WAS USED FOR THE STATISTICAL ANALYSIS IN THE DATA PRESENTED. 161

FIGURE 6.10: REPRESENTATIVE IMAGES OF ISCHEMIC HINDLIMB SAMPLES AFTER IMMUNOSTAINING WITH GREEN COLOUR (488 EMISSION) LECTIN BINDING REPRESENTING THE CAPILLARIES, AND RED (CY3 EMISSION) ASMA STAINING IDENTIFYING THE ARTERIES. NUCLEI COUNTERSTAINED WITH DAPI (BLUE). A, B QUANTITATIVE ANALYSIS OF THE CAPILLARIES IN NORMAL AND LIGATED LEGS RESPECTIVELY. C, D A-SMA-POSITIVE ARTERY STAINING IN NORMAL AND LIGATED LEGS RESPECTIVELY. 161

FIGURE 6.11: SCATTER PLOT OF THE RESTING BLOOD FLOW (ML/MIN/G) MEASURED WITH $^{13}\text{N-NH}_3$ VERSUS THE BLOOD FLOW RATIO MEASURED WITH DOPPLER IMAGING IN THE NORMAL LEGS. THE REGRESSION LINE WAS FITTED USING THE LEAST SQUARE METHOD. THE $N=4$. PEARSON CORRELATION COEFFICIENT $R = 0.9$ REVEALED A GOOD CORRELATION BETWEEN THE BLOOD FLOW (PET RESULTS) AND BLOOD FLOW RATIO (DOPPLER RESULTS). 162

FIGURE 6.12: SCATTER PLOT OF THE RESTING BLOOD FLOW (ML/MIN/G) MEASURED WITH $^{13}\text{N-NH}_3$ VERSUS THE BLOOD FLOW RATIO MEASURED WITH DOPPLER IMAGING IN THE LIGATED LEGS. THE REGRESSION LINE WAS FITTED USING THE LEAST SQUARE METHOD. THE $N=4$. PEARSON CORRELATION COEFFICIENT $R = 0.99$ REVEALED A GOOD POSITIVE CORRELATION BETWEEN THE BLOOD FLOW (PET RESULTS) AND BLOOD FLOW RATIO (DOPPLER RESULTS). 163

FIGURE 6.13: SCATTER PLOT OF THE RESTING BLOOD FLOW (ML/MIN/G) MEASURED WITH $^{13}\text{N-NH}_3$ VERSUS THE CAPILLARY DENSITY (N/MM²) IN THE NORMAL LEGS. THE REGRESSION LINE WAS FITTED USING THE LEAST SQUARE METHOD. THE $N=4$. PEARSON CORRELATION COEFFICIENT $R = 0.91$ REVEALED A GOOD CORRELATION BETWEEN THE BLOOD FLOW (PET RESULTS) AND CAPILLARY DENSITY (HISTOLOGICAL RESULTS)..... 163

FIGURE 6.14: SCATTER PLOT OF THE RESTING BLOOD FLOW (ML/MIN/G) MEASURED WITH $^{13}\text{N-NH}_3$ VERSUS THE CAPILLARY DENSITY (N/MM²) IN THE LIGATED LEGS. THE REGRESSION LINE WAS FITTED USING THE LEAST SQUARE METHOD. THE $N=4$. PEARSON

CORRELATION COEFFICIENT $R = 0.94$ REVEALED A GOOD CORRELATION BETWEEN THE BLOOD FLOW (PET RESULTS) AND CAPILLARY DENSITY (HISTOLOGICAL RESULTS).....	164
FIGURE 6.15: SCATTER PLOT OF THE RESTING BLOOD FLOW (ML/MIN/G) MEASURED WITH $^{13}\text{N-NH}_3$ VERSUS THE ARTERY DENSITY (N/MM ²) IN THE NORMAL LEGS. THE REGRESSION LINE WAS FITTED USING THE LEAST SQUARE METHOD. THE $N=4$. PEARSON CORRELATION COEFFICIENT $R = 0.97$ REVEALED A GOOD CORRELATION BETWEEN THE BLOOD FLOW (PET RESULTS) AND CAPILLARY DENSITY (HISTOLOGICAL RESULTS).....	164
FIGURE 7.1: THE EXPERIMENTAL DESIGN FOR THE DIABETIC MODEL GROUPS.	172
FIGURE 7.2: MICE BODY WEIGHT (G) OF ALL GROUPS AT 13 WEEKS. DIABETIC MICE GAINED MORE WEIGHT OVER THE STUDY THAN LEAN MICE. DATA SHOWN AS INDIVIDUAL VALUES, MEAN AND SEM. A SIGNIFICANT INCREASE IN THE BODY WEIGHT AT WEEK 13 AMONG THE DIABETIC MICE, INCLUDING NV, WT AND LAV GROUPS, COMPARED TO THE LAV GROUP. SYMBOLS * $P < 0.05$, ** $P < 0.005$, *** < 0.0005 AND **** $P < 0.0001$ INDICATE STATISTICAL DIFFERENCE. THE ONE-WAY ANOVA WAS USED FOR THE STATISTICAL ANALYSIS IN THE DATA PRESENTED.....	176
FIGURE 7.3: CHEST HAIR REGROWTH AFTER DEPILATION. CHEST HAIR REGROWTH EVALUATION AT WEEK 4 (AFTER DEPILATION FOR ECHOCARDIOGRAPHY) WAS FASTER IN LAV-TREATED MICE THAN IN MICE GIVEN NV OR WT GENE THERAPY. THE SYMBOL **** INDICATES THERE IS A STATISTICAL SIGNIFICANCE BETWEEN THE COMPARED GROUPS ($P < 0.0001$). BOTH THE LAV AND LEAN GROUPS WERE SIMILAR IN THE HAIR RE-GROWTH RATE ($P = 0.20$). THE ONE-WAY ANOVA WAS USED FOR THE STATISTICAL ANALYSIS IN THE DATA PRESENTED.	177
FIGURE 7.4: THE SUVs FOR THE FOUR GROUPS. THE SYMBOL ** INDICATES A SIGNIFICANT DIFFERENCE ($P < 0.005$) BETWEEN THE LC (NON-DIABETIC) AND THE THREE DIABETIC GROUPS. THE SUVs WERE SIMILAR AMONG THE DIABETIC GROUPS ($P > 0.05$). THE ONE-WAY ANOVA WAS USED FOR THE STATISTICAL ANALYSIS IN THE DATA PRESENTED.	178
FIGURE 7.5: THE MGM VALUES FOR THE FOUR GROUPS IN THE UNIT OF ML/G/MIN. DATA SHOWN AS INDIVIDUAL VALUES, MEAN AND SEM. THERE WAS NO SIGNIFICANT DIFFERENCE ($P > 0.05$) BETWEEN THE THREE DIABETIC GROUPS. HOWEVER, THERE WAS A SIGNIFICANT DIFFERENCE BETWEEN THE LC GROUP AND BOTH NV AND WT GROUPS WITH P VALUES LESS THAN 0.0186 AND 0.0052 RESPECTIVELY. NOTABLY, THERE WAS NO SIGNIFICANT DIFFERENCE BETWEEN THE LC AND THE LAV-TREATED GROUPS ($P = 0.341$). THE ONE-WAY ANOVA WAS USED FOR THE STATISTICAL ANALYSIS IN THE DATA PRESENTED.	180
FIGURE 7.6: THE CO (ML/MIN) MEASURED BY THE ECHOCARDIOGRAPHY (AT WEEK 13) FOR THE PET/CT SCANNED MICE GROUPS. DATA SHOWN AS INDIVIDUAL VALUES, MEAN AND SEM. THERE WAS NO STATISTICAL DIFFERENCE BETWEEN THE DIABETIC GROUPS IN WHICH $P > 0.05$. HOWEVER, THE CO WAS SIGNIFICANTLY HIGHER IN THE LC (NON-DIABETIC) GROUP COMPARED TO THE DIABETIC GROUPS. SYMBOLS * $P < 0.05$, ** $P < 0.005$ INDICATE STATISTICAL DIFFERENCE. THE ONE-WAY ANOVA WAS USED FOR THE STATISTICAL ANALYSIS IN THE DATA PRESENTED.....	182
FIGURE 7.7: THE LVEF% MEASURED BY THE ECHOCARDIOGRAPHY (AT WEEK 13) FOR THE PET/CT SCANNED MICE GROUPS. DATA SHOWN AS INDIVIDUAL VALUES, MEAN AND SEM. THERE WAS NO STATISTICAL DIFFERENCE BETWEEN THE DIABETIC GROUPS IN WHICH $P > 0.05$. HOWEVER, THE LVEF% WAS SIGNIFICANTLY HIGHER IN THE LC (NON-DIABETIC) GROUP COMPARED TO THE DIABETIC GROUPS. SYMBOLS * $P < 0.05$, ** $P < 0.005$ INDICATE STATISTICAL DIFFERENCE. THE ONE-WAY ANOVA WAS USED FOR THE	

STATISTICAL ANALYSIS IN THE DATA PRESENTED. THE ONE-WAY ANOVA WAS USED FOR THE STATISTICAL ANALYSIS IN THE DATA PRESENTED. 182

FIGURE 7.8: THE ECHOCARDIOGRAPHY CO (ML/MIN) FOR ALL MICE GROUPS (AT WEEK13) INCLUDING THE SCANNED AND HARVESTED ONES (N=8/GROUP). THERE WAS A STATISTICAL DIFFERENCE BETWEEN THE LC COMPARED TO THE WT AND NV (DIABETIC GROUPS). THE CO VALUES OF THE LAV GROUP WERE STATISTICALLY HIGHER THAN THE OTHER DIABETIC GROUPS (WT AND NV). SYMBOLS *P<0.05, **P<0.005 INDICATE STATISTICAL DIFFERENCE. THE ONE-WAY ANOVA WAS USED FOR THE STATISTICAL ANALYSIS IN THE DATA PRESENTED. 183

FIGURE 7.9: THE ECHOCARDIOGRAPHY LVEF% FOR ALL MICE GROUPS (AT WEEK 13) INCLUDING THE SCANNED AND HARVESTED ONES (N=8/GROUP). THERE WAS A STATISTICAL DIFFERENCE BETWEEN THE LC COMPARED TO THE DIABETIC GROUPS. THE LVEF% VALUES FOR THE LAV GROUP WERE STATISTICALLY HIGHER THAN THE WT AND NV (DIABETIC) GROUPS. SYMBOLS *P<0.05, **P<0.005, *** < 0.0005 AND **** P < 0.0001 INDICATE STATISTICAL DIFFERENCE. THE ONE-WAY ANOVA WAS USED FOR THE STATISTICAL ANALYSIS IN THE DATA PRESENTED. 183

FIGURE 7.10: THE CAPILLARY DENSITY (UNIT OF N/MM²) IN THE FOUR GROUPS. THERE WAS A SIGNIFICANT DIFFERENCE BETWEEN THE LC (NON-DIABETIC) AND THE THREE DIABETIC GROUPS. IN ADDITION, THERE WAS ALSO A SIGNIFICANT INCREASE IN THE CAPILLARY DENSITY IN THE LAV GROUP COMPARED TO THE OTHER DIABETIC ONES. SYMBOLS *P<0.05, **P<0.005, *** < 0.0005 AND **** P < 0.0001 INDICATE STATISTICAL DIFFERENCE. THE ONE-WAY ANOVA WAS USED FOR THE STATISTICAL ANALYSIS IN THE DATA PRESENTED. 185

FIGURE 7.11: THE ARTERY DENSITY (UNIT OF N/MM²) IN THE FOUR GROUPS. THERE WAS A SIGNIFICANT DIFFERENCE BETWEEN THE LC (NON-DIABETIC) AND THE THREE DIABETIC GROUPS. IN ADDITION, THERE WAS ALSO A SIGNIFICANT INCREASE IN THE ARTERY DENSITY IN THE LAV GROUP COMPARED TO THE OTHER DIABETIC ONES. SYMBOLS *P<0.05, **P<0.005, *** < 0.0005 AND **** P < 0.0001 INDICATE STATISTICAL DIFFERENCE. THE ONE-WAY ANOVA WAS USED FOR THE STATISTICAL ANALYSIS IN THE DATA PRESENTED. 185

FIGURE 7.12: THE MGM (ML/G/MIN) VERSUS THE CO (ML/MIN) MEASURED USING PET AND ECHOCARDIOGRAPHY RESPECTIVELY. BOTH PARAMETERS WERE GENERATED FROM THE SAME MOUSE. THE GRAPH SHOWS A STRONG CORRESPONDENCE BETWEEN THE MGM AND THE CO. THERE WAS A STRONG POSITIVE CORRELATION BETWEEN THE TWO PARAMETERS IN WHICH THE PEARSON R WAS 0.893. 186

FIGURE 7.13: THE MGM MEASURED USING THE PET DATA (ML/G/MIN) VERSUS THE LVEF% MEASURED BY THE ECHOCARDIOGRAPHY. BOTH PARAMETERS WERE GENERATED FROM THE SAME MOUSE THE DATA IN THE GRAPH SHOWS A STRONG CORRESPONDENCE BETWEEN MGM AND THE LVEF%. THERE WAS A STRONG POSITIVE CORRELATION BETWEEN THE TWO PARAMETERS IN WHICH THE PEARSON R WAS 0.760. 186

FIGURE 7.14: THE MGM (ML/G/MIN) VERSUS THE CAPILLARY DENSITY (N/MM²) VALUES. THE TWO PARAMETERS WERE NOT GENERATED FROM THE SAME MOUSE. THE GRAPH SHOWS A STRONG CORRESPONDENCE BETWEEN THE MGM VALUES AND THE CAPILLARY DENSITY. THERE WAS A STRONG POSITIVE CORRELATION BETWEEN THE TWO PARAMETERS IN WHICH THE PEARSON R WAS 0.710. 187

FIGURE 7.15: THE MGM (ML/G/MIN) VERSUS THE ARTERY DENSITY (N/MM²) VALUES. THE TWO PARAMETERS WERE NOT GENERATED FROM THE SAME MOUSE. THE GRAPH SHOWS A STRONG CORRESPONDENCE BETWEEN THE MGM AND THE CAPILLARY DENSITY. THERE WAS A STRONG POSITIVE CORRELATION BETWEEN THE TWO PARAMETERS IN WHICH THE PEARSON R WAS 0.876. 187

FIGURE 8.1: LIFE PHASE EQUIVALENT FOR C57BL/6J MICE COMPARED WITH HUMANS BEINGS (CATHERINE HAGAN 2017)..... 194

FIGURE 8.2: THE EXPERIMENTAL DESIGN FOR THE AGEING MODEL OF THE EARLY TREATMENT GROUP..... 196

FIGURE 8.3: THE EXPERIMENTAL DESIGN FOR THE AGEING MODEL OF THE LATE TREATMENT GROUP. 197

FIGURE 8.4: THE MBF VALUES (ML/MIN/G) AT REST CONDITION FOR ALL THE MICE GROUPS DURING EARLY AND LATE TREATMENT. THE DATA ARE PRESENTED AS THE MEAN ± STD, N=6/GROUP. THERE WAS A STATISTICAL DIFFERENCE BETWEEN THE LAV GROUP COMPARED TO THE OTHER CONTROL GROUPS. THE SYMBOL * INDICATE STATISTICAL SIGNIFICANCE IN WHICH P VALUES IS * < 0.05, ** < 0.005, *** < 0.0005). THE ONE-WAY ANOVA WAS USED FOR THE STATISTICAL ANALYSIS IN THE DATA PRESENTED. 203

FIGURE 8.5: THE MBF VALUES AT REST CONDITION FOR ALL GROUPS DURING EARLY AND LATE TREATMENT. THE DATA ARE PRESENTED AS THE MEAN ± STD, AND THE N=3/GROUP AT EARLY TREATMENT PHASE AS WELL AS THE LATE ONE. THERE WAS NO SIGNIFICANT DIFFERENCE BETWEEN THE EARLY AND LATE TREATMENT WITHIN ALL GROUP. THE LAV SCORED HIGHER MBF VALUES IN THE LATE TREATMENT BUT NOT TO THE LEVEL OF STATISTICAL SIGNIFICANCE. NS INDICATE NO SIGNIFICANCE (P>0.05). THE TWO-WAY ANOVA WAS USED FOR THE STATISTICAL ANALYSIS IN THE DATA PRESENTED. 203

FIGURE 8.6: THE MBF VALUES AT REST AND STRESS CONDITIONS AMONG THE FOUR GROUP. THE DATA ARE PRESENTED AS THE MEAN ± STD. BOTH EARLY AND LATE TREATMENT MICE WERE INCLUDED IN THE GRAPH (N=5/GROUP AT REST AS WELL AS STRESS CONDITIONS). THE STRESS MBF HAD INCREASED SIGNIFICANTLY IN THE LAV GROUP COMPARED TO THE REST VALUES (P<0.005). THE RISE IN THE STRESS MBF WAS NOT SIGNIFICANT IN THE CONTROL GROUPS (P>0.05). THE WT GROUP SCORED LOWER MBF DURING STRESS COMPARED TO REST CONDITIONS. THE TWO-WAY ANOVA WAS USED FOR THE STATISTICAL ANALYSIS IN THE DATA PRESENTED. 204

FIGURE 8.7: THE MBF VALUES (ML/MIN/G) AT STRESS CONDITION FOR ALL THE MICE GROUPS DURING EARLY AND LATE TREATMENT (N=6/GROUP). THE DATA ARE PRESENTED AS THE MEAN ± STD THERE WAS A STATISTICAL DIFFERENCE BETWEEN THE LAV GROUP MBF STRESS VALUES COMPARED TO THE OTHER CONTROL GROUPS (P VALUES * < 0.05, ** < 0.005, *** < 0.0005). THE ONE-WAY ANOVA WAS USED FOR THE STATISTICAL ANALYSIS IN THE DATA PRESENTED. 204

FIGURE 8.8: THE LVEF% VALUES AMONG THE FOUR GROUPS AT EARLY TREATMENT. LVEF% WAS SIMILAR DURING THE EARLY TREATMENT PHASE WITHIN ALL THE GROUPS WITH P>0.05. THE DATA ARE PRESENTED AS MEAN ± STD, N=3/GROUP. THE SYMBOL NS REPRESENT NO SIGNIFICANT DIFFERENCE IN WHICH P>0.05. THE ONE-WAY ANOVA WAS USED FOR THE STATISTICAL ANALYSIS IN THE DATA PRESENTED. 207

FIGURE 8.9: THE LVEF% VALUES AMONG THE FOUR GROUPS AT LATE TREATMENT. THE LVEF% OF THE LAV GROUP WAS SIGNIFICANTLY HIGHER COMPARED TO THE OTHER CONTROL GROUPS WITH P<0.005. THE DATA ARE PRESENTED AS MEAN ± STD, N=3/GROUP. THE SYMBOL ** REPRESENT SIGNIFICANT DIFFERENCE IN WHICH P>0.005. THE ONE-WAY ANOVA WAS USED FOR THE STATISTICAL ANALYSIS IN THE DATA PRESENTED. 207

FIGURE 8.10: THE LVEF% VALUES AMONG THE FOUR GROUPS AT EARLY AND LATE TREATMENT. LVEF% WAS SIMILAR DURING THE EARLY AND LATE TREATMENT WITHIN THE CONTROL GROUPS WITH P>0.05. HOWEVER, THE LAV GROUP HAD A SIGNIFICANTLY HIGHER

VALUE IN THE LVEF% DURING THE LATE TREATMENT COMPARED WITH THEIR VALUES AT EARLY TREATMENT PHASE. THE DATA ARE PRESENTED AS MEAN \pm STD, N=6/GROUP IN WHICH IT SUBDIVIDED EQUALLY INTO EARLY AND LATE TREATMENT GROUPS. THE SYMBOL * REPRESENT SIGNIFICANT DIFFERENCE IN WHICH P <0.05. THE TWO-WAY ANOVA WAS USED FOR THE STATISTICAL ANALYSIS IN THE DATA PRESENTED. 208

FIGURE 8.11: THE CO VALUES (ML/MIN) AMONG THE FOUR GROUPS AT EARLY TREATMENT. THERE WAS A STATISTICAL DIFFERENCE BETWEEN THE LAV GROUP WITH RESPECT TO THE OTHER CONTROL ONES (N=3) (P<0.004). THE DATA ARE PRESENTED AS MEAN \pm STD. THE SYMBOL ** REPRESENT SIGNIFICANT DIFFERENCE IN WHICH P<0.005. THE ONE-WAY ANOVA WAS USED FOR THE STATISTICAL ANALYSIS IN THE DATA PRESENTED..... 208

FIGURE 8.12: THE CO VALUES (ML/MIN) AMONG THE FOUR GROUPS AT LATE TREATMENT. THERE WAS A STATISTICAL DIFFERENCE BETWEEN THE LAV GROUP WITH RESPECT TO THE OTHER CONTROL ONES (N=3) (P<0.004). THE DATA ARE PRESENTED AS MEAN \pm STD. THE SYMBOL * REPRESENT SIGNIFICANT DIFFERENCE IN WHICH P<0.05. THE ONE-WAY ANOVA WAS USED FOR THE STATISTICAL ANALYSIS IN THE DATA PRESENTED..... 209

FIGURE 8.13: THE CO VALUES (ML/MIN) AT EARLY AND LATE TREATMENT PHASES WITHIN EACH GROUP. THE DATA ARE PRESENTED AS MEAN \pm STD, N=3/TREATMENT PHASE/GROUP. THERE WAS NO STATISTICAL DIFFERENCE BETWEEN THE EARLY AND LATE TREATMENT ACROSS ALL THE GROUPS. THE SYMBOL (NS) REPRESENTS NO SIGNIFICANT DIFFERENCE IN WHICH P>0.05. THE TWO-WAY ANOVA WAS USED FOR THE STATISTICAL ANALYSIS IN THE DATA PRESENTED. 209

FIGURE 8.14: COMPARISON OF THE CAPILLARY DENSITY (N/MM²) FOR ALL GROUPS AT EARLY TREATMENT. THE DATA ARE PRESENTED AS MEAN \pm STD, N=6/GROUP. THE CAPILLARY DENSITY IN THE LAV GROUP WAS STATISTICALLY HIGHER THAN THE OTHER CONTROL GROUPS. THE SYMBOL * REPRESENTS SIGNIFICANT DIFFERENCE WITH P VALUES * < 0.05, ** < 0.005, *** < 0.0005. THE ONE-WAY ANOVA WAS USED FOR THE STATISTICAL ANALYSIS IN THE DATA PRESENTED. 211

FIGURE 8.15: COMPARISON OF THE ARTERY DENSITY (N/MM²) FOR ALL GROUPS AT EARLY TREATMENT. THE DATA ARE PRESENTED AS MEAN \pm STD, N=6/GROUP. THE ARTERY DENSITY IN THE LAV GROUP WAS STATISTICALLY HIGHER THAN THE OTHER CONTROL GROUPS. THE SYMBOL * REPRESENTS SIGNIFICANT DIFFERENCE WITH P VALUES * < 0.05, ** < 0.005, *** < 0.0005, ****<0.0001. THE ONE-WAY ANOVA WAS USED FOR THE STATISTICAL ANALYSIS IN THE DATA PRESENTED. 211

FIGURE 8.16: COMPARISON OF THE CAPILLARY DENSITY (N/MM²) FOR ALL GROUPS AT LATE TREATMENT. THE DATA ARE PRESENTED AS MEAN \pm STD, N=6/GROUP. THE CAPILLARY DENSITY IN THE LAV GROUP WAS STATISTICALLY HIGHER THAN THE OTHER CONTROL GROUPS. THE SYMBOL * REPRESENTS SIGNIFICANT DIFFERENCE WITH P VALUES * < 0.05, ** < 0.005, *** < 0.0005. THE ONE-WAY ANOVA WAS USED FOR THE STATISTICAL ANALYSIS IN THE DATA PRESENTED. 212

FIGURE 8.17: COMPARISON OF THE ARTERY DENSITY (N/MM²) FOR ALL GROUPS AT LATE TREATMENT. THE DATA ARE PRESENTED AS MEAN \pm STD, N=6/GROUP. THE ARTERY DENSITY IN THE LAV GROUP WAS STATISTICALLY HIGHER THAN THE OTHER CONTROL GROUPS. THE SYMBOL * REPRESENTS SIGNIFICANT DIFFERENCE WITH P VALUES *** < 0.0005. THE ONE-WAY ANOVA WAS USED FOR THE STATISTICAL ANALYSIS IN THE DATA PRESENTED..... 212

FIGURE 8.18: REPRESENTATIVE IMAGES OF ISOLECTIN B4 (GREEN) POSITIVE ENDOTHELIAL CELLS (REPRESENTING THE CAPILLARY DENSITY) AND α -SMOOTH MUSCLE ACTIN (RED) POSITIVE SMOOTH MUSCLE CELLS (REPRESENTING THE ARTERY DENSITY), WITH NUCLEI

IDENTIFIED BY DAPI (BLUE). THERE WAS A SIGNIFICANT INCREASE IN THE CAPILLARY AND ARTERY DENSITY IN THE LAV GROUP COMPARED TO THE OTHER CONTROL GROUPS AT BOTH EARLY AND LATE TREATMENT. 213

FIGURE 8.19: COMPARISON OF THE REST MBF VALUES (ML/MIN/G) FOR ALL THE AGED MICE GROUPS DURING EARLY AND LATE TREATMENT AND THE REST MBF VALUES OF THE HEALTHY YOUNG MICE. THE DATA ARE PRESENTED AS THE MEAN \pm STD, N=6/GROUP. THERE WAS A SIGNIFICANT INCREASE IN THE MBF VALUES IN THE HEALTHY MICE COMPARED TO THE CONTROL GROUPS INCLUDING NV AND WT (P VALUE < 0.005). THE LAV GROUP SHOWED SIMILAR REST MBF COMPARED TO HEALTHY YOUNG GROUP WITH NO STATISTICAL DIFFERENCE (NS). THE SYMBOL * INDICATE STATISTICAL SIGNIFICANCE IN WHICH P VALUES IS * < 0.05, ** < 0.005, *** < 0.0005 AND ****<0.0001). THE ONE-WAY ANOVA WAS USED FOR THE STATISTICAL ANALYSIS IN THE DATA PRESENTED. 214

FIGURE 8.20: SCATTER PLOT OF THE CO (ML/MIN) AS A FUNCTION OF THE MBF (ML/MIN/G). THE REGRESSION LINE WAS FITTED USING THE LEAST SQUARE METHOD. THE N=6/GROUP. PEARSON COEFFICIENT R = 0.713 SHOWS THAT THERE IS A STRONG CORRELATION BETWEEN THE CO AND THE MBF. 214

FIGURE 8.21: SCATTER PLOT OF THE CAPILLARY DENSITY (N/MM²) AS A FUNCTION OF THE MBF (ML/MIN/G). THE REGRESSION LINE WAS FITTED USING THE LEAST SQUARE METHOD. THE N=6/GROUP AND PEARSON COEFFICIENT R = 0.818 SHOWS THE EXISTENCE OF POSITIVE SIGNIFICANT CORRELATION BETWEEN THE CAPILLARY DENSITY AND THE MBF. 215

FIGURE 8.22: SCATTER PLOT OF THE CAPILLARY DENSITY (N/MM²) AS A FUNCTION OF THE CO (ML/MIN). THE REGRESSION LINE WAS FITTED USING THE LEAST SQUARE METHOD. THE N=6/GROUP AND PEARSON COEFFICIENT R = 0.683 SHOWS THE EXISTENCE OF POSITIVE SIGNIFICANT CORRELATION BETWEEN THE CAPILLARY DENSITY AND THE CO. 215

List of Tables:

TABLE 2.1: RISK FACTORS ASSOCIATED WITH THE CVDs. THE CVDs RISK FACTORS CAN BE DIVIDED INTO MODIFIABLE AND NON-MODIFIABLE RISK FACTORS. THE LIST OF CVDs RISK FACTORS IS EXTENSIVE, AND THEY ARE BEYOND THE SCOPE OF THIS THESIS.	30
TABLE 3.1: MEDISO NANO-SCAN 122S SMALL-BORE PET/CT IMAGING SYSTEM MANUFACTURED BY MEDISO MEDICAL IMAGING SYSTEM, BUDAPEST, HUNGARY.	71
TABLE 3.2: THE PHYSICAL CHARACTERISTICS OF BOTH ^{18}F -FDG AND ^{13}N -NH ₃ (WIELAND ET AL. 1991).....	71
TABLE 4.1: THE PHYSICAL CHARACTERISTICS INCLUDING $T_{1/2}$ AND PR OF BOTH ^{18}F AND ^{13}N (MADDAHI AND PACKARD 2014).....	88
TABLE 4.2: SHOWS THE IQ PHANTOM REGIONS.....	95
TABLE 4.3: THE PET IMAGE ACQUISITIONS, CORRECTIONS AND RECONSTRUCTION METHODS APPLIED IN THE IMAGE QUALITY PHANTOM TEST USING THE NEMA NU 4-2008 STANDARD.....	98
TABLE 4.4: THE REASONABLE VALUES OF THE RCs OF THE RODS ACCORDING TO THE NEMA NU 4 – 2008 STANDARDS.....	100
TABLE 4.5: THE REASONABLE VALUES RECOMMENDED BY NEMA NU 4 – 2008 STANDARDS FOR THE UNIFORMITY STD% AND SOR _{STD%} FOR BOTH COMPARTMENTS.	100
TABLE 4.6: SHOWS THE RC VALUES AND THEIR STD% FOR THE FIVE RODS IN THE FOUR REPEATED IQ TESTS OF ^{18}F	102
TABLE 4.7: SHOWS THE RC VALUES AND THEIR STD% FOR THE FIVE RODS IN THE FOUR REPEATED IQ TESTS OF ^{13}N	103
TABLE 4.8: THE MAXIMUM, MINIMUM, AND STD% VALUES THAT WERE RECORDED IN THE UNIFORM REGION FOR ^{18}F IN THE FOUR IQ TESTS.....	103
TABLE 4.9: THE MAXIMUM, MINIMUM, AND STD% VALUES THAT WERE RECORDED IN THE UNIFORM REGION FOR ^{13}N IN THE FOUR IQ TESTS.....	103
TABLE 4.10: THE SOR AND STD% VALUES FOR ^{18}F IN THE AIR AND WATER COMPARTMENTS.	104
TABLE 4.11: THE SOR AND STD% VALUES FOR ^{13}N IN THE AIR AND WATER COMPARTMENTS.	104
TABLE 4.12: THE MULTIPLE COMPARISON TESTS THAT WERE APPLIED FOR ^{18}F & ^{13}N . THE P-VALUES SHOWED THAT THERE WERE STATISTICAL DIFFERENCES IN THE 1-, 2-, 3-, AND 4-MM ROD SIZES. HOWEVER, IN THE 5-MM ROD THERE WERE NO STATISTICAL DIFFERENCES BETWEEN THE TWO RADIOTRACERS.	107
TABLE 5.1: THE MBF VALUES DURING REST AND STRESS CONDITIONS IN THE ADENOSINE GROUP IN UNIT OF ML/MIN/G.	136
TABLE 5.2: THE MBF VALUES DURING REST AND STRESS CONDITIONS IN THE DOBUTAMINE GROUP IN UNIT OF ML/MIN/G.	137
PHYSICAL CONDITION	139
^{18}F -FDG SCAN MGM (K_{FDG}) IN A UNIT OF ML/G/MIN	139
TABLE 5.3: THE MGM (K_{FDG}) UPTAKE IN ML/MIN/G IN HEALTHY MICE DERIVED FROM THE TACS OF THE LV DURING THE 10-40 AND 15-20 MINUTES OF THE FDG SCAN RESPECTIVELY.	139
TABLE 5.4: THE SUVs FOR FDG AND ^{13}N -NH ₃ REST SCANS IN HEALTHY MICE. THE VALUES WERE DERIVED FROM AVERAGING THE VOIs OF THE LV DURING THE WHOLE DURATION OF THE DYNAMIC SCANS. THE CORRELATION VALUE BETWEEN THE TWO SUVs GROUP WAS 0.8216, INDICATING A GOOD POSITIVE CORRELATION.	139

TABLE 6.1: THE BLOOD FLOW AND BLOOD FLOW RATIO FOR BOTH LEGS IN ALL MICE PRE- AND POST-SURGERY AT DAY 0, 3, AND 7. THE FLOW IN THE LEFT LEG WAS REDUCED FOLLOWING SURGICAL LIGATION.....	155
TABLE 6.2: THE BLOOD FLOW VALUES (ML/MIN/G) FOR BOTH LEGS USING ¹³ N-NH ₃ AND 1TC.	157
TABLE 6.3: THE CALCULATED SUVs FOR BOTH LEGS USING 18F-FDG SCANS.	157
TABLE 6.4: THE CAPILLARY AND ARTERY DENSITY IN (N/MM ²) IN BOTH THE NORMAL AND LIGATED LEGS.	160
TABLE 7.1: THE SUVs FOR ALL THE GROUPS. THERE WAS A SIGNIFICANT DIFFERENCE BETWEEN THE LEAN GROUP (NON-DIABETIC) AND THE DIABETIC GROUPS (P<0.005).	178
TABLE 7.2: THE MGM VALUES FOR ALL THE GROUPS IN THE UNIT OF ML/G/MIN. THERE WAS A SIGNIFICANT DIFFERENCE BETWEEN THE LEAN GROUP (NON-DIABETIC) AND THE DIABETIC GROUPS (P VALUES WERE <0.005).	179
TABLE 7.3: ECHOCARDIOGRAPHY (AT WEEK 13) FOR ALL MICE GROUPS THAT WERE SCANNED WITH PET/CT SCANNER.....	181
TABLE 7.4: THE ECHOCARDIOGRAPHY RESULTS FOR ALL MICE IN THE FOUR GROUPS. THE HEALTHY LC GROUP WAS SIGNIFICANTLY HIGHER IN ALL THE PARAMETERS COMPARED TO THE DIABETIC GROUPS AT 13 WEEKS. IMPORTANTLY, THERE WAS A STATISTICAL DIFFERENCE BETWEEN THE LAV GROUP VS. THE OTHER TWO DIABETIC IN TERMS OF LVEF%, CO AND LV MASS AT 13 WEEKS.....	181
TABLE 7.5: THE CAPILLARY AND ARTERY DENSITY OF ALL THE HARVESTED MICE GROUPS.....	184
TABLE 8.1: THE MBF VALUES (ML/MIN/G) UNDER THE REST AND STRESS CONDITIONS DURING EARLY AND LATE TREATMENT PHASES ALONG WITH THEIR RECORDED HR, CFR, CO. THE CO (MEASURED BY THE ECHOCARDIOGRAPHY IN ML/MIN) WERE RECORDED FOR EACH MOUSE. THE CFR VALUES (MBF AT STRESS/MBF AT REST) WERE CALCULATED FOR ALL GROUPS. THE PEARSON CORRELATION COEFFICIENT (R) MEASURED BETWEEN THE MBF AT REST AND THE CO WAS 0.713 INDICATING A STRONG POSITIVE RELATION BETWEEN THEM.....	202
TABLE 8.2: THE ECHOCARDIOGRAPHY MEASUREMENTS FOR ALL THE GROUPS AT EARLY AND LATE TREATMENT.....	206
TABLE 8.3: THE CAPILLARY AND ARTERY DENSITY (#/MM ²) FOR ALL THE GROUPS AT EARLY AND LATE TREATMENT.	210

Chapter 1:

Overview

1.1 Thesis Overview:

Cardiovascular diseases (CVDs) are the leading causes of death worldwide. There are many types of CVDs, including coronary artery diseases (CADs), peripheral artery diseases (PADs), congenital and infected heart diseases, clotting and venous diseases, cerebrovascular diseases, and aortic diseases (Wang et al. 2010). The incidence of CVDs is known to increase when associated with risk factors such as diabetes mellitus (DM), age, family history, high cholesterol, and high blood pressure (hypertension) (Flora and Nayak 2019; Sun et al. 2020). To better assess CVDs and associated risk factors, clinicians have extensively used measurement tools and imaging modalities to achieve accurate diagnoses and subsequently apply the best treatment plan (Saraste et al. 2009; Jones et al. 2014).

Cardiac imaging is used as a tool to evaluate cardiac function through the possibility to quantify or measure different types of physiological indices or biomarkers by generating structural and functional information concerning the cardiovascular system (CVS) in homeostasis and in pathological conditions (Pien et al. 2005; Wang et al. 2010; Lin et al. 2014). Further information can be obtained by monitoring the heart in different physiological states, including rest and stress (Shrestha and Seo 2015; Guerraty et al. 2020). These imaging modalities include ultrasound (US) imaging, magnetic resonance imaging (MRI), X-ray computed tomography (CT) imaging and positron emission tomography (PET) imaging (Jones et al. 2014). These modalities vary in sensitivity and resolution perspectives, as they produce data via different molecular or physical mechanisms and over different time scales (Santos et al. 2015). Molecular changes are initiated prior to any morphological changes being detectable. As the molecular and systematic changes interact via feed-back loops, there could be major advantages in the early observation of the molecular changes (Liu and Gotlieb 2010; Gotlieb 2020).

PET imaging is a molecular imaging modality that allows the non-invasive detection of metabolism, biological function, and blood flow changes (Mawlawi and Townsend ; Rischpler et al. 2012; Nappi and El Fakhri 2013; Slomka et al. 2014; Gotlieb 2018). It involves the administration of positron-emitting radiotracers that can detect and track metabolic changes on molecular and cellular scales (Bertoldo et al. 2014; Maddahi and Packard 2014). Most modern PET scanners are integrated with a

CT system, generating both functional and structural information. This information can be used to differentiate between normal and abnormal tissues, detecting changes in the cardiac metabolic pathways initiated at any disease onset, thus avoiding gross structural changes within the CVS and early treatment (Di Carli et al. 2007).

Depending on the aim of the study, PET/CT imaging could quantify physiological indices, such as cardiac metabolism (CM) and myocardial blood flow (MBF), through using the concepts of pharmacokinetic modelling (Morris et al. 2004; Watabe et al. 2006; Turkheimer et al. 2014; Cochran et al. 2017). Indeed, PET/CT imaging is the gold standard of non-invasive quantification of MBF (Schöder et al. 1999; Kaufmann and Camici 2005; Ziadi and Beanlands 2010). Much evidence suggests that measurement of CM and MBF can play a crucial role in diagnosing CVDs and evaluating novel drugs or treatment trials (J et al. 1993; Schöder et al. 1999; Ziadi and Beanlands 2010; Slomka et al. 2014; Guerraty et al. 2020).

The genetics of long-living individuals plays a vital role to protect them against age-related diseases, as demonstrated by Genome-wide association studies (Erikson et al. 2016; Deelen et al. 2019). Their progeny also has a low rate of CVDs, indicating that healthy phenotype can be transferred vertically through generations (Villa et al. 2015a; Dang et al. 2020; Dossena et al. 2020). These findings inspire the idea of transferring healthy genes as a novel method for treating CVDs, especially with diabetic or aged individuals (Dang et al. 2020).

We have identified a variant of the BPI fold– containing family B member 4/palate lung and nasal epithelium clone 4 (BPIFB4/ LPLUNC4) that is associated with healthy longevity in several groups of long-lived individuals. Studies have recently been undertaken or are ongoing regarding alterations in immunity and CVDs in these ‘super-centenarians’, in an effort to understand where and how the longevity associated variant (LAV) exerts its effect (Villa et al. 2015a; Villa et al. 2015c; Spinelli et al. 2017; Villa et al. 2018; Di Pardo et al. 2020). Moreover, these studies also reported that forcing the expression of the longevity-associated variant (LAV) gene that encodes the BPIFB4 protein (also called LAV- BPIFB4) in an aged cohort, has repaired age-related endothelial dysfunction (Villa et al. 2015a; Villa et al. 2015c; Spinelli et al. 2017; Villa et al. 2018; Liberale and Camici 2020). Further studies using mouse models have demonstrated a beneficial effect of LAV gene treatment in improving vascular reparative processes through activating certain signalling pathways and reduce endothelial dysfunction (Spinelli et al. 2017; Villa et al. 2018; Malavolta et al. 2019).

Therefore, LAV- BPIFB4 could be an exciting and novel treatment for CVDs, diabetes, and age-related diseases, but these diseases have a complex pathogenic basis that should not be examined using

histological or structural imaging alone. PET/CT imaging is a diagnostic tool that merges the concepts of anatomical and molecular information and allows early detection of metabolic changes at a molecular level by providing prognostic information or quantitative measurement of vital biomarkers. Taken together, this means that PET/CT is beneficial diagnostic tool to investigate a biological process and therapeutic intervention.

1.2 Thesis Hypothesis:

The small Mediso PET/CT scanner is suitable to evaluate cardiac function and therefore determine the suitability of treatments in murine models of diabetes and ageing.

1.3 Thesis objectives:

In this thesis I will evaluate the feasibility of the micro-PET/CT system to evaluate cardiac function in mice using ^{18}F fluorine labelled fluorodeoxyglucose (^{18}F -FDG) and ^{13}N Nitrogen labelled ammonia (^{13}N - NH_3) as radiotracers of choice. First, Mediso micro-PET/CT system will be evaluated in terms of generated image quality for both radiotracers and according to methodological guidelines supplied by the National Electrical Manufacturers Association (NEMA) standard for preclinical PET/CT scanners and the manufacturer's instructions to ensure the highest possible accuracy of the obtained results. After that, I will develop and standardize imaging protocols to assess myocardial glucose metabolism (MGM) and MBF using ^{18}F -FDG and ^{13}N - NH_3 in a murine model. These protocols will be further validated using a diseased model, namely hindlimb ischemia (HLI) model, to test the ability of PET/CT imaging in detecting metabolic and blood flow changes. Importantly, these protocols will be further applied to investigate the efficiency of the LAV- BPIFB4 gene as a promising treatment to improve cardiac function, angiogenesis, and cell survival in different murine models, including diabetic, ageing models.

1.3.1 Objectives outline:

1. Evaluate the quantitative accuracy of Mediso micro-PET/CT scanner using ^{18}F -FDG and ^{13}N - NH_3 according to NEMA standards and manufacturer guidelines.
2. Standardizing PET/CT imaging protocols in healthy mice to measure MGM and MBF using ^{18}F -FDG and ^{13}N - NH_3 , respectively.
3. Since HLI is one of the main complications caused by diabetes and CVDs, HLI model will be used to test the ability of PET/CT imaging in detecting metabolic and blood flow changes.
4. Applying the standardized imaging protocols in two murine models to test the efficacy of LAV- BPIFB4 gene in improving cardiomyocyte function and MBF. These models include:

- Diabetic model.
- Ageing model.

1.4 Thesis outline:

This chapter includes a brief overview, thesis rationale and objectives of the research. The next chapter will discuss the essential clinical and physical background as well as a general introduction that should lead the reader from the general subject area into our topic that will be investigated. Chapter 3 is the methodology chapter, which contains most of the methodological aspects that were applied in the thesis; still, more details will be explained in each relevant chapter. In Chapter 4 I will evaluate both ^{18}F -FDG and ^{13}N - NH_3 as radiotracers of choice to achieve accurate PET quantification in terms of image quality and according to NEMA standards. Chapter 5 covers the experiments done to optimize and standardize the imaging protocols along with quantifications of MGM and MBF among healthy mice. This chapter will also discuss the different technical challenges associated with the murine model and micro-PET/CT and how they were tackled. After that, chapter 6 will explore the ability of the micro-PET/CT scanner to detect changes in myocardial blood following HLI. In addition, chapters 7 and 8 will use the previously validated imaging protocols on diabetic and ageing respectively to test the effects of LAV gene therapy on cardiac function and MBF. General discussion identifying the novelty of the research along with a general conclusion, recommendations, and possible future work will be included in Chapters 9 and 10 respectively. For simplicity purposes, the thesis structure is represented using a schematic diagram in Figure 1.1.

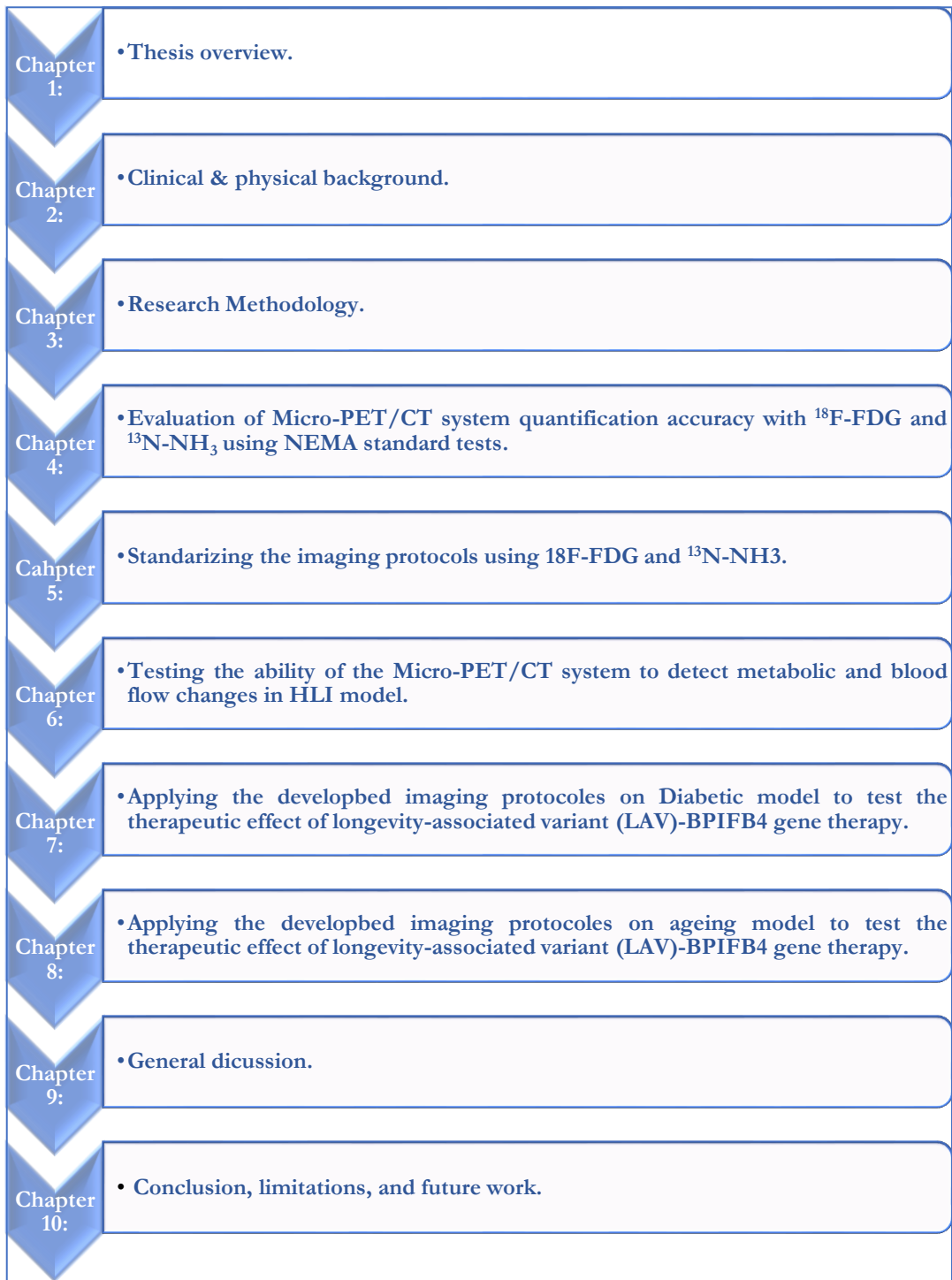


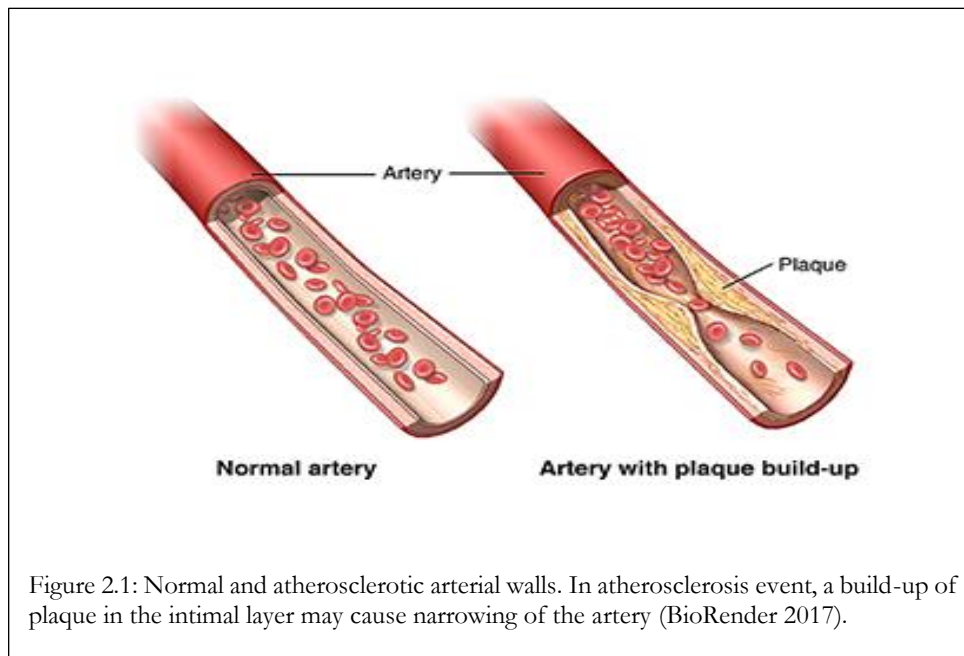
Figure 1.1: Flow chart for the thesis structure.

Chapter 2:

General Background

2.1 Introduction:

CVDs are among the leading causes of death worldwide despite the significant advances in the medical field and diagnostic technologies (Wang et al. 2016a; Kishore et al. 2018). They are defined as any disorder associated with the heart, blood vessels in the body, and blood (Keating and Sanguinetti 1996; Gotlieb 2020; Sun et al. 2020). The underlying pathogenesis of many CVDs is the development of atherosclerosis plaques (Keating and Sanguinetti 1996; Chien 2004; Liu and Gotlieb 2010; Chan et al. 2012; Gotlieb 2020). Atherosclerotic plaque formation occurs in the intimal layer of the arteries, resulting in narrowing and eventual hardening of the arterial walls, as in figure 2.1 (Libby et al. 2019). The plaque consists of fat, cholesterol, calcium, fibrin and other cellular waste products (Oikonomou et al. 2018). In addition, atherosclerotic events and plaque formation contribute to several types of CVDs such as CADs, cerebrovascular diseases, aortic diseases, PADs, myocardial infarction (MI), stroke, cardiac arrhythmia, and heart failure (Sun et al. 2020).



2.2 Risk factors associated with CVDs:

The identification of CVDs risk factors has played a crucial role in treating and preventing them (Berenson et al. 2005; Flora and Nayak 2019). Researchers have classified these risk factors into modifiable and nonmodifiable risk factors, some of which are outlined in table 2.1 (Flora and Nayak 2019). Modifiable risk factors are defined as the factors that can be changed or managed under clinical supervision (Flora and Nayak 2019; Şahin and İlgün 2022). The main modifiable risk factors include DM, hypertension (high blood pressure), and hyperglycaemia (high blood sugar) (Flora and Nayak 2019; Şahin and İlgün 2022). Considerable evidence has shown that early diagnosis and treatment of modifiable risk factors could significantly prevent the incidence of CVDs (Flora and Nayak 2019; Şahin and İlgün 2022). On the other hand, the non-modifiable risk factors cannot be changed, including age, gender and genetic factors (Flora and Nayak 2019).

Modifiable risk factors	Non-Modifiable risk factors
Food diet	Age
Sedentary lifestyle	Gender
Smoking	Genetic or heredity factors
Hypertension	Autoimmune diseases

Table 2.1: Risk factors associated with the CVDs. The CVDs risk factors can be divided into modifiable and non-modifiable risk factors. The list of CVDs risk factors is extensive, and they are beyond the scope of this thesis.

2.3 Overview of Cardiovascular system (CVS):

Before proceeding to the molecular base of CVDs, a brief introduction to the cardiovascular system (CVS) is needed. The CVS components include of the heart, blood vessels, and blood, and its function is to deliver oxygenated blood to all the body's system as well as taking away carbon dioxide and waste in a closed-loop system (Aaronson et al. 2020). There are two types of circulation: arterial and venous circulation (Aaronson et al. 2020). In arterial circulation, oxygen-rich blood is pumped to the whole body but with one exception in which the pulmonary veins carry the oxygenated blood from the lung to the heart (Aaronson et al. 2020). In contrast, the venous circulation returns the deoxygenated blood and waste from body systems to the heart for oxygenation processes to occur (Aaronson et al. 2020). Each CVS component has its cellular and histological structures as well as its physiological function, but they share many similarities in terms of histological structure.

Firstly, in mammals the heart is a four-chamber organ that pumps blood to the whole body (Aaronson et al. 2020). The four chambers include the right atrium (RA), right ventricle (RV), left

atrium (LA), and left ventricle (LV) as illustrated in figure 2.2 (Aaronson et al. 2020). During venous circulation, the deoxygenated blood enters the RA and passes to the RV, which pumps it to the lung for gas exchange to occur (Aaronson et al. 2020). Following oxygenation, the blood is transported back to the LA through the pulmonary veins. The blood is then transported into the LV (the largest chamber), which pumps it to the whole body via the aorta, the largest artery in the circulatory system. In addition, the heart muscle gets its blood supply from coronary circulation, in which the right and left coronary arteries branch off from the aorta. Some of the disorders that affect the coronary arteries might lead to CADs which are caused by narrowing or blockage of the coronary circulation (Walden and Tomlinson 2011).

Histologically, the heart consists of three layers which are the epicardium (the outer layer responsible for the structural support of the heart), the myocardium (the middle layer where the contractile and conduction events occur), and the endocardium (the inner layer that is the heart cavity lining and vessels) as in figure 2.2 (Anderson et al. 2013). On the cellular basis, the heart consists of cardiomyocytes (CMs) which account for ~70–85% of the heart volume, fibroblasts (FBs), endothelial cells (ECs), and perivascular cells (Anderson et al. 2013; Aaronson et al. 2020).

Secondly, the blood vessels are responsible for carrying blood around the body. The walls of large arteries consist of three layers; the tunica intima (including the endothelium (where direct blood contact occurs) and intimal smooth muscle cells (SMCs) and their matrix (smaller arteries may not have SMC in the intima)), the tunica media (the middle and thickest layer consisting of multiple lamellae of SMC and extracellular matrix (ECM) such as collagen and elastin), and the tunica externa or adventitia (the outermost layer which is made of cells and loose collagen fibers) as seen in figure 2.3 (Crock 1996). On the other hand, the veins carry out the deoxygenated blood and waste from the body's systems back to the heart. Similar to arteries, the veins have three layers but with smaller amounts of smooth muscle and elastic tissue, thinner walls and bigger lumens when compared to arteries. Moreover, capillaries allow the interchange of nutrients and wastes between the blood and the tissue cells.

Finally, the blood is the transport medium that has both cellular and non-cellular components (Basu and Kulkarni 2014; Aaronson et al. 2020). The cellular one's can be represented mainly by red blood cells (erythrocytes), white blood cells (leukocytes), and platelets (Basu and Kulkarni 2014). Plasma and is made of 90% water, dissolved nutrients, such as gases, hormones, proteins, ions and many more enzymes, cytokines, growth and clotting factors (Basu and Kulkarni 2014).

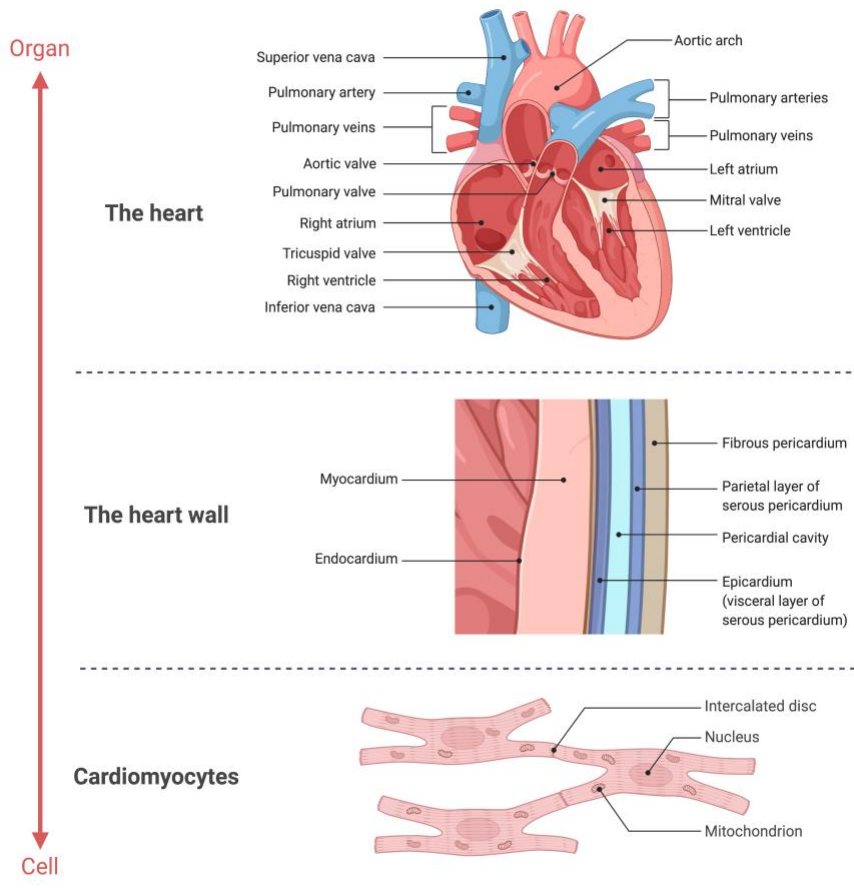
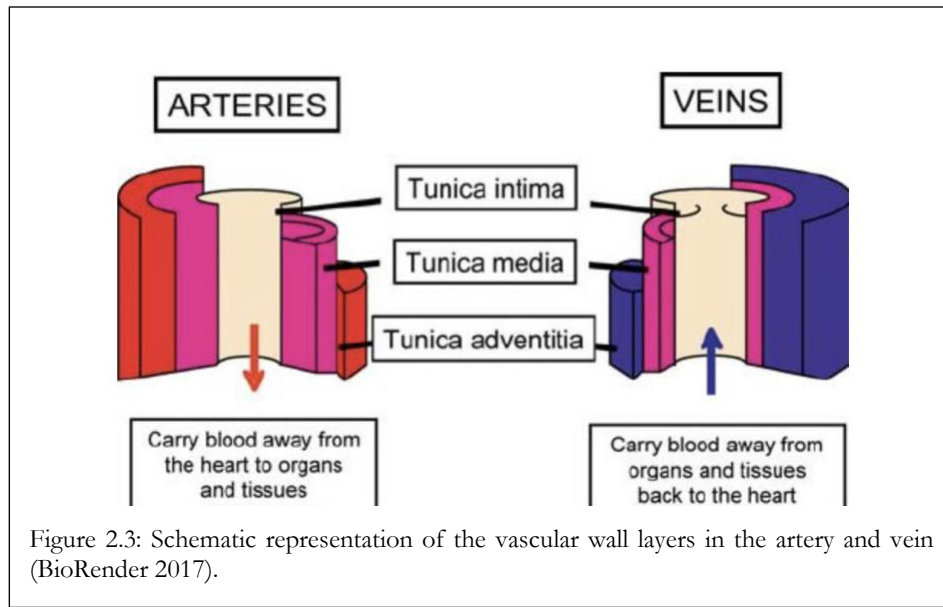


Figure 2.2: Schematic representation of the mammalian heart. Included the anatomy of the four chambers, representation of the myocardial histological layers and a cartoon of the main cellular component of the heart which is the cardiomyocytes (BioRender 2017).



2.4 The metabolic and genetic adaptation during CVDs:

During pathological condition, the cardiac muscle undergoes some metabolic changes to enhance cell survival (Gewirtz and Dilsizian 2017; Kolwicz 2018). These adaptations involve changes in cardiomyocyte fuel source and its utilization in response to disease onset (Gewirtz and Dilsizian 2017; Kolwicz 2018). Various studies reported an adjustment in adenosine triphosphate (ATP) generation in mitochondria characterized by a switch from β -oxidation of fatty acid (FA), as a primary source of energy, to glucose oxidative metabolism (Krebs cycle) (Keating and Sanguinetti 1996; Depre et al. 1999; Kolwicz and Tian 2011; Kolwicz et al. 2013; Kundu et al. 2015). Nonetheless, this switch does not exclude fatty acid oxidation, which is the favoured process under normal conditions (Depre et al. 1999; Kolwicz et al. 2013; Werner et al. 2016). Indeed, both energy sources, FA, and glucose participate differently under variable physiological, pathological, or metabolic conditions (Schulze et al. 2016; Werner et al. 2016; Young 2016).

Several investigations have reported changes in gene expression in human and animal models in response to disease, physiological or environmental conditions (Shoghi et al. 2008; Stefano et al. 2016; Lee et al. 2017). In addition, several genetic programs are activated in the case of ischemia that appear to increase cell survival (Kalogeris et al. 2016; Gewirtz and Dilsizian 2017). These genetic programs may also affect fatty acid and glucose metabolism (Kalogeris et al. 2016; Gewirtz and Dilsizian 2017).

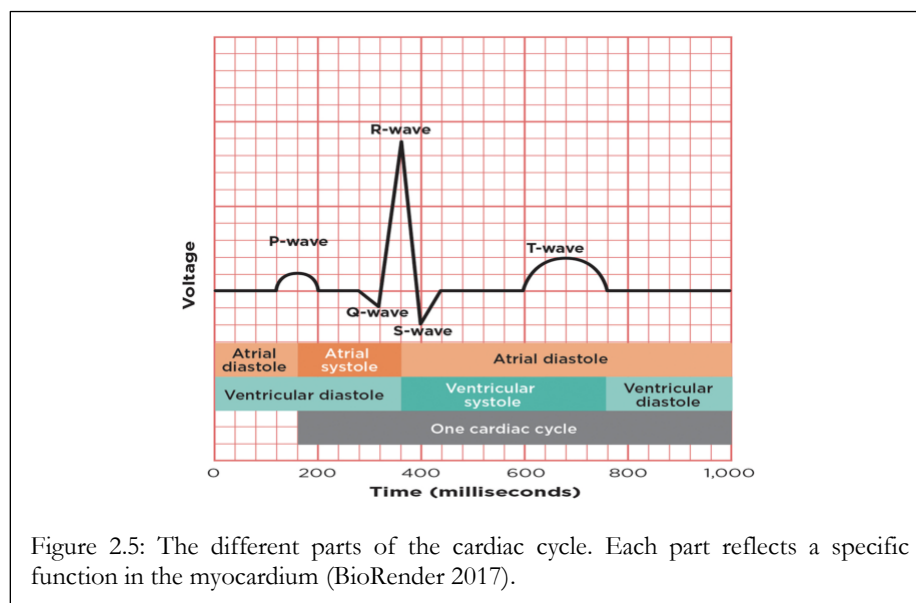
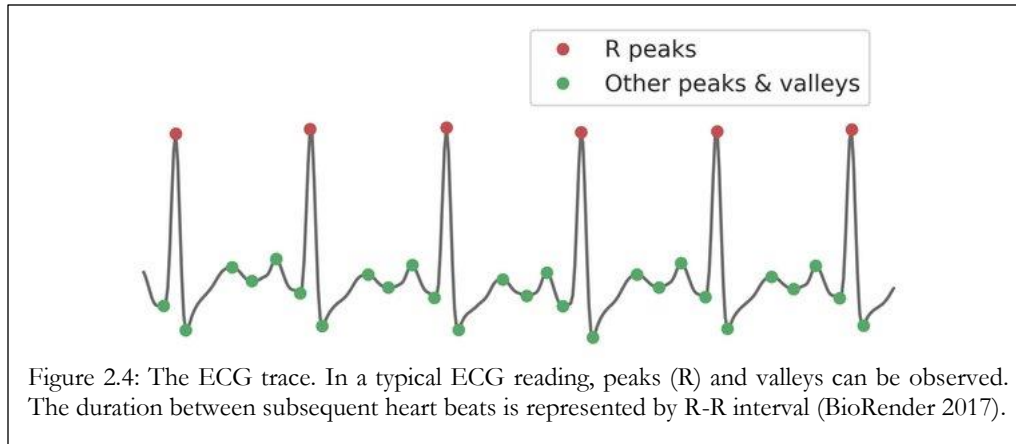
Assessing the onset of CVDs is challenging due to its multifactorial origins resulting from the interplay between genetic and environmental factors (Chien 2004; Liu and Gotlieb 2010; Gotlieb

2020). In addition, genetic factors might be an important aspect to investigate CVDs and possible treatments (Walden and Tomlinson 2011). Some evidence have assumed that once a disease gene is identified, its encoded protein can be investigated to determine the disease-associated mutation (Muller 1994; Flora and Nayak 2019). Accordingly, disease prediction, diagnosis, prevention, and treatment can be aided by genetic testing and gene therapy (Levi and Coronel 1997; Sinnaeve et al. 1999; Khurana et al. 2001; Morishita 2002).

2.5 Ways to evaluate or scan the CVS:

In recent years, a number of studies in the field of CVS measurement and imaging has led to a better understanding of normal and abnormal health states (Wang et al. 2010; Jones et al. 2014; Santos et al. 2015). The various imaging modalities enable the visualization of the structure and function of CVS as well as quantifying vital biomarkers that can allow early detection of pathological conditions or test the effectiveness of novel drugs (Saraste et al. 2009; Jones et al. 2014). Each modality can provide various range of spatial, temporal, structural, and functional information concerning CVS and CVDs (Jones et al. 2014). They include electrocardiogram (ECG), echocardiography, laser doppler imaging, MRI, X-ray CT imaging and PET imaging (Saraste et al. 2009; Phoon and Turnbull 2016; Lindsey et al. 2018; Rehman et al. 2021). All medical modalities will be described briefly except for PET/CT imaging which will be described comprehensively, covering most of its aspects, as the main scope of this research.

First, ECG is the cheapest and simplest measurement tool of the CVS, but it is on a non-imaging basis (Jones et al. 2014). It can detect abnormalities in the electrical activity of the heart by placing electrodes over the body through which it can trace and measure heart electrical signals (Jones et al. 2014; Serhani et al. 2020). The output measurement is in the form of a graph which is divided into different segments called peaks and valleys as seen in figure 2.4 (Jones et al. 2014). Each part of the graph represents a function in a certain area of the heart as in figure 2.4 (Jones et al. 2014). Through the ECG graph, only the structural abnormalities can be revealed, which could be considered as a late stage in any disease condition (Jones et al. 2014). As a result, the ECG cannot measure the blood flow or pumping capability of the heart, and it also might underestimate some of the heart regions (Jones et al. 2014). Recently, some imaging modalities offered a scanning option that is coupled with an ECG tool, and this provides an additional source of information on a beat-by-beat basis, such as gated PET imaging (Juarez-Orozco et al. 2019). This will be handled in more detail in the relevant sections.



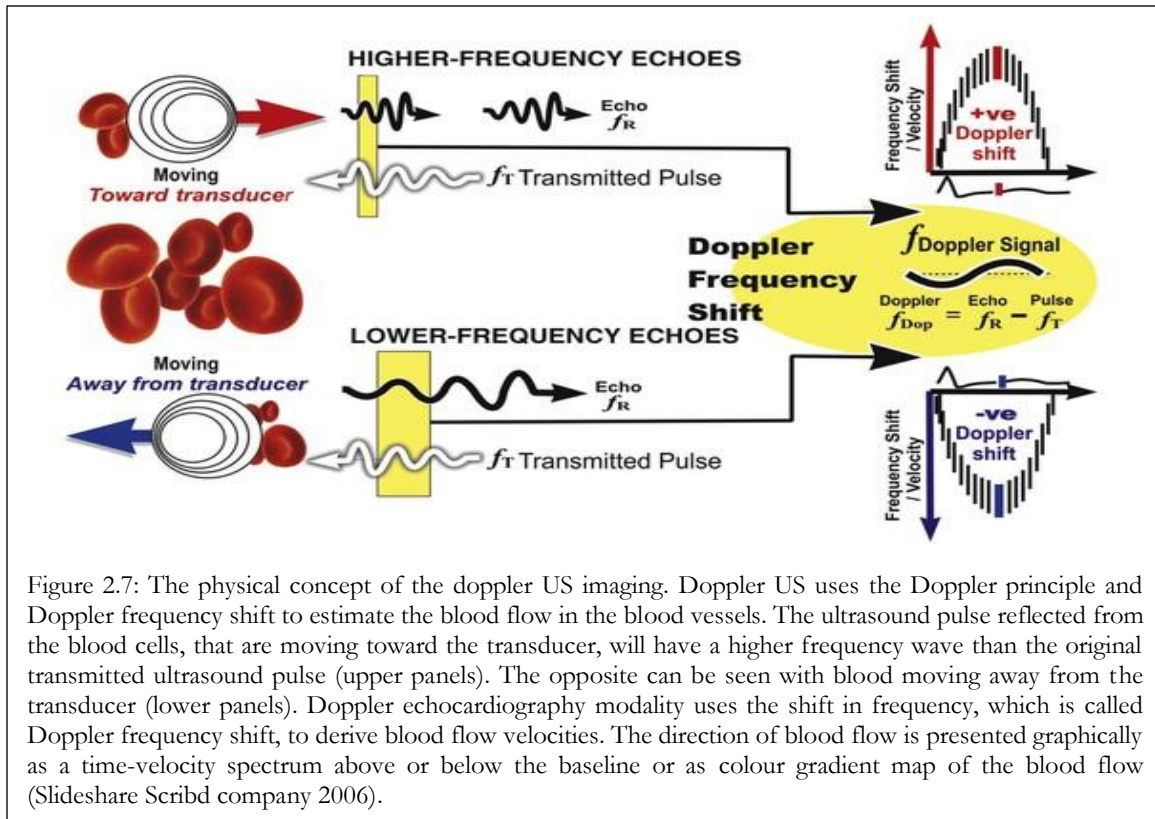
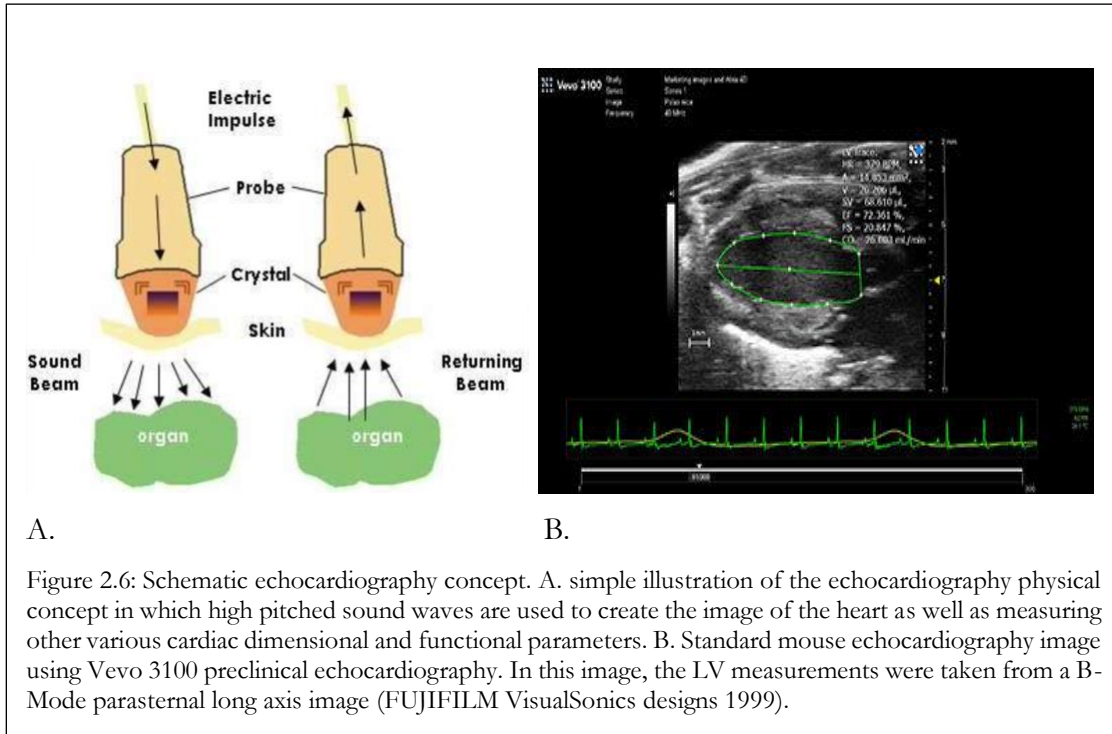
In contrast, echocardiography is a non-invasive imaging modality that allows the measurement of cardiac volume, the visualization of wall motion and structural defects, and the assessment of cardiac valve or intracardiac masses (Jones et al. 2014; Rehman et al. 2021). This tool is based on using a transducer that is held against the skin and emits ultrasound waves (ranging between 8-18 MHz) which travel through the blood and soft tissue and then get reflected as in figure 2.6 (Villanueva and Wagner 2008). Consequently, the reflected waves are detected again by the transducer and digitized to generate a real-time dynamic image of the heart with a longitudinal resolution of 150 μm and a frame rate (FR) of 15-40 frames per second (Villanueva and Wagner 2008). Additionally, denser tissue has a brighter appearance in the images because they reflect more waves (Villanueva and Wagner 2008). The produced images can either be 2-dimensional (2D) or 3- dimensional (3D) images and are used to measure different cardiac structural and physiological parameters (Villanueva and Wagner 2008).

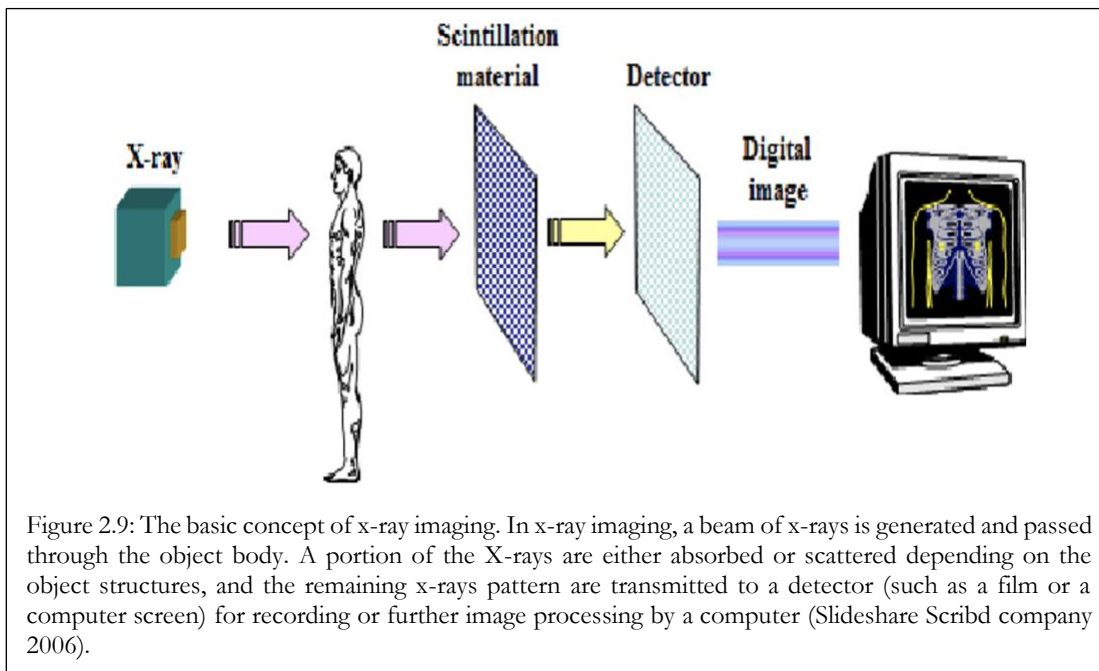
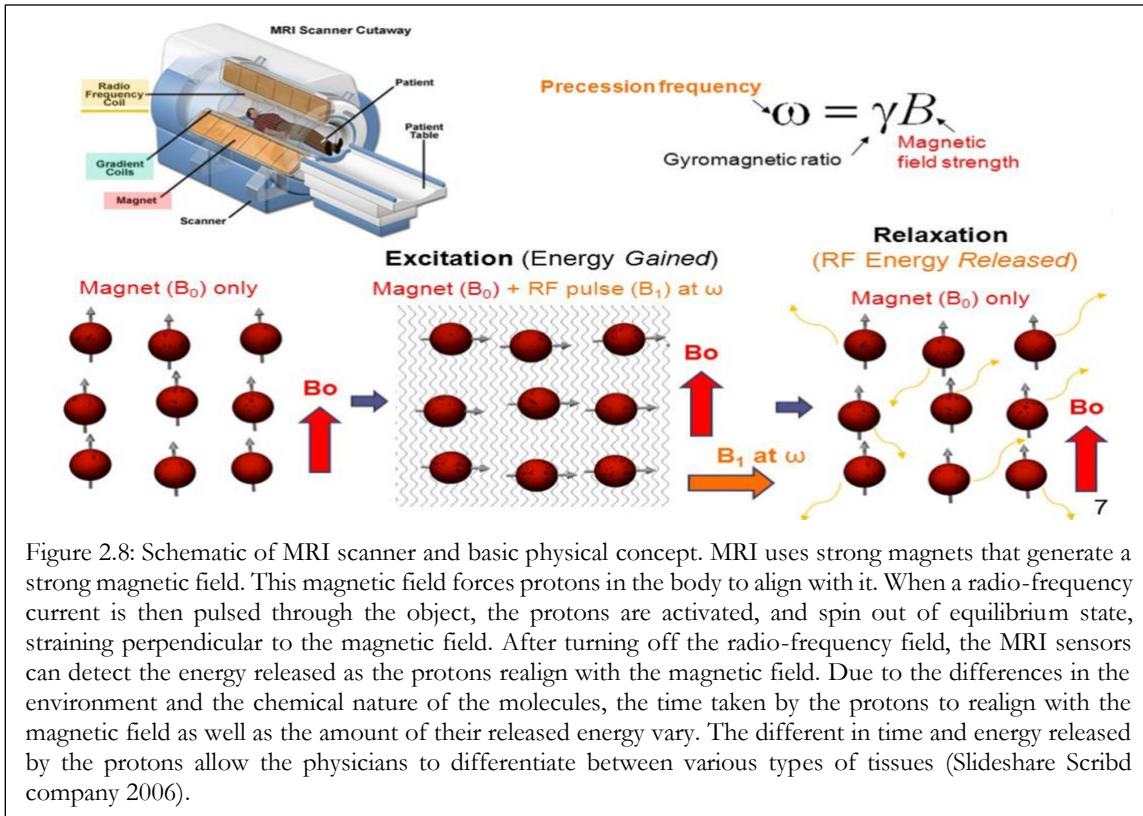
Likewise, Doppler US imaging is a type of US imaging that represents blood flow within the heart chambers as in figure 2.7 (Hoskins 1990; Hartley et al. 2007). This technique involves sending waves that hit the blood cells and bounce back to the transducer (Hoskins 1990). The reflected waves are then detected and digitized according to their direction and frequency using the Doppler concept (Hoskins 1990). The images are generated and represented with a colour gradient map of the blood flow (Hoskins 1990). Both echocardiography and laser Doppler imaging have been used in some of the studies presented in this thesis.

Another advanced imaging modality is MRI which is a non-invasive imaging tool that does not involve the use of ionizing radiation (Jones et al. 2014; Vassiliou et al. 2018). It is based on exposing the body to a strong magnetic field combined with a radiofrequency (RF) current as in figure 2.8 (Jones et al. 2014; Vassiliou et al. 2018). First, the magnetic field excites the protons in water (which makes up nearly 70% of the body) by changing their rotational axis to align with the direction of the magnetic field (Jones et al. 2014; Vassiliou et al. 2018). This is followed by turning on the RF current which will pull the protons against their original direction (equilibrium) (Saraste et al. 2009; Jones et al. 2014). Following the termination of the RF current, the protons return to their equilibrium with simultaneous emission of energy that can be detected and digitized by the MRI scanner to produce a 3D image (Saraste et al. 2009; Jones et al. 2014). Moreover, the rotational changes of the protons are controlled by the chemical properties of the molecules as well as their tissue environment (Smith and Webb 2010; Jones et al. 2014). MRI imaging generates high-resolution images that give both morphological and functional details about the organ of interest (Smith and Webb 2010; Jones et al. 2014). In the context of the CVS, MRI can measure the wall thickness of both the heart and vessels, identify acute MI and assess its extent through measuring absolute tissue water-proton (^1H) longitudinal relaxation times (Smith and Webb 2010).

Other imaging modalities that are widely implemented in medicine are x-ray imaging and CT imaging, both of which have the same physics principle and involve the use of ionizing radiation (Saraste et al. 2009). Conventional X-ray imaging has been used for many years to evaluate lung abnormalities and calculate the cardiac ratio (the horizontal distance that is taken by the heart/horizontal distance of the entire chest cavity) by producing 2D images (Smith and Webb 2010). To acquire an image X-ray source emits radiation which passes through the subject and is picked up by radiographic film or an electronic detector placed on the opposite side of the subject as figure 2.9 (Smith and Webb 2010). The intensity of X-rays detected in the 2D images by the detector/film is

proportional to the density of tissue that the X-rays have passed through on their way to the detector (Smith and Webb 2010).





As an extension of this technology, CT imaging generates 3D volume images by using a rotating X-ray source and detector pair which circle around the subject acquiring a series of 2D images or projections from different angles which are then used to reconstruct a 3D image as in figure 2.10 (Smith and Webb 2010). The amount of radiation that is absorbed or attenuated during transmission is called the attenuation coefficient (AC), and it has a unique value for each material (Smith and Webb 2010).

Finally, PET imaging, which is the focus of this research and will receive the greatest attention, can produce physiological information at a molecular level; thus, it is a molecular imaging tool (King et al. 2002; Slomka et al. 2014). Nowadays, most PET systems are combined with a CT scanner that provides anatomical details as well as allowing the calculation of attenuation correction (Kapoor et al. 2004; Basu et al. 2011). Another important benefit of using PET is that its radiotracers can be labelled with a biological substrate (such as glucose, water (H₂O), carbon dioxide (CO₂) or oxygen (O₂), etc.) or pharmaceutical (then called radiopharmaceutical) to study blood flow, metabolism, and pharmacology without changing their biological behaviours (Kapoor et al. 2004; Basu et al. 2011). The PET system detects the radiation by detecting the two gamma photons that are generated following the annihilation event. The annihilation takes place when the emitted positron (β^+) come at rest and then collides with another the electron (e^-) as in figure 2.11, this also will be discussed further in later sections (Kapoor et al. 2004; Basu et al. 2011).

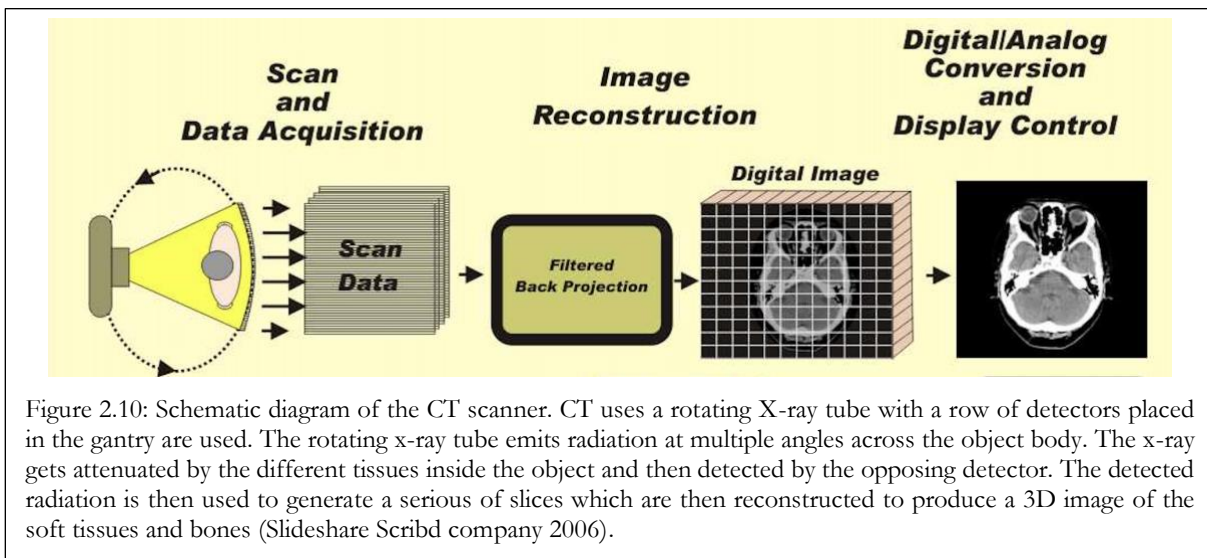


Figure 2.10: Schematic diagram of the CT scanner. CT uses a rotating X-ray tube with a row of detectors placed in the gantry are used. The rotating x-ray tube emits radiation at multiple angles across the object body. The x-ray gets attenuated by the different tissues inside the object and then detected by the opposing detector. The detected radiation is then used to generate a series of slices which are then reconstructed to produce a 3D image of the soft tissues and bones (Slideshare Scribd company 2006).

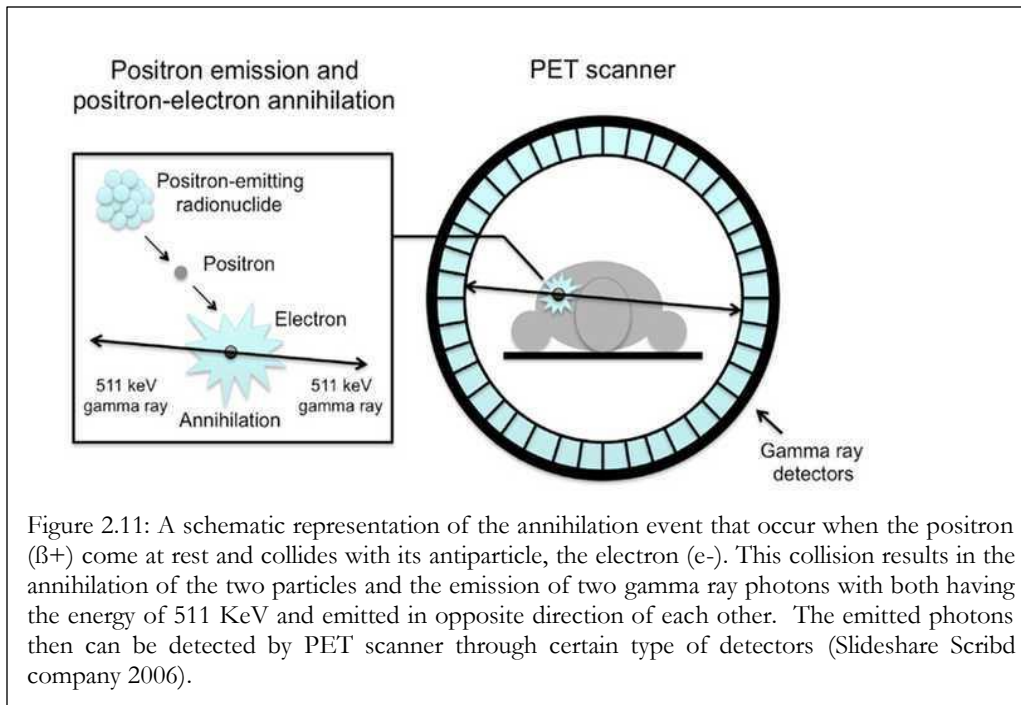


Figure 2.11: A schematic representation of the annihilation event that occur when the positron (β^+) come at rest and collides with its antiparticle, the electron (e^-). This collision results in the annihilation of the two particles and the emission of two gamma ray photons with both having the energy of 511 KeV and emitted in opposite direction of each other. The emitted photons then can be detected by PET scanner through certain type of detectors (Slideshare Scribd company 2006).

The following sections will describe the PET physics and its imaging system, the decay mode of PET radionuclides, scan types, image reconstruction, the hybrid PET/CT scanner, and the concept of pharmacokinetic modelling.

2.6 PET basic principle:

PET imaging is based on the administration of a radionuclide that undergoes emission through β^+ decay (Kapoor et al. 2004; Basu et al. 2011). Positron (β^+) emission is a type of radioactive decay that occurs in proton-rich radionuclides where the number of protons (Z) is greater than the number of neutrons (N) (Kapoor et al. 2004; Basu et al. 2011). The neutron to proton ratio (N/Z) will be low relative to the nearest stable nuclei (Kapoor et al. 2004; Basu et al. 2011). Therefore, this will result in the conversion of the proton to a positron (β^+), neutron (n), and a neutrino (ν) as in equation (Eq.) 2.1 (Kapoor et al. 2004; Basu et al. 2011).



The decay of the radionuclide is not random, but it follows an exponential law and the radioactivity at any given time can be calculated through Eq. 2.2 below (Kapoor et al. 2004; Basu et al. 2011).

$$\text{Eq. 2.2} \quad A_t = A_o e^{-\lambda t}$$

In which, A_0 and A_t are the radioactivity at time zero (or the initial time) and t (the time at which the radioactivity need to be measured) respectively. The λ is the decay constant and is related to the half-life as in Eq. 2.3 (Kapoor et al. 2004; Basu et al. 2011).

$$\text{Eq. 2.3} \quad \lambda = \frac{0.693}{t_{1/2}}$$

The half-life ($t_{1/2}$) is defined as the time required for the radionuclide to decay to half of its initial activity (Kapoor et al. 2004; Basu et al. 2011). The SI unit of the radioactivity is Becquerel (1 Bq = 1 decay/second) and its traditional unit is Curie (1 Ci = 3.7×10^{10} Bq) (Kapoor et al. 2004; Basu et al. 2011). Another commonly used scale factor is one mCi which is equal to 37 MBq (Basu et al. 2011).

Following emission, the positron travels a finite distance (depending on the radionuclide) before it loses all its kinetic energy and combines with an electron (e^-) in the medium resulting in an annihilation process. The annihilation process emits two gamma photons with 511 Kev, and in an opposite direction of 180° apart as previously illustrated in figure 2.11 (Kapoor et al. 2004; Basu et al. 2011). This process occurs when a subatomic particle hits its antiparticle (in this case, β^+ and e^- which have the same mass and opposite charge), resulting in the annihilation of both particles (Kapoor et al. 2004; Basu et al. 2011).

2.7 PET system components:

The main purpose of the PET system is to calculate the distribution and concentration of radiotracers within the subject, this is achieved by detecting the number and direction of gamma photon pairs emitted by the subject (Kapoor et al. 2004; Basu et al. 2011). The PET scanner consists of multiple solid scintillation (crystals arranged in a ring around the subject), photomultiplier tubes (PMTs), pulse height analysers (PHA), and electronics, including an annihilation coincidence detection (ACD) window and display computers (Kapoor et al. 2004; Basu et al. 2011). Each component will be discussed separately, and then an overall description of the PET detection system will be illustrated.

2.7.1 Solid scintillation crystal (detectors):

Different types of detectors are available on the market, and each has its performance characteristics and uses in various fields. The solid scintillation detectors are the ones of choice in PET systems due to the considerable improvement in their detection efficiency, especially when made of high-density material (Cherry et al. 2012). The term scintillation detector is used due to the crystal property of producing lights or flashes following radiation absorption (Cherry et al. 2012).

Most manufacturing companies have adopted the block detector design in PET systems (Cherry et al. 2012). The crystal in each block has partial cuts on the frontal surface and is connected to 2-4 PMT's

as showed in figure 2.12 (Cherry et al. 2012). These cuts are in the form of elements that may vary in number and can be either 6x8, 7x8, or 8x8 elements, 3 to 6.5 mm in length and about 3 cm in depth (figure 2.12) (Cherry et al. 2012). In addition, each element is considered as an individual detector, and its size is an essential characteristic in defining the spatial resolution of the PET system (will be discussed later) (Cherry et al. 2012). All detector blocks are arranged in an array with partial or full rings, with circular or hexagonal shapes (Cherry et al. 2012). For example, the Siemens PET scanner has 32,448 crystals within 192 block detectors and four PMT's per block (Kudo et al. 2002).

When the coincidence events (photons) are emitted from the scanned object, they are detected by the solid scintillation detectors, which interact with the detected photons in three main mechanisms discussed below.

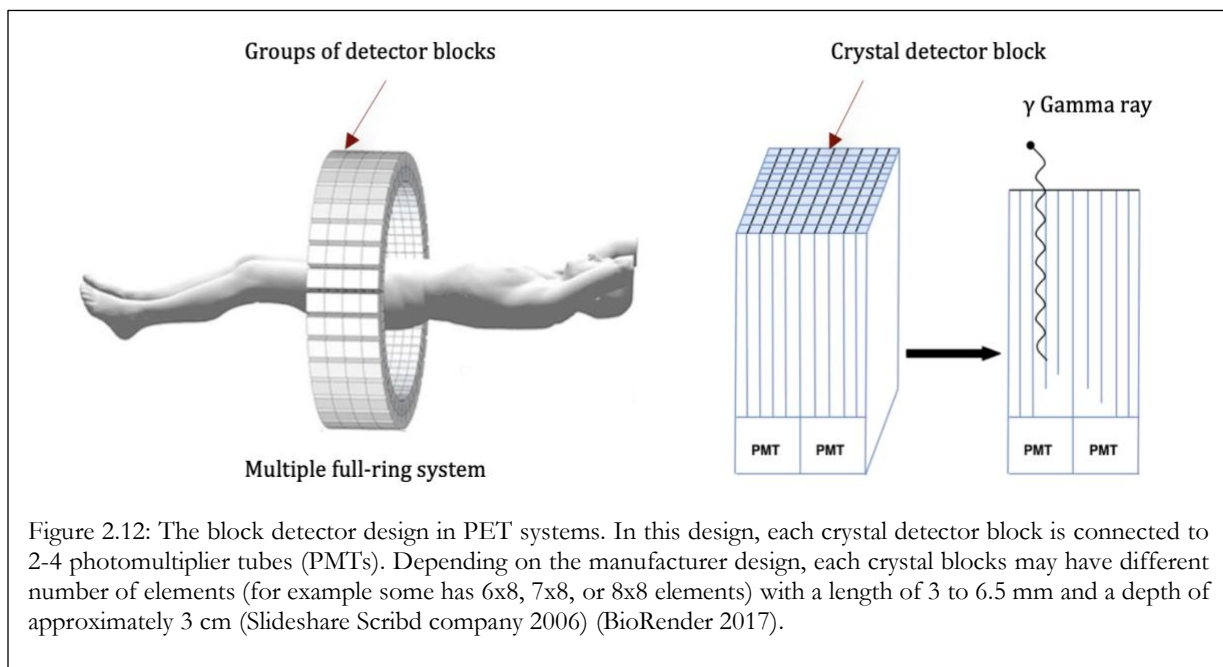


Figure 2.12: The block detector design in PET systems. In this design, each crystal detector block is connected to 2-4 photomultiplier tubes (PMTs). Depending on the manufacturer design, each crystal blocks may have different number of elements (for example some has 6x8, 7x8, or 8x8 elements) with a length of 3 to 6.5 mm and a depth of approximately 3 cm (Slideshare Scribd company 2006) (BioRender 2017).

2.7.1.1 Interaction of photon with matter:

There are three dominant mechanisms of the interaction of a photon with the matter, including the photoelectric effect, Compton scattering, and pair production, which all are subjected to the law of momentum and energy conservation (Cherry et al. 2012). In the photoelectric effect (figure 2.13), the incident photon transfers all of its energy to an orbital electron called photoelectric absorption (Cherry et al. 2012). This results in an electron ejection (called photoelectric electron), the atom being in an excitation and ionization state. Another outer shell electron fills the vacancy created by the ejected electron, ultimately resulting in the emission of a characteristic x-ray or auger electron. It is the

predominant interaction within the low energy photons, and thus its probability decreases dramatically with increasing photon energy. In addition, photoelectric interaction is proportionally related to the absorber's atomic number (Z) and a critical point to consider in the context of crystal density and detection efficiency (Cherry et al. 2012).

While in Compton scattering, the photon collides with an outer shell electron causing a partial transfer of its energy to this electron (Cherry et al. 2012). This results in knocking out of an electron and the scattering of the photon in a different direction (figure 2.14). The scattered photon might undergo another photoelectric absorption or Compton scattering until it ultimately loses all its energy. Indeed, Compton scattering is the major interaction type in the energy range 0.1-10 Mev and is independent of the atomic absorber number (Z).

Finally, pair production interaction occurs when the photon that passes through the absorber has an energy greater than 1.02 MeV (Cherry et al. 2012). In this interaction mechanism, the photon interacts with the nucleus causing the emission of both positive and negative electrons. The positive electron or positron (β^+) will lose its kinetic energy and then be annihilated with another electron, producing two gamma-ray photons as previously mentioned (figure 2.11-2.14). Pair production is the dominant interaction of higher energy (greater than 10 MeV) photons.

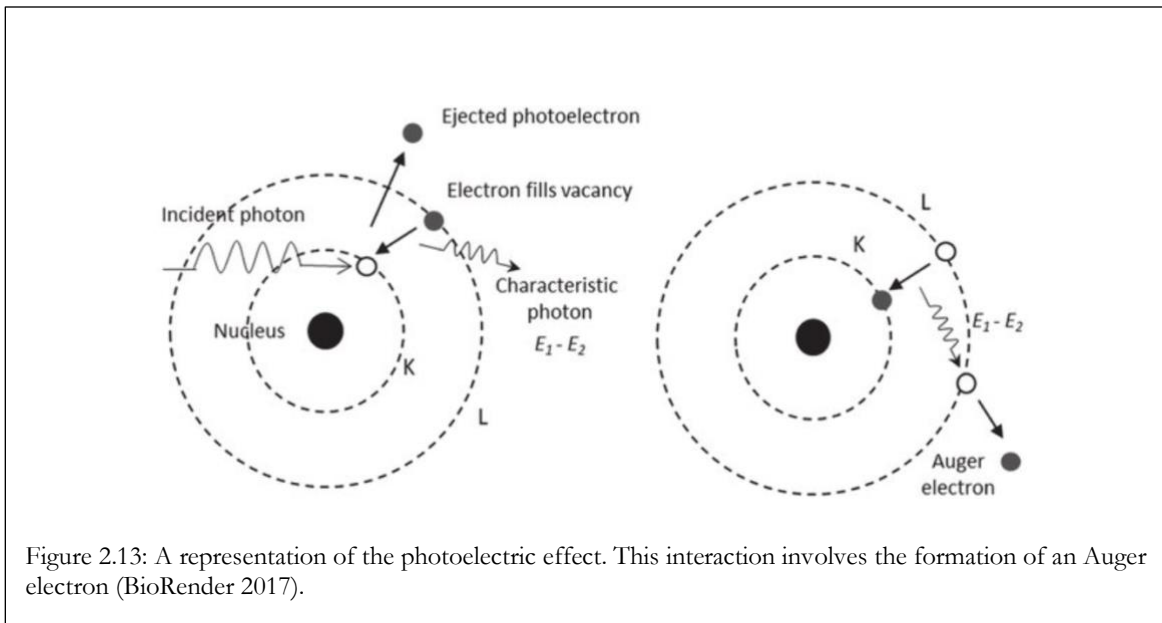
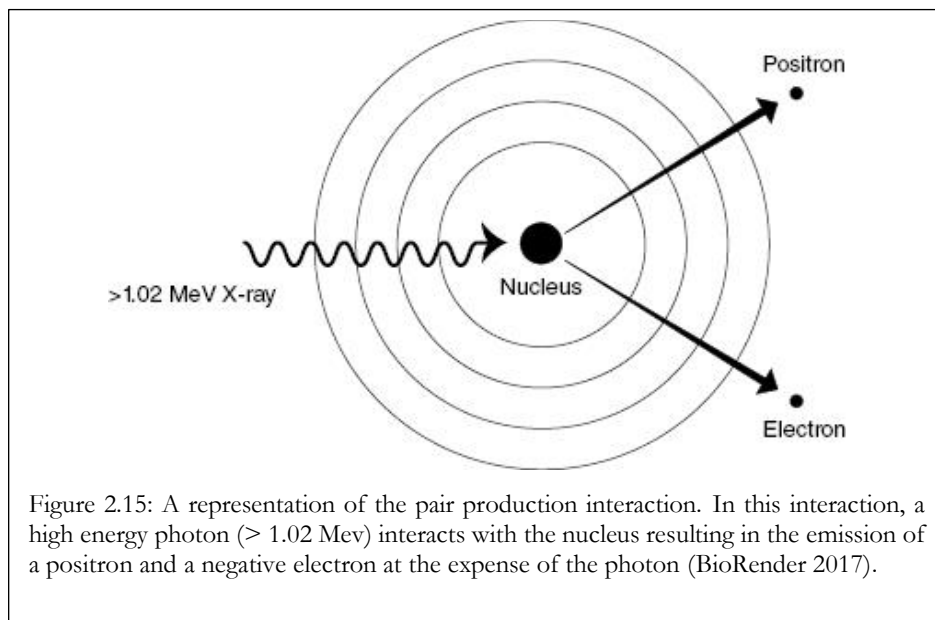
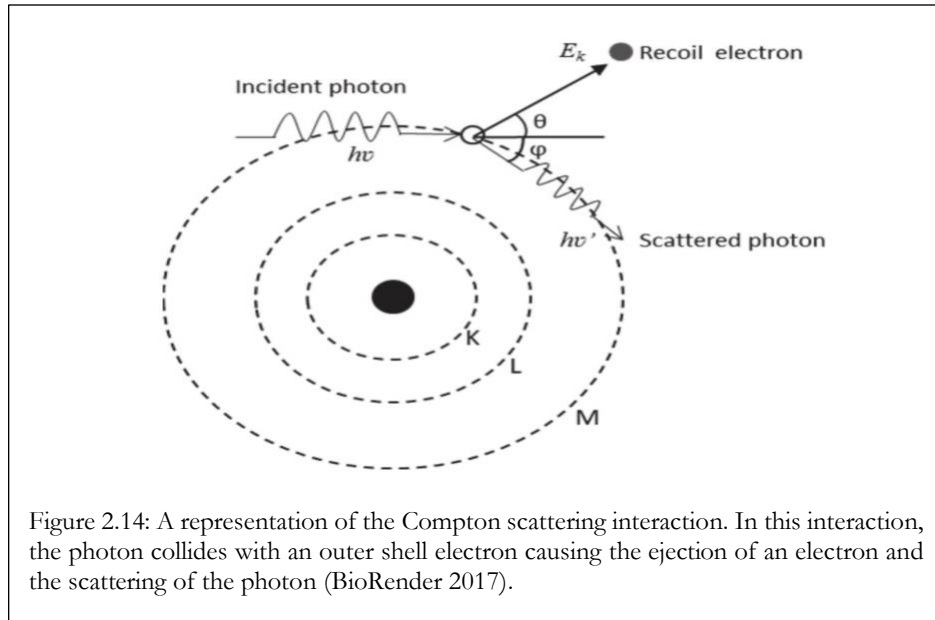


Figure 2.13: A representation of the photoelectric effect. This interaction involves the formation of an Auger electron (BioRender 2017).



2.7.2 Photomultiplier tubes (PMTs):

PMTs are vacuum glass tubes that are fixed into crystals with certain optical grease or light pipes (Cherry et al. 2012). An individual PMT consists of three parts, including a photocathode, dynodes (in the middle), and an anode as in figure 2.16 (Cherry et al. 2012). The photocathode is made of metal that releases electrons following light absorption. When applying a high voltage (1000 V), the produced electrons are accelerated and amplified until they reach the anode. Subsequently, the light

photons are converted to electrical pulses in the PMTs. The output pulse is proportional to the number of scintillation photons released from the crystal (Cherry et al. 2012).

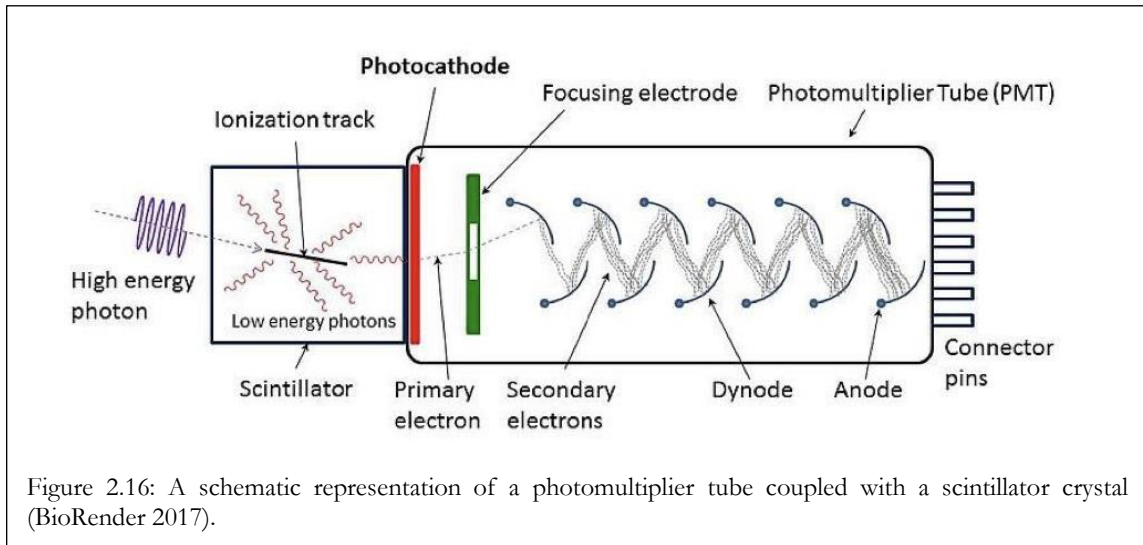


Figure 2.16: A schematic representation of a photomultiplier tube coupled with a scintillator crystal (BioRender 2017).

2.7.3 Preamplifier, amplifier, and pulse height analysers (PHA):

The pulses produced from PMTs are initially amplified by the preamplifier, where it also undergoes adjustments in shape and impedance to match the subsequent circuits in order to be processed correctly (Cherry et al. 2012). Next, further amplification occurs in the amplifier, which then transfers the pulse to the PHA. The PHA filters the pulse and accepts only those within the preselected energy window (Cherry et al. 2012). The energy window is set to have a baseline, lower and upper values, which normally are 511 Kev, 350, and 650 Kev, respectively. This is because the annihilated photons might scatter or have more distance to travel (thus more attenuation,) resulting in differences in the energies of the detected photons (Cherry et al. 2012).

2.7.4 Annihilation coincidence detection (ACD) circuits:

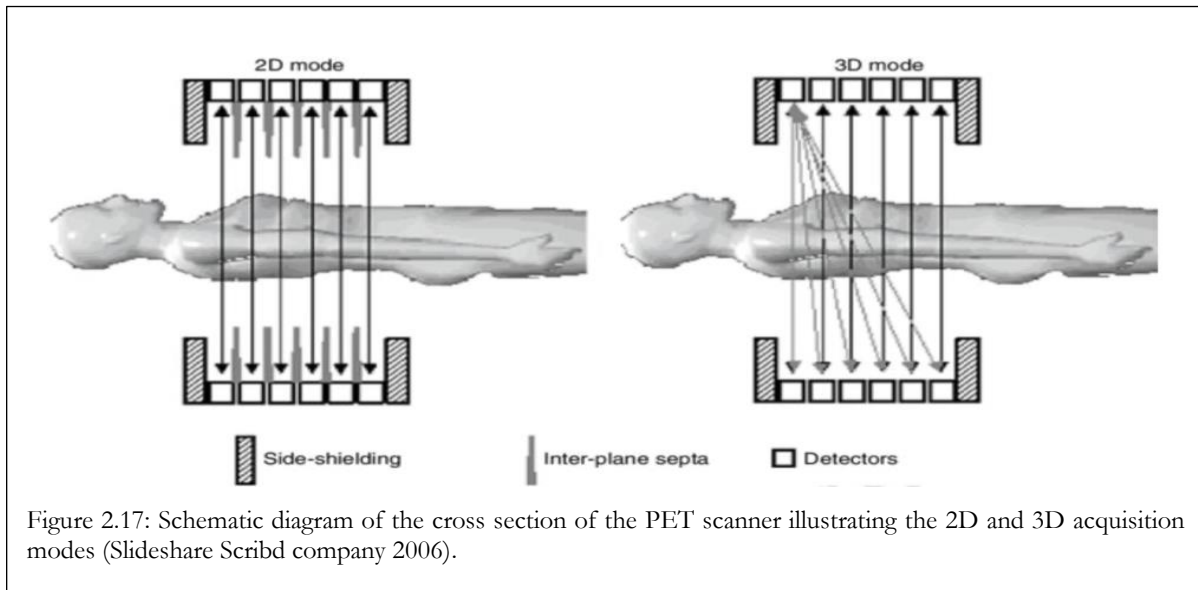
Afterwards, these pulses are used to determine the X and Y positions of the two detectors which detect the annihilated photons (Cherry et al. 2012). Each detector element is connected to a set of opposite detector elements, in axial positions, by the annihilation coincidence detection (ACD) circuits. The maximum number of the opposite detectors, that are connected together, can be the half number ($N/2$) of the total detectors that exist in the PET scanner (N) (Cherry et al. 2012). The ACD circuits will only accept coincidence photons from opposite detectors simultaneously and within a finite timing window considering the difference in the travel distance of both photons. One photon will travel more distance than the other, and subsequently, it will take more time to reach the detector.

The detected signals should occur within a certain time window to be counted as a coincidence event. The uncertainty in the detection time is called the timing resolution or coincidence timing window (Cherry et al. 2012).

The PET imaging system uses the advantage of β^+ emission through using the annihilation coincidence detection ACD window, which electronically collimates and only accepts the annihilated photons coincidentally through two opposing detectors, within a narrow energy window and acceptable geometry (Cherry et al. 2012). The location of each annihilation process is calculated by assigning a line of response (LOR) between the two detectors which detected the coincidence event. Some scanners can define the coincidence location through the time of flight (TOF). The TOF is defined as the difference in arrival time between the two photons along the LOR (Cherry et al. 2012). The most likely location can be measured through Eq 2.4:

$$\text{Eq. 2.4} \quad d = \frac{c\Delta t}{2}$$

In which d is the location of the annihilation event, Δt is the TOF, and c is the speed of the light or photon = 3×10^8 m/s. This method of defining the annihilation location allows a better spatial resolution. Compared to SPECT imaging, the PET scanner applies electronic collimation, which significantly increases its detection efficiency up to 10-20 times in 2D mode and up to 150 times in 3D mode as in figure 2.17.

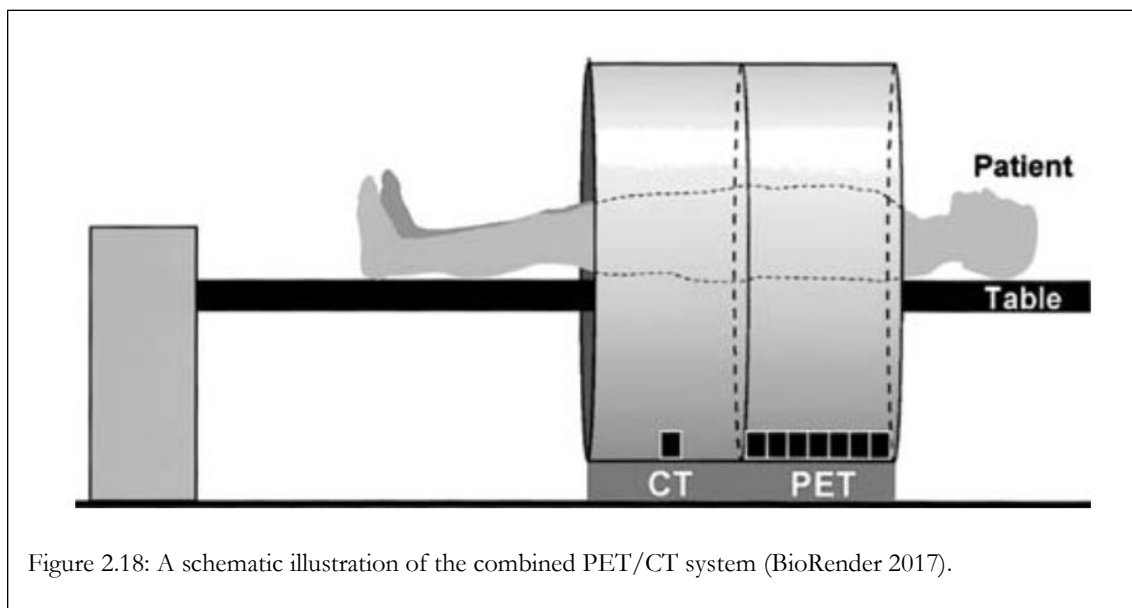


Note that after assigning a LOR for each coincidence event between the opposing detectors, all LORs that pass through a single point are stored in the form of a sinusoidal curve in a histogram

called a sinogram (Cherry et al. 2012). In a sinogram, all necessary corrections are applied since they will significantly improve true image representation and result in accurate interpretation and quantification of the tracer biodistribution from PET images (Cherry et al. 2012).

2.8 Combined PET/CT imaging:

Over the past few years, PET systems have developed significantly by combining them with CT scanners as in figure 2.18 (Jan et al. 2006). The ability to generate data from two different imaging modalities improves the diagnostic value and quantification accuracy of the images (Jan et al. 2006). This improvement is due to the combination of molecular and anatomical information from PET and CT scanners respectively. CT images also provide good estimation of attenuation correction through producing images with accurate anatomical localization (Yap et al. 2004; Jan et al. 2006).



Images from the two modalities are fused together by what is called image co-registration (Turkheimer et al. 2014). This concept defines the optimal spatial transformation between two different sources of images (Turkheimer et al. 2014). The co-registration requires two steps which are, finding the transformation parameters and applying the transformation by mapping image A directly to image B (Turkheimer et al. 2014). There are several types of transformation to co-register PET and CT images including rigid-body, affine and non-linear but they are beyond the scope of this research (Turkheimer et al. 2014). Details on different type of image co-registration were discussed explicitly by Turkheimer and his colleagues (Turkheimer et al. 2014).

In the next sections, we will address the commonly applied corrections in PET/CT imaging.

2.9 Applied correction in PET images:

2.9.1 Attenuation correction:

AC originated from the fact that photons may be attenuated differently depending on the density of the material and the distance travelled between the opposing detectors (Cherry et al. 2012). Less dense material may falsely appear with a higher uptake when compared to higher density ones (Cherry et al. 2012). This is because photons have fewer attenuation events in lower density mediums, resulting in more photons reaching the detectors. AC is measured in all LORs using either a CT base image or PET transmission image if not combined with a CT scanner (Cherry et al. 2012).

2.9.2 Types of coincidence events, scatter, and random corrections:

2.9.2.1 Types of coincidences:

It is crucial in PET imaging to only consider true events representing the two annihilated photons that originated from the same position (figure 2.19). However, this is not the real situation as other types of events could be recorded falsely by the PET scanner, including multiple coincidences, a random coincidence, and a scatter coincidence.

First, multiple coincidences can occur when three photons are recorded within the same ACD window, but the computer will simply discard them (figure 2.19).

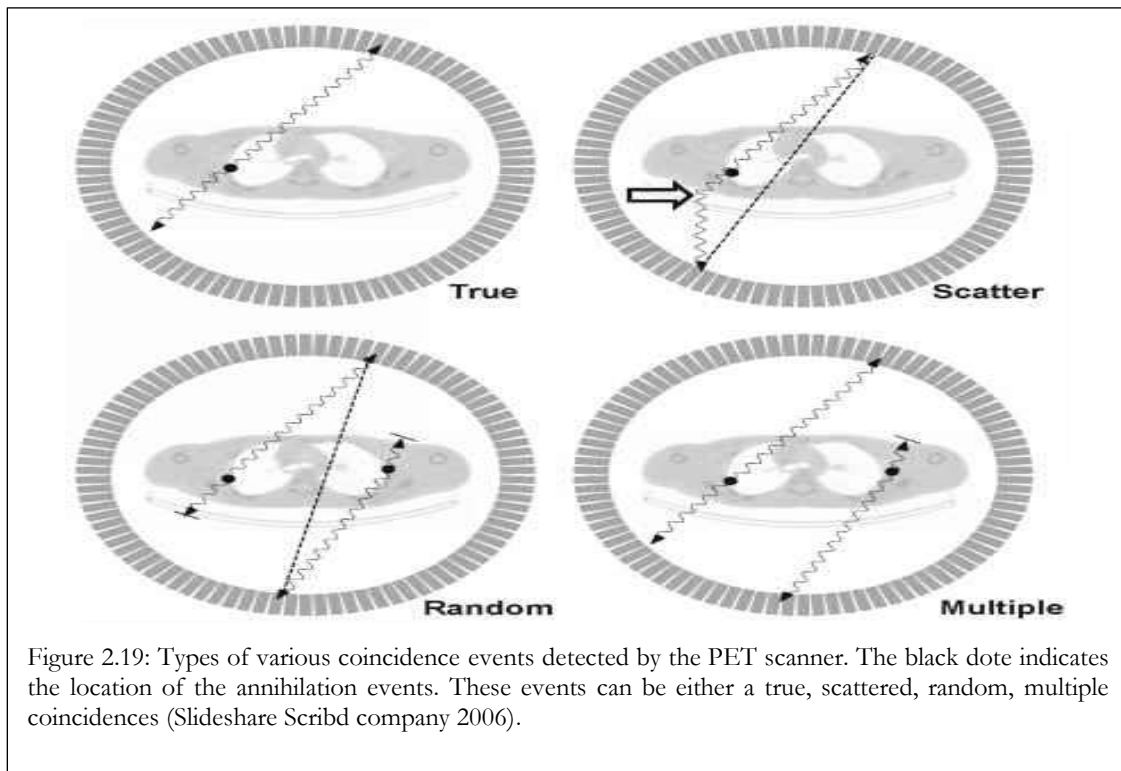


Figure 2.19: Types of various coincidence events detected by the PET scanner. The black dot indicates the location of the annihilation events. These events can be either a true, scattered, random, multiple coincidences (Slideshare Scribd company 2006).

On the other hand, a random coincidence arises when two photons originated from different annihilation events and are falsely registered as one event (figure 2.19). It appears as a uniform background in the image, decreasing its contrast.

Finally, a scatter coincidence occurs when one or both annihilated photons are scattered by Compton scattering, which causes photons to lose part of their energy and then deflect into different directions (figure 2.19). This type of coincidence degrades the contrast in the image severely and causes quantitative errors between the injected activity and the intensity in the image (Cherry et al. 2012). The percentage of scattering events can be very high, especially in a 3D mode PET (figure 2.17).

Earlier PET scanners consisted of only one ring scanner, but modern ones include multiple rings forming a cylindrical shape of detectors (Cherry et al. 2012). An important part in these PET scanners was the septa which made of tungsten or lead material placed between detectors rings. This configuration of the PET scanner is called 2D acquisition mode (figure 2.17). The existence of the septa prevents the detection of annihilated photon emitted obliquely with respect to the detector plane. However, recent PET scanners have 3D acquisition mode in which the septa were removed leading to a significant improvement in the sensitivity of the PET scanner and an increase in the detection of scatter photons (figure 2.17). Generally, in the 3D acquisition mode, the scattering events might reach 60% to 70%. This high percentage is due to several reasons, firstly because it is simply caused by the scattering of one of the annihilated photons. Another reason is the use of denser crystals in PET systems, and these have a low light output resulting in a lower energy resolution (Cherry et al. 2012). Therefore, there is a need to widen the energy window within the PHA to ensure the recording of all photopeak events. Consequently, more scatter events are registered whether they are produced by the object or the scintillator crystal.

2.9.2.2 Scatter correction (SC):

PHA is the first step of eliminating scatter events, but this simple process is less efficient due to the use of a wider energy window and the fine difference in energy values between the scatter and true events. Registering scatter and random coincidences results in assigning false LORs, but this can be corrected through two main methods.

The first method is applied by using two images: the transmission image (previously obtained to apply the AC and the emission image (scatter-contaminated image) (Cherry et al. 2012). The transmission image is used to estimate the attenuation, primarily due to Compton scattering at 511 Kev, while the emission image represents the distribution of the scattering events (Cherry et al. 2012).

Using both images and with applying simple mathematical assumptions, the SC is performed by subtracting the estimated scatter events from individual profiles of registered coincidences. This method will improve the signal to noise ratio (SNR) by removing the low-frequency background signals in the image (Cherry et al. 2012).

The second method is based on deriving projection profiles outside the object directly. The concept of this method originates from the fact that low-frequency events are mostly scattered events (Cherry et al. 2012). The data in the tails of projection profiles are extrapolated or interpolated across the entire profile. The extrapolated or interpolated data, which represents scatter distribution, is then subtracted from each projection before reconstruction (Cherry et al. 2012).

2.9.2.3 Random correction:

Random coincidences are commonly corrected using a standard delayed-coincidence method which determines the random events rate in each LOR (Saha 2010; Cherry et al. 2012). As the name suggests, this method implies the use of a delayed time window in which only one detector along any LOR is set to have a timing window longer than the coincidence resolving time of the circuit. Consequently, there will be no true coincidence in the delayed coincidence time window, and the number of the delayed coincidences detected is a good estimate for the random events. These random events that were detected by the delayed time window can be subtracted from the prompt signal or stored in a separate sinogram for later image processing and reconstruction (Saha 2010; Cherry et al. 2012).

2.9.3 Deadtime:

The PET scanner system requires a finite time to resolve and process any coincidence event, in which any event that occurs within this finite time won't be detected and is known as the dead time of the system (Saha 2010; Cherry et al. 2012). The loss of photons during the deadtime causes a pile-up effect, and it becomes significant at higher count rate scans (Vicente et al. 2007a). In the preclinical PET system, the deadtime can be evaluated using a uniform 37-mm diameter phantom that is filled with radioactivity (^{11}C with $T_{1/2}$ of 20.38 minutes) and allows it to decay during scanning time (Cherry et al. 2012). The resulting images should be decay-corrected, and then the radioactivity concentrations are plotted as a function of known activity concentration which was measured by counting an aliquot of the mixture in a calibrated well counter. Ideally, the results would be a horizontal line over the range of typical radioactivity levels. The deadtime correction method is commonly performed by scaling up

the recorded count rate globally based on a mathematical relationship between measured and true count rates (Cherry et al. 2012).

2.9.4 Normalization:

Normalization is an essential correction in the PET system that accounts for variability in detectors sensitivity and efficiencies (Saha 2010; Cherry et al. 2012). This correction is important to produce a uniform image, and there are several methods applied to achieve it. The commonly used protocol requires a 20-minute scan for a cylindrical phantom that is filled with uniform radioactivity of ^{18}F (2 mCi). Through this scan, the single detector efficiency factors are calculated from component-based normalization factors (NF) (Cherry et al. 2012).

2.10 Types of image acquisition in PET system:

In PET imaging, the organ under investigation is visualized by injecting a radiopharmaceutical that emits radiation, and the scanner detects this radiation in the form of events at certain times (Cherry et al. 2012). The detected events will represent the distribution of the molecules which are already labelled with a radioactive atom. Thus, the distribution of the radiolabelled molecule and its kinetic behaviour inside the body can be visualized through a PET scanner.

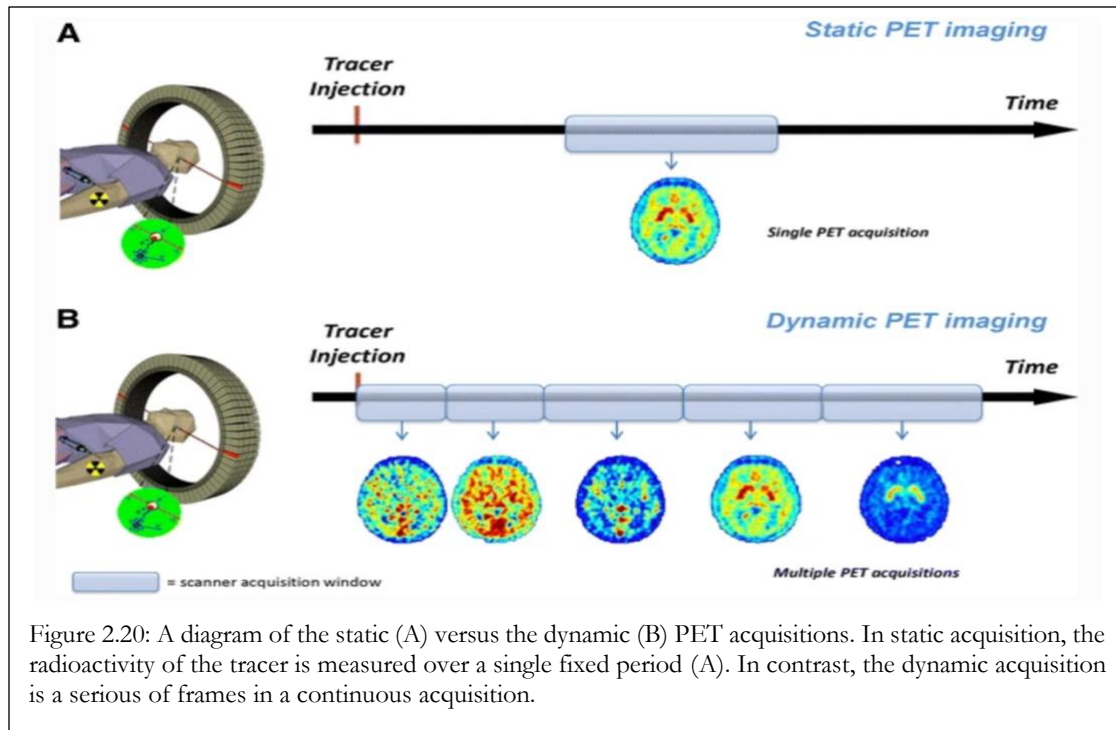
There are various types of imaging acquisitions that can be acquired by a PET scanner, including static imaging, dynamic imaging, gated imaging, and whole-body imaging. The choice of acquisition will depend mainly on the required information.

2.10.1 Static acquisition:

In static acquisition, the scanner will visualize the distribution of the radiopharmaceutical at a certain time following injection; hence, the temporal resolution is not a relevant factor, but spatial resolution is a crucial one as in figure 2.20 (Turkheimer et al. 2014). Each acquired static image represents only a one-time frame that has a set of sinograms. After that, statistics can be measured in absolute activity, % of injected activity or standard uptake value (SUV) which is a popular unit that is used mostly in PET imaging and the nuclear medicine field and will be explained in the next chapter.

2.10.2 Dynamic acquisition:

On the other hand, dynamic acquisition shows changes in the radiopharmaceutical distribution over time by acquiring multiple sequential images (Turkheimer et al. 2014). The variation between these images is used to measure distribution changes within a specified time duration. Therefore, the dynamic acquisition allows the quantification of the exchange rate within body compartments (figure 2.20), which is known as pharmacokinetic modelling and will be discussed in detail later.



2.10.3 Gated acquisition:

Another important mode of acquiring the data is gated acquisition which utilizes the ability of the PET scanner to register all coincident events (list mode) as well as the physiological ECG signal (Croteau et al. 2003). Gated acquisition uses these two sources of information by connecting each coincidence event with the myocardial contractile phase or respiratory cycle phase (Cherry et al. 2012). The contractile data is obtained by placing the ECG in three areas on the mouse, which are: into the right paw, left paw, and left leg, all of which can detect the R-waves of the cardiac cycle (Cherry et al. 2012). R-R intervals of the heart are then divided into an equal number of bins to create a mean range of the cardiac cycle within a \pm acceptance window as in figure 2.21. Therefore, any R-R interval lying outside this range is rejected. Through the cardiac-gated acquisition, the PET can estimate important cardiac parameters such as ventricular volume, ventricular ejection fraction, wall thickness and wall motion. These parameters play a vital role in evaluating cardiac viability and ventricular function.

2.10.4 Whole-body acquisition:

As the name suggests, this type of acquisition offers a whole-body scan and, depending on the axial field of view (FOV) size and the object dimension; hence, the bed might need to be moved to cover all the body. The scanner might need one or several movements to cover all body areas from head to toe. The axial FOV length might not cover the whole object length; thus, several bed positions will be required with an overlapping distance to compensate for the loss in sensitivity in the peripheral

directions of the FOV. The overlapping distance can vary according to the manufacturer's recommendation, but it should achieve the optimum image quality in terms of signal to noise ratio (SNR) and contrast to noise ratio (CNR). Technically, every bed position requires a specific duration to collect enough counts that can be specified by the user before scan initiation (Cherry et al. 2012).

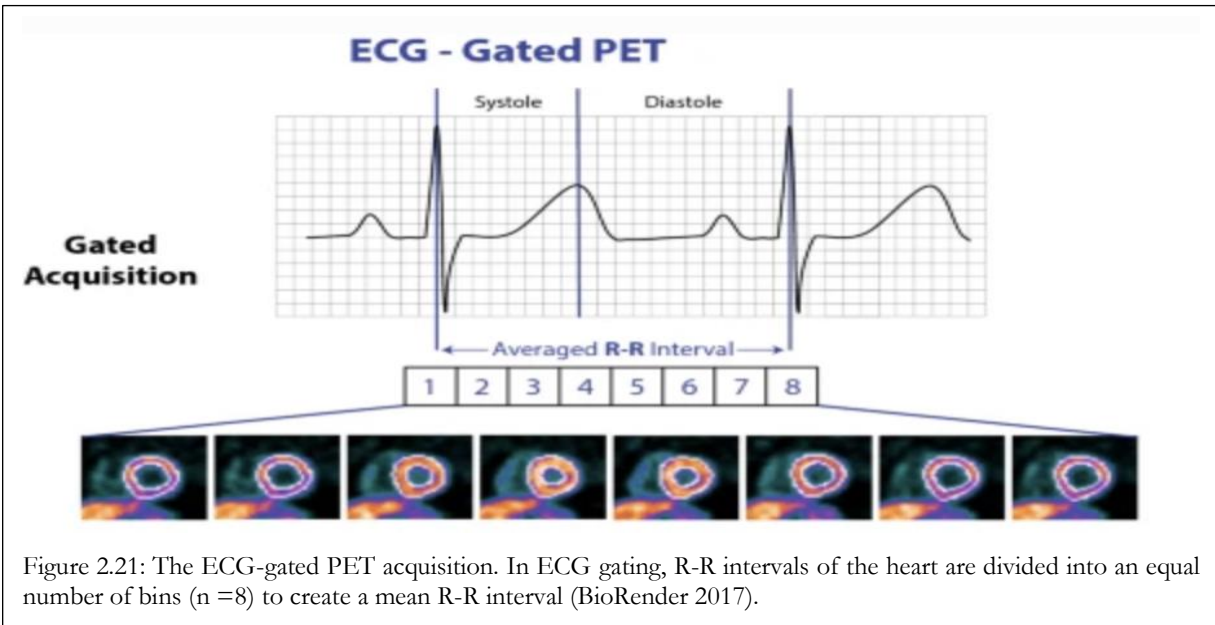


Figure 2.21: The ECG-gated PET acquisition. In ECG gating, R-R intervals of the heart are divided into an equal number of bins ($n=8$) to create a mean R-R interval (BioRender 2017).

2.11 Data reconstruction:

A basic limitation in PET imaging is that the images are produced in 2D projections from a 3D object (Cherry et al. 2012). Tomographic reconstruction is a series of mathematical processes aimed to produce a 3D representation of the scanned object from 2D tomographic images within a selected plane. Image reconstruction can be performed via two main methods, including filtered back projection (FBP) and iterative reconstruction (IR) (Cherry et al. 2012).

2.11.1 Filtered back-projection (FBP):

FBP is the most common method of image reconstruction in PET imaging because of its simplicity, accuracy, and fast computation speed (Cherry et al. 2012). For simplicity purposes, the concept of this method is explained by considering a point source in the PET scanner as in figure 2.22 (Cherry et al. 2012). All the recorded coincidence events are proportional to the radioactivity within each LOR. These measured counts are called line integrals for the individual LOR. The full set of line integrals across the detector is called a projection profile, and they are produced from different angles of the point source (Cherry et al. 2012). The counts recorded in the individual projection profile are back

projected by dividing them uniformly across all pixels that fall within the same projection path (figure 2.22) (Cherry et al. 2012). Through repeating this process for all projection profiles, all lines are added together and superimposed, forming the activity distribution but in a blurred version (figure 2.22). The blurring artifact remains even with increasing the number of projection profiles, and thus, a discrete Fourier transform (DFT) technique is used. Briefly, Fourier transform is an alternative representation of the image in a spatial frequency domain that is originally in image space or spatial domain. In DFT, each projection profile is produced by the summation of sine and cosine functions in different spatial frequencies. Following this, an estimation of the scatter contribution is derived by conversion: a ramp filter (high pass filter) is applied for each line resulting in the filtered image in the frequency domain. Next, the inverse Fourier transform (IFT) is performed to produce the image in the spatial domain (Cherry et al. 2012).

2.11.2 Iterative reconstruction (IR) algorithm:

Conceptually, IR estimates initial image profiles and then compares them with the actual recorded ones (Cherry et al. 2012). The estimated image can simply be a blank or uniform image (Cherry et al. 2012). Later, the projection profiles of the estimated image are calculated by summing up all the counts that fall in the projection path in a process called forward projection which has the inverse manner of back-projection. Next, the generated projection set in the form of a sinogram is compared to the actual recorded projection sinogram, and the differences are calculated. In most cases, the estimated image will not resemble the true image. The compare and update processes are repeated to achieve minimum acceptable differences (Cherry et al. 2012).

Performing IR involves the use of two basic algorithms, one of which is responsible for comparing the estimate and true profiles and the other one aims to update the estimated image according to the output difference produced by the previous algorithm (Cherry et al. 2012). However, operating these two algorithms require a sophisticated computer with large storage space since each iteration process is equivalent to a separate back-projection procedure. Due to this, several methods have been developed to accelerate the iteration process, but the predominant one is ordered subset expectation maximization (OSEM) (Saha 2010; Cherry et al. 2012). A small number (or subset) of projection angles are initially used for iteration in this method. As the image is refined, a larger number of iterations will be used. The expectation-maximization term refers to a type of algorithm that incorporates statistical factors in which a greater weight is assigned to the high-count elements in the profile (Cherry et al. 2012). Likewise, less weight is applied to the low-count elements in the profile. In contrast, FBP method applies a uniform statistical weighting factor to all elements in the profile (Cherry et al. 2012).

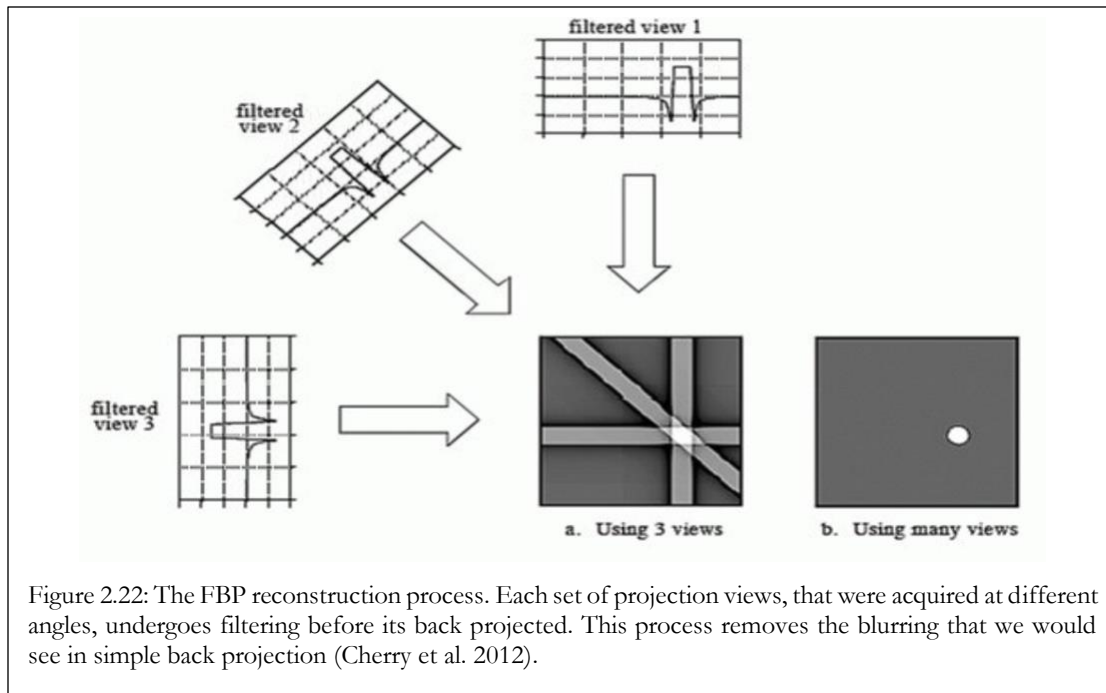


Figure 2.22: The FBP reconstruction process. Each set of projection views, that were acquired at different angles, undergoes filtering before its back projected. This process removes the blurring that we would see in simple back projection (Cherry et al. 2012).

2.12 Overview of PET quantification methods:

Generally, image analysis in PET can be done through both visual interpretation and quantitative approaches, but the applied approach depends on the goal of the analysis. The quantification approaches are applied in PET imaging to relate the measured radioactivity concentration to the underlying physiological process. Turkheimer and his colleagues have explored the common quantification techniques in PET imaging which include absolute quantification, % injected dose, standardized uptake value (SUV), tissue plasma ratio (RATIO), pharmacokinetic modelling (PKIN), spectral analysis modelling, and graphical methods (Turkheimer et al. 2014). As far as this research is concerned, only SUV and PKIN will be discussed in the introduction chapter.

2.12.1 The standard uptake value (SUV):

The SUV approach can be made using static images; in contrast, PKIN modelling needs a dynamic acquisition to be performed (Turkheimer et al. 2014). The SUV is a semiquantitative measure and is routinely performed in clinical practice and for research purposes to obtain the metabolic uptake of the radiotracer and compare the value to a different region within the same or other object or scan (Turkheimer et al. 2014). It is mostly applicable for an irreversibly binding tracer, but it can be used for reversibly binding tracers that have slow kinetics within compartments (Turkheimer et al. 2014). The SUV can be calculated by measuring radioactivity concentration within a predefined region

divided by the normalized injected dose as in equations 2.5-2.6, but there are indeed different formulas to calculate it (Turkheimer et al. 2014).

$$\text{Eq. 2.5} \quad SUV = \frac{\text{measured activity concentration}}{\text{injected dose}/a}$$

$$\text{Eq. 2.6} \quad a = \frac{\text{body weight}}{\text{body surface area}}$$

Depending on the SUV calculation method, the SUV might have no unit and become dimensionless when assuming 1 ml of tissue weight 1 g (Boellaard 2009; Kinahan and Fletcher 2010; Turkheimer et al. 2014). In clinical settings, there are other forms of SUV such as SUV_{mean} or SUV_{max} which both could be used to assess the tracer uptake in ROI. As their names suggest, the SUV_{mean} represents the average tracer concentration within ROI, while the SUV_{max} reflects the maximum value measured in the ROI (Turkheimer et al. 2014). The choice of the used SUV form is dependent on the robustness of the region delineation and segmentation (Turkheimer et al. 2014). For example, SUV_{mean} represents the general tracer distribution but it significantly affected by the drawn ROI, While the SUV_{max} offers a lower statistics of the tracer distribution but it less sensitive to the ROI delineation (Turkheimer et al. 2014).

Another study by Adams and his colleagues (Adams et al. 2010) reported the significant impact of scanner acquisition and reconstruction parameters on SUV measurements. Therefore, they suggested that imaging should be conducted using the same image acquisition and reconstruction protocols for a precise SUV assessment.

2.12.2 Pharmacokinetic modelling (PKIN) or compartmental modelling:

Dynamic PET acquisition allows the study of a tracer kinetic through PKIN or compartmental modelling, figure 2.23 is an example of compartmental modelling to measure ¹⁸F-FDG metabolism using two-tissue compartment (2TC) model that will be explained in the next sections (Turkheimer et al. 2014). Unlike other PET quantification techniques, compartmental modelling uses a detailed mathematical model to describe the system under investigation (Turkheimer et al. 2014). It allows a profound understanding of the physiological process of the biological system; hence it is also able to detect the abnormal patterns caused by a pathological condition (Turkheimer et al. 2014).

In compartment modelling, it is important to note that the term compartment is not always a spatial location within the organ or tissue, but it can be a state of the radiotracer molecules, for example, freely or bound molecules (Turkheimer et al. 2014). This quantitative technique can trace the movement of molecules starting from its administration, possible interaction, and the washout process

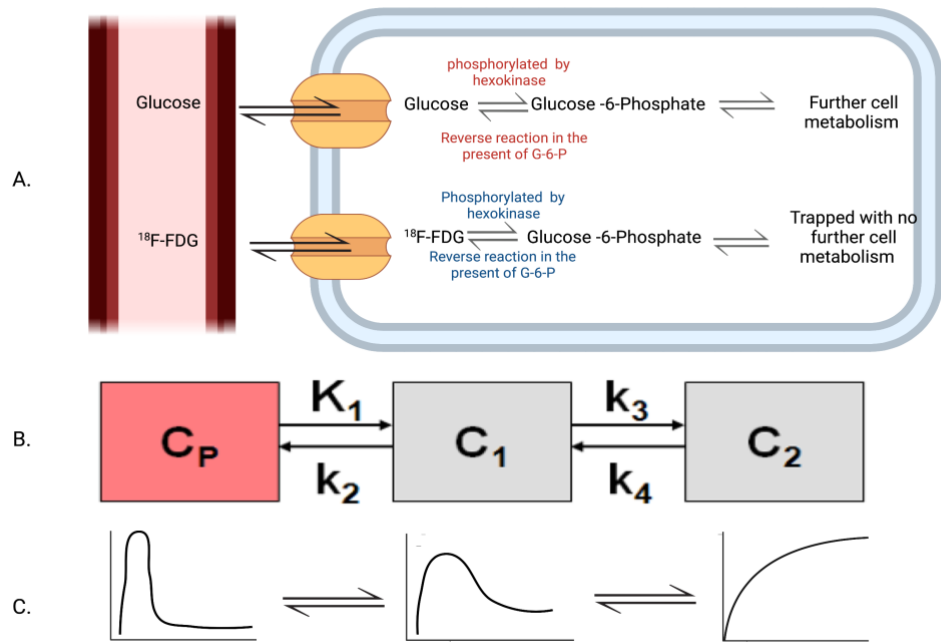


Figure 2.23: The compartmental modelling used in quantifying glucose metabolic rate with ¹⁸F-FDG.

A. Shows glucose and ¹⁸F-FDG cellular uptake and metabolism in which both pass through the cellular membrane by glucose transporter membrane proteins. Inside the cells, both are phosphorylated by hexokinase enzyme (HK) and this process can be also reversed in the presence G-6-P enzyme. The phosphorylated G-6-P can be further metabolised in the cells, whereas the phosphorylated ¹⁸F-FDG cannot be further metabolized and thus is trapped.

B. a simplified example of 2TC model that can be used in case of ¹⁸F-FDG uptake measurement in which:

C_p = The concentration of the tracer in the plasma blood compartment (Which also called the input function).

C_1 = The concentration of the tracer in the tissue (under investigation) compartment representing the non-bound tracer.

C_2 = The tissue (under investigation) compartment representing the specifically bound tracer.

K_1 = The fraction of tracer transported from the plasma blood into compartment C_1 , with a unit of ml/cm³/min.

K_2 = The fraction of tracer that diffuses back to the plasma with a unit of 1/min or min⁻¹.

K_3 = The fraction of tracer that moves to compartment C_2 . It represents the fraction of the tracer that is specifically bound or the rate of ¹⁸F-FDG phosphorylation or uptake. It has a unit of min⁻¹.

K_4 very small as the ¹⁸F-FDG trapped irreversibly, therefore K_4 is set to zero.

C. Represents the dynamic measurements of the ¹⁸F-FDG in the form of curves and the differential equation can be derived as follows:

$$\frac{dC_1(t)}{dt} = K_1 C_p(t) - (K_2 + K_3) C_1(t) \quad \text{with } C_1(0) = 0$$

$$\frac{dC_2(t)}{dt} = K_3 C_1(t) \quad \text{with } C_2(0) = 0$$

The option of the compartment model is determined first by defining the compartmental structure of the used tracer and the system under investigation, and secondly, by specifying the input and output data that can accurately represent a physiological process or biomarker (Turkheimer et al. 2014).

The basic concept of any compartment model involves a finite number of compartments with arrows between them to represent the radiotracer fluxes (exchange) with all possible pathways as in figure 2.23 (Turkheimer et al. 2014). Notably, the radiotracer exchange can be due to either the transport or the tracer being chemically metabolized, or both (Turkheimer et al. 2014). This can be illustrated simply by one tissue compartment model (1TC) and will be described in the next section.

Refinements to avoid the need for blood sampling allow accurate calculation of the blood input function, and the use of a reference tissue as an input function allows for tracer administration as in bolus injection. Additionally, in the case of bolus infusion, it allow direct readouts without reference region (Turkheimer et al. 2014).

2.13 Commonly used compartment models:

2.13.1 One tissue compartment model (1TC):

The 1TC model is the simplest used model in compartment modelling in which it represents the radiotracer flux from blood vessel (blood compartment) into tissue (tissue compartment) as in figure 2.24 (Turkheimer et al. 2014). Therefore, the flux of the radiotracer could be a relevant estimation of the blood flow to an organ (Turkheimer et al. 2014). It consists of 1 tissue compartment, as the name suggest, and blood compartment (Turkheimer et al. 2014). The description of the 1TC model can be applicable to all other compartment models but with including of more parameters (Turkheimer et al. 2014). Generally, each compartment reflects an amount of well-mixed and kinetically homogeneous chemical material (radiotracer) in a physical place. Moreover, in all models, a blood compartment represents the concentration of the non-metabolized radiotracer in the arterial plasma, which is known as the input function (Turkheimer et al. 2014). The tracer exchange between different compartments can be described by first-order differential equations based on two variables, tracer concentration and kinetic rate constants (Turkheimer et al. 2014). Notably, all used differential equations are time-dependent; thus, it is mandatory to acquire dynamic PET data.

2.13.2 Two tissue compartment model (2TC):

The two-tissue compartment (2TC) modelling is the most widely used compartment model for the ^{18}F -FDG to measure the glucose metabolism in both the brain and the heart (Turkheimer et al. 2014). Figure 2.25 represents the 2TC model along with all the derived equations. Equations in figure 2.25

represents the rate of change of the tracer concentration in C_1 at any time, measured through the fraction of the tracer that is taken up from the plasma compartment minus the total fraction of the tracer that is moving out of it, either to C_2 by irreversible trapping (K_3) or by the backflow to the plasma compartment (K_2). Therefore, the net uptake of the tracer in the tissues (K_i) (when dealing with irreversible tracers):

$$Eq. 2.7 \quad K_i = \frac{K_1 K_2}{K_2 + K_3}, \text{ with a unit } \frac{\text{of ml}}{\text{min}} / \text{g}$$

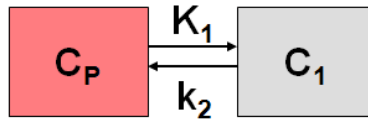


Figure 2.24: 1TC model used in compartmental modelling.

In which:

C_P = The concentration of the tracer in the blood plasma compartment.

C_1 = The concentration of the tracer in the tissue (under investigation) compartment.

K_1 = The fraction of tracer transported from the plasma blood into compartment C_1 , with a unit of $\text{ml}/\text{cm}^3/\text{min}$ = blood perfusion.

K_2 = The fraction of tracer that diffuses back to the plasma with a unit of $1/\text{min}$ or min^{-1} .

The K_1 used to represent the blood perfusion or blood flow with a unit of $\text{ml}/\text{min}/\text{g}$.

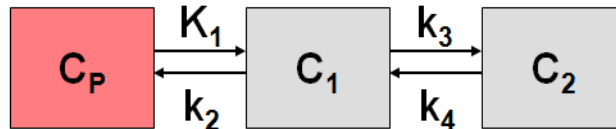


Figure 2.25: The 2TC model.

In which:

C_P = The concentration of the tracer in the plasma blood compartment.

C_1 = The concentration of the tracer in the tissue compartment (under investigation) representing the non-bound tracer.

C_2 = The tissue compartment (under investigation) representing the specifically bound tracer.

K_1 = The fraction of tracer transported from the plasma blood into compartment C_1 , with a unit of $\text{ml}/\text{cm}^3/\text{min}$.

K_2 = The fraction of tracer that diffuses back to the plasma with a unit of $1/\text{min}$ or min^{-1} .

K_3 = The fraction of tracer that moves to compartment C_2 . It represents the fraction of the tracer that is specifically bound or the rate of $[^{18}\text{F}]$ FDG phosphorylation. It has a unit of min^{-1} .

K_4 = The fraction of tracer that moves back to the intermediate compartment with the unit of $\text{ml}/\text{cm}^3/\text{min}$. (If the tracer is irreversibly trapped with no movement out of the tissue, then $K_4 = 0$, which is the case in FDG quantification).

The differential equations of the 2TC model can be written as:

$$\frac{dC_1(t)}{dt} = K_1 C_P(t) - (K_2 + K_3) C_1(t) \quad \text{with } C_1(0) = 0$$

$$\frac{dC_2(t)}{dt} = K_3 C_1(t) \quad \text{with } C_2(0) = 0$$

2.14 The application of compartmental modelling:

In molecular imaging, the quantitative compartmental modelling was used mainly in brain PET imaging, but it was then extended to other physiological systems such as cardiology, skeletal leg muscle, and cancer (Bertoldo et al. 2014). Due to the complexity of dynamic PET acquisition and the need for blood measurements, quantitative PET techniques were applied primarily in preclinical studies, including rodents, rabbits, or nonhuman primates (NHPs) (Vaska et al. 2006; Wu et al. 2007). Many attempts have been conducted to apply compartment modelling in clinical studies but with more straightforward mathematical assumptions such as deriving the input function from the PET image. Interestingly, promising results were recorded when using an image-derived input function IDIF with PET tracers that have a minimal or negligible metabolite such as ^{18}F -FDG and ^{13}N - NH_3 and will be discussed in detail in the relevant chapter (He et al. 2019). The IDIF requires additional information as it is impossible to distinguish between the radioactive tracer from its radioactive metabolites or the radioactive plasma from the whole-blood kinetics (He et al. 2019; Huang et al. 2019). Until recently, there have been multiple preclinical attempts to validate the IDIF and refine the quantification methodologies using an animal model and micro-PET/CT scanner (Thackeray et al. 2015; He et al. 2019; Huang et al. 2019).

2.15 The use of the murine model:

Animal models have been used extensively for biomedical research, and they have played a considerable role in the acceleration of many biological discoveries and new treatments (Rodrigues 2016; Emini Veseli et al. 2017). They are used to understand human diseases or specific physiological mechanisms that are difficult to investigate or have been prohibited in humans (Gallagher and Rapp 1997; Rodrigues 2016; Emini Veseli et al. 2017). Furthermore, any novel drug must go through many animal trials before being tested in humans to investigate its dosimetry, biodistribution, possible route of administration, washout, effectiveness, and toxicity (Denayer et al. 2014). However, any research that requires the use of animal models must certainly explain and justify their need while ensuring at the same time their welfare with a framework regulated by the Animals (Scientific Procedures) Act 1986 and national and international legislation and regulations.

Different animal types have been used in research, including large or small animals such as primates, sheep, pigs, and zebrafish. Still, mice is used in the majority of the research (Denayer et al. 2014). Moreover, mice are the commonly selected species in research fields for several reasons, including their compact size, which makes them easy to accommodate and handle and their short life span that

facilitates the monitoring of various disease and physiological conditions over time (Denayer et al. 2014). Furthermore, many studies and experiments have been carried out on mice explaining their anatomy, physiology, and genome and how these aspects are generally similar to humans (McMurray and Cox 2011; Vanhooren and Libert 2013; Denayer et al. 2014). Over and above these reasons, mice can be genetically engineered and mutated or can undergo surgical intervention to understand disease origin, gene function, drug development besides assessing specific therapeutic interventions. Several examples of murine models used in this research will be discussed briefly in this review and more in-depth in the relevant chapter.

2.16 Examples of murine models:

2.16.1 Diabetes mellitus:

DM is a chronic metabolic disease characterized by a relative or absolute lack of insulin, leading to hyperglycaemia (Jia et al. 2018). It is usually associated with various complications such as neuropathy, nephropathy, and retinopathy and is considered one of the major risk factors of CVDs (Adeshara et al. 2016). There are different classifications of DM, but the most common include two types which are type 1 diabetes (T1D) and type 2 diabetes (T2D) (Alberti and Zimmet 1998).

T1D, also known as juvenile-onset diabetes, is thought to be an autoimmune disease because of the autoimmune destruction of pancreatic beta cells that are responsible for producing insulin (Alberti and Zimmet 1998; Petersmann et al. 2019). It is common among children and young individuals, while T2D is more commonly found in middle-aged adults (Alberti and Zimmet 1998; Petersmann et al. 2019). T2D, which is the most common, is best described by insulin resistance in muscle liver and fat cells which leads to the insulin producing beta cells in the pancreas losing their ability to compensate with higher insulin levels (Alberti and Zimmet 1998; Petersmann et al. 2019).

In T1D animal models, the deficiency in insulin production can be achieved by different mechanisms (Maqbool et al. 2019). These mechanisms either involve chemical ablation of the beta cells or certain breeding patterns by which mice are genetically predisposed to spontaneously develop autoimmune diabetes (Maqbool et al. 2019).

On the other hand, an animal model of T2D is designed in obese or non-obese mice with varying levels of insulin resistance or beta-cell failure (Maqbool et al. 2019). Since obesity is closely associated with T2D, most T2D mice models are obese (Maqbool et al. 2019). Obesity can be induced by a naturally existing mutation or genetic alteration; otherwise, it can be induced by a fat-rich diet. In this research, we have used T2D murine model.

2.16.2 Ageing:

Ageing is associated with a generalized deterioration of the organism systems (Denayer et al. 2014). As outlined above, mice are the most commonly used animal model to study ageing, different diseases, and metabolic pathways in normal and abnormal conditions (Denayer et al. 2014). Their genetics are similar to those of a human and can be genetically modified (Denayer et al. 2014). Moreover, they have a manageable life expectancy of 1-2 years, allowing the examination of the ageing process or monitoring the effectiveness of therapeutic interventions or new drugs (Denayer et al. 2014).. Extended experiments over their life span, along with genetic mapping strategies, the use of different imaging and assessment techniques, all have provided a novel insight into the ageing process.

2.16.3 The hindlimb ischemic model:

The hindlimb ischemia (HLI) model has been widely used to investigate regenerative vascular mechanisms and test novel therapies (Padgett et al. 2016). There are several comprehensive protocols for the IHL model; however, the basic protocol is achieved by the surgical ligation of the femoral artery (Padgett et al. 2016). Consequently, this ligation causes angiogenesis in the distal regions and in the femoral collateral regions, thus, this model was often used to evaluate reparative processes such as angiogenesis and arteriogenesis (Padgett et al. 2016).

The use of cardiac PET imaging in murine models is a growing field as it allow the evaluation of CVDs, test therapies or new radiopharmaceuticals to be used in PET imaging (Prior 2017). Recent micro-PET/CT scanners offer sufficient spatial and temporal resolutions to cope with the small size and fast beating of the mice heart (Prior 2017). Moreover, cardiac PET imaging can assess different cardiac biomarkers, but we will be focusing on namely MBF and MGM (Prior 2017). In the next sections we will address the potential utility of these two biomarkers in evaluating cardiac function, the different cardiac PET radiotracers as well as the various challenges that are associated with cardiac imaging in mice.

2.17 The potential utility of MBF, CFR, and MGM in cardiac PET imaging:

MBF and coronary flow reserve (CFR) values have been reported to be vital prognostic biomarkers of the CVS and CVDs, yet their quantification remains underused in clinical settings (Shah et al. 2016; Ramandika et al. 2020). Guerraty et al. (Guerraty et al. 2020) have compared the relative contribution of both MBF and CFR as predictors of major CVDs, among a broad and diverse population, with the conventional cardiac risk factors such as diabetes and hypertension. They found that decreased MBF or CFR is more strongly linked with CVDs than traditional risk factors like hypertension, diabetes,

and obesity. This suggests that MBF and CFR have superior predictive values for CVDs compared to traditional CVS risk factors.

In the absence of pathological conditions, MBF represents the microvascular function in the heart, whereas a low MBF might indicate either CADs or CVS risk factors. A considerable amount of literature has been published on the relationship between MBF and CVS risk factors, where they confirm that these factors significantly affect MBF and CFR values (Fukushima et al. 2011; AlGhatrif et al. 2013; Murthy et al. 2014; Shrestha and Seo 2015). Previous studies reported a general reduction in MBF and CFR values following a lifetime exposure to certain risk factors such as diabetes, hypercholesterolemia, age, and hypertension (Anjan et al. 2015; Shah et al. 2016; Ramandika et al. 2020; Sinha et al. 2021).

CFR is defined as the ratio of hyperaemic MBF to resting MBF; hence a reduction in its value indicates a higher resting MBF compared to the stress one (Ramandika et al. 2020). The quantification of MBF and CFR, can be used to test the impact and efficiency of novel drugs or treatment intervention through the use of imaging modalities such as PET/CT imaging (Sinha et al. 2021).

Besides the obvious clinical predictive value of MBF in detecting CVDs, there is overwhelming evidence of the importance of cardiac metabolism (CM) quantification in the evaluation and detection of CVS and CVDs (Keating and Sanguinetti 1996; Werner et al. 2016; Kolwicz 2018; Thackeray and Bengel 2018; Fanjul et al. 2020). Indeed, CM might reflect the metabolic pathways needed for continuous ATP production and cardiac contractility (Schwarzer and Doenst 2016; Young 2016). In addition, these pathways could undergo adaptive remodelling in response to disease or physiological conditions; thus, they can also be utilized as essential biomarkers for CVS function (Schrepper 2016; Werner et al. 2016; Kolwicz 2018; Fanjul et al. 2020).

There is a close connection between CM and cardiac contractility, this could indicate that changes in contractile function could be accompanied with changes in CM (Schulze et al. 2016). Increased contraction will require increase in the energy demand (Schwarzer and Doenst 2016). Likewise, CM is linked with the contractile function, as is the case during ischemia, where there is a lack of energy supply due to oxygen reduction (Schwarzer and Doenst 2016). Considering that CM also comprises all biosynthesis processes for cardiomyocyte constituents, it is clear that CM quantification, which may be represented using different energy substrates metabolism, includes a set of important biomarkers that could reflect physiological and pathological states of the heart, such as ischemia, diabetes, hypertrophy, acute myocardial infarction and heart failure (Schrepper 2016).

By measuring the concentration of substrates and metabolites in arterial or venous compartments and within an organ of interest, it is possible to measure the rate of substrate metabolism (Schrepper 2016; Schulze et al. 2016). This was the principle of using a tracer to trace the desired molecule and its metabolic process inside the cell (Cochran et al. 2017). The tracer can be the substrate or its analogue, exemplified by the radioactive labelling of ^{18}F -FDG to assess glucose metabolism (Cochran et al. 2017). The advantage of this approach is its higher sensitivity and the ability to use it in *in vivo* animal models and in humans under different physiological conditions (Cochran et al. 2017). This approach uses nuclear imaging modalities, including SPECT/CT and PET/CT imaging, which may provide reliable quantification techniques for cardiac metabolism (vom Dahl et al. 1993; Watabe et al. 2006; Cochran et al. 2017).

2.18 PET/CT as a quantification tool for MBF and CM:

Despite the great advance in disease prevention and treatment in recent years, CVDs remain a predominant cause of death worldwide (Şahin and İlğün 2022). Nuclear imaging techniques could provide a lot of crucial information in different aspects of the CVS at a molecular and cellular level (Jones et al. 2014; Santos et al. 2015). Many clinical studies reported that SPECT/CT and PET/CT imaging might be feasible tools in quantifying different aspect of the CVS (Bateman 2012; Nappi and El Fakhri 2013; Chow et al. 2014; Lin et al. 2014; Dewey et al. 2020). Nonetheless, much evidence revealed the superiority of PET when compared to SPECT in clinical applications, which include: (1) higher sensitivity (2-3 order of magnitude) and higher spatial resolution (by 3-4 mm); (2) higher temporal resolution, especially when accompanied with a CT that provides accurate attenuation correction (Bateman 2012; Manabe et al. 2018; Patel et al. 2019). Importantly, the superiority of PET over SPECT imaging in the clinical settings is not the case in mice, indeed, it is the other way around (Bateman 2012; Manabe et al. 2018; Patel et al. 2019). Moreover, some of the PET tracers have a short half-life with a higher first pass extraction fraction in the heart which means that the majority of the radiotracer is removed from the blood or plasma in the first pass to the myocardium resulting in a better representation of MBF (Bateman 2012; Manabe et al. 2018; Patel et al. 2019).

PET imaging is a powerful tool in assessing the cardiovascular system as it provides physiological data at a molecular level which is a crucial factor for studying the prognosis and genesis of different diseases (Nekolla et al. 2009; Thackeray and Bengel 2018; Manapragada et al. 2021). Most modern PET scanners are combined with CT imaging in a configuration that was introduced previously. This combined imaging adds comprehensive anatomical and functional insights of the scanned organ in a

single examination session (Nadig et al. 2022). The key benefit of quantitative analysis via PET/CT imaging is that it is not subjected to inter or intra-reader variability that is mainly dependent on their expertise in the field (Turkheimer et al. 2014; Sunderland and Christian 2015).

PET/CT imaging can provide an accurate assessment of myocardial viability through cardiac metabolism quantification as well as an estimation of the global and regional myocardial perfusion, apoptosis, and gene expression (Knaapen et al. 2010; Manapragada et al. 2021).

Depending on the investigated biomarker, PET uses different types of radionuclide (radioisotope) labelled pharmaceuticals, each of which aims to examine a specific organ or quantify a particular physiological biomarker or process (Shahhosseini 2011; Maddahi and Packard 2014).

2.19 Micro-PET/CT imaging of murine models:

There was a persistent need to adopt the existing clinical imaging modalities to fit the small size of the murine model. As a result, many conventional clinically used imaging modalities such as CT, MRI, ultrasound, SPECT, and PET imaging have been adapted to suit rodent models (Kreissl et al. 2006). This research focuses on using a micro-PET/CT scanner to scan mice, a machine that has similar physical concepts and design as the traditional clinical PET/CT scanner.

The micro-PET/CT scanner produces a scan showing the 3-D distribution of the administered radiotracer at a specific time (static acquisition) or over a time-period (dynamic acquisition), with a high resolution up to a millimetre scale. Moreover, micro-PET/CT allows the multiple scans to be performed on a single animal at different time-points (Lindsey et al. 2018; Vasudevan et al. 2020; Fischer et al. 2021a). This is not the case in end-point studies using histological analysis (Phoon and Turnbull 2016). By their very nature, these require a larger number of animals that need to be killed before tissue harvesting (Phoon and Turnbull 2016).

Like most imaging modalities, small PET/CT has many challenges that need to be tackled to ensure high image quality in terms of high SNR, accurate spatial and temporal resolution, while minimising acquisition time (Khalil 2017). Our attempts to improve quantification accuracy in this way will be shown in more detail in a later chapter. Examples of our improvements include standardisation of the imaging environment, preservation of body temperature, and use of anaesthetics that do not interfere with the metabolic process. Additionally, the small size of a mouse heart and its rapid heart rate requires a specific spatial resolution and sophisticated gated acquisition. Furthermore, measuring input function or applying spill over and partial volume correction are all factors that need to be performed carefully. These technical challenges will be discussed explicitly in the relevant chapter.

One of the advantages of PET radionuclides is that they are parts of the basic constituents of bio-organic molecules inside the cell (Khalil 2017). Furthermore, most PET radionuclides can be labelled with an energy substrate without being physically or chemically altered (Fischer et al. 2021a). The radiolabeling of an energy substrate consumed by the cell can reflect important approaches in cellular metabolic pathways (Khalil 2017). The most commonly used radionuclide in PET imaging is fluorine ^{18}F -FDG (Khalil 2017). Other frequently used radionuclides include ^{13}N , oxygen-15 (^{15}O), rubidium-82m (^{82}Rb) and carbon-11 (^{11}C) (Khalil 2017). Generally, in PET cardiology, radionuclides are used to measure myocardial viability or MBF (Khalil 2017).

^{18}F -FDG is an analogue of glucose and is the most widely used PET radiotracer in cardiology and oncology for in vivo study of glucose metabolism (Fischer et al. 2021a). ^{18}F -FDG in the bloodstream enters the cardiomyocytes through diffusion and the regulation of specific transporters called sarcolemmal glucose transporters (Fischer et al. 2021a). Phosphorylation via hexokinase converts the ^{18}F -FDG to ^{18}F -FDG-6-phosphate (Fischer et al. 2021a). Normal glucose is phosphorylated and enters different metabolic pathways such as the glycolytic pathway, glycogen production and ribose synthesis (Fischer et al. 2021a). ^{18}F -FDG-6-phosphate is irreversibly trapped in the cardiomyocytes with no further metabolism (glycogen synthesis or aerobic glycolysis) (Fischer et al. 2021a). This trapping of ^{18}F -FDG-6-phosphate is proportional to the transport rate of glucose and hexokinase activity which both represent glucose uptake and metabolism (Fischer et al. 2021a). Therefore, ^{18}F -FDG has been approved by the Food and Drug Administration (FDA) and is considered to be the gold standard for myocardial viability assessment (Fischer et al. 2021a).

Typically, a cardiac FDG scan includes a perfusion scan element, using a flow radiopharmaceutical, which is since FDG has a low extraction fraction by the myocyte and therefore cannot be used to reflect the MBF. Myocardial perfusion imaging (MPI) involves administering a suitable radiopharmaceutical to assess the blood perfusion (flow) to the heart (Manapragada et al. 2021). Regions with reduced blood flow might indicate an obstruction in the coronary arteries or CADs (Guerraty et al. 2020; Manapragada et al. 2021). Myocardial regions that have a decreased perfusion, but preserved or increased glucose consumption (also called flow-metabolism mismatch) usually indicate a viable myocardium (Vasudevan et al. 2020). Non-viable regions have reduced blood flow and FDG uptake (this is known as a matched defect) (Vasudevan et al. 2020). Myocardial perfusion, also called MBF, is a smaller measure than the coronary blood flow with a unit of ml/min) as it reflects the amount of blood per mass of myocardial tissue with a unit of ml/min/g (Manapragada et al. 2021). The combined PET/CT imaging has a higher sensitivity and temporal resolution when compared to

other modalities like SPECT imaging; thus, it is considered the gold standard for MBF quantification in rest and stress conditions (Manapragada et al. 2021).

There are several available blood flow tracers, including $^{13}\text{N-NH}_3$, $^{15}\text{O-H}_2\text{O}$, ^{82}Rb and $^{18}\text{F-flurpiridaz}$, which is a newly developed tracer with a promising clinical potential that is still under examination (Manapragada et al. 2021). The ideal flow tracer should have a higher extraction fraction by the heart, a low clearance rate from tissue to the blood, and a small positron range (Manapragada et al. 2021). Furthermore, they should have a half-life period that is sufficiently long for them to be transferred to the lab or imaging centre (Manapragada et al. 2021). It is preferable that these tracers can be synthesized efficiently and reliably to be used routinely (Manapragada et al. 2021). Flow tracers, like $^{13}\text{N-NH}_3$ and $^{15}\text{O-H}_2\text{O}$ have a short half-life which is ideal for multiple scans (Manapragada et al. 2021). On the other hand, the $^{18}\text{F-FDG}$ that has approximately two hours half-life and thus will not allow another radiopharmaceutical to be injected following its administration.

The FDA has approved the use of $^{13}\text{N-NH}_3$ as an MBF tracer in 2000 (Manapragada et al. 2021). It is a cyclotron product with a half-life of 9.8 minutes (Manapragada et al. 2021). Once injected, $^{13}\text{N-NH}_3$ diffuses freely through the cellular membrane to localise in the myocardium, brain, liver, kidneys, and skeletal muscle (Manapragada et al. 2021). The myocardial trapping mechanism is not fully understood, but studies suggest that the ammonia enters the glutamine pool via the glutamine synthase and is then converted into glutamic acid and carbamyl phosphate (Manapragada et al. 2021).

$^{13}\text{N-NH}_3$ is almost an ideal perfusion tracer. It has a high first-pass extraction fraction from the vascular pool (more than 80%) and a linear myocardial uptake covering a wide range of MBF rates. It has high retention in the myocardium, with a minimal back-diffusion, which could improve the image quality (Manapragada et al. 2021).

One of the aims of this research is to evaluate the beneficial effect of LAV- BPIFB4 gene therapy on the mice cardiac function using micro-PET/CT imaging. Therefore, we will briefly highlight gene therapy as a method to treat different types of diseases.

2.20 Gene therapy:

Gene therapy is a technique that has been used to treat or prevent diseases or pathological conditions either by replacing a mutated gene, inhibiting a mutated gene, or inserting a new gene, all of which aim to cause a therapeutic or regenerative effect in the body's systems (Levi and Coronel 1997; Rincon et al. 2015). There are various challenges involved in the process, and the first is finding the optimal methods to deliver the normal gene copies to the target cells (Nayerossadat et al. 2012;

Bulcha et al. 2021). The vector (or vehicle) is a molecular carrier that should allow the gene to be delivered to the target by crossing the cell membrane and then ultimately releasing it into the cell nucleus (Nayerossadat et al. 2012; Bulcha et al. 2021). To do this, there are different types of vectors used as a delivery system. They are generally divided into viral and non-viral vectors, each one with its advantages and disadvantages (Nayerossadat et al. 2012; Bulcha et al. 2021). AAV vector is a viral vector that was used in this research. It is produced from a naturally existing parvovirus and cannot replicate independently, but rather relies on a helper virus such as adenovirus or herpes simplex for replication processes (Nayerossadat et al. 2012; Bulcha et al. 2021).

Uncovering the secrets behind human genetics is a promising tool to understanding the variation between individuals with respect to certain traits, longevity, susceptibility to diseases and response to therapeutics. Recent studies indicated that exceptional longevity is an inherited trait, and some groups of long-living individuals (LLIs) can be highly resistant to diseases, especially those associated with ageing, and have a low incident rate of CVDs (Villa et al. 2015a; Villa et al. 2015b; Dang et al. 2020; Di Pardo et al. 2020; Faulkner et al. 2020). The offspring of LLIs often have the same healthy phenotype, which correspondingly opened the possibility of transferring the healthy genes across the population. Our collaborators have identified a Longevity-associated variant-BPIFB4 (LAV- BPIFB4) may be a novel therapeutic approach to reduce endothelial dysfunction and enhance vascular reparative processes (Villa et al. 2015a; Villa et al. 2015b; Dang et al. 2020; Di Pardo et al. 2020; Faulkner et al. 2020). Subsequently, one of the aims of this research is to assess the therapeutic effect of the LAV- BPIFB4 gene using the power of micro-PET/CT imaging and its quantitative tools.

2.21 Gaps of knowledge:

Both MBF and MGM is vital physiological biomarkers that could provide predictive values in understanding normal and abnormal metabolic processes of the CVS and their related diseases. In murine model, quantifying those two biomarkers is associated with many challenges. In this research, we will test the ability of our micro- PET/CT imaging to evaluate cardiac function through quantifying these biomarkers. This goal is associated with multiple technical considerations, which will be tackled in this research. Quantitative analysis using micro-PET/CT scanner cannot be achieved without testing its physical performance as well as developing and standardizing imaging protocols that could produce accurate and repeatable. These validated imaging protocols might play a crucial role in assessing the influence of novel drugs or therapeutic interventions such as gene therapy on the CVS.

An examination of the genes associated with healthy longevity has helped scientists to identify LAV- BPIFB4 gene which has been associated with longevity and preventing age-related diseases through promoting cell survival and function (Villa et al. 2015a; Villa et al. 2015b; Dang et al. 2020; Di Pardo et al. 2020; Faulkner et al. 2020). While a number of experimental approaches have been performed to assess and understand how the LAV-BPIFB4 gene exerts its effect, none has evaluated its impact on MBF and MGM using different murine models and micro-PET/CT imaging, and this is perhaps the most interesting gap to be explored.

2.22 Conclusion:

Closing these gaps in our knowledge will be a complex process since it involves multiple disciplines, including imaging protocols, the radiotracer of choice and image quality, and using these protocols in different disease models and physiological conditions.

The next chapters will explain the applied methodology in our attempts to develop standard imaging protocols after ensuring the reliability of the micro-PET/CT scanner using ^{18}F -FDG and ^{13}N - NH_3 . This is followed by further validation of these protocols in a disease model namely HLI. Finally, the validated imaging protocols will be used to test the LAV- BPIFB4 gene's efficiency as a novel treatment in improving cardiac function and MBF in several murine models, including diabetic and ageing models.

Chapter 3:

Methodology

3.1 Materials and methods:

3.1.1 The PET/CT Scanner:

All PET/CT imaging procedures were carried out by the researcher in the Wales research and diagnostic Positron Emission Tomography Imaging Centre (PETIC), Cardiff University, UK, using a Mediso Nano-Scan 122S small-bore PET/CT imaging system manufactured by Mediso Medical Imaging systems, Budapest, Hungary. This scanner is made for preclinical (research) uses only, and it's integrated with heating and gas tubes to maintain an average temperature and anaesthesia, respectively. It is also incorporated with an ECG monitor to allow gated acquisition. Moreover, its main advantage is high spatial resolution (SR) due to using a superfine crystal size table 3.1. Further improvement in SR was obtained by the 3D OSEM reconstruction method with a value of 0.7 mm compared to 1.25 mm achieved with the filtered back-projection (FBP) method. The single axial field of view (FOV) is 10 cm, allowing a whole-body mouse scan in one FOV (one-bed position).

The combined CT scanner allows high SR with ten μm isotropic voxel size, low exposure dose (< 10 mGy) and minimal scan duration. Additionally, this scanner has a temporal resolution of 1.2 ns, enabling more accurate correction and quantification. More configuration details and physical performance are detailed in the table.3.1.

3.1.2 The used Cyclotron:

The IBA CYCLONE[®] 18/9 Cyclotron (Ion Beam Applications, IBA, Belgian) was used to produce the radionuclides needed in this research including the ^{18}F and ^{13}N . The production processes were carried out by a member in the production team in PETIC.

3.1.3 Radionuclides (radiotracers) used in this research:

In this research, two radiotracers were used, ^{18}F -FDG and ^{13}N , to quantify glucose metabolism (MGM) and myocardial blood flow (MBF), respectively.

3.1.3.1 ^{18}F -Fluorine-fluorodeoxyglucose (^{18}F -FDG):

^{18}F -FDG is an analogue of glucose, with uptake linearly proportional to the that of exogenous glucose. This radiotracer is used to assess GM in the myocardium, where it is transported by facilitated diffusion with an irreversible binding. In this research, ^{18}F -FDG was used in all scans for myocardial

glucose metabolism (MGM) assessment (details in the table 3.2). ^{18}F -FDG was produced onsite in PETIC, Cardiff University.

3.1.3.2 ^{13}N -ammonia (^{13}N - NH_3):

^{13}N - NH_3 was used in the imaging procedures for quantifying MBF. It has a 9.96 min half-life which requires an onsite cyclotron (Wieland et al. 1991). It has an extraction fraction (EF) of 80% with a mean positron range (PR) of 0.7 mm (table 3.2). The neutral NH_3 molecule diffuses readily through the plasma and cell membrane.

Physical Characteristic	Value	Benefit
Single axial FOV	10 cm	Allow the whole-body mouse to be scanned in one FOV
Gantry opening	16 cm	Allow scanning bigger animal
Crystal size	1.12x1.12x13 mm	Superfine crystal results in improved spatial resolution
Total number of crystals	36504	
SR with 3D OSEM	0.7 mm	The higher the SR, the better the generated image quality
SR with FBP	1.25	
Sensitivity	8%	The higher the sensitivity, the higher the imaging quality
Count rate for mouse	850-kilo counts per second (kcps)	A higher count rate allows high radioactivity studies
Temporal resolution	1.2 ns	improved temporal and energy resolution will provide high quantification accuracy and good resolution
Energy resolution	19%	
Combination with CT	Yes	Support higher resolution with a low dose CT scan

Table 3.1: Mediso Nano-Scan 122S small-bore PET/CT imaging system manufactured by Mediso medical imaging system, Budapest, Hungary.

Agent	Physical Half-life	Mean Positron range in water (mm)	Production	Extraction
^{13}N - NH_3	9.96 min	1.5	Cyclotron	80%
^{18}F -FDG	110 min	0.66	Cyclotron	1%-3%

Table 3.2: The physical characteristics of both ^{18}F -FDG and ^{13}N - NH_3 (Wieland et al. 1991).

3.2 Animal models:

All animal experiments and imaging procedures in this research were approved by the British Home Office (Project License PPL 30/3373), the University of Bristol and conducted according to the Care and Use of Laboratory Animals (The Institute of Laboratory Animal Resources, 1996). The project license of this research (Bristol University Project License PPL 30/3373) only allows non-recovery PET/CT procedures; thus, each mouse was terminated after performing sequential scans. Each mouse was dissected after termination to collect tissue, blood, and urine for histological analysis. DbDb or Dblean ([C57BLKS/J-Leprdb/LeprWT Dock7+ (wt/db), Envigo]), or C57BL/6J (Charles River, Margate, Kent, UK) mice were used in the experiments. In the healthy model, which was used for standardising the imaging protocols, mice were obtained from Charles River as one of the main suppliers for Cardiff university. For the diabetic, ageing and hindlimb ischemic animal models, mice were transferred from Bristol university after performing the approved protocols such as the injection of a therapeutic gene or surgical hindlimb ligation. Importantly, mice were allowed to recover for week after the transfer process in order to reduce stress and discomfort due to transportation that might affect the results.

3.3 Therapeutic gene name:

Four-missense single-nucleotide polymorphism variant of the bactericidal/permeability-increasing fold-containing family B memberfour4 or (*BPIFB4*) gene.

3.4 Variants of the gene:

1. Control group: Wild-type isoform (WT) of the gene BPIFB4 or WT-BPIFB4.
2. Control group: A virus marker with green fluorescent protein (GFP) group.
3. Experimental group: Longevity-associated variant (LAV) of the gene BPIFB4 or LAV-BPIFB4.

3.5 Gene cloning:

BPIFB4 cDNA gene (for both WT and LAV isoforms) was cloned as described by Di Pardo et al. (Di Pardo et al. 2020; Puca et al. 2020).

3.6 Vector Production:

Vector production and purification of adeno-associated viral vectors serotype 9 (AAV9) was performed as described by both Villa et al. and Puca et al. (Villa et al. 2015b; Puca et al. 2020).

3.7 Gene delivery method:

Both LAV-BPIFB4 and WT-BPIFB4 were systematically delivered using a tail-vein injection of vehicle or the AAV9 containing the appropriate variant (Dang et al. 2020).

The following sections briefly outlined mice different models, their groups and supplier.

3.8 Healthy mice:

Healthy mice were used to optimize imaging protocols and validate baseline studies. twenty female mice (C57BI/6) with an age of 8 weeks (bodyweight 25–30 g) were purchased from Charles River, one of the leading Cardiff university suppliers.

3.9 Hindlimb mice model:

Hindlimb ischemia was induced in the left leg for four healthy male mice (strain: C57BL/6J) aged about eight weeks (bodyweight 20–30 g), obtained from Charles River, Margate, Kent, UK. The surgical induction of HLI was performed by one of our research group members in Bristol university. More details on the ligation process anaesthesia and the used imaging tools will be explained in the relevant chapter.

3.10 The diabetic mice model:

These mice were used to study the effect of a single intravenous injection of the therapeutic LAV-BPIFB4 gene in type 2 diabetic induced mice. Four groups of male mice aged nine weeks (number per group(n)= 8 with more details in figure 3.1) were received from Bristol university for ¹⁸F-FDG scanning to evaluate the effectiveness of gene therapy on MGM among the four groups.

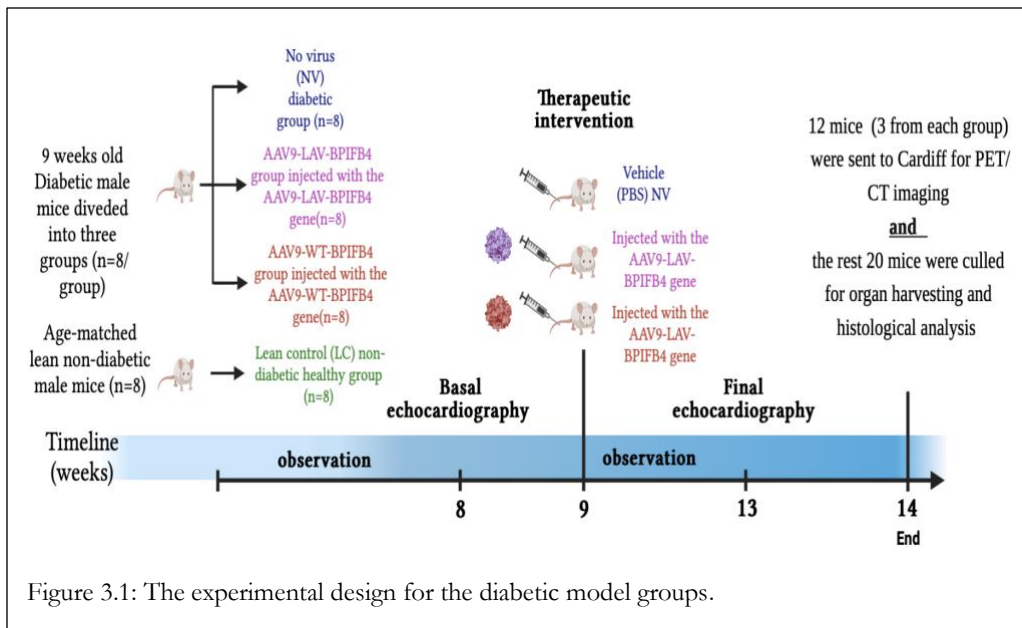
3.10.1 Mice groups for the diabetic model:

Note that the group name indicates the injected gene variant, and a healthy or diabetic state.

1. Lean control (LC) group: healthy (heterozygous) non-diabetic mice (C57BLKS/J-Leprdb/LeprWT Dock7+ (wt/db), Envigo).
2. LAV group: induced diabetic male C57BLKS/J-Leprdb/Leprdb/Dock7+ [db/db] mice (obtained from Envigo, Bicester, Oxfordshire, UK. Mice in this group were injected intravenously with AAV9-LAV-BPIFB4 under isoflurane anaesthesia.
3. WT group: induced diabetic male C57BLKS/J-Leprdb/Leprdb/Dock7+ [db/db] mice (obtained from Envigo, Bicester, Oxfordshire, UK). They were injected intravenously with AAV9-WT-BPIFB4 under isoflurane anaesthesia.
4. No virus (NV) group: induced diabetic male C57BLKS/J-Leprdb/Leprdb/Dock7+ [db/db] mice (obtained from Envigo, Bicester, Oxfordshire, UK) and they were injected

with phosphate buffer saline as a vehicle (PBS). This group is named no virus (NV) as no virus was injected.

At 9 weeks of age, the mice were injected with either AAV9-LAV-BPIFB4, AAV9-WT-BPIFB4 or vehicle as previously mentioned and illustrated in figure 3.1. One month later, echocardiography was performed (at week 13) on all mice using Vevo-3100 echocardiography system (Fujifilm VisualSonics Inc, Toronto, Canada) with more details will be given in later section. A subset of mice was transported from Bristol to Cardiff for them to be scanned using PET/CT, to assess MGM and MBF. More details will be given in later sections.



3.11 Ageing mice model:

This model was used to investigate the effect of a single intravenous injection of the therapeutic gene in aged mice. The ageing model included 94 female C57BI/6 mice was divided into two groups, early treatment (treatment started at 14 months old; follow-up for 4 months) and late treatment (treatment started at 18 months old; follow-up for 1 month) groups as in figures 3.2-3.3. The early treatment group included 54 mice (42 female and 12 male mice each), but only female mice were sent for PET/CT imaging. On the other hand, the late treatment group included 40 female mice as in figures 3.2-3.3. It is important to emphasize that the mice in these experiments were healthy aged mice. The mice in the early group were 18 months old, while the late group mice were 19 months old when performing the PET/CT scans. Each ageing group was subdivided into four treatment groups

(3 mice each). Importantly, both the early and late treatment groups were treated with the same genes. Figures illustrate the experimental design for the early and late treatment with more details given in the relevant chapter.

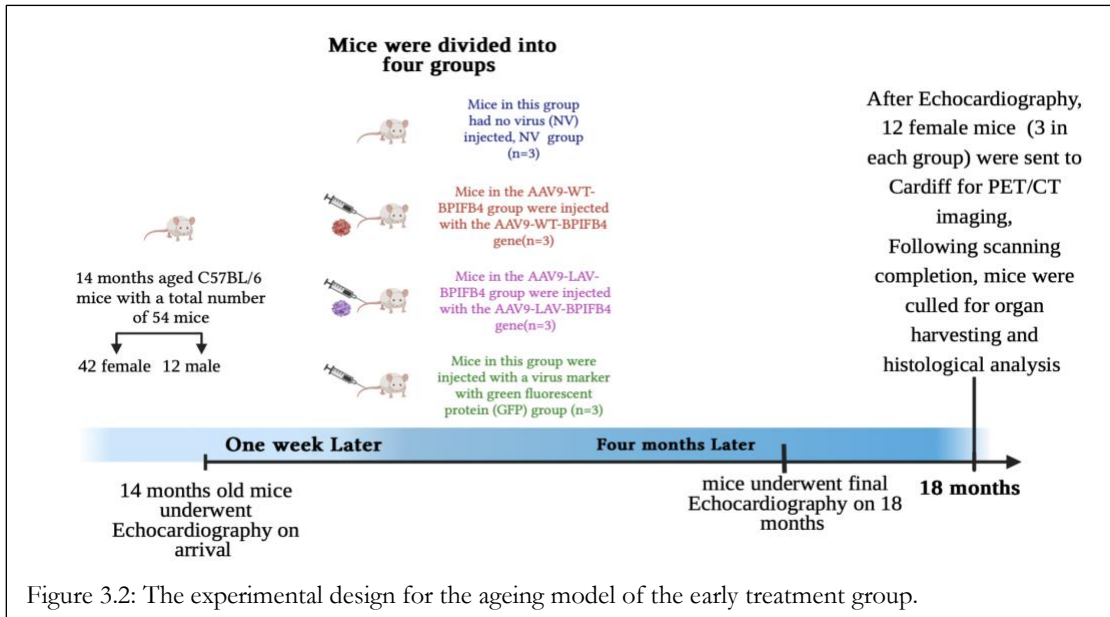


Figure 3.2: The experimental design for the ageing model of the early treatment group.

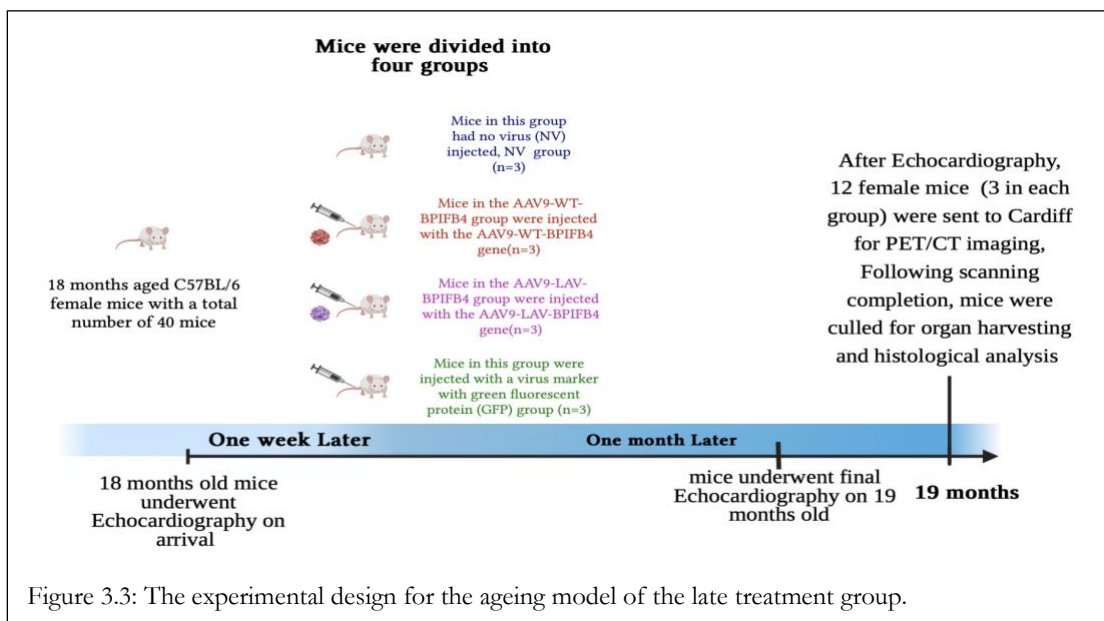


Figure 3.3: The experimental design for the ageing model of the late treatment group.

3.11.1 Mice groups for ageing model:

Both the early and late treatment groups are subdivided into four groups, and they include:

1. GFP group: mice were injected with a virus marker of green fluorescent protein (GFP) group.

2. No virus (NV) group: mice in this group were injected with vehicle (PBS).
3. WT group: mice were injected intravenously with AAV9-WT-BPIFB4 under isoflurane anaesthesia.
4. LAV group: mice in this group were injected intravenously with AAV9-LAV-BPIFB4 under isoflurane anaesthesia.

3.12 Hindlimb mice model:

Hindlimb ischemia was induced in the left leg for four healthy male mice (strain: C57BL/6J) aged about eight weeks (bodyweight 20–30 g), obtained from Charles River, Margate, Kent, UK. More details on the ligation process will be explained in the relevant chapter.

3.13 Imaging protocols:

This research was conducted as part of extensive studies involving several quantification criteria; however, it will focus only on the pieces that have been carried out by the researcher. The imaging protocols were designed to be completed in one day, as the project license only allows one-day imaging under general anaesthesia, which is referred to as terminal anaesthesia. Justification of the protocol's design will be discussed in the related chapter.

These imaging protocols were applied on healthy, ageing and hindlimb ischemic models (HLI) with some differences in the dynamic scan duration. In contrast, in the diabetic model, imaging was limited to the ^{18}F -FDG protocol, which is the same protocol applied in all the other mice models.

3.13.1 Imaging protocols for diabetic model:

As previously mentioned, twelve mice were obtained from colleagues at Bristol University and classified into four groups (3 mice per group).

The mice were fasted for one hour and warmed to 37°C and before being anaesthetised using 2% isoflurane. Isoflurane was administered via induction box that was connected to an O₂ carrier gas cylinder. Intraperitoneal (IP) injection of 100-150 µl of Iohexol CT contrast agent (647 mg/ml) was given just before the radiotracer injection to distinguish between the liver and the kidneys in the CT scan. This was followed by intravenous tail vein injection of 32±8 MBq of ^{18}F -FDG within a volume of 0.1 ml. The mice were then transferred to a pre-warmed imaging scanner bed which was supplied with a small tooth bar (attached to a nose cone) to maintain anaesthesia (using ~2% isoflurane of O₂ (1L/min) nose tube), and ECG electrodes to measure heart rate. A 16 second CT scout scan was acquired, followed by 60 minutes whole-body dynamic PET scan. Afterwards, cardiac gated acquisition was acquired for a duration of 20 minutes, and then lastly, a 2.5-minutes whole-body CT

scan was performed (480 projections, one rotation, 50 kVp). The CT scan was used to calculate attenuation correction. Images of both PET and CT are automatically co-registered.

3.13.2 Imaging protocols for healthy, ageing and HLI models:

In these three models, each mouse was moved individually to a warming box for a duration of about 5 minutes to facilitate finding the tail vein for cannulation. In addition, a cannula was freshly made on the day of the scanning and flushed with heparin saline to prevent blood clotting due to the prolonged imaging time and the administration of various radiotracers. Next, the mouse was positioned in the scanning bed and cannulated via tail vein gently and carefully with several plaster layers applied on the top of the cannula to prevent motion.

Mice in these models underwent scans in the following order: CT Scout view, $^{13}\text{N-NH}_3$ rest scan, $^{13}\text{N-NH}_3$ stress scan, $^{18}\text{F-FDG}$ scan and whole-body CT scan. Following completion, the mouse was moved rapidly to the dissection table, where the cardiac puncture was performed, followed by organs collection, as explained in the following sections.

3.13.2.1 $^{13}\text{N-NH}_3$ rest scan:

In each mouse acquisition, $^{13}\text{N-NH}_3$ (30-100 MBq in 20-60 μL) was injected through a tail vein cannula. Following administration, a 20 min dynamic PET scan was performed. The actual acquisition started a few seconds prior to the administration of ^{13}N -ammonia to catch all the myocardial flow processes.

3.13.2.2 $^{13}\text{N-NH}_3$ stress scan:

Ten minutes later, the stress scan was initiated by a single bolus IP injection of dobutamine (0.75 $\mu\text{g/g}$) without moving the animal (Puhl et al. 2016). The stress scan commenced 5 minutes after the injection, in order to make sure that the heart was under stress. When the heart rate increased to about 600 bpm (measured by ECG pads placed on paws), the second dose of $^{13}\text{N-NH}_3$ (30-100 MBq in 20-60 μL) was injected intravenously, and a 20 min dynamic PET scan was performed. Image acquisition was initiated a few seconds prior to the radiotracer injection by applying the same image acquisition process as in the rest scan.

3.13.2.3 $^{18}\text{F-FDG}$ scan:

Following the ammonia scans, an injection of ~ 20 MBq of $^{18}\text{F-FDG}$ in ≈ 20 μL was administered via the same cannula line, and a 40-minute whole-body dynamic PET scan was acquired immediately after administration.

3.13.2.4 CT scan:

Following FDG scans, a 2.5-minute whole-body CT scan (480 projections, one rotation, and 50 kVp) was performed to calculate attenuation corrections as well as allow co-registration of images which in turn give a better visualisation of structural and functional information from the CT and PET respectively.

3.13.2.5 Culling process:

The culling process was different depending on whether or not the histological analysis was carried out. In HLI, diabetic, and ageing models and following all scans completion, and while the mouse was under the anaesthesia, blood was taken into an EDTA-coated syringe (23-gauge needle) via cardiac puncture (the needle was inserted under the left elbow directly into the heart). After termination, organs and tissues were harvested. In the healthy model, the mouse was terminated either using overdose of euthatal or by cervical dislocation technique.

3.14 Image reconstruction:

All PET scans were acquired in list mode acquisition, and images were reconstructed with Mediso's Nucline NanoScan reconstruction software (v 3.04.010.0000) using the Tera-Tomo 3D reconstruction algorithm with four iterations and six subsets, on 0.4 mm isotropic 3D voxel grids and an energy-window of 400-600 KeV. More details on the used framesets will be included with details in each chapter; however, it is important to note that due to variation in the injection time following scan activation, the reconstruction frame time varied according to the starting points of the injection. This is because that we only interested in the time during and following the radiotracer injection, and the time before in the injection will be discarded. Attenuation (CT based) and scatter corrections, median and spike filters, as well as normalisation, were all applied to the reconstructed images. Additionally, CT scans were reconstructed with a 0.25 mm voxel size using the cone-beam filtered back-projection method, and a cosine filter was applied. The PET images were co-registered to the CT images to allow absolute quantitation of the PET data.

3.15 The data analysis software:

Processing and analysing medical images from hybrid modality like PET/CT scanner are challenging procedures because they involve the use of multiple sources of functional and anatomical information. The commercial PMOD version 3.91 (PMOD Technologies Ltd. Zurich, Switzerland) was the software of choice in all the analyses due to the sophisticated capability of compartmental modelling that offers a wide range of parameters to be examined. Accordingly, following the

reconstruction, all scans were exported to PMOD software in DICOM format (Digital imaging and communication in Medicine) which is a commonly used image format that facilitates transferring and analysing images from different devices, scanners, servers, and networks.

PET data quantification is defined as the extraction of physiological parameters of a system from the study of radiotracer kinetic and uptake. Quantification can be simply described as input/output in which the input parameters were the PET scans, and the output was the measurement of a physiological biomarker that can describe the function of an organ.

In this research, the applied PET quantitative tools were SUV and compartment modelling that were mentioned in earlier chapters. Details on the applied models will be discussed closely in each chapter. Generally, PMOD consists of integrated sets of tools, each of which tackles different aspects in the image analysis starting from the simple drawing of volumes of interest (VOIs) and their related statistics to the level of compartmental modelling that includes different complicated mathematical models. Three tools have been used in this research which are Image processing and VOI analysis (PBAS), general kinetic modelling (PKIN) and Cardiac PET modelling (PCARD).

First, the PBAS tool was used to define VOIs within tissues by drawing contours around the area in a 3D plane. PMOD offers a large platform to draw VOIs via either contour outlines, geometric objects, linear VOIs or VOIs with holes, which can be helpful in the case of the myocardium but discussing them in detail is beyond the scope of this research. Next, a wide range of statistics can be generated, including TACs and SUVs. The TACs can be aggregated later to the PKIN tool for further kinetic modelling analysis.

Next, the PKIN tools was used to study the radiotracer pharmacokinetics within time. There are several comprehensive modelling available in this tool, but details of those used (1TCM, 2TCM and ammonia de Grado (type of 1TCM) will be given in the relevant chapter.

Finally, PCARD tools were the main tools for compartmental modelling in the myocardium, but it is also closely connected to PKIN tools in which all the produced TACs for the blood and tissues from the PCARD tool can be smoothly opened in PKIN for further modelling options.

3.16 Echocardiography:

The echocardiography results using Vevo-3100 echocardiography system (Fujifilm VisualSonics Inc, Toronto, Canada) along with MX400 or MX550D transducer were used to measure various cardiac dimensional and functional parameters (Katare et al. 2010; Katare et al. 2011). All echocardiography results were performed by a member in our research group in Bristol university. In

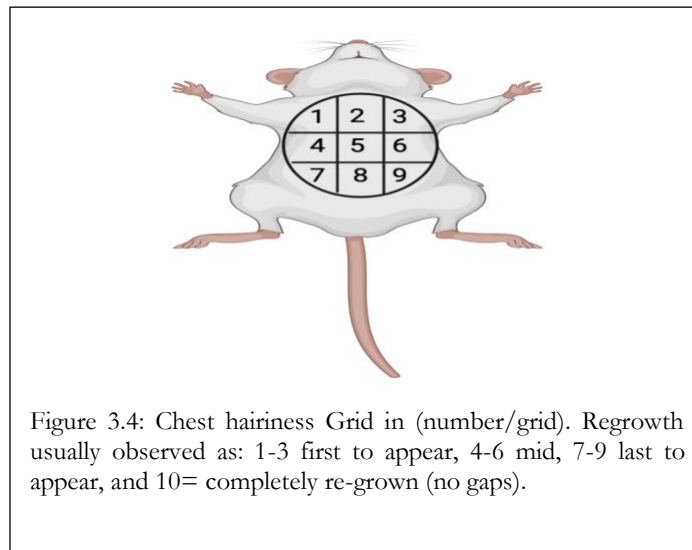
the diabetic model the MX400 was used, while MX550D was used for the ageing model. During the procedure, each mouse was anesthetized using isoflurane starting with 2.5% but this percentage was adjusted as appropriate to keep the heart rate close to 450 bpm. The echocardiography procedure generally lasted for about one hour.

3.17 Laser Doppler imaging:

The doppler imaging was used only in the HLI model to assess blood flow in the HL of the mouse. This imaging was carried out by one of our research group members in Bristol university. It was performed using the moorLDI2 laser Doppler blood flow imager (Moor Instruments, Millwey Rise Industrial Estate, Weycroft Ave, UK). The laser source was moorLDI2-VR; 633nm, Max 2.5mW, 1.2mm beam using the high resolution of 0.05 mm/pixel and scan speed of 4ms/pixel.

3.18 Hair re-growth grid:

We have assessed the hair re-growth pattern in the diabetic model as illustrated in figure 3.4.



3.19 Organ harvesting:

For histology analysis, organs harvesting, and blood collection were performed and will also be explained in each chapter. In both ageing and diabetic models, the blood was collected directly from the heart through the cardiac puncture technique using ethylenediamine tetraacetic acid (EDTA)-coated syringe and 23-gauge needle, which were kept in ice prior to blood withdraw, to prevent blood clotting. Next, blood was centrifuged for 10 min with no break, around 2000-3000 revolutions per minutes (rpm), and then the plasma was removed, flash frozen and stored at -80 °C freezer.

Following cardiac puncture procedures, organs were harvested from the diabetic, ageing and HLI models. The collected organs either were flash-frozen in liquid nitrogen or dropped-fixed in 4% paraformaldehyde (PFA) for 24 hours at lab temperature. The PFA created covalent cross-links between the molecules, and thus gluing them together into an insoluble meshwork. In the PFA fixed samples, the PFA was changed to phosphate buffered saline (PBS) on the next day. Both Frozen and fixed organs were kept at -80 °C and -20°C fridge respectively for later use. Afterwards, myocardial tissue samples were embedded in optimal cutting temperature compound (OCT) and then were cut at 8 µm sections using a cryostat. The sections were kept in the freezer for later staining.

3.20 Immunohistochemistry staining:

Immunohistochemistry staining was performed to quantify the capillary and arteriole density in each tissue using isolectin GS-IB4 (IB4, I21414, Life Technologies, USA) and specific antibody anti- α -smooth muscle actin (α SMA; C6198, Sigma, UK). Most of the immunohistochemistry staining were performed by the researcher but some staining were performed by another research member in Bristol university.

The staining procedures started with antigen retrieval step with citrate buffer (ph 6) for 10 minutes using the microwave heating at medium to high power. Note that the citrate buffer was prepared previously using the ionizing water and citrate buffer powder (with a concentration of 10:1). Following that, the sections were left to cool at room temperature for 40 minutes and then washed with PBS. The sections were blocked with blocking buffer (5% Goat serum (GS) + 5% bovine serum albumin (BSA) in PBS) for 30 minutes at room temperature. The primary antibody and lectin were applied together (biotinylated isolectin GS-IB₄ 1:200, and α SMA-Cy3 1:400) in blocking buffer and the sections incubated overnight at 4 °C. In the primary antibodies blocking step, I have prepared negative control samples either by using PBS and the Dako A0944 mouse IgG2a. The next day, the sections were washed with PBS and the lectin labelled with secondary marker streptavidin-Alexa488 (LT S32354, Life Technologies. 1:200) in PBS at room temperature for 1 hour. After washing, the nuclei were stained with DAPI (4',6-diamidino-2-phenylindole) with concentration of 1:1000 in PBS for 5 minutes, DAPI is used to bind to DNA.

3.21 Fluorescence microscopy:

The Vascular density was measured by counting the capillaries in at least 10 fields (images) were captured in all sections at 20 X magnification. This procedure was carried out by the researcher. After staining, the sections were analysed using optical or fluorescence microscopy (Zeiss Axio observer

microscope, Cat # 1026044910, Germany). The staining with green colour (488 emission) lectin binding representing the capillaries, and red (Cy3 emission) α SMA staining identifying the arteries. All fields were saved in TIF (Tagged image file) format in an external hard drive-in order to be analysed with Image J software.

3.22 Image J software:

For capillary and arteriole density quantification, the image J (Fiji version 2.5.0, LOCI, University of Wisconsin, USA) was used. The area and number of capillaries and arteries were identified in at least 20 fields per section. Final data were generated as the number of capillary or artery per mm². This analysis was indeed performed by the researcher.

3.23 Statistical analysis:

Statistical analyses were conducted using GraphPad Prism (version 9.4.0, USA), through which data were represented with their individual values, mean and STD. After testing for normality, comparisons were generated using a variety of tests, including unpaired Student's *t*-test or 1- or 2-way analysis of variance (ANOVA), as appropriate. The mean values of two groups or data sets were tested for statistically significant using the unpaired *t*-test. Moreover, the means of the four treated groups with respect to one variable were compared using 1-way ANOVAs, whereas 2-way ANOVA tests were used to examine the effect of gene treatment in the four groups with respect to two different variables (the response to the gene therapy at different time points). Differences were considered significant when $P < 0.05$.

Chapter 4:

Evaluation of Micro-PET/CT system quantification accuracy with ^{18}F -FDG and ^{13}N - NH_3 using NEMA standard tests

4.1 Introduction:

Preclinical PET/CT systems are widely used to assess the efficiency of a novel treatment in an animal model or to validate and standardize the application of current and new radiotracers to be translated to human studies. The power of PET imaging lies in its ability to produce quantitative measurement of vital biomarkers, thus giving information about the underlying physiology. As already discussed, several quantitative or semi quantitative techniques are commonly used to extract or quantify physiological biomarkers. SUV is a well-known semi-quantitative example and is usually determined by drawing ROI around the organ or tissue of interest. This ROI is used to measure the radiotracer concentration through which its metabolic process could be quantified. Compartmental modelling (or PKIN modelling) requires dynamic acquisition during PET scanning in order to study the radiotracer kinetic in tissues. Compartmental quantification can be seen in the case of ^{18}F -FDG and ^{13}N - NH_3 , in which they are used to assess critical biomarkers such as glucose metabolism and MBF, respectively. These techniques rely on the fact that the micro-PET/CT system generates accurate and reproducible results, which cannot be achieved without standardization in both the performance measurements of the micro-PET/CT system and the imaging protocols. The diagnostic value of the small animal PET imaging is directly connected to the validity and reproducibility of the obtained data. If the data are not reproducible, the results will be somewhat questionable.

In this chapter I will discuss the standard performance tests of the micro-PET/CT scanner, such as spatial resolution (SR), sensitivity and scatter fractions (SF), and the image quality (IQ) test, which is routinely highlighted in quantitative PET studies. The standardization of the imaging protocols will be discussed in the next chapter. In addition, this chapter will describe our first experiments in the standardization and optimization processes for ^{18}F -FDG and ^{13}N -ammonia quantification. These

experiments comprise the mandatory performance test needed to generate accurate quantitative data: an image quality test for both tracers. As several studies have demonstrated that the IQ test accounts for important factors of the PET system, such as SR, sensitivity, and SF tests (Wong et al. 2012; Meechai et al. 2015; Hallen et al. 2018; Teuho et al. 2020), we have not performed these tests separately. I have performed statistical analyses to assess the degree of variability in measurement when using different radiotracers. Importantly, our IQ assessment, including image acquisition and reconstruction parameters, is aligned with the National Electrical Manufacturers Association (NEMA) and manufacturer standards.

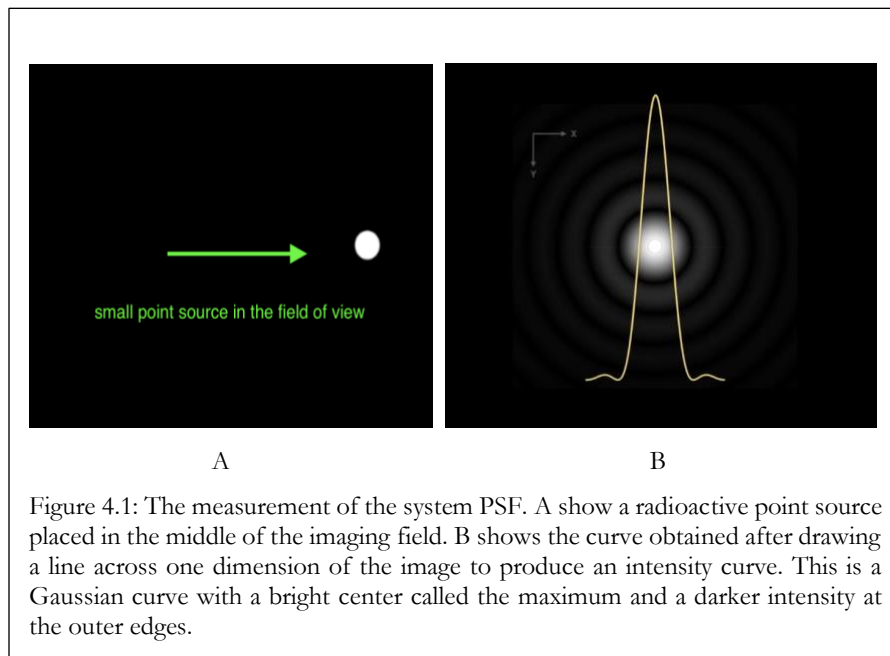
When using micro-PET systems, performance measurements are different from clinical performance measurements because of the need to adapt to the small size of the laboratory animals. In the past two decades, much work has been conducted to construct preclinical PET systems suitable for these animal models (Lewellen 2008). In 2000, preclinical PET systems became available with all the physical characteristics of the clinical PET system. The performance of these preclinical systems had developed rapidly, but the development of standardized methods to assess their reliability and accuracy is lacking.

The NEMA published a set of standards (NU 4/2008) that include methodologies for assessing scanner performance of the micro-PET/CT systems (Association 2008; Disselhorst et al. 2010). The purpose of these methodology protocols was to ensure that the performance of the different preclinical PET scanners can be compared to each other through comparing their performance values following the application of NEMA standard imaging protocol (Force 2008; Teuho et al. 2020). Before this, vendors could not provide precise specifications and standards similar to those in clinical imaging systems under NEMA guidelines. Nowadays, vendors offer a manual with all the guidelines to perform these evaluations along with their expected normal ranges to ensure the accuracy and reproducibility of the micro-PET/CT system as a diagnostic and quantitative imaging tool.

These measurements include SR, sensitivity, SF, count loss and random coincidence, and image quality. Each of these parameters and their standard measuring method will be underlined in detail in the following sections. More focus will be given to the NEMA IQ test since it is often considered to assess the quantitation accuracy of the PET system. Therefore, a test of IQ calibration was carried out as a necessary part of obtaining reliable quantitative data.

4.1.1 Spatial resolution (SR):

In the PET system, spatial resolution (SR) is defined as the ability of the imaging system to distinguish between two infinitely small point sources in the object as separate points in the produced image of the object (Saha 2010). In simpler terms, it is the ability of the system to detect or visualize the details of an object (Cherry et al. 2012). For a conceptual and practical understanding of many concepts of SR in any imaging system, this requires knowledge of the system's point spread function (PSF) (Saha 2010; Smith and Webb 2010; Cherry et al. 2012). This can be exemplified by placing a tiny point source in the imaging field, scanning it, and then drawing a line across one dimension of the produced image to check the intensity across that line, as in figure 4.1 (Smith and Webb 2010; Cherry et al. 2012). It shows a bright center called the maxima with much darker outer edges, where the intensity line creates a Gaussian distribution curve. (Smith and Webb 2010; Cherry et al. 2012).



Small point sources in the imaging field appear as a PSF or a Gaussian distribution curve in the generated image (Smith and Webb 2010; Cherry et al. 2012). Moreover, when there are two radioactive point sources in the image separated by a distance smaller than the PSF of the system (Yang et al. 2004; Smith and Webb 2010), their Gaussian curves will blur together to form only one curve, as shown in figure 4.2. Figure 4.2 also reveals that the minimum diameter of the Gaussian curve, either in the axial or lateral direction, is approximately equal to the full width at half maximum (FWHM) (Smith and Webb 2010; Cherry et al. 2012).

Accordingly, a larger PSF results in a lower SR, and the system loses its capability to resolve the two separated point sources as two separate objects, as described in figure 4.2 (Smith and Webb 2010; Cherry et al. 2012). Several studies have demonstrated that the PSF is larger in the axial Z direction than the lateral XY direction (DeGrado et al. 1994; Mawlawi et al. 2004; Surti et al. 2005; Moses 2011). Additionally, as seen in figure 4.3, the SR reduces as we move away axially (in the XY plane) from the center (Surti et al. 2005; Moses 2011).

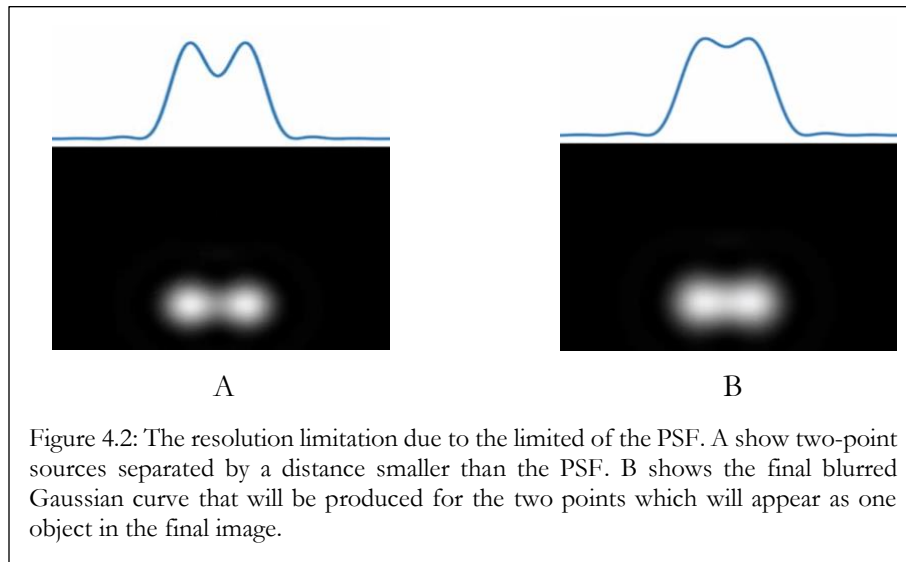
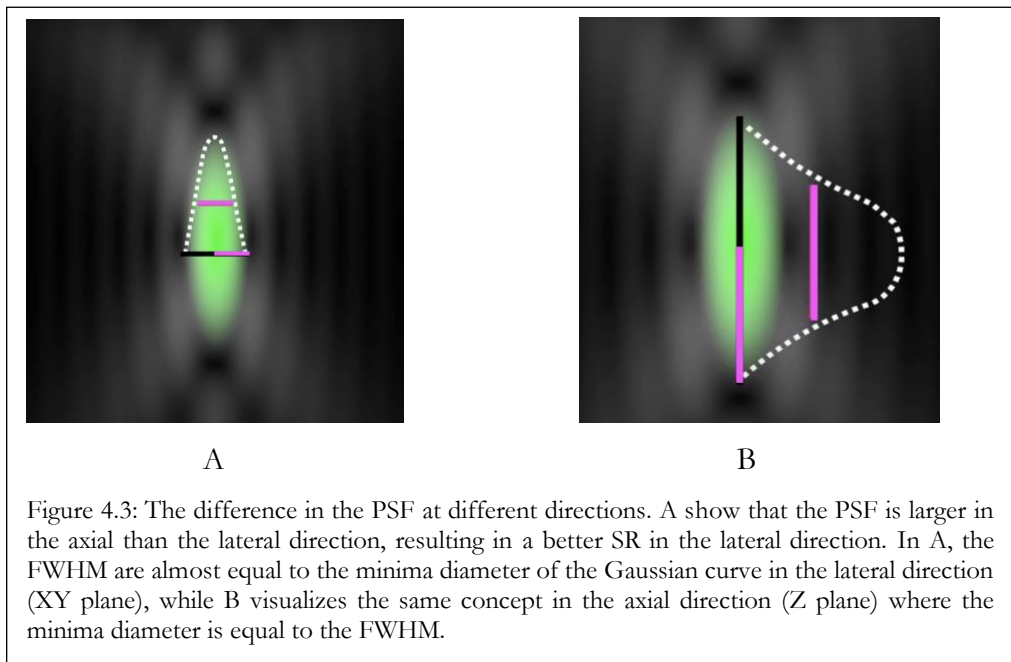


Figure 4.2: The resolution limitation due to the limited of the PSF. A show two-point sources separated by a distance smaller than the PSF. B shows the final blurred Gaussian curve that will be produced for the two points which will appear as one object in the final image.

Generally, the FWHM of the PSF in an imaging system is about 1.4 to 2 times the smallest resolvable object (Smith and Webb 2010; Moses 2011; Cherry et al. 2012). For example, if the FWHM of the PSF is 10 mm, the system can resolve an object ranging between 5 and 7 mm in width (Cherry et al. 2012). In a recent preclinical PET scanner, the SR had a value ranging between 1.5 and 2.5 mm, measured at the FWHM of the PSF within the central field of view (cFOV) (Surti et al. 2005; Cherry et al. 2012). The SR is greatly dependent on the radial offset. Several studies reported that SR values worsen down to 2.5 mm FWHM at the radial offset of 25 mm (Mawlawi et al. 2004; Surti et al. 2005; Moses 2011; Sato et al. 2016). Multiple factors might affect the SR of the image, such as the scintillator size (also called crystal size), the point of annihilation and the positron range of the used radiotracer (Smith and Webb 2010; Cherry et al. 2012).

To begin with, reducing the scintillator size will significantly improve the SR; however, it will reduce the sensitivity of the imaging system to detect photons (Smith and Webb 2010; Moses 2011; Cherry et al. 2012; Sato et al. 2016). In the case of a micro-PET, it is not practical to decrease the scintillator size enough to completely compensate for the reduction in size of a mouse compared to a human; this has led to the development of a scanner with scintillator sizes of only 0.975 mm (Weber and Bauer

2004; Saha 2010). A smaller crystal results in a decreased detection count and a higher signal to noise ratio (SNR) (Smith and Webb 2010; Sato et al. 2016). Another issue that limits the SR of PET in mice is that the point where the annihilation event occurs is not the point of positron emission (Cherry et al. 2012; Sato et al. 2016). This happens because of the positron range (PR), which is defined as the finite distance travelled by the positron in the tissue before losing its kinetic energy and being annihilated (Saha 2010; Smith and Webb 2010). The PR is a distinct characteristic of any radiotracer; table 4.1 contains several radiotracers with their PR (Maddahi and Packard 2014). In addition, in the annihilation event, any residual kinetic energy will cause annihilated photons to be emitted at less than 180°, creating non-collinearity and losing the accurate position (Smith and Webb 2010; Cherry et al. 2012). These factors all contribute to, and might degrade the PET image quality (Saha 2010; Cherry et al. 2012). Nonetheless, many approaches to solutions have been proposed by several investigations, such as the PR correction factor (Phelps et al. 1975).



4.1.1.1 Measurement of SR with the NEMA NU 4-2008 standard:

According to the NEMA NU 4-2008 standard, SR can be calculated on a weekly basis by a ^{22}Na point source with an activity of 0.52 MBq, embedded in a 1 cm³ acrylic tube with a diameter of 0.25 mm (Association 2008; Prasad et al. 2011; Sato et al. 2016). According to NEMA guidelines, the SR should be measured at the cFOV and one-fourth of the axial FOV in multiple radials and axial distances (0, 2, 5, 10, 15, 20, 30, and 40 mm) from the center (Force 2008; Prasad et al. 2011). For all the acquired scans, list mode should be initiated (Force 2008).

Following completion, the scans must be reconstructed with a 2D filtered back-projection and a ramp filter (high pass filter)(Force 2008; Prasad et al. 2011). The cut-off set in this filter must be at the Nyquist frequency, which is defined as the highest frequency that can be coded for a specific sampling rate for the signal to be reconstructed (Smith and Webb 2010; Cherry et al. 2012). Lastly, the FWHM can be calculated for the lateral and axial offset positions (Smith and Webb 2010; Cherry et al. 2012).

Agent	Physical half-life	Mean Positron range (mm)	Production
N^{13}	9.96 min	1.7	Cyclotron
F^{18}	110 min	0.66	Cyclotron
O^{15}	2.06 min	4.14	Cyclotron
Rb^{82}	1.25 min	8.6	Generator

Table 4.1: The physical characteristics including $T_{1/2}$ and PR of both ^{18}F and ^{13}N (Maddahi and Packard 2014).

4.1.2 Sensitivity:

In PET imaging, sensitivity can be described as the ability of the system to detect radiation and it is generally represented by the percentage between the emitted and measured annihilated photons (Saha 2010; Smith and Webb 2010; Cherry et al. 2012). As with SR, sensitivity is affected by multiple factors such as the detector material, the packing fraction, the crystal size and the solid-angle coverage of the detector ring (Saha 2010; Smith and Webb 2010; Cherry et al. 2012). Numerous studies have reported that scanners with larger axial FOVs and small ring diameters often have improved sensitivity (Weber and Bauer 2004; Sato et al. 2016). Furthermore, there is a trade-off between sensitivity and resolution in which a thinner crystal will enhance the spatial resolution, but at the expense of reducing the sensitivity (Cherry et al. 2012). However, fewer detected counts will generally lead to noisy and low contrast images (Cherry et al. 2012).

4.1.2.1 Measurement of sensitivity with the NEMA NU 4-2008 standard:

The NEMA standard recommends measuring the sensitivity centred at the scanner FOV using the ^{22}Na point source, as in the SR measurements (Association 2008). Additionally, the background should be measured by acquiring a scan without the radioactive point source (Association 2008). The acquisition should be set to stop after the scanner collects 10,000 actual events, and the time taken to complete the scan should be recorded (Association 2008). After that, the previously recorded time must be used for all the later acquired scans for subsequent positions stepped in the axial direction in

order to cover all FOVs (Association 2008). A plot of the axial sensitivity against the absolute sensitivity for each slice can be generated (Association 2008).

4.1.3 Scatter fractions (SF) and counting rate measurements:

In a clinical PET scanner, scatter is an essential factor that might reach a 36% fraction of the total measured events in the 3D mode PET scanner (Podoloff and Stearns 2004). On the other hand, in the micro-PET scanner, the scatter fraction (SF) is often in the range of 8% in mice and 20% in rat studies (Yang et al. 2004). Although the scatter contribution in mice seems to be low, this is not the case when scanning multiple mice at once, which is a protocol that has been applied in many preclinical institutions (Wong et al. 2012). Recently, data from a simulation study reported an increase of 25% to 64% in the SF when scanning more than three mice simultaneously (Wong et al. 2012). These results confirm that the SF in preclinical imaging is a crucial factor when imaging several mice at the same time. However, this is not a problem in the studies presented here, as mice were only scanned one at a time. Several types of algorithms can be applied to correct scattered events (Vicente et al. 2007b). Importantly, all rely on the availability of structural information, which can be obtained from MRI or CT scans. CT-based SC was applied in all the scans in this project, leading to a more accurate scatter or attenuation correction calculation. Indeed, before applying scatter correction, the scatter events were eliminated, initially using a PHA that has an energy window set with a maximum and minimum window. This was to detect and record any annihilation coincidence that underwent a small-scattered angle and loss of energy (Saha 2010; Cherry et al. 2012). Nevertheless, this simple process is less efficient due to the slight difference in energy values between the scatter and actual events; hence there is always a need to apply SC (Saha 2010; Cherry et al. 2012).

In general, modern clinical and preclinical PET systems have fast acquisition and processing of coincidence events, enabling them to distinguish between true, scatter, and random coincidence events described earlier in the introduction. Nonetheless, the PET system requires a finite time to fully process and register each photon or (coincidence event). This is called the dead time, during which any new events will not be detected (Saha 2010). This is a limitation of the PET scanner, especially at a high-counting rate scan, causing a pile-up effect which is defined as the loss of photons during the deadtime interval of the system (Vicente et al. 2007b). This pile-up effect can add or subtract counts from the final coincidence events detected (Vicente et al. 2007b).

For example, two pile-up photons may fall within the energy window and thus add up to the total number of registered events (Vicente et al. 2007b). Similarly, a two pile-up true coincidence could be pushed out of the upper energy window limit, resulting in a loss of counts (Vicente et al. 2007b).

Ultimately, the generated image would have a low statistical quality, which may lead to mispositioning of actual events (Vicente et al. 2007b).

4.1.3.1 Measurements of SF and count rate performance:

In compliance with NEMA NU 4 – 2008 specifications, particular mouse and rat phantoms can assess the SF and count rate performance (Association 2008). The two phantoms are made of a solid, circular cylinders built from high-density polyethylene (Association 2008). The mouse phantom measures 70 ± 0.5 mm in length and 25 ± 0.5 mm in diameter, while the rat phantom measures 150 ± 0.5 mm in length and 50 ± 0.5 mm in diameter (Association 2008). The measurement for each phantom involves placing a line source filled with ^{18}F inserted inside the highly scattered phantom (Association 2008). The ^{18}F activities are 105 MBq for the mouse-sized phantom and 150 MBq for the rat-sized one (Association 2008). After that, each phantom undergoes scanning acquisition for 10 hours. Following this, sinograms should be generated without applying any correction (Association 2008). The rows of the generated sinograms must be centred at their maxima, and the sum of all rows should then be measured (Association 2008). The NEMA standard includes a signal window of 7mm around the maxima in which any counts outside the signal window are considered to be scatter or random events (Association 2008).

4.1.4 Image quality (IQ):

Studies involving small animal imaging require a high standard image quality (IQ) to generate accurate quantification. Generally, IQ is dependent on the image reconstruction parameters, the applied image corrections, and the choice of the radiotracer (Teuho et al. 2020). Each radiotracer has unique physical characteristics that dramatically impact in vivo measurements, such as cardiac metabolism or MBF (Teuho et al. 2020). The preclinical data precision, repeatability, validity, and translatability are of utmost importance (Sato et al. 2016). Consequently, technical, and non-technical factors that might influence the quality and quantification process need to be investigated.

Animal handling and imaging protocols have the most significant impact on preclinical studies and the quality of the produced images. The next chapter will discuss, validate, and standardize protocols in detail. Naturally, the administrated radiotracer also has a significant influence on the IQ. When using different radiotracers, the IQ should be explored to have a standard or acceptable image (Association 2008). Accordingly, phantom studies have been recommended by the NEMA NU 4 – 2008 to test the quality and the quantification accuracy of PET images when using the same or different radiotracers (Association 2008; Teuho et al. 2020). The NEMA IQ phantom tests include

checking specific image parameters and performance metrics, such as partial volume effects (PVE) and their correction through recovery coefficient (RC) methods, spill-over ratios, image uniformity and the standard deviation percentage (STD%) of radioactivity concentration along the uniform region of the phantom. It may be possible to measure SR via the RC values in the IQ phantom (Prieto et al. 2010; McDougald et al. 2020). Indeed, in this chapter, the SR of our PET scanner was evaluated through RC values similar to the methods applied by Prieto et al. and McDougald et al. (Prieto et al. 2010; McDougald et al. 2020). Importantly, as recommended by the NEMA NU 4 – 2008, specific image acquisition and analysis protocol have been applied. In addition, vendors also provide guidelines to achieve comparable image parameters and high IQ according to NEMA standards.

To understand how the NEMA IQ phantom tests are performed, brief details on the investigated parameters, including PVE and spill-over need to be introduced.

4.1.4.1 Partial volume effect (PVE), spill-over and the tissue fraction effect:

PET quantification is one of the most promising applications through which changes in metabolism or physiological parameter can be detected as a function of time (Soret et al. 2007; Zhong et al. 2013b).

Such information would be beneficial to proceed with or eliminate the use of a novel drug as in the case of this project. Weber and his colleagues (Weber et al. 1999) reported highly reproducible data in a clinical trial with ^{18}F -FDG (with an SD of about 9%) for the measurement of tumour metabolism in their attempt to test the validity of a new drug. This fact might make PET imaging ideal for novel drug approval; however, there are several challenges associated with the system and the radiotracers of choice (Visser et al. 2008; Disselhorst et al. 2010). Understanding these challenges is of foremost importance, especially in monitoring the response to therapeutic intervention (Soret et al. 2007).

One of these factors is a phenomenon called partial volume effect (PVE) which causes the intensity values in the generated images to differ from the true source region in the object. PVE occurs due to two factors which are the limited SR of the PET scanner and the image sampling (Soret et al. 2007).

The first factor in PVE is the loss of SR of the system, which appears as 3D image blurring, originating either from the scanner design (for instance, the crystal thickness) or the reconstruction method (Soret et al. 2007). In this context, the PVE is defined as the underestimation or overestimation of radioactivity concentration in the source region of the generated PET images, which can consequently lead to misinterpretation of the data. Underestimation usually arises in a source

region that is surrounded by other high radioactivity regions (also called hot regions). The effect becomes significant when the source region is smaller than the scanner SR (Vaska et al. 2006; Sato et al. 2016). The underestimation is also called a spill-out, because part of the signal from the source spills outside the source region, as can be seen in figure 4.4 (Soret et al. 2007). Similarly, the overestimation of radioactivity in the source region due to the surrounding hot regions is called spill-in (Soret et al. 2007; Meechai et al. 2015). Indeed, both spill-in and spill-out are generally referred to as the spill-over effect which are illustrated in figure 4.5. Both PVE and spill-over are the results of multiple factors such as the region size, the radioactivity in the surrounding regions and the SR of the scanner. All of these factors have been explored along with their correction methods in more detail in a review article by Soret et al. (Soret et al. 2007).

The second concept causing PVE is image sampling (Soret et al. 2007). In a PET image, the biodistribution of the radionuclide is generated or sampled on a voxel grid (Soret et al. 2007; Meechai et al. 2015). Certainly, the voxel contours will not perfectly match the actual object contours and, consequently, each individual voxel might include different types of tissue. This phenomenon is called the tissue fraction effect, as shown in figure 4.6 (Soret et al. 2007). Importantly, the intensity in each voxel is the mean of all signal intensities of the underlying tissues, which contribute to this voxel (Soret et al. 2007).

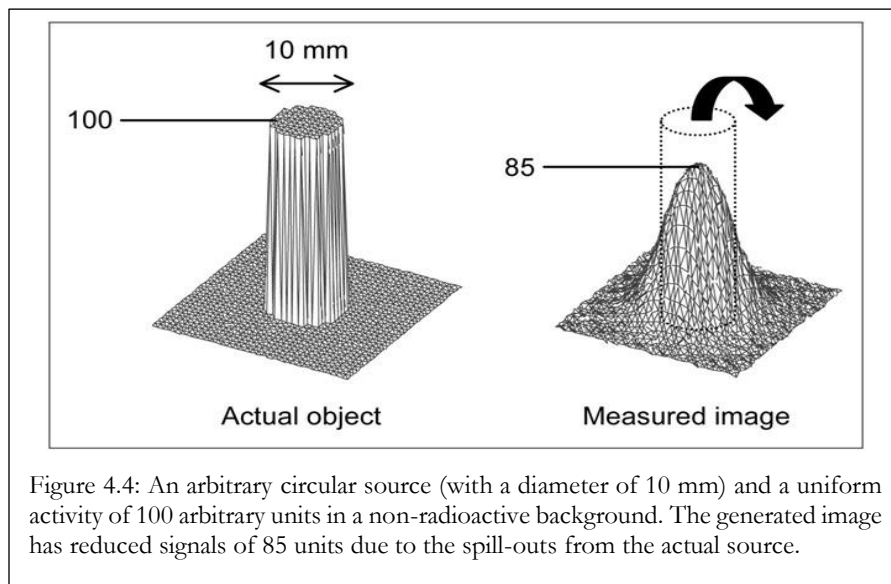
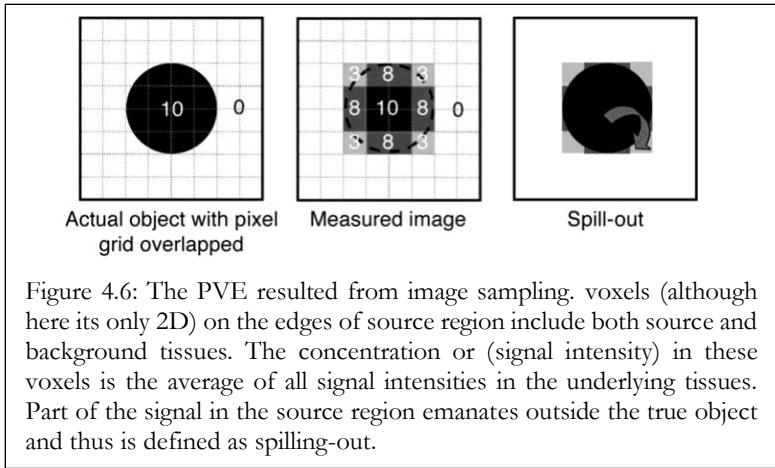
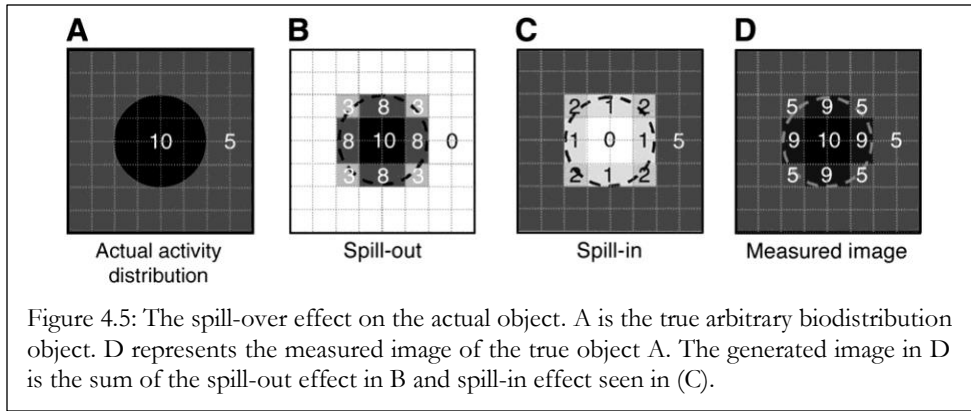


Figure 4.4: An arbitrary circular source (with a diameter of 10 mm) and a uniform activity of 100 arbitrary units in a non-radioactive background. The generated image has reduced signals of 85 units due to the spill-outs from the actual source.



Generally, even if the imaging system has the perfect SR suitable for the scanned object, PVE will persist due to the image sampling limit (Soret et al. 2007; Meechai et al. 2015). Importantly, Hoffman and his co-worker recommended performing PVE, spill-over and tissue fraction effect corrections, as they are crucial in the accuracy of quantitative results, especially in small animals (Hoffman et al. 1979).

A frequently applied method to correct for PVE is the use of the NEMA IQ phantom, which will be discussed in the following sections. The phantom contains a cold region placed in a hot uniform field to measure the SOR ratio as shown in figure 4.7 (Association 2008; Gontijo et al. 2017).

Additionally, the IQ phantom (figure 4.7) contains different sphere sizes that can be filled with a known concentration of the used radiotracer and then scanned (Association 2008).

The fraction of the activity, which is recovered in each sphere of the generated image, is calculated by comparing the generated image sphere concentrations to the previously known amount in the spheres (Association 2008). The calculated fraction is called the recovery coefficient (RC), which has a recommended range in each sphere size according to the manufacturer guidelines and NEMA standard (Association 2008; Gontijo et al. 2017).

4.1.4.2 The importance of an image quality test when using different radiotracers:

It is popular in preclinical imaging to perform multiple scans with different radiotracers; hence it is preferable to carry out and compare the IQ performance test for each used radiotracer (Association 2008; Gontijo et al. 2017; Teuho et al. 2020). This comparison is recommended to study and standardise the performance for each radiotracer using the same preclinical PET scanner, according to the NEMA IQ standard (Teuho et al. 2020).

In preclinical imaging, the commonly used radionuclides include Carbon-11 (^{11}C), ^{13}N , ^{18}F and Zirconium (^{89}Zr), with each having its own unique half-life ($T_{1/2}$), positron energy, and PR (Teuho et al. 2020). Increasing PR could degrade the IQ and the resolution of PET images (Teuho et al. 2020). Liu et al. (Liu and Laforest 2009) investigated image resolution and its relation to the positron range by testing different radiotracers. Additionally, Disselhorst et al. (Disselhorst et al. 2010) have evaluated the IQ in small animal PET/CT scanners with ^{18}F , ^{89}Zr , Gallium (^{68}Ga), and Iodine (^{124}I) (Disselhorst et al. 2010). Both Liu et al. and Disselhorst et al. (Liu and Laforest 2009; Disselhorst et al. 2010) emphasize the necessity to perform the IQ evaluation for any used radiotracers in the micro-PET/CT scanner, especially when using compartmental modelling quantification which was applied in this research. Teuho and his colleagues (Teuho et al. 2020) have compared the IQ test among different vendors. In general, differences in $T_{1/2}$ and PR values lead to variations in counting statistics, SR, and the percentage of noise, if the same image acquisition was applied (Teuho et al. 2020). Nevertheless, this can be optimised according to the goal of the scans; for example, in some studies, the counting statistics have greater importance than the spatial resolution to a certain limit (Teuho et al. 2020).

In the light of this evidence, it is essential to assess the IQ parameters for any used radiotracers in a standardised fashion to study the radiotracer and system-dependent factors that could influence the obtained results in quantitative studies.

4.1.4.3 Image quality phantom test:

The purposes of the NEMA IQ phantom test are to ensure the accuracy of the quantitative results obtained from the small animal using the preclinical PET scanner and is recommended to be performed quarterly (every 3 months). According to the NEMA NU 4-2008 standard, the IQ phantom is made up polymethylmethacrylate (PMMA) and its geometry is subdivided into several regions each of which evaluate a specific performance measurement, as shown in figure 4.7 and table 4.2.

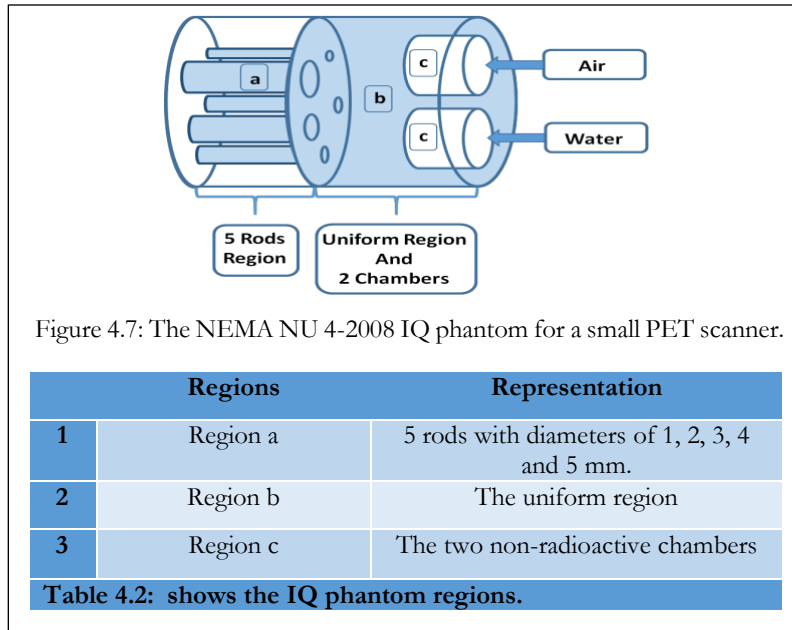
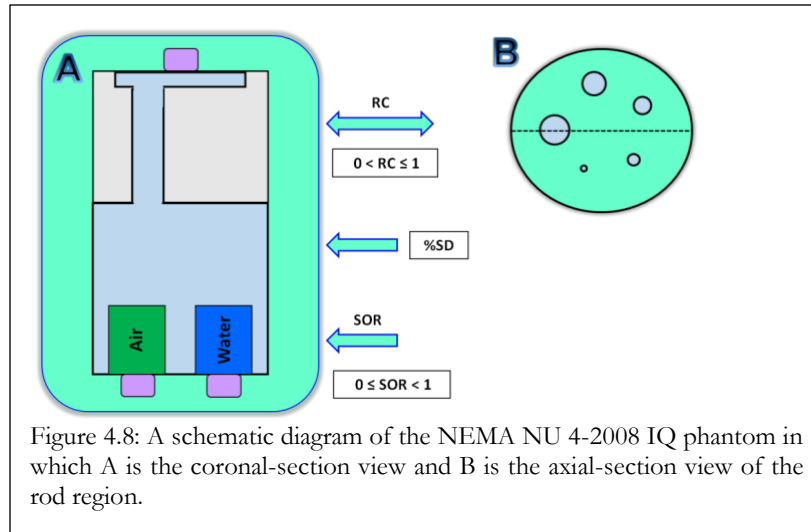


Figure 4.7: The NEMA NU 4-2008 IQ phantom for a small PET scanner.

The first region (a) of the IQ phantom geometry is solid with 5 fillable rods that have diameters of 1, 2, 3, 4, and 5 mm (Gontijo et al. 2017). The RC in each sphere of the rods is measured as the ratio between the measured radioactivity concentration in the rods and the radioactivity concentration in the uniform region (b) (Gontijo et al. 2017).

The middle region is the uniform region (b) and is used to measure the maximum, minimum and the mean radioactivity concentration as well as the SD percentage of different points in the uniform region (Gontijo et al. 2017).

The third region (c) in the IQ phantom is a fillable cylindric chamber with two compartments, each of which has an internal length of 14 mm and inner diameter of 8 mm (Gontijo et al. 2017). The first compartment is filled with air and the other one with non-radioactive water (Gontijo et al. 2017). The two non-radioactive compartments are designed to calculate the spill-over ratio (SOR) in air and water (Association 2008; Gontijo et al. 2017). SOR is defined as the ratio between the cold compartment (air or water) relative to the mean of the radioactive (hot) background compartment (Gontijo et al. 2017). Theoretically, the values of both RC and SOR in these regions are limited to between 0 and 1 as illustrated in figure 4.8 in which $0 < RC \leq 1$ and $0 \leq SOR < 1$ (Association 2008; Gontijo et al. 2017).



4.2 Objective:

The aim of this chapter is to evaluate and standardize the physical performance of the Mediso micro-PET/CT scanner in terms of overall image quality for both ^{18}F and ^{13}N , as they are the tracers used in this research. The assessment of the performance will be carried out according to the NEMA NU 4 – 2008 and the manufacturer guidelines. Each radionuclide has its own unique half-life and positron range; thus, we will also compare the image quality parameters between the two radionuclides. Moreover, we intend to explore the quantification accuracy by assessing the repeatability in uniformity values of the two radionuclides. The IQ parameters will include the recovery coefficient (%RC), image uniformity, its related percentage standard deviation ($\text{SDT}^{\%}$), spill-over ratio (SOR) and $\text{SD}^{\%}_{\text{SOR}}$.

4.3 Materials and Methods:

4.3.1 PET/CT scanner:

The Mediso nano-Scan 122S small-bore PET/CT imaging system is manufactured by the Mediso medical imaging system, Budapest, Hungary. All the scanner specifications have been previously mentioned in the methodology chapter.

4.3.2 Radionuclides (or radiotracers):

The radionuclides selected for this research are ^{18}F and ^{13}N . ^{18}F is the most widely used and is required in order to perform the NEMA NU4-2008 IQ measurements. ^{13}N is mostly used for MBF measurements. It has different properties with a higher PR but lower $T_{1/2}$ when compared to ^{18}F , as illustrated in table 1. Both radionuclides were produced from the Cyclotron model Cyclone 18/9 in the Wales PETIC centre, Cardiff University, UK.

4.3.3 The IQ phantom:

The NEMA NU 4-2008 IQ phantom previously described in figures 4.7 and 4.8 was used in the IQ test. The cylindrical phantom is 50 mm in length with a diameter of 30 mm. It consists of different regions, defined earlier, each of which aim to evaluate a certain aspect in the IQ test as shown in figure 8.

4.3.4 The analysis software:

Both vivo-quant software and the Mediso NEMA test program, that is integrated with the scanning system, were used.

4.3.5 The IQ phantom test:

The designated phantom was filled with approximately 3.7 MBq of the radiotracer (either ^{18}F or ^{13}N) and mixed with water to ensure that the radiotracer mixed homogeneously without air bubbles. The phantom was then placed in the dose calibrator, where the radioactivity amount and the time were recorded. Importantly, the recorded radioactivity should be higher than the required dose when measured in the dose calibrator so as to allow sufficient time for the phantom to be transferred to the scanner bed. Following this, the phantom was positioned in the bed holder of the Mediso micro-PET/CT scanner and imaging was initiated strictly at 3.7 MBq for 20 minutes, using whole body acquisition. Both CT and PET acquisitions and reconstruction are illustrated in Table 4.3. These parameters were applied, as recommended by Mediso and NEMA NU 4-2008, to ensure the optimal scanner performance.

Scanner	Mediso nano-Scanner 122S small-bore PET/CT
Acquisition	PET scan: 3.7 MBq for 20 minutes, followed by whole body CT scan for attenuation correction
PET mode	3D
PET protocol	whole body acquisition
Energy window	400-600 Kev
Coincidence Mode	1-3
Detector model	Full ring
Corrections applied	Decay correction, dead time correction, random correction, median filtering, AC, SC, and normalization.
Reconstruction method	Iterative reconstruction (IR)
Voxel size	0.4 mm isotropic 3D voxel grids
Number of iterations	4
Number of subsets	6

Table 4.3: The PET image acquisitions, corrections and reconstruction methods applied in the image quality phantom test using the NEMA NU 4-2008 standard.

Once the PET and CT scans were completed, the reconstruction was initiated using iterative reconstruction (IR) with 4 iterations, 6 subsets and 0.4mm isotropic 3D voxel grids (table 4.3). Importantly, normalization and random correction were applied prior to the image reconstruction process. This test was repeated 4 times to assess the repeatability of the data specifically for the uniformity region.

4.3.6 Data analysis of the IQ phantom:

After completing the reconstruction process, the IQ phantom images were opened to start the IQ phantom evaluation that complies with the NEMA NU 4 – 2008 standard using the Mediso NEMA IQ program to evaluate the RCs, uniformity and SOR. For the measurement of these three parameters, volumes of interest (VOIs) were positioned in the centre of the specified region. Furthermore, CT images were used to assist with the positioning of the regions accurately.

4.3.6.1 RC measurements:

For RC calculation, the reconstructed slices covering the central 10 mm depth of region (a) were averaged to produce a single slice (Association 2008). Next, circular ROIs were drawn around each rod (i) with a diameter equal to twice the physical diameter of the rod as illustrated in figure 4.9.

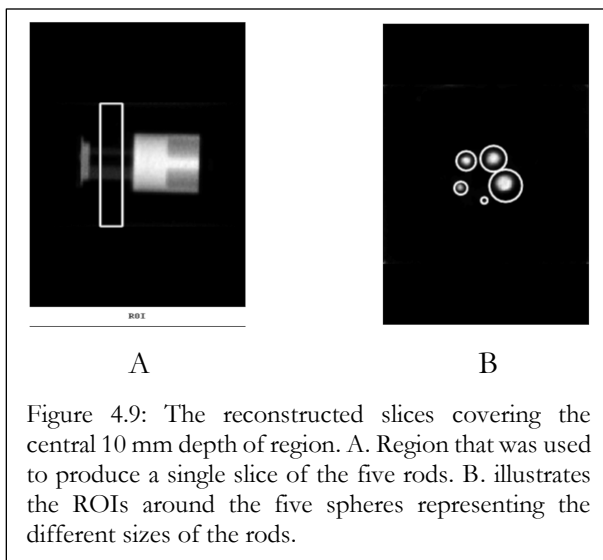


Figure 4.9: The reconstructed slices covering the central 10 mm depth of region. A. Region that was used to produce a single slice of the five rods. B. illustrates the ROIs around the five spheres representing the different sizes of the rods.

The pixels with maximum values in each ROI were defined using an in-house MATLAB code. After that, the location of these pixels was used to plot a line profile (the radioactivity values) through the central 10 mm direction for each rod (i). The mean value and STD of all rod profiles were measured using their line profiles (Association 2008; Gontijo et al. 2017). Ultimately, the RC for each rod was measured by dividing the measured radioactivity concentration in the ROI of each rod by the mean of the radioactivity concentration in the uniform region (b) as seen in equation 4.1 (Association 2008; Gontijo et al. 2017).

$$Eq. 4.1 \quad RC = \frac{\text{the measured radioactivity concentration in the ROI of each rod}}{\text{the measured radioactivity concentration in the uniform region (b)}}$$

According to the NEMA NU 4 – 2008 standards, the reasonable values of the RCs of the rods when using ^{18}F are illustrated in table 4.4 (Association 2008).

4.3.6.2 Uniformity measurement:

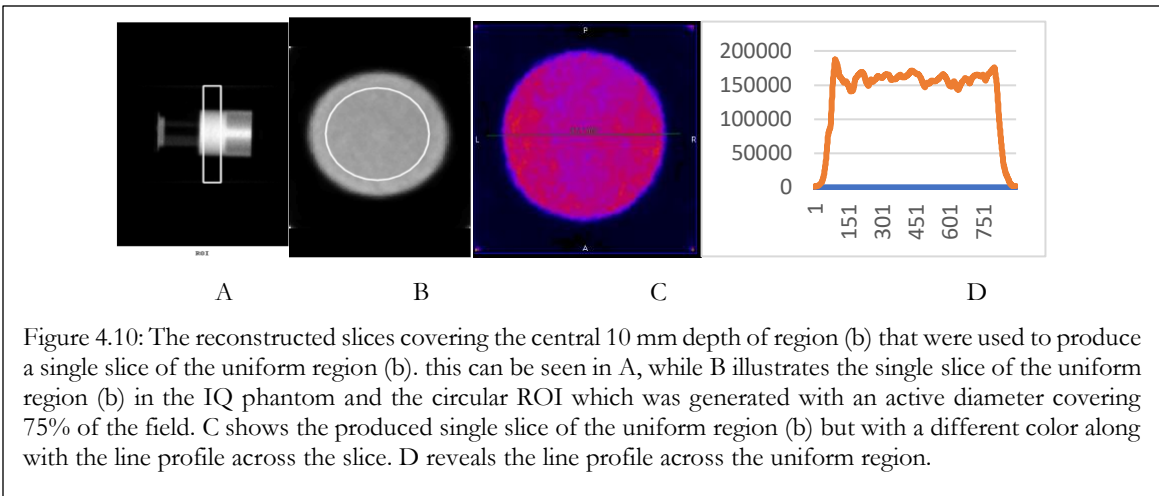
For uniformity assessment, a 22.5 mm diameter (which is 75% of active diameter) cylindrical VOI with a 10 mm depth were drawn in the centre of the uniform region (b) of the image quality phantom as in figure 4.10. The maximum, minimum and the STD% in the VOI were calculated. The uniformity STD% should be less than 15%, as recommended by the NEMA standard in table 4.5.

Rod size	RC- reasonable values
1 mm	0.1 – 0.4
2 mm	0.75 – 1.0
3 mm	0.8 – 1.1
4 mm	0.9 – 1.15
5 mm	0.9 – 1.19

Table 4.4: The reasonable values of the RCs of the rods according to the NEMA NU 4 – 2008 standards.

Uniformity	
STD%	15%
SOR	
Air filled compartment	<15%
Water filled compartment	<15%

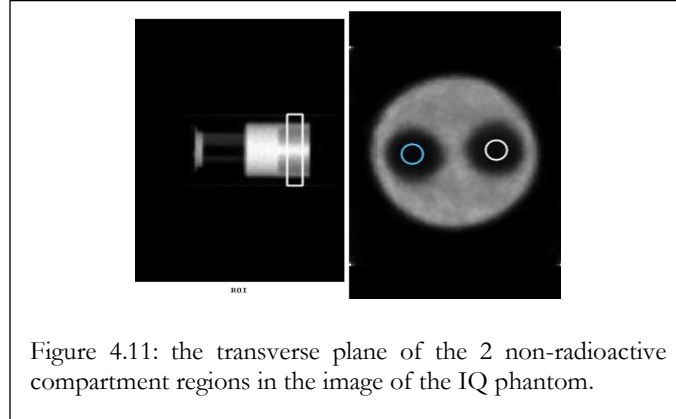
Table 4.5: The reasonable values recommended by NEMA NU 4 – 2008 standards for the uniformity STD% and SOR_{STD%} for both compartments.



4.3.6.3 SOR measurements:

The spill-over ratio (SOR) was measured as a ratio of the mean in each cold cylinder (both in air and water) to the mean value in the uniform region (b) as shown in figure 4.11. The STD% of SOR of any cylinder i was calculated through equation 4.2.

$$Eq. 4.2 \quad \%SD_{SOR,i} = 100 \cdot \sqrt{\left[\frac{STD_i}{Mean_i}\right]^2 + \left[\frac{STD_{uniform\ region}}{Mean_{uniform\ region}}\right]^2}$$



4.4 Results:

Images representing a coronal view of the NEMA IQ phantom, and a trans-axial view of the three regions (a, b, and c) with their ROIs are shown in figure 4.12. It can be noted that ^{13}N has poorer image quality particularly in the rod sections, in which they appear blurred when compared to the ^{18}F rod images.

The RCs for the five rods using both ^{18}F and ^{13}N , along with their STD%, are presented in tables 4.6 and 4.7 respectively. Radiotracer specific differences can be noted in the RCs across the five rods, as well as the rest of the images, to a degree as illustrated in figure 4.12. These differences were expected due to the PR differences of the two radiotracers. The PR of ^{13}N is larger than that of ^{18}F , resulting in a lower image quality of the ^{13}N images. Importantly, the RCs of ^{18}F were within the reasonable limits that are suggested by the NEMA standard as in table 4.4. In contrast, the RCs of ^{13}N were slightly lower in the 2-, 3-, and 5-mm rods, and became worse in the 1 mm rod as shown in table 4.6 and figure 4.12. The lowest RC values were recorded at the 1 mm rod size when using both ^{18}F and ^{13}N , with values ranging from 0.1 to 0.12 and 0.05 to 0.06 respectively.

Moreover, the maximum RC values were recorded at the 5 mm rod size using ^{18}F with values between 1.09 and 1.17 in the four attempts. Similarly, the highest RC values were noted at the 5 mm

rod using ^{13}N , ranging between 0.79 and 1.02. Furthermore, the highest variability in $\text{STD}\%_{\text{RC}}$ was noted in the 1 mm rod size for ^{18}F and at the 2 mm rod size for ^{13}N with values of 43.3% and 40.7% respectively. In contrast, the lowest variability of $\text{STD}\%_{\text{RC}}$ was recorded in the 3 mm rod size for ^{18}F and ^{13}N with value of 13.1% and 16.5% respectively.

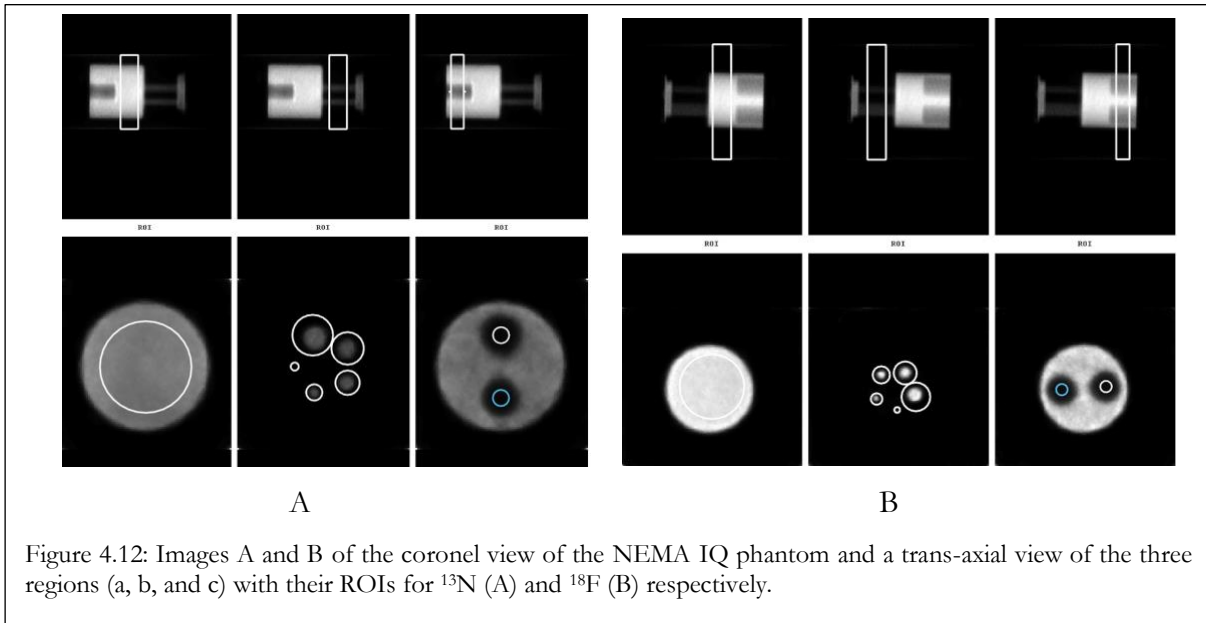


Figure 4.12: Images A and B of the coronal view of the NEMA IQ phantom and a trans-axial view of the three regions (a, b, and c) with their ROIs for ^{13}N (A) and ^{18}F (B) respectively.

Radiotracer	Test number	Rod size 1 mm		Rod size 2 mm		Rod size 3 mm		Rod size 4 mm		Rod size 5 mm	
		RC	STD%	RC	STD%	RC	STD%	RC	STD%	RC	STD%
^{18}F	Test1	0.1	37.3%	0.79	32.3%	1.07	22.2%	1.09	22.5%	1.09	18.8%
	Test 2	0.11	43.3%	0.75	23.7%	1.03	18.5%	1.17	21.2%	1.18	16.9%
	Test 3	0.11	38.0%	0.83	27.7%	1.02	13.1%	1.12	15.3%	1.12	16.3%
	Test 4	0.12	33.3%	0.80	17.0%	1.1	15.4%	1.15	14.1%	1.17	14.5%
	Average	0.11	37.9%	0.79	25.1%	1.05	17.3%	1.13	18.5%	1.14	16.6%

Table 4.6: shows the RC values and their STD% for the five rods in the four repeated IQ tests of ^{18}F .

Radiotracer	Test number	Rod size		Rod size		Rod size		Rod size		Rod size	
		1 mm		2 mm		3 mm		4 mm		5 mm	
		RC	STD%	RC	STD%	RC	STD%	RC	STD%	RC	STD%
¹³ N	Test1	0.05	33.5%	0.66	39.7%	0.70	17%	0.76	23.1%	0.79	18.9%
	Test 2	0.05	35%	0.65	40.7%	0.70	17.2%	0.76	23.3%	0.78	20.8%
	Test 3	0.05	34%	0.67	37.1%	0.70	16.5%	0.77	22.6%	0.8	20.3%
	Test 4	0.06	38.8%	0.66	37.5%	0.74	36.2%	0.74	24.5%	1.02	23.3%
	Average	0.05	35.3%	0.66	38.75%	0.71	21.7%	0.75	23.3%	0.84	20.8%

Table 4.7: shows the RC values and their STD% for the five rods in the four repeated IQ tests of ¹³N.

Both table 4.8 and 4.9 provide the results of the uniformity evaluation with the maximum, minimum, and mean radioactivity concentration as well as the STD% for the two radiotracers. In addition, the SOR values and their SD% obtained from the water and air-filled compartments of the IQ phantom are reported in tables 4.10 and 4.11 for both radiotracers.

Radiotracer	Maximum concentration	Minimum concentration	Average concentration	STD%	
¹⁸ F	counts Bq/cm ³	counts Bq/cm ³	counts Bq/cm ³		
	Test 1	221034.49	120640.20	153736.31	5.9%
	Test 2	210730.44	114110.89	153494.08	6.3%
	Test 3	220324.21	114552.42	155980.76	6.5%
	Test 4	237221.55	131158.79	176146.44	5.8%

Table 4.8: the maximum, minimum, and STD% values that were recorded in the uniform region for ¹⁸F in the four IQ tests.

Radiotracer	Maximum concentration	Minimum concentration	Average concentration	STD%	
¹³ N	counts Bq/cm ³	counts Bq/cm ³	counts Bq/cm ³		
	Test 1	369578.57	189512.33	276294.11	8.1%
	Test 2	385117.40	189512.33	276038.17	8.4%
	Test 3	361242.39	196998.36	276919.01	7.9%
	Test 4	396781.10	136190.99	229166.15	8.7%

Table 4.9: the maximum, minimum, and STD% values that were recorded in the uniform region for ¹³N in the four IQ tests.

According to the NEMA standards, the acceptable limit of the SD% for uniformity assessment is to be less than 15%. Notably both radiotracers produced an SD%_{SOR} within the acceptable range. In

addition, the SORs were higher in water than air for both tracers. Generally, the $SD\%_{SOR}$ did not show any clear trend when using the two radiotracers.

Radiotracer	Compartment	SOR	STD% _{SOR}
¹⁸F			
Test 1	Air	0.08	15.3%
	water	0.12	15.7%
Test 2	Air	0.09	14.2%
	water	0.10	15.0%
Test 3	Air	0.08	14.2%
	water	0.11	15.1%
Test 4	Air	0.08	15.0%
	water	0.09	15.6%
Table 4.10: The SOR and STD% values for ¹⁸F in the air and water compartments.			

Radiotracer	Compartment	SOR	STD% _{SOR}
¹³N			
Test 1	Air	0.09	15.1%
	water	0.12	15.4%
Test 2	Air	0.11	13.5%
	water	0.12	14.1%
Test 3	Air	0.09	15.3%
	water	0.12	15.6%
Test 4	Air	0.12	15.2%
	water	0.13	15.6%
Table 4.11: The SOR and STD% values for ¹³N in the air and water compartments.			

4.5 Discussion:

The IQ phantom results generated from Mediso Nano-Scan 122S small-bore PET/CT imaging system was assessed according to the NEMA NU 4 –2008 standards. NEMA and most vendors usually recommend performing the IQ phantom test prior to important quantitative studies (Prasad et al. 2011; Goertzen et al. 2012; Sato et al. 2016; Chen et al. 2020). In addition, previous investigations on the IQ have only been carried out using ¹⁸F, ¹¹C, ⁶⁸Ga and ⁸⁹Zr radiotracers (Teuho et al. 2020).

To the best of our knowledge, there is little published data on using ^{13}N in the IQ phantom test particularly in a small animal PET/CT scanner, but this is no surprise as the NEMA NU 4 –2008 standards provide guidelines on only using ^{18}F for IQ evaluation.

Although ^{18}F and ^{13}N have differences in half-life between, we were able to run a 20-minute imaging acquisition as in the standard NEMA image quality evaluation protocol. The consistency in acquisition time was essential to assess the variability of the scanner performance when using non ^{18}F tracers, although there might be another option to be used which is using counts rather than time. However, this was not the case in a previous study by Tueho et al. (Disselhorst et al. 2010; Teuho et al. 2020) where they compared the image quality phantom results with different radiotracers but used a radionuclide specific acquisition. As previously mentioned, the image reconstruction was IR which was also the reconstruction method applied in all the scans of this research and recommended by NEMA standards.

4.5.1 RC% analysis:

The RC% is defined as the ability of the PET system to recover radioactivity concentration within the targets at different sizes, hence, it is partly a form of measure of the SR of the system (Srinivas et al. 2009; Disselhorst et al. 2010; Teuho et al. 2020). In fact, it has been reported that poor SR leads to more PVE and low RC values, hence, the assessment of the RCs of the system using a variable tracer reflects its SR (Srinivas et al. 2009; Disselhorst et al. 2010; Kim et al. 2021). In the IQ test, the ideal RC value is equal to 1 which indicates the capability of the system to resolve radioactivity at different sizes when compared to the uniform region of the IQ phantom.

The small rods in the IQ phantom represent the capillary measurements. Our experiments show that the PR limits and degrades the SR for a small animal PET/CT scanner. In fact, these results are in line with other observations reported by different studies carried out by Liu et al. (Liu and Laforest 2009), Disselhorst et al. (Disselhorst et al. 2010), and Teuho et al. (Teuho et al. 2020). These studies have performed the IQ phantom test in various types of small animal PET/CT scanners using different radiotracers (^{18}F , ^{61}Cu , ^{68}Ga , $^{94\text{m}}\text{Tc}$, and ^{86}Y) which all have a different PR and half-life.

In our experiments, the RC% values across all rods exhibit a similar trend among both tracers in which the minimum RC% was reported in the 1 mm rod, while the maximum values were seen in the 5 mm rod. In the ^{18}F phantom, the RC% values for the five rods were within the acceptable ranges established by the NEMA standards. The lowest RC% values were in the 1 mm rod, reflecting that it is dependent on the structure size as well as the PR of the used radiotracer and the SR of the PET

system. We also noticed the dependency of RC% on the acquisition time which has the same duration (20 minutes) for the two radionuclides despite the difference in the half-life. Consequently, the RC% values can be improved generally by increasing the initial activity or increasing the acquisition time especially for short-lived tracers like ^{13}N .

In the ^{13}N phantom, all rods showed lower RC% values when compared to our measured ones with the ^{18}F IQ phantom which was within the normal limit of the NEMA standard. This was expected to happen due to the longer PR and shorter half-life of ^{13}N . Importantly, in literature there were no previous RC% values for ^{13}N produced from a preclinical IQ phantom. Accordingly, the values were compared to the ^{18}F values of the NEMA NU 4 –2008 standards. This resulted in statistical differences in RC values between the two radiotracers in the 1-, 2-, 3- and 4-mm rods as can be seen in graph 4.1 and table 4.12 in which the p-values are less than 5%. On the other hand, there were no statistical differences in RC values among the two tracers in the 5 mm rod size in which the p-values were higher than 5%, as can be noted figure 4.13 and table 4.12.

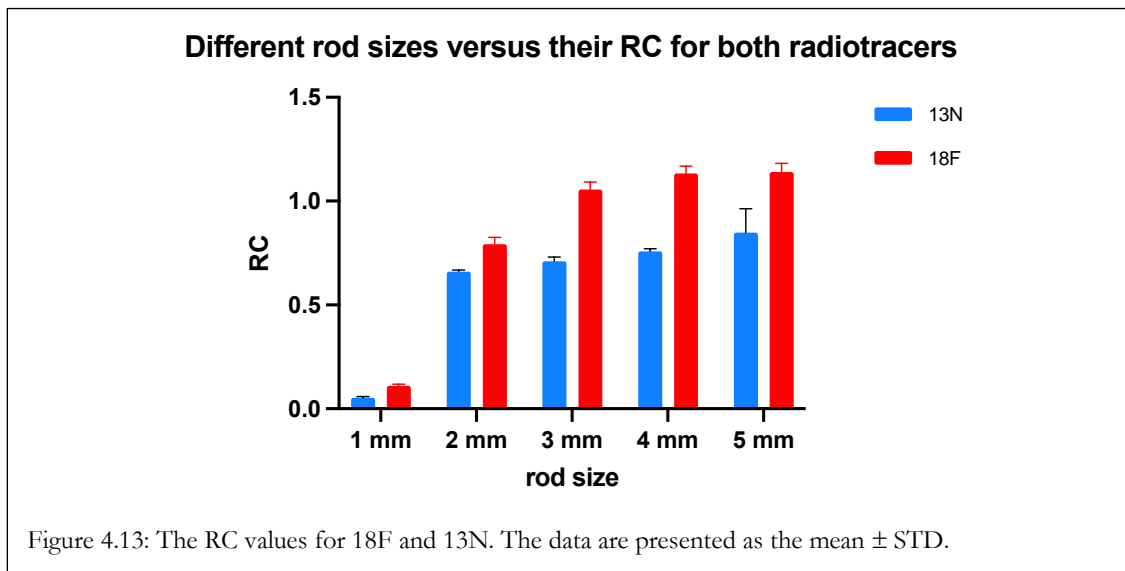
In the light of the above findings, the differences in RC% between the two radionuclides are explained by their specific physical characteristics, including PR and half-life. The shorter half-life of the ^{13}N resulted in lower counts and more noise, which all contributed to the reduced RC% across various rods size when compared to ^{18}F . This was resolved by increasing the acquisition time or the amount of injected activity with the ^{13}N scans. Another related parameter that is important is the effect of the applied reconstruction method on the RC% measurements. The iterative reconstruction method (IR) was applied in all IQ tests as recommended by the NEMA standard. Several studies demonstrated that IR methods produce a better phantom image quality and improved RC% values in contrast with the filtered back-projection method (FBP) (Sato et al. 2016).

For repeatability assessment, the IQ test was repeated using the same parameters and under the same experimental conditions for each radiotracer. Note that the IQ phantom tests were conducted four times only for each radiotracer because of the difficulty to produce ^{13}N from the cyclotron.

The SD% values across the repeated experiments within each tracer were evaluated considering that the repeatability of the values can be reflected by their standard deviation and the closeness of the results. Consequently, any variability in the generated results within each radiotracer test will lead to a lower repeatability level.

The RC% values across the rods were stable for both tracers, as illustrated in figures 4.14 and 4.15. The low SD% values of the repeated tests reflected the high repeatability of the produced results. The highest variation was reported with the 4- and 5-mm rod sizes across both tracers.

In summary, ^{18}F phantom tests produced results that are in line with the NEMA standard, while ^{13}N results were slightly lower, as expected because of its physical characteristics including PR and short half-life. This can be overcome by increasing the acquisition time or the radioactivity of the ^{13}N . Importantly, both radiotracers showed high reproducibility. Consideration should be given to the physical factors of the radiotracers, such as PR and half-life, and the applied reconstruction method to ensure optimal image quality and RC% for all rod sizes.



Sidak's multiple comparison test					
^{13}N - ^{18}F	Mean diff.	95.00% CI of diff.	Below threshold?	Summary	Adjusted P Value
1 mm	-0.05750	-0.07200 to -0.04300	Yes	***	0.0009
2 mm	-0.1325	-0.2050 to -0.06002	Yes	**	0.0089
3 mm	-0.3450	-0.4140 to -0.2760	Yes	***	0.0005
4 mm	-0.3750	-0.4945 to -0.2555	Yes	**	0.0018
5 mm	-0.2925	-0.5951 to 0.01008	No	ns	0.0549

Table 4.12: The multiple comparison tests that were applied for ^{18}F & ^{13}N . The p-values showed that there were statistical differences in the 1-, 2-, 3-, and 4-mm rod sizes. However, in the 5-mm rod there were no statistical differences between the two radiotracers.

The rod size versus the obtained RC for ^{18}F

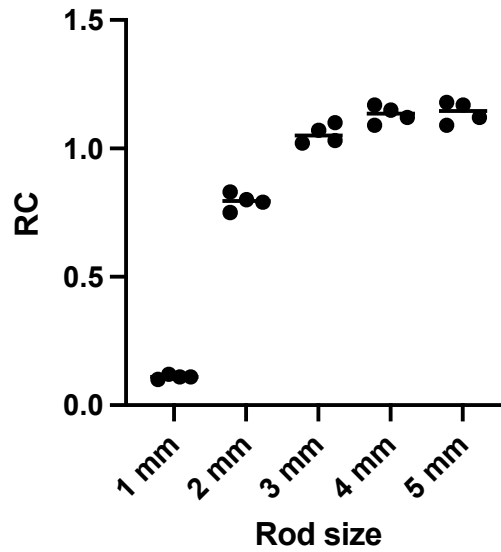


Figure 4.14: The four attempts of the IQ tests using ^{18}F . The data along each rod size were close reflecting high repeatability.

The rod size versus the obtained RC for ^{13}N

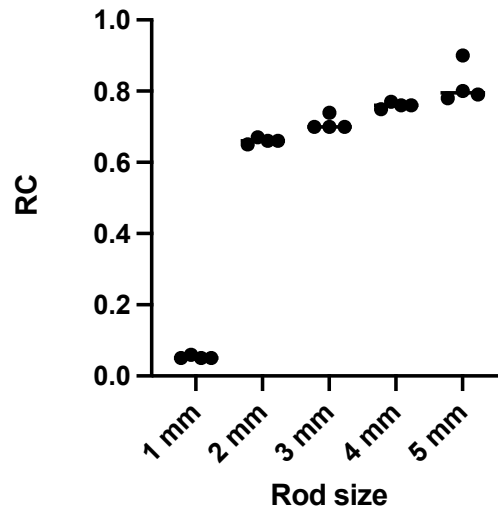
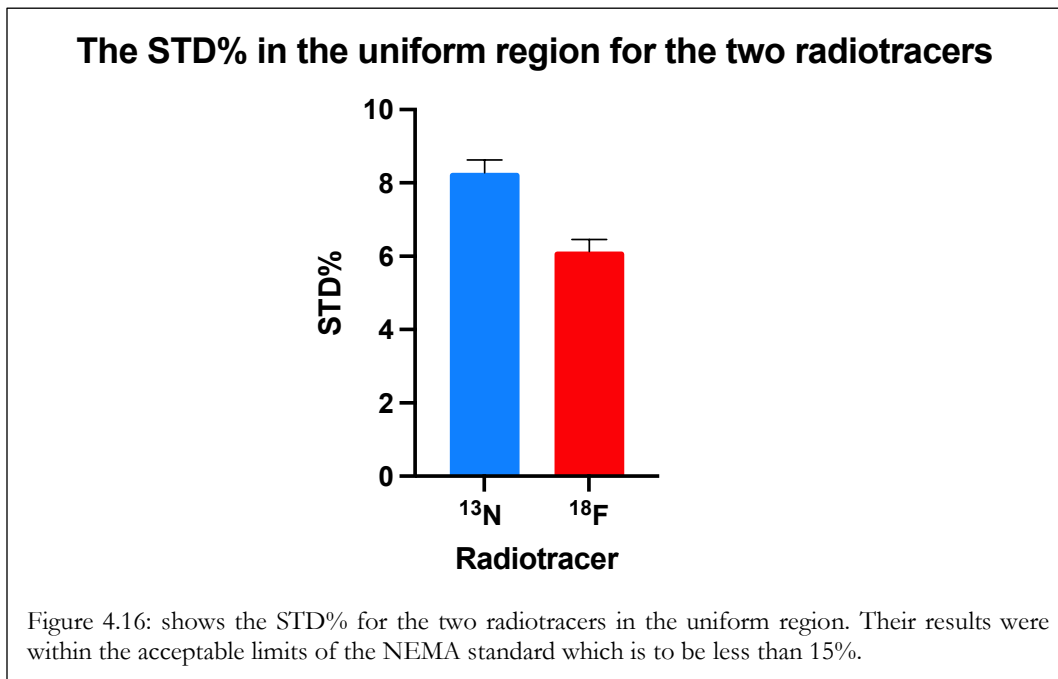


Figure 4.15: The four attempts of the IQ test using ^{13}N . The data along each rod size were close reflecting high repeatability.

4.5.2 Uniformity analysis:

Uniformity is a measurement of the PET system response to a uniform region (Saha 2010). It is an important parameter in the IQ test as it indicates the quantification accuracy of the imaging system. It is expected that the imaging system produces a uniform response throughout the FOV. Importantly, the measurement of the STD% in the uniform region represents the uniformity of the PET system (Disselhorst et al. 2010; Teuho et al. 2020). Consequently, a higher STD% reflects a nonhomogeneous FOV that lead to an inaccurate quantification of the PET results (Saha 2010; Teuho et al. 2020).

Overall, the uniformity results of the IQ phantom measurements match the NEMA standard which allows a variation or STD% to be less than 15%. Both radionuclides produced a STD% within the acceptable range with the ^{13}N value being higher than the ^{18}F as shown in tables 4.8 & 4.9 and figure 4.16. This can be explained by the higher PR of ^{13}N as well as its shorter half-life. Indeed, a shorter half-life has a significant impact on the counting statistics which will subsequently affect the counting response of the system. If the total radioactivity or the counting statistics are low, the STD% in the uniform region will increase, as demonstrated by Teuho et al. (Teuho et al. 2020).

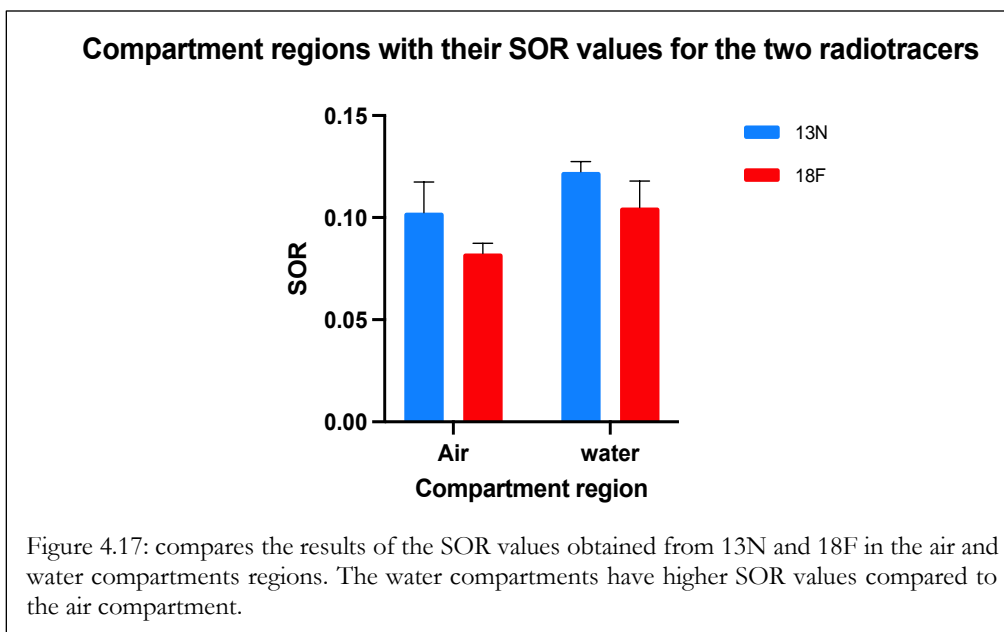


4.5.3 SOR analysis:

Both radiotracers were in the normal range of SOR and $STD\%_{SOR}$ as shown in tables 4.10 and 4.11. ^{13}N had larger SOR values than ^{18}F in both the water and air regions (tables 4.10-4.11, figure 4.17). This finding is similar to the results of previous studies, where it was demonstrated that lower PR radiotracers have a lower spill-over ratio and vice versa (Disselhorst et al. 2010; Teuho et al. 2020). The larger PR of ^{13}N (1.73 mm) when compared to ^{18}F (0.66 mm) resulted in a larger SOR of ^{13}N . Importantly, there is a need to emphasise that the positron range can result in mispositioned details in the image to a different degree depending on the scanned organ. It is not always the case that these mispositioned details are equal in value to the PR value of the used radiotracer (Carter et al. 2020). This study explained, through using results produced from Monte Carlo Simulations of Preclinical QC and Small Animal Jaszczak phantoms, that the PR in the case of ^{18}F added 0.4 mm in the heart tissue of a mouse which is less than the ^{18}F PR (Carter et al. 2020). Moreover, data from several sources have identified that the experimental PR for different radionuclides were lower than the theoretical PR (Champion and Le Loirec 2007; Carter et al. 2020). For example, ^{13}N and ^{18}F have theoretical PRs of 1.73 mm and 0.66 respectively, which is similar to a previous study which identified PRs of 1.3 mm (^{13}N) and 0.54 (^{18}F) (Champion and Le Loirec 2007).

The SOR values for both radiotracers in water were higher than those in air as identified in tables 4.10 and 4.11. As the attenuation level in water is greater than the one in air, this causes positrons emitted from the surrounding hot region in the bodies of the phantom to be annihilated in the water-filled compartment (Disselhorst et al. 2010). Subsequently, the water compartment would have a larger SOR in any radiotracer. Therefore, the air compartment might be a better indicator of the system data correction performance, as suggested by Disselhorst et al. (Disselhorst et al. 2010).

Another assessed value in the SOR analysis is the $STD\%_{SOR}$ parameter which is a measure of the variability in the cold compartments with respect to the uniform compartment in the phantom (Gontijo et al. 2017). Generally, our $STD\%_{SOR}$ measurements did not show any radiotracer specific pattern, but importantly, they were within the accepted limit ($< 15\%$) as identified in tables 4.10 and 4.11. Overall, it is recommended to have a low $STD\%_{SOR}$ in the cold regions for an efficient derived data correction, especially with radionuclides that have a PR significantly larger than the one in ^{18}F (Teuho et al. 2020).



4.6 Conclusion:

The aim of this chapter was to characterize the performance of our Mediso Nano-Scan 122S small-bore PET/CT imaging system with respect to the generated IQ using the NEMA NU 04 – 2008 standards and the IQ phantom.

The RCs of ¹⁸F were within the NEMA acceptable ranges, reflecting the capability of the scanner to produce images with good SR. However, the ¹³N RCs were lower than those of ¹⁸F, corresponding to our choice not to increase the acquisition time to compensate for the loss in counting statistics, despite the shorter half-life of ¹³N. For consistency, the acquisition time was kept at 20 minutes for both radiotracers, as recommended by NEMA standard for ¹⁸F. In future studies, we could mitigate this by increasing the acquisition time for ¹³N thus increasing the counting statistics and improve the SR.

Importantly, our study has shown that the Mediso PET/CT scanner produced accurate and repeatable uniformity values for the used radiotracers. This study has also indicated that all SOR values were in the reasonable NEMA range. Additionally, the STD% values in the uniform region and in the cold compartments ($STD\%_{SOR}$) were aligned with NEMA standards in both tracers.

In conclusion, the overall results indicate that the Mediso 122S small-bore PET/CT scanner is suitable for preclinical imaging-based research. Another important contribution of this chapter is that ¹³N images produced lower RC values in regard to the NEMA standard, but this was expected with the combination of the increased positron range of ¹³N, the short-life and a short acquisition time.

There is room for further improvement in the ^{13}N RCs values and SR by increasing the starting activity or increasing the acquisition time which will lead to higher counting statistics and ultimately better SR.

Finally, quantification accuracy using micro-PET/CT is based mainly on two concepts: standard performance measures and imaging protocols. The present chapter is the initial step in verifying the physical performance of the scanner to achieve a higher level of accuracy. The following chapter will develop, standardize, and validate the applied imaging protocols.

Chapter 5:

Assessing the accuracy and repeatability in the PET/CT imaging protocol in healthy murine studies

5.1 Introduction:

The increased use of molecular biology techniques in the study of organ function has demanded a corresponding improvement in molecular imaging. Many imaging modalities have been adapted or redesigned for *in vivo* studies, including PET imaging. The main advantage of PET imaging is its ability to non-invasively quantify a biological process related to a specific cellular function or biomarker in a living organism (Cicone et al. 2017). In the field of cardiovascular imaging, PET has contributed to understanding the anatomy and the pathophysiology of the CVS within the last two decades. There is growing interest to use the small animal model in cardiac imaging either to simulate human diseases or to test new radiotracers.

Murine models have been used widely in cardiac PET imaging to provide simulation of human CVS and CVDs (Cicone et al. 2017). Recent developments in micro-PET/CT imaging have resulted in improvements in spatial and temporal resolutions that could cope with the small size and rapid movement of the mouse heart.

Generally, there are two main purposes for combining mouse models and PET/CT imaging which are either to develop novel or standard imaging protocols, or to test and characterize new therapies (such as gene or drug treatments). In this chapter, I will develop a standardised set of imaging protocols to establish baseline parameters in animal models. Therefore, I will first review cardiac PET/CT imaging protocols commonly applied in rodents to measure cardiac biomarkers, namely MGM and MBF, and evaluate their strengths and weaknesses. After that, this chapter will address the potential sources of variability and technical errors common in small animal radionuclide imaging, such as animal preparation, type of anaesthetic, duration of the scans, and the performance of the micro-PET system. Due to these sources of variability and errors, there are challenges and considerations in each step of murine PET imaging. They will be discussed to understand their effect

on the results and justify our choices for optimal imaging methods. Finally, the standardised imaging protocols will be applied to the healthy model to set out the baseline studies, assess their repeatability, and compare them to the other literature results. In later chapters I will use the updated protocols in the evaluation of a novel therapeutic intervention.

Despite the promising results that have been reported with the micro-PET system, there is a relatively small body of literature that is concerned with the quantitative assessment of cardiac function and MBF in mice. A concise review of the most important findings regarding the use of micro-PET imaging in measuring cardiac function, MGM and MBF in rodents will be outlined.

5.1.1 Previous studies to assess cardiac metabolism in mice:

A healthy heart can adapt to changes in the physiological body environment by switching from one energy substrate to another, ensuring a continuous supply of energy required for contractile function (Taegtmeyer et al. 2004; Vasan 2006; Kolwicz and Tian 2011). However, this flexibility may be lost in response to a chronic condition or heart disease, causing maladaptation (Taegtmeyer et al. 2004; Shah and Brownlee 2016). Both cardiac adaptation and maladaptation are controlled by metabolic signals that regulate the transcription in essential cardiac regulatory genes (Taegtmeyer et al. 2004). Metabolic changes in adapted or maladapted hearts may ultimately lead to functional and structural remodelling in the myocardium (Taegtmeyer et al. 2004; Shah and Brownlee 2016). Some of the cardiac functional and structural remodelling are accompanied by changes in energy substrate metabolism (Keating and Sanguinetti 1996; Schulze et al. 2016). The study of cardiac metabolism can allow us to predict or interpret changes in cardiac function (Vasan 2006; Schwarzer and Doenst 2016).

Numerous studies have attempted to carry out *in vivo* study of the heart through exploring metabolic pathways that are associated with its function or response to a stimuli or disease (Keating and Sanguinetti 1996; Yamamoto et al. 1996; Zhong et al. 2013a; Hue et al. 2016; Vasudevan et al. 2020). Understanding these metabolic pathways may allow us to develop pharmacological or gene interventions that might restore cardiac function. For this purpose, the mouse model has been widely utilized to evaluate the metabolism and function of the heart using molecular imaging (Zhong et al. 2013a; Phoon and Turnbull 2016).

PET/CT imaging has emerged as a quantitative tool for cardiac function and MBF assessment. The first molecular imaging studies to assess cardiac function in mice were performed using a SPECT/CT scanner and pinhole collimator that offered SR in the range of millimetres (Meikle et al. 2005; Beekman and van der Have 2007; Rowland and Cherry 2008). The SPECT system has generally low sensitivity and SR, requiring a high injected dose and long acquisition time in the clinical setting

(Yap et al. 2004). However, in a preclinical setting, the SPECT system has a better resolution and sensitivity compared to the PET system.

Preclinical PET/CT systems have much higher sensitivity and SR, allowing a deeper understanding of myocardial physiology on a molecular level (Stegger et al. 2006; Higuchi et al. 2007; Gargiulo et al. 2012). Therefore, it has been increasingly utilized for the non-invasive assessment of cardiac function and pathophysiology in mice.

¹⁸F-FDG is the most common PET radiotracer, and it has been used extensively in animal studies to quantify glucose metabolism in two major organs, namely the heart and brain (Toyama et al. 2004; Gargiulo et al. 2012). Since mice have low glycogen reserve and rapid metabolism, their FDG uptake can vary when applying different experimental paradigms (Toyama et al. 2004; Zhong et al. 2013a). Toyama and colleagues found that the uptake of FDG uptake in mouse brain and heart was influenced by the type and route of anaesthetic used (Toyama et al. 2004). Consideration must be given to all aspects of the experimental design in mice in order to reduce variability (Toyama et al. 2004).

Although PET is routinely used to measure metabolism and perfusion, it might also be used to assess the contractile function in mice. An interesting study carried out by Yang et al. (Yang et al. 2005) demonstrated the ability to study heart contraction (including assessment of systolic and diastolic function and the LV volume). These studies used cardiac-gated micro-PET ¹⁸F-FDG imaging in normal mice and rats, and in rats that had undergone MI surgery, with good correlation between PET and ultrasound measurements in the rats. In addition, using gated acquisition and the ¹⁸F-FDG as a radiotracer, the EF can be ultimately calculated (Croteau et al. 2004; Yang et al. 2005). Similarly, Croteau and his colleagues (Croteau et al. 2004) reported the reliability of accurate systolic function assessment in normal and infarcted rats scanned with micro-PET system and ¹⁸F-FDG (Croteau et al. 2004).

PET and MRI have been used to quantify cardiac ischemia and infarction size in the rat. The researchers obtained good correlation between functional parameters and histological assessment of cardiac necrosis (Higuchi et al. 2007). Wu and his co-workers were able to quantitatively assess glucose metabolism in mice hearts by calculating the IF using a developed blood-sampling device and small PET scanner. They successfully measured glucose metabolism by applying three compartment model. In this study, the rate constant K_4 , representing glucose metabolism, ranged between 0.024 -0.149 mL/min/g (Wu et al. 2007). Other groups have also measured glucose metabolism in different regions of infarcted heart in mice using PET/MRI or PET/CT scanners (Büscher et al. 2010; Greco et al. 2012; Buonincontri et al. 2013).

However, the use of $^{13}\text{N-NH}_3$ in cardiac performance is not as straightforward. A comparison of $^{18}\text{F-FDG}$ and $^{13}\text{N-NH}_3$ in healthy and infarcted male rats showed a constant overestimation of LV volume with $^{13}\text{N-NH}_3$, which resulted in underestimation of the ejection fraction (EF) in infarcted animals. (Szymanski et al. 2012).

5.1.2 Previous PET studies on MBF quantification:

MBF quantification using PET perfusion imaging has been validated by previous studies as an useful cardiovascular biomarker of disease (Vasan 2006; Lin et al. 2014; Anjan et al. 2015; Shrestha and Seo 2015), with reduced global MBF and MBFR associated with poorer cardiovascular outcome (Yamamoto et al. 1996; Anjan et al. 2015; Guerraty et al. 2020).

There are a number of mouse models that allow the use of MBF to study CVDs (Jogiya et al. 2013a), including transgenic, ageing, diabetic, MI, and HLI models. In addition, evaluating MBF is more powerful when combined with cardiac metabolism assessment, different imaging modalities or longitudinal studies. For example, PET/CT or PET/MRI scanners can offer both structural and function molecular imaging and combining their results with histological analysis will validate the obtained data (Jogiya et al. 2013a).

The feasibility of assessing essential parameters in cardiovascular function in mice was performed using a small animal PET system with $^{18}\text{F-FDG}$ (Kreissl et al. 2006). Parameters analysed included cardiac output (CO), cardiac index and stroke volume (SV). They were derived from drawing VOIs around the LV, generating TAC and applying all the required corrections such as decay and PVE corrections (Kreissl et al. 2006). In this study, the cardiac output was measured through the Stewart-Hamilton method, in which blood flow in vessels (CO) was calculated by dividing the total injected radioactivity, derived from the TAC of the input function (IF), by the total radioactivity in the LV VOI, which was calculated from its TAC (Kreissl et al. 2006). The cardiac index was calculated by dividing the CO by the weight of the mouse (Kreissl et al. 2006). SV was also calculated by dividing CO by the mouse heart rate (HR) (Kreissl et al. 2006). The obtained CO was 20.4 ± 3.4 mL/min with STD% of $10\% \pm 6\%$ per mouse (Kreissl et al. 2006). Another study quantified CO from MRI and thermodilution procedures in murine model, with 9.3-19.2 mL/min calculated when using thermodilution, and 10.8-17.5 mL/min when calculated from MRI images (Kober et al. 2005; Nahrendorf et al. 2006; Makowski et al. 2010).

MBF values from PET flow measurements in non-ischemic rats (Kudo et al. 2002; Herrero et al. 2006; Lamoureux et al. 2012) have been found to be age-related and (as in mice) highly dependent on the anaesthetic type and its concentration (Cicone et al. 2017). Kudo and his colleagues reported a

50% reduction of $^{13}\text{N-NH}_3$ uptake in the infarcted regions of the rat's myocardium (Kudo et al. 2002). Additionally, a study by Inubushi and his co-workers demonstrated a reduction in the $^{13}\text{N-NH}_3$ uptake in C57BL/6 mice following the administration of the α -2 agonist clonidine, which has negative chronotropic effect of causing a reduction in MBF and heart rate (Inubushi et al. 2004). The same group also indirectly estimated that a 14% decrease in $^{13}\text{N-NH}_3$ uptake would correspond to a 50% reduction of MBF (Inubushi et al. 2004).

There are various fluorinated PET flow tracers, such as ^{18}F -flurpiridaz, tested in rodents and are still under investigation in clinical trials (Rischpler et al. 2012; Cicone et al. 2017). In addition, for the first time, the reliability of using Rubidium-82 (^{82}Rb) was demonstrated in detecting infarction size in rat's myocardium, and despite the long PR of ^{82}Rb , its image quality was acceptable (Clemmensen et al. 2017).

To date, only a few studies were performed to quantify MBF in mice using $^{13}\text{N-NH}_3$. They all focused on calculating $^{13}\text{N-NH}_3$ accumulation in myocardium regions through simple SUV quantification with no compartmental modelling application (Inubushi et al. 2004; Nkepeng et al. 2019).

Repeated, reproducible in-vivo evaluation of MGM and MBF in mice through compartmental modelling remains a challenge. It requires an imaging protocol that is applicable and accurate enough to identify slight changes while considering most technical aspects such as animal handling, acquisition type and duration, and data analysis. The following sections will address most of the technical challenges and errors faced in the PET imaging of mice.

5.2 Technical Challenges in mice imaging:

Several studies indicated that the metabolic flexibility of the heart of using different energy substrates is usually dominated by its physiological conditions (Cicone et al. 2017). Under normal conditions, the heart produces 70 - 90% of its energy from fatty acid (FA) metabolism, with glycolysis acting as a secondary source (10% - 30%) (Cicone et al. 2017). Cardiac metabolic pathways are complicated, and many physiological, environmental, and genetic factors involved, either directly or indirectly (Gargiulo et al. 2012; Cicone et al. 2017).

Many PET radiotracers have been developed to track different metabolic pathways representing cardiac function (Cicone et al. 2017). There is less known about FA analogue radiotracers in cardiac PET imaging for clinical or preclinical applications, mostly likely due to the complexity of their metabolic pathways in pathological conditions (Cicone et al. 2017).

The glucose-analogue radiolabelled tracer ^{18}F -FDG has been used widely in cardiac PET imaging for MGM quantification in clinical and animal research, due to its long half-life, small PR, broad availability, and prominent cardiac uptake (Cicone et al. 2017). ^{18}F -FDG is used as a reference standard when assessing other imaging agents or performance characteristics of the imaging system, which we did in the previous chapter.

As mentioned earlier, it is essential to standardize many experimental variables when planning longitudinal studies in mice because they interfere with the accuracy of the results. Indeed, many studies reported that several factors could significantly impact the kinetic and biological distribution of ^{18}F -FDG in the murine model. These experimental factors create challenges, especially with PET quantitative imaging in mice. These challenges might include animal handling and preparation, type, route and amount of anaesthesia, input function derivation, and compartmental modelling variables. Most of the critical challenges will be outlined in the next sections to justify the applied imaging methodology in this and the following chapters.

5.2.1 Animal handling:

Gentle manipulation when handling mice is an essential aspect since physical stress during restraint will corticosteroid and epinephrine release and cause stimulation of the cardiovascular and respiratory systems (Gargiulo et al. 2012). This stimulation will also increase glucose intake, response to anaesthesia, and changes in body temperature (Hildebrandt et al. 2008; Gargiulo et al. 2012), and further several pieces of evidence suggests that an increase of the radiotracer uptake in inter-scapular brown fat and paraspinal muscles due to injection distress may influence myocardium visualization (Fueger et al. 2006; Hildebrandt et al. 2008). Therefore, in our imaging protocols, mice were allowed to rest for one week following delivery to avoid any distress caused by physical movement and changes in the environment.

Another essential aspect that needs attention in mice handling is the impact of dietary state and ambient temperature which are also known to influence cardiac uptake (Kober et al. 2005). It has been reported that these two factors interfere severely with the radiotracer biodistribution, particularly when using ^{18}F -FDG (Kober et al. 2005). This effect is not seen in humans, but might be due to mice having about 7-fold higher metabolic rates per body weight than humans (Fueger et al. 2006). Moreover, several investigations have been carried out to assess the influences of fasting, warming and type of anaesthesia on rodent PET studies when using ^{18}F -FDG. They indicated that Fasting and warming the mice could all improve the FDG uptake in tumours, possibly by reducing inter-scapular brown fat uptake imaging (Fueger et al. 2006). Fueger and his co-worker had demonstrated that FDG uptake in

tumour imaging was greatly enhanced when mice were fasted and warmed before imaging (Fueger et al. 2006). They also recommended using isoflurane for anaesthesia, because using ketamine/xylazine might induce marked hyperglycaemia (Fueger et al. 2006). In addition, they highly recommended warming up the mice before FDG scan; indeed, keeping patients warm is a standard protocol applied in clinical practice (Fueger et al. 2006).

However, as previously outlined under resting conditions, the primary source of energy in the heart relies on FA metabolism. Still, it switches to glucose metabolism as a primary fuel source in response to ischemia, catecholamine, or insulin intake. Consequently, it has been reported that mouse hearts should utilize FA as the main energy source, which will result in decreased glucose or FDG uptake (Higuchi et al. 2007; Kreissl et al. 2011). In human studies, glucose administration is frequently used to enhance image quality. One attempt to standardize ^{18}F -FDG PET imaging protocols was conducted in mice in which glucose loading was carried out, leading to a 50 fold increase in the myocardium FDG uptake (Simões et al. 2004). Another study by Lee et al. (Lee et al. 2005) has compared the impacts of ketamine-xylazine (Xy/Ke) and pentobarbital anaesthesia on FDG uptake in fasted mice. In this study, they demonstrated that long-term fasting (20 hours) in mice reduced the metabolic effect of both anaesthetic agents and improved the ^{18}F -FDG heart uptake. In contrast, they also indicated that short-term fasting in mice (4 hours) when using both Xy/Ke anaesthesia and pentobarbital anaesthesia led to a significant rise of blood ^{18}F -FDG activity and less myocardium uptake. Therefore, they indicated that the choice of anaesthetic agent and the fasting duration are vital factors that significantly interfere with the biodistribution of the ^{18}F -FDG (Lee et al. 2005).

Interestingly, a study conducted by Kober et al. (Kober et al. 2005) compared the MBF in mice using MRI imaging and under two different anaesthetic regimens, namely Xy/Ke and isoflurane. They indicated that under ketamine 100 mg/kg and xylazine 5mg/kg or isoflurane 1.25%, the average MBF in the LV were in similar ranges (Kober et al. 2005). The reported MBF in mice was 6.0 – 1.9 ml/min/g under Xy/Ke and 6.9 – 1.7 ml/min/g under 1.25% isoflurane (Kober et al. 2005). However, when increasing the isoflurane concentration to 2% or more, both MBF and FDG uptake raised significantly to 16.9 – 1.8 ml/min/g with no remarkable change in the heart rate (Kober et al. 2005). It has been shown that isoflurane affects the blood flow and vascular resistance in various tissues, including the myocardium. Moreover, its vasodilatory effect on coronary micro-vessels is dose dependent. Its mechanism has been assessed in multiple animal models and was found to be based on opening mitochondrial adenosine triphosphate regulated potassium (mitoK_{ATP}) channels (Toyama et al. 2004; Kober et al. 2005).

Another critical problem in mice is the volume of the radiotracer bolus which should not exceed 1% of the body weight (a mouse with 20 g can be given 0.2 ml) for the risk of iatrogenic hypervolemia in the heart or lung tissues (Gehling et al. 2018). The radioactivity of short, lived radiotracers will decrease rapidly, resulting in the need to inject another or a larger dose. This is of particular importance in mice imaging, and mice are usually injected with a radiotracer dose higher than humans with respect to their body weight (Miyashita et al. 2007; Gargiulo et al. 2012). The dose of FDG that is usually given to mice is ~ 7.5 MBq, which is 50 times greater than the amount given to humans (370 MBq) (as a ratio to body weight) (Gargiulo et al. 2012). Increasing the injected dose is a crucial factor to improve the image quality but will also lead to a more significant radiation dose (Gargiulo et al. 2012). Another related factor to injected volume is its administration route which can interfere with the kinetic and biological distribution of the radiotracer (Gargiulo et al. 2012). The two common routes for administration in mice are intravenous (IV) and intraperitoneal (IP) injection (Gargiulo et al. 2012). Most radiotracers in preclinical imaging are injected IV (Miyashita et al. 2007; Gargiulo et al. 2012), and this is the preferred route of administration in mice due to its faster circulation rate, a tracer kinetic closer to that found clinically and its minimal residuum in the peritoneum (Gargiulo et al. 2012).

In contrast, the IP route can introduce some variability, especially if the organ of interest is in the abdominal region. Still, the IP route generally allows a larger volume to be injected into mice (up to 1 mL) (Gargiulo et al. 2012). Importantly, Fueger and his colleagues demonstrated that after 1 hour of injecting ^{18}F -FDG, its biodistribution following IV or IP injections is comparable but this is only applicable with a long live radiotracer like ^{18}F (Fueger et al. 2006). They also demonstrated that FDG reaches the equilibrium state in the myocardial tissue within 40-60 minutes following the administration suggesting that the optimum duration of ^{18}F -FDG scan is 40-60 minutes (Fueger et al. 2006).

In light of the above evidence, in our imaging protocols, all radiotracers were administered as intravenous injection via infusion pump at a fixed rate to minimize the percentage error, interference of the tracer kinetics within mouse body, and variation of the tracer kinetics between mice. If used, pharmacological stress agents were injected intraperitoneally (thus minimizing the volume injected i.v.).

5.2.2 Compartmental modelling:

The combination of tracer kinetic modelling (compartmental modelling) and PET imaging is an outstanding and comprehensive tool for quantifying physiological cardiac biomarkers and detecting their changes in response to disease (Lafrest et al. 2005). Compartmental modelling has been used

for many years in neurological and oncological PET imaging through calculating glucose metabolic rate using ^{18}F -FDG as can be seen in figure 2.23 (Choi et al. 1999; Laforest et al. 2005; Zhong and Kundu 2013). In cardiology, the quantitative radiotracer distribution and kinetics represent the recent and major improvement in clinical and preclinical studies. Therefore, obtaining reliable and reproducible quantitative data from PET is a great goal, especially when assessing a new radiotracer, drug, or treatment intervention. Different cardiac radiotracers are used in compartmental modelling, including ^{18}F -FDG ^{13}N - NH_3 , to measure myocardial function and perfusion in patients with CVDs over the last decade. However, there is a lack of literature investigating this aspect of cardiac PET imaging in mice.

In simple terms, compartmental modelling uses differential mathematical equations that describe changes of the radiotracer concentration over time, as in figure 2.23 (Turkheimer et al. 2014). There are complex multi-compartment modelling options that can quantify cardiac viability, MGM, MBF, FAs metabolism in both normal and abnormal conditions of the myocardium (Laforest et al. 2005; Turkheimer et al. 2014). The choice of the model relies on the general understanding of the examined physiological process, and the amount of data available that will be explained in the relevant section of this chapter. As a rule of thumb, to apply any compartmental model, this requires two key parameters of radioactivity over time, which include the tracer activity in the arterial blood compartment (or also called input function IF), and the radioactivity in the organ of interest as shown in figure 2.23 (Laforest et al. 2005). The change in time required for the radiotracer to travel from blood to the organ will dramatically affect the tracer kinetics (Laforest et al. 2005; Zhong and Kundu 2013; Massey et al. 2021). Therefore, compartmental modelling in small animals micro-PET requires accurate measurement of the IF.

Measuring the radioactivity in the blood over time (the IF) is the fundamental element towards successfully applying the compartmental model to measure biomarkers such as MGM and MBF (Laforest et al. 2005; He et al. 2019; Massey et al. 2021). The IF describes the influx of radiotracer from the blood into a single or multi-compartment within an organ of interest (Laforest et al. 2005; Massey et al. 2021). Several methods have been proposed to measure the IF in humans and small animals, which are either based on blood sampling or image-derived input function (IDIF) (Wu et al. 1996; Laforest et al. 2005). Several methods have been established to measure the blood activity concentration in clinical studies; however, applying these methods in rodents needs more consideration due to the difficulty of vascular access, smaller blood volume and the higher heart rate compared to larger animals or humans (Laforest et al. 2005).

5.2.2.1 Arterial blood sampling:

Blood sampling is considered the reference method for measuring the actual radioactivity in the blood. This method involves withdrawing blood samples rapidly and with small amounts at timed intervals from the main vessels (Laforest et al. 2005; Sharp et al. 2005). The radiotracer injection is done via a catheter inserted in the femoral or jugular vein (Laforest et al. 2005). In addition, another catheter is placed in the carotid artery for collecting the blood samples (Laforest et al. 2005). The withdrawn blood volume is about 5 μL using micropipette disposable tubes (Laforest et al. 2005; Sharp et al. 2005). After that, the micropipette is weighted before and after blood collection and the radioactivity is measured using a gamma counter (Laforest et al. 2005). Importantly, this method allows blood flow measurements and metabolite analysis (Laforest et al. 2005). Radio metabolite measures vary when using different radiotracers, but they are used to correct the total blood activity for accurate compartmental modelling (Laforest et al. 2005).

However, it is not possible to collect successive blood samples from small animals like mice over a limited period of time due to the small total blood volume (approximately 1.5 – 2.5 ml or 6-8% of body weight). Importantly, automatic blood sampling has been applied successfully in mice. An alternative method to measure the IF is via IDIF method which has been proposed and validated in several studies (Fang and Muzic 2008; Thorn et al. 2013).

5.2.2.2 Image derived input function (IDIF):

Deriving the IF from the dynamic PET images is a simple and non-invasive method that can be performed directly by drawing VOI over vascular structures or ventricular cavities (Laforest et al. 2005; Sharp et al. 2005). On the other hand, IDIF is significantly affected by the system SR due to the smaller size of mice's hearts and arteries compared to the system SR. This might result in smaller regions having lower readings than the actual activity because of PVE, while regions close to the hot area (high radioactivity) might appear more intense due to spill over (Laforest et al. 2005; Sharp et al. 2005). In addition, the blood pool radioactivity is blurred into the surrounding tissue and vice versa (Laforest et al. 2005).

For better estimate IDIF, it is recommended to apply PVE and spill over corrections, which cause a degradation in the SR, in the defined VOIs (Laforest et al. 2005; Sharp et al. 2005). The application of PVE correction is necessary for accurate quantitative PET imaging (Erlandsson et al. 2016). A previous study reported that addition of anatomical information, such as MRI images, could allow accurate PVE correction (Erlandsson et al. 2016). Moreover, temporal resolution of the PET system

affects its ability to generate short frames during dynamic acquisition, which subsequently will reduce the counts per frame leading to the higher statistical uncertainty of the data (Laforest et al. 2005). A PET scanner with higher SR and sensitivity can detect more counts per frame and permit a more accurate estimation of the IDIF and TACs for all regions (Laforest et al. 2005). Huang et al. (Huang et al. 2019) reported that IDIF generated from a VOI over the inferior vena cava (IVC) and PVE correction compared well with the one obtained from VOI over left ventricular blood pool (LVBP) and PVE and spillover corrections. Massey et al. (Massey et al. 2021) demonstrated that IDIF derived from drawing region around LV compared well with arterial blood samples in rats. Therefore, in our imaging protocol, the IDIF were derived from the LVBP VOI by applying PVE and spillover corrections.

5.2.3 Available software for Compartmental modelling:

There are several software's available for quantifying MGM and MBF through applying the concept of kinetic modelling using PET images (Slomka et al. 2014). The level of agreement between them is excellent (Slomka et al. 2014; Dunet et al. 2016). Computerized quantitative measurement of MBF under rest and stress conditions is a more accurate method than non-quantitative visual interpretation subject to assessor variability (Slomka et al. 2014; Dunet et al. 2016). In the information presented in this chapter and the following PET-based chapters, all data were analysed using the commercial PMOD version 3.91 (PMOD Technologies Ltd. Zurich, Switzerland). The software's cardiac quantification element relies on deriving the IF and defining the LV region before applying segmentation (if possible). This will be explained further in the methodology section of this chapter.

5.3 Pharmacological stress agent, dobutamine versus adenosine:

β 1-adrenergic receptor stimulation primarily works on the activation of cAMP-dependent protein kinases, which are a family of enzymes with activity dependent on cyclic AMP (cAMP). They also contribute to regulating FA and glucose metabolism (Puhl et al. 2016). The sympathetic nervous system regulates cardiac function via cardiac β 1-adrenergic receptors stimulation; however, intense stimulation might induce fast and substantial chronotropic (increase HR), inotropic (increase contractility) and lusitropic (increase relaxation phase during diastole) effects on the myocardium (Puhl et al. 2016). Unfortunately, continual β 1-adrenergic receptor activation may lead to hypertrophy and cardiac remodelling (Johnson and Peters 2010; Tyrankiewicz et al. 2013; Puhl et al. 2016).

Importantly, the use of β 1-adrenergic drugs plays a key role in understanding the myocardium in normal or pathological conditions, assessing how genetic alteration or pharmacological intervention might interfere with the signalling pathways (Puhl et al. 2016).

Many imaging modalities and protocols use the aspect of the cardiac stress process to better detect the severity of CVDs, especially CADs (Puhl et al. 2016). Many cardiac stress tests, whether clinical or preclinical studies, involve the use pharmacologic stress agents that are administered to induce cardiac hyperaemia (increase in blood flow rate) (Johnson and Peters 2010). The pharmacological stress agent (often a vasodilator) is administered if the subject is unable to increase cardiac stress via exercise, whether due to pathological conditions or if the imaging protocol does not allow movement or a change of position (Johnson and Peters 2010; Tyrankiewicz et al. 2013; Puhl et al. 2016).

The most extensively used vasodilators are adenosine, dipyridamole, and dobutamine but they differ in sensitivity and specificity for detecting ischemia of protocols (McGuinness and Talbert 1994; Croteau et al. 2004; Johnson and Peters 2010). An ideal stress agent must be effective, safe and have a simple administration protocol (Puhl et al. 2016). The choice of the agents should be made according to the design of the experiment, ensuring optimum results (Puhl et al. 2016). In addition, Puhl and his co-worker have tested different dobutamine protocols in C57/Bl6J mice, and they reported comparable stressing effects on the heart when dobutamine was administered via IV (infusion) and IP (with bolus injection) (Puhl et al. 2016).

In our designed imaging protocols, we performed two sets of experiments using adenosine injected IV and dobutamine injected IP.

5.4 Objectives:

In this chapter, I will develop and standardize cardiac PET imaging protocols in healthy mice and use ^{18}F -FDG and ^{13}N - NH_3 to assess MGM and MBF, respectively. Following standardization, the results of both MGM and MBF will be used as a baseline to test their repeatability. In addition, our results will be compared to studies where other imaging modalities have been used.

The layout of the chapter will be in the following order:

1. Develop and standardize imaging protocols and test the ability of pharmacological stress agents, namely adenosine and dobutamine, to induce a physical stress effect that our Mediso micro-PET/CT scanner can detect.
2. Quantifying MBF using ^{13}N - NH_3 in healthy mice to generate baseline datasets and assess their accuracy and repeatability.

3. Quantifying MGM using ^{18}F -FDG in healthy mice to generate baseline datasets and assess their accuracy and repeatability.
4. Evaluate the correlation between the ^{18}F -FDG uptake (MGM) and the metabolic trapping of ^{13}N - NH_3 in rest conditions and the possibility to use the later one as a predictive biomarker in CVDs.
5. Assess the correlation between ^{18}F -FDG and ^{13}N - NH_3 (in rest scan) SUV results and whether it can provide additional insight to the kinetic modelling results.

5.5 Material and methods:

5.5.1 Animal and the sample size:

All animal experiments performed in this chapter were carried out according to the guidance and approval of the British Home Office and Bristol University (under PPL 30/3373) using the Care and Use of Laboratory Animals Guide (The Institute of Laboratory Animal Resources, 1996). Two sets of healthy female C57BI/6J mice aged about eight weeks (bodyweight 25–30 g) were obtained from Charles River, one of the main Cardiff university suppliers. The first set ($n=6$) was used to assess the ability of adenosine to induce stress effect in mice when injected via IV route of administration. The other set of mice ($n=12$) tested the ability of dobutamine to induce physical stress via bolus IP injection that our Mediso micro-PET/CT scanner can detect. The mice were housed in standard cages with an environment of a 12-hours light-dark cycle during which both temperature and humidity were monitored daily. Mice had free access to water and food. In order to calculate the number of animals needed in our experiments, we used power calculations.

5.5.2 The micro-PET/CT Scanner:

The Mediso Nano-Scan 122S small-bore PET/CT imaging system manufactured by the Mediso medical imaging system, Budapest, Hungary. All the scanner specifications have been previously mentioned in the methodology chapter.

5.5.3 Radiotracers:

^{18}F -FDG and ^{13}N - NH_3 were used to quantify MGM and MBF, respectively.

5.5.4 Type of pharmacological stress agent:

Our imaging protocol involves injecting ^{13}N - NH_3 under two physical conditions rest and stress. To induce stress effect, two drugs were used and compared, adenosine and dobutamine. The applied imaging protocols for the two pharmacological stress agents are illustrated in figures 5.2 and 5.3.

5.5.4.1 Adenosine:

It is a drug that induces hyperemic coronary flow to the myocardium by stimulating the A2A adenosine receptors that are found on the smooth muscle of the coronary vessels (Layland et al. 2014). This stimulation causes a vasodilation response in the coronary vessels (Layland et al. 2014). Previous clinical studies suggested that intravenous administration of adenosine decreases HR variability and increases the HR by reducing parasympathetic and raising the cardiac sympathetic tone (Rongen et al. 1999). These effects of the adenosine made it relevant to be used in stress scan to diagnose ischemia, or in heart failure (Rongen et al. 1999; Guieu et al. 2020). Importantly, adenosine is known of its effects in vasodilation, and reducing both the heart rhythm and blood pressure (Guieu et al. 2020). Adenosine has a fast onset of action, which occur in less than 10 seconds following administration, and a short half-life of 20 seconds (Layland et al. 2014). In our protocol, adenosine was injected via i.v. cannula with a dose of 2.5 µg/kg in 50 µL to promote the vasodilation and increase the blood flow (Layland et al. 2014).

5.5.4.2 Dobutamine:

Dobutamine is a β 1-adrenergic receptor agonist, which binds specifically to this receptor type generating a hyperaemic response through increasing cardiac output and HR (Vallet et al. 1991; Puhl et al. 2016). Its action is rapid (onset of action within 2 minutes) with a short half-life requiring repeated injections for prolonged effects, which won't be a problem in mice if injected via IP route (Puhl et al. 2016). In our imaging protocols, the dobutamine was administered via a single bolus IP injection with a dose of 0.75 µg/g as previously tested and justified by Puhl et al. (Puhl et al. 2016). This protocol proved its reliability and accuracy and was applied mainly to avoid breaking the IV cannula, especially with multiple i.v. injections and the limited volume allowed to be injected intravenously in mice.

5.5.5 Study design:

5.5.5.1 Animal Preparation:

On the day of the scanning, mice were kept fasting for one hour and warmed up at 37°C for about 5 minutes for better vein visualization. It is important to emphasize that the blood glucose was not measured following fasting. Next, each mouse was anaesthetized in a closed induction box with 3% of isoflurane in oxygen for 2-5 minutes until immobile. Following induction of anaesthesia, the mouse was weighed and placed in the prone position in a pre-warmed scanner bed, which was supplied with a small tooth bar (attached to a nose cone to maintain anaesthesia), a breathing pad and ECG pads measure breathing and heart rate, respectively. A hand-made 27G cannula (polyethylene tube with I.D

0.28 mm and O.D 0.61 mm) with an approximate length of 2 cm was made one hour before the scanning time. The cannula was flushed with heparin to prevent blood clotting due to the prolonged imaging time and to limit the dead volume of the various radiotracers and drugs. the tail vein was cannulated gently and carefully, with several layers of tape applied on the top of the cannula and tail to limit motion. If dobutamine was to be used, an IP cannula was inserted and fixed after positioning on the scanner bed, prior to the IV cannulation.

Since all mice should undergo only non-recovery procedures as stated in the project license (Bristol University Project License PPL 3003373), all required imaging scans were performed sequentially for each mouse which was then terminated following the completion of the scans. Imaging protocols were acquired for each mouse with the following order: CT Scout view, $^{13}\text{N-NH}_3$ rest scan, $^{13}\text{N-NH}_3$ stress scan, $^{18}\text{F-FDG}$ scan, and CT scan, using two different pharmacological agents as illustrated in figures 5.1. and 5.2.

5.5.5.2 $^{13}\text{N-NH}_3$ rest scan:

$^{13}\text{N-ammonia}$ (30 ± 2 MBq) was injected in each mouse acquisition through the tail vein cannula. Following administration, a 10 min dynamic PET scan was performed. The actual acquisition started a few seconds before administering $^{13}\text{N-ammonia}$ to catch all the myocardial flow processes.

5.5.5.3 $^{13}\text{N-NH}_3$ Stress scan:

Ten minutes later the stress scan was initiated without moving the animal by injecting pharmacologic stress stimuli using adenosine or dobutamine. In the case of the adenosine group, the adenosine was infused using the i.v. cannula over 2 minutes at $2.5 \mu\text{g}/\text{kg}$ in 50 ul ($0.0625 \mu\text{g}$ per 25g mouse, $n=6$), as outlined in the figure 5.1. In the dobutamine group, the dobutamine was injected 10 minutes after completing the rest scan as a single IP injection ($0.75 \mu\text{g}/\text{g}$, $n = 12$) as in figure 5.2.

In both groups, when the heart rate increased to about 600 bpm (measured by ECG pads placed on paws), the second dose of $^{13}\text{N-NH}_3$ (30 ± 2 MBq) was injected. Image acquisition was initiated a few seconds before the radiotracer injection by applying the same image acquisition as in the rest scan.

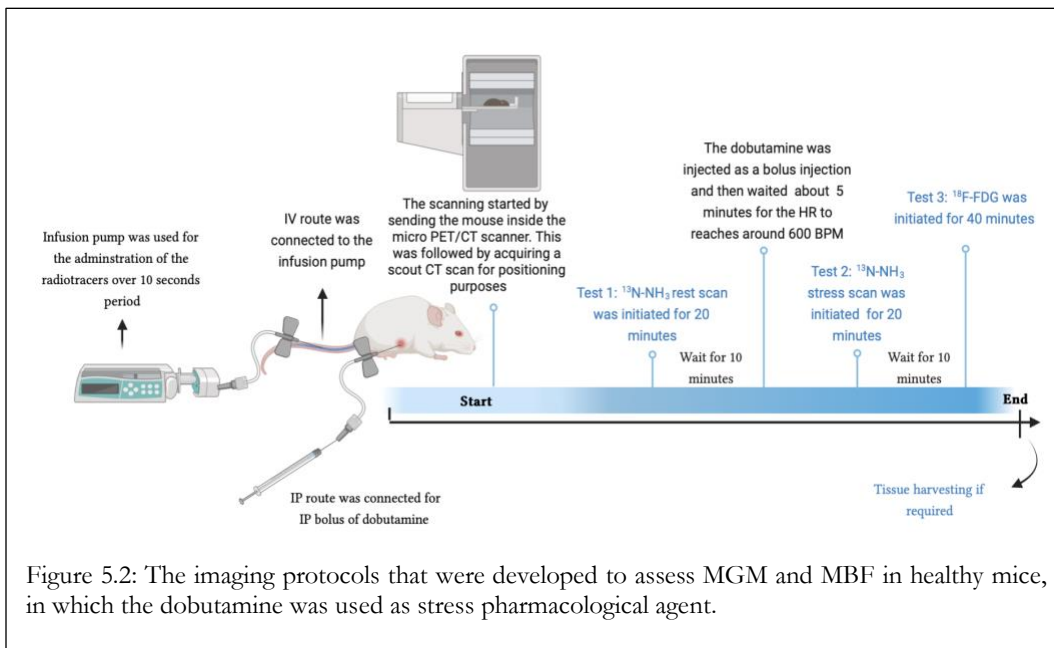
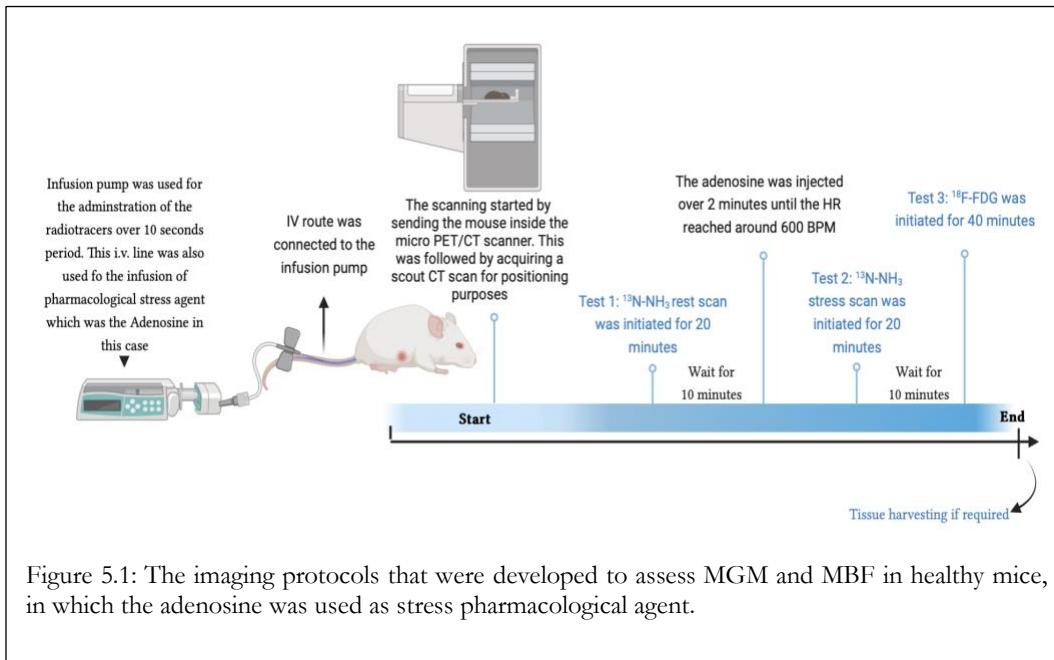
5.5.5.4 $^{18}\text{F-FDG}$ scan:

Following the ammonia scans, an injection of ~ 20 MBq of $^{18}\text{F-FDG}$ ≈ 20 ul was administrated via the same iv cannula line, and a 40-minute whole-body dynamic PET scan acquired immediately.

5.5.5.5 CT scan:

Following FDG scans, a 2.5-minute whole-body CT scan was performed with acquisition parameters that include: 480 projections in a semi-circular method, one rotation, 50 kVp, 300 ms

exposure time, 1-4 binning and a maximum FOV was used. The CT scan was used to calculate attenuation corrections as well as allow co-registration of images which in turn give a better visualization of structural and functional information from the CT and PET respectively.



5.5.6 Reconstruction of PET images:

All PET scans were acquired in list mode acquisition, and images were reconstructed using iterative reconstruction with a voxel size of 400 μm using interview fusion software. The framesets of both ammonia rest and dynamic stress scans were 35 frames (1x60 secs; 24x5secs;4x30sec; 6x150sec, with a whole duration of 20 minutes).

In contrast, the FDG scans were reconstructed with a total of 47 frames with framesets of 36x5secs; 6x30secs;4x60secs;1x1800secs and a whole duration of 40 minutes. Additionally, CT scans were reconstructed with a 250 μm voxel size and Sinograms were produced using the 2-dimensional filtered back-projection method. Attenuation (CT based) and scatter corrections, as well as normalization, were applied to the reconstructed images. Following the reconstruction, all images were exported to PMOD software for further Kinetic modelling and data analysis. All PET images were corrected for dead time, scatter, and radiation decay. The CT images were also used to apply attenuation correction.

5.5.7 Data analysis and the used software:

PMOD was the software of choice in all the analyses due to the sophisticated capability of kinetic modelling and the wide range of parameters that could be obtained. The investigation was divided into three sections which included: firstly, the measurement of MBF in both rest and stress using 1TC model and ammonia dynamic scans along with repeatability assessment of the obtained results, through Coefficient of variation (COV) and STD%, and accuracy through comparing our calculated values with values in literature measured with other imaging modalities or protocols.

Secondly, the assessment of MGM using FDG scans and 2TC model along with repeatability and accuracy assessment as in MBF values. The last section of analysis comprises quantifying the metabolic trapping of ammonia using ammonia rest scan and 2TC model, comparing it to the glucose uptake that was measured from FDG scan, and evaluating the degree of correlation between these two data sets.

In PMOD and Prior to applying the kinetic model relevant to the radiotracer and the required biomarker, two steps need to be performed, including the orientation of images, and defining the dynamic ranges through which the VOIs of IDIF and LV will be drawn.

5.5.7.1 Orientation of PET images and dynamic range of the VOIs:

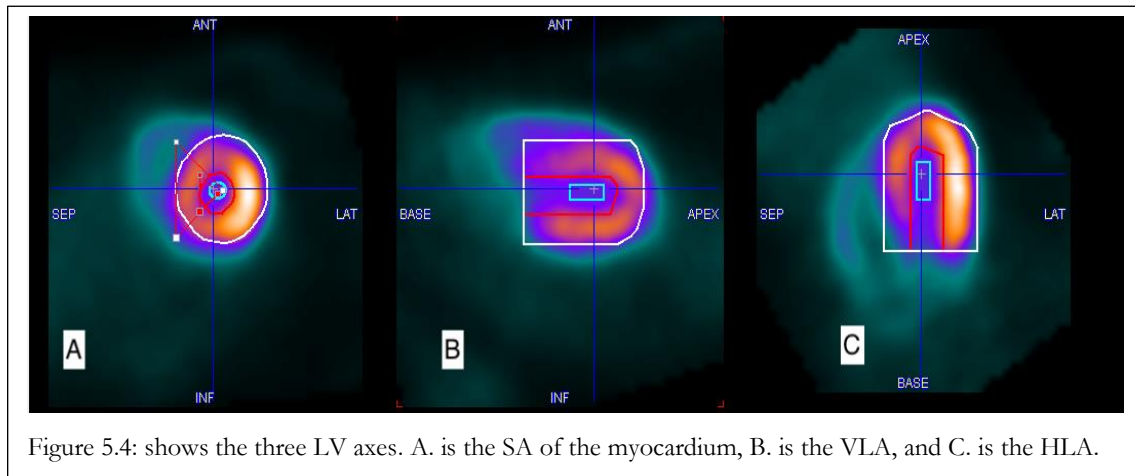
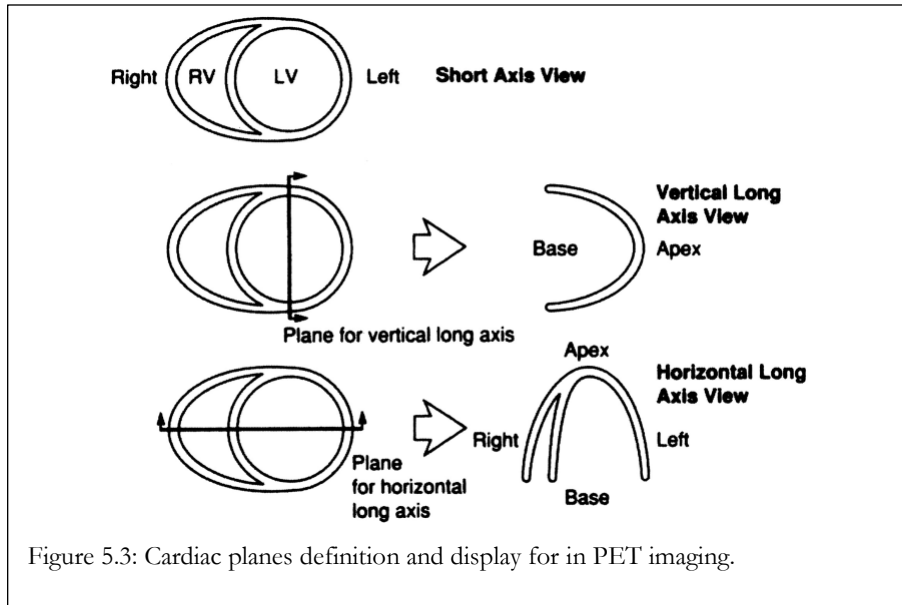
Both PET and 2D echocardiography, which are the most used cardiac imaging modalities, have identified the orientation of the heart in reference to the long axis of the LV, which is the line connecting the ventricular apex to the centre of the mitral valve (Cerqueira et al. 2002). The planes

include short axis (SA), Horizontal long axis (HLA) and vertical long axis (VLA) (Cerqueira et al. 2002). This orientation approach ensures the best display of the myocardial chambers for viewing the distribution of coronary blood flow to the heart (Cerqueira et al. 2002). For these reasons, this orientation approach has been applied widely in clinical and preclinical studies (Cerqueira et al. 2002). Therefore, the SA refers to the plane perpendicular to the long axis of the LV, as illustrated in figure 5.3. In contrast, HLA is parallel to the plane of the long axis of the LV, as seen in the figure 5.3. The HLA is the line drawn from the mid ventricle level between the LV centre and the transition between the diaphragm free wall of the RV as in the figure 5.3. Moreover, The VLA is the plane perpendicular to the HLA plane, as seen in the figure 5.3. Accordingly, after loading all PET images, the first step is to fit the reorientation of the myocardium. The three LV axes in PET images including SA, VLA, and HLA are illustrated in figure 5.4.

The next step was to define the dynamic range from which the VOIs and corresponding TACs were derived, as seen in the figure 5.5. The main two VOIs that need to be drawn are LV, which is the largest chambers representing the myocardium, and the LVBP that is used to derive the IDIF as illustrated in figure 5.6. As we have three analysis steps, including MBF, MGM, and metabolic trapping of ammonia, the dynamic range was identified differently. Indeed, the dynamic range did vary slightly among mice due to the differences in the injection time.

5.5.7.2 Deriving Image Derived Input Function (IDIF):

For IDIF, VOI was drawn in the left ventricular cavity, which is the blood pool region also called LVBP as in figure 5.6. Note that the VOI was positioned manually in the LV blood pool during the initial time of the dynamic frames, where the tracer bolus injection was clearly visible. The RC for the measured LVBP radioactivity was estimated by convolving LVBP VOI with the 2D gaussian PSF (previously measured by the manufacturer engineer), which represents the resolution of the Mediso micro-PET scanner. Another VOI was generated in the background region (RV region as in figure 5.6 A) and used to correct for spill-in of radioactivity from the RV into the LVBP region. Finally, the true LVBP activity was calculated; this approach of applying IDIF was justified by several lines of evidence (Thorn et al. 2013; Thackeray et al. 2015; Huang et al. 2019).



5.5.7.3 MBF analysis:

Following the estimation of the IDIF curve, other VOIs were drawn over the LV in the three planes, including its outer and inner wall, as seen in figure 5.6. TACs were generated for the dynamic frames in the specified VOIs for the LV and LVBP. The two TAC curves, including the LV and the LVBP (IDIF), were used for the compartmental (kinetic) modelling. For MBF quantification with $^{15}\text{N-NH}_3$, the 1TC DeGrado model was used, as seen in the figure 5.7.

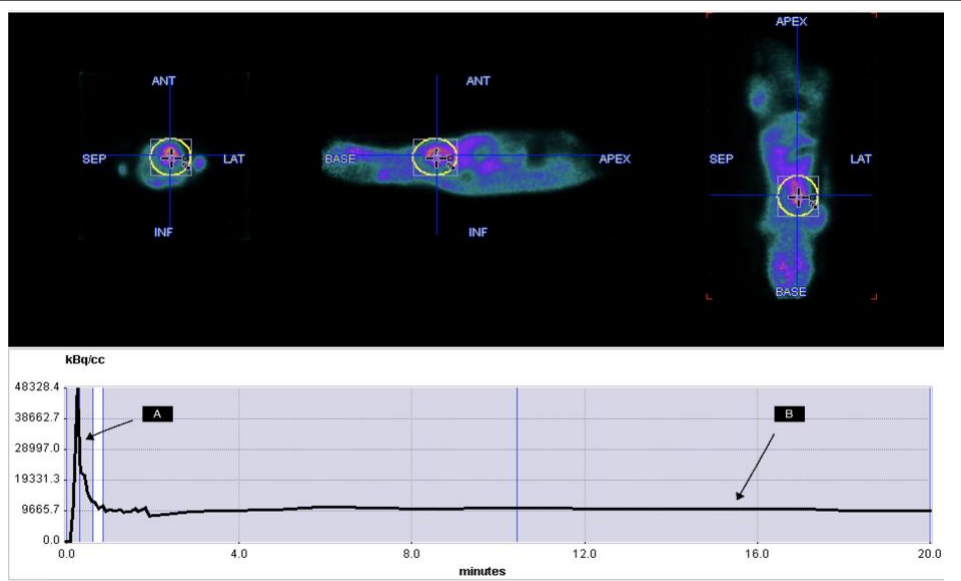


Figure 5.5: The dynamic range step that need to be specified in deriving and drawing the VOIs for the LV and LVBP. A. shows the dynamic range from which IDIF was derived, while B. shows the dynamic range of the LV VOIs, but generally in MBF analysis, LV VOI was derived from the early 2-3 minutes of the ammonia scan. In MGM analysis, the VOI was derived from the last 20 minutes of FDG scan which is the equilibrium state. Finally, in the assessment of ammonia metabolic trapping, LV VOI was derived from the last 15-20 minutes of the ammonia scan.

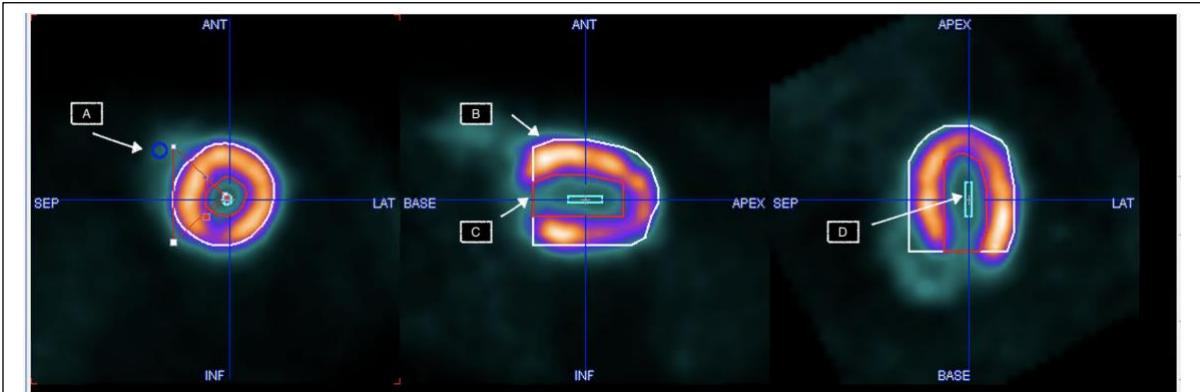


Figure 5.6: The myocardium VOIs that were drawn in all the three planes. For clarity reasons, arrows for each VOI were identified in separate plane but they are all existed in all three planes in which, A. is the RV VOI, in the SA plane, to correct for spill-in activity from RV into LVBP for IDIF calculation. Both B, which represent the epicardium VOI or the outer wall, and C, which represent the endocardium VOI or the inner wall of the myocardium, are in the VLA plane. D. is the LVBP VOI in the HLA plane.

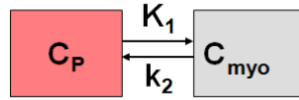


Figure 5.7: Shows the 1TC (or DeGrado) model that was used for MBF estimation with $^{13}\text{N-NH}_3$ as a radiotracer.

in which the:

C_P = The concentration of radioactivity in the plasma blood compartment or also called the input function.

C_{myo} = The radioactivity concentration in the myocardium compartment.

K_1 = The fraction of the radioactivity that diffuses from C_P into C_{myo} . It is the blood perfusion or blood flow with unit of $\text{ml}/\text{cm}^3/\text{min}$.

K_2 = The fraction of tracer that diffuses back to the plasma with a unit of $1/\text{min}$ or min^{-1} .

In the 1TC model, including the DeGrado model, the arterial radioactivity concentration is assumed to be the same throughout the body (DeGrado et al. 1996). The radiotracer concentration in the C_{myo} proportionally increases with the extraction fraction of activity from the plasma blood, which is dependent on the used radiotracer (in our case, $^{13}\text{N-NH}_3$ has 80-90% EF) (DeGrado et al. 1996). Because extraction can be expressed as a first-order differential process, the transport of the radiotracer is also dependent on the plasma blood concentration (DeGrado et al. 1996).

In addition, the backwards transfer of radioactivity from the myocardium to the blood compartment is proportional to the myocardium radioactivity concentration (DeGrado et al. 1996). Consequently, both C_P and C_{myo} are competing, so that the change over time of the total radiotracer concentration in the myocardium ($dC_{myo}(t)/dt$) can be written in the form of differential equation as in equation. 5.1:

$$Eq. 5.1 \quad \frac{dC_{myo}(t)}{dt} = K_1 C_P(t) - K_2 C_{myo}(t)$$

In which K_1 is a flow-dependent component and has unit $\text{ml}/\text{cm}^3/\text{min}$; in contrast, K_2 is the fraction of mass that diffuses back in a unit of time. For example, if K_2 is equal to 0.1 min^{-1} , that means the radioactivity diffuses back from C_{myo} into C_P at a rate of 10% per minute (DeGrado et al. 1996). Notably, the radioactivity concentration in the arterial blood function is then measured as the parent concentration, which means its need to be corrected for plasma percentage, and this was done

automatically in the PMOD used tool after loading the TACs (for both LV and LVBP) in the PKIN (compartmental modelling) tool.

As we applied the 1TC (DeGrado) model, the MBF was calculated using only the first 4 minutes of the dynamic data following radiotracer administration. This was mainly to prevent the buildup of the metabolite as well as the washout fraction.

5.5.7.4 MGM analysis:

For MGM measurement, images were quantified using the 2TC model, as in the figure 5.8, and the 10-40 minutes dynamic range during which the FDG came into an equilibrium state between all compartments.

Following reorientation, specifying the dynamic range that was required for VOIs generation (including LV and LVBP), VOIs creation and generating their corresponding TACs, all curves were loaded in the kinetic tool of the PMOD in which the 2TC model for the FDG was used. Using both LV and LVBP TACs, the relative FDG uptake was estimated using the 2TC model. Rates constants were K_1 (inward into C_p in $\text{ml}/\text{cm}^3/\text{min}$), K_2 (outward to C_p in a unit of min^{-1}), K_3 (phosphorylation in min^{-1}), and K_4 (dephosphorylation in min^{-1}) of ^{18}F -FDG as illustrated in the figure 5.8. Accordingly, the MGM constant of ^{18}F -FDG, also denoted as K_{FDG} (in a unit of $\text{ml}/\text{g}/\text{min}$), can be calculated using the following equation 5.2.

$$\text{Eq. 5.2} \quad \text{MGM or } K_{\text{FDG}} = \frac{K_1 \cdot K_3}{K_2 + K_3}$$

5.5.8 Statistic:

All data were analysed using GraphPad Prism (version 9.3.0). To assess the repeatability of the data, the coefficient of variation (CV) and STD% were used. The CV is defined as the STD divided by the mean. In addition, a paired two-tailed Student's *t*-test was used to evaluate the statistical significance between rest and stress MBF values with P value less than 0.05 to be statistically significant. Moreover, the correlation between data was estimated using Pearson *r*, in which *r* is equal to or less than 1.

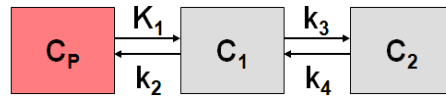


Figure 5.8: The 2TC model that was used for FDG uptake estimation.

In which:

C_p = The concentration of the tracer in the plasma blood compartment.

C_1 = The concentration of the tracer in the tissue (under investigation) compartment representing the non-bound tracer.

C_2 = The tissue (under investigation) compartment representing the specifically bound tracer.

K_1 = The fraction of tracer transported from the plasma blood into compartment C_1 , with a unit of $\text{ml}/\text{cm}^3/\text{min}$.

K_2 = The fraction of tracer that diffuses back to the plasma with a unit of $1/\text{min}$ or min^{-1} .

K_3 = The fraction of tracer that moves to compartment C_2 . It represents the fraction of the tracer that is specifically bound or the rate of ^{18}F -FDG phosphorylation or uptake. It has a unit of min^{-1} .

K_4 very small as the ^{18}F -FDG trapped irreversibly.

$$K_{\text{FDG}} = \frac{K_1 \cdot K_3}{K_2 + K_3} \text{ in unit of ml/min/g}$$

5.6 Results:

5.6.1 MBF analysis results:

Animals in this section were divided into two groups according to the type of stress-inducing drug given, as illustrated in figures 5.1-5.2. In the adenosine group, the MBF results for the rest scan had a COV of 15.12% (which is less than 20%, suggesting good repeatability), and STD% of 0.65, as seen in table 5.1. Similarly, the MBF stress values in the same group were also repeatable with a coefficient of variation of 10.99% and STD% of 0.406.

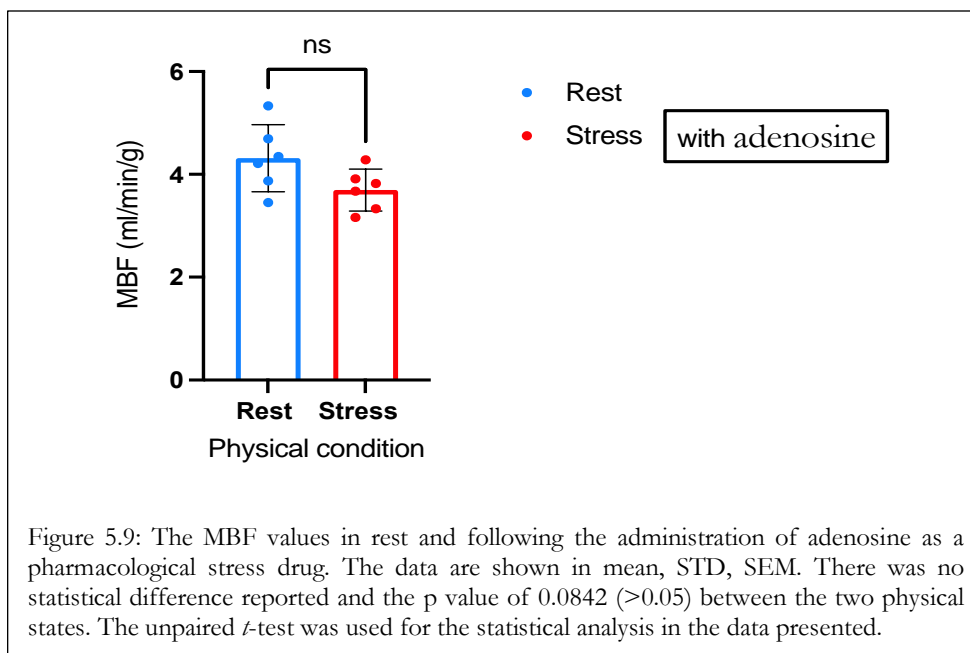
There was no difference in MBF between the rest and stress states (as induced by adenosine) ($p=0.0842$), figure 5.9. In the dobutamine-treated group, the MBF values in rest and stress scans were different ($p < 0.0001$) and reproducible (STD% of 1.25 and 1.466 and COV of 19.98% and 11.03%, respectively, as shown in the table 5.2 and figure 5.10).

Importantly, in both groups, the MBF values in rest scans were comparable to the MBF values in mice recorded previously (Kober et al. 2005; Raheer et al. 2007; Jogiya et al. 2013b). The MBF stress values in mice given dobutamine were also similar to previous studies, indicating the successful stimulation of hyperemic response caused by dobutamine injection (Kober et al. 2005; Raheer et al. 2007; Jogiya et al. 2013b).

Raher et al. measured the MBF in mice using microspheres and the values were 6 ± 0.5 ml/g/min during baseline scans and they raised to 14 ± 2 ml/g/min following adenosine administration (Raher et al. 2007). In addition, the mean MBF at rest measured by Jogiya and his co-worker was 4.1 ± 0.5 ml/g/min, which was increased to 9.6 ± 2.5 ml/g/min during the administration of dipyridamole (Jogiya et al. 2013b). Croteau et al. (Croteau et al. 2014) also reported MBF in mice to be 4.0 ± 1.3 ml/g/min at rest state in mice. Furthermore, Naresh et al. (Naresh et al. 2015) measured the murine MBF using first-pass perfusion MRI, and it was 5.7 ± 0.8 ml/g/min, which reached 11.86 ± 0.6 ml/g/min following Regadenoson administration. In another study that measured the effect of anesthesia on mice MBF, the MRI recorded MBF was 6.9 ± 1.7 ml/g/min at rest (Kober et al. 2005).

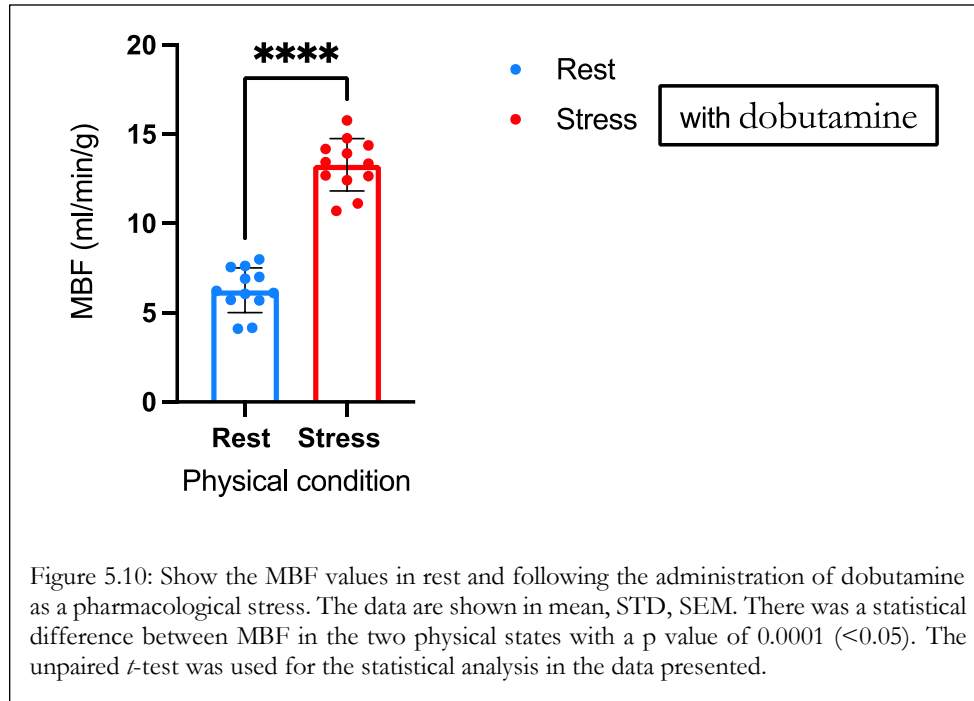
Physical condition	MBF (ml/min/g) at rest	HR (BPM) at rest	MBF (ml/min/g) at stress	HR (BPM) at stress
Mouse 1	5.33	450-490	3.33	213-370
Mouse 2	3.45	388-430	3.16	160-281
Mouse 3	4.21	350-440	3.67	120-147
Mouse 4	4.35	323-430	3.82	90-176
Mouse 5	3.87	260-388	3.91	110-190
Mouse 6	4.69	430-560	4.28	200-390
Mean	4.31	-	3.69	-
Std.Deviation	0.6526	-	0.4060	-
Coefficient of Variation (COV)	0.2664	-	0.1657	-

Table 5.1: The MBF values during rest and stress conditions in the adenosine group in unit of ml/min/g.



Physical condition	MBF (ml/min/g) at rest	HR (BPM) at rest	MBF (ml/min/g) at stress	HR (BPM) at stress
Mouse 1	4.16	423-467	11.13	623-867
Mouse 2	5.69	400-520	13.93	610-573
Mouse 3	6.11	380-540	14.77	680-763
Mouse 4	7.56	425-542	12.65	535-682
Mouse 5	4.11	288-430	10.71	590-690
Mouse 6	7.62	438-550	12.43	638-550
Mouse 7	5.72	432-530	13.44	632-730
Mouse 8	6.06	431-550	14.18	619-720
Mouse 9	6.22	516-560	14.38	616-720
Mouse 10	7.99	379-444	15.78	690-840
Mouse 11	6.9	488-532	12.69	620-811
Mouse 12	7.01	418-526	13.35	610-820
Mean	6.263	-	13.29	-
Std.Deviation	1.251	-	1.466	-
Coefficient of Variation (COV)	0.3612	-	0.4232	-

Table 5.2: The MBF values during rest and stress conditions in the dobutamine group in unit of ml/min/g.



5.6.2 MGM analysis results:

Table 5.3 shows the K_{FDG} FDG uptake (MGM) derived using the 2TC model from the the ^{18}F -FDG TACs during the 10-40 minutes dynamic range of FDG scans performed following ammonia scans in the dobutamine group. Note that there were no FDG scans for two mice in the dobutamine group. The MGM values were repeatable with STD% of 0.004 and a coefficient of variation of 17.59%, representing good repeatability of the generated MGM data. Although few studies have measured MGM in mice, the values obtained from these studies were 0.025 ± 0.004 , which were in the same range of our generated MGM values illustrated in table 5.3 (Wu et al. 2007; Kreissl et al. 2011).

5.6.3 SUVs for ^{18}F -FDG and ^{13}N - NH_3 rest scans:

The SUVs were calculated for both ^{18}F -FDG and ^{13}N - NH_3 rest scans and the results are shown in table 5.4. The SUVs were estimated for ^{18}F -FDG and ^{13}N - NH_3 using the whole duration of the dynamic scans, which is an independent weight value with no unit. There was a good positive correlation between the two parameters ($r = 0.8216$) within each mouse. Accordingly, this might be used as additional insight for the assessment of CVDs using perfusion tracer only, which was, in our case, ^{13}N - NH_3 . In fact, several investigations have reported the SUVs in the myocardium to be 3.48 ± 1.73 g/ml with the ^{18}F -FDG, which was the same range as our recorded results confirming their accuracy (Lee et al. 2005; Fueger et al. 2006; Kreissl et al. 2011).

Physical condition	^{18}F -FDG scan MGM (K_{FDG}) in a unit of ml/g/min
Mouse 1	0.027
Mouse 2	0.025
Mouse 3	0.026
Mouse 4	0.021
Mouse 5	0.014
Mouse 6	0.019
Mouse 7	0.024
Mouse 8	0.025
Mouse 9	0.026
Mouse 10	0.025
Std.Deviation	0.02326
Std.Error of Mean	0.004091
Variation Coefficient	0.001294
Coefficient of Variation	17.59%

Table 5.3: The MGM (K_{FDG}) uptake in ml/min/g in healthy mice derived from the TACs of the LV during the 10-40 and 15-20 minutes of the FDG scan respectively.

Physical condition	SUV in ^{18}F -FDG scan	SUV in ^{13}N - NH_3 scan
Mouse 1	4.18	1.15
Mouse 2	3.4	1.03
Mouse 3	3.002	1.027
Mouse 4	2.39	0.3
Mouse 5	2.13	0.68
Mouse 6	3.07	1.03
Mouse 7	3.45	1.02
Mouse 8	3.3	1.024
Mouse 9	2.2	0.308
Mouse 10	4.19	1.08
Mean	3.131	0.8649
Std.Deviation	0.7351	0.3199
Variation Coefficient	23.48%	36.99%
Correlation coefficient (r)	0.8216	

Table 5.4: The SUVs for FDG and ^{13}N - NH_3 rest scans in healthy mice. The values were derived from averaging the VOIs of the LV during the whole duration of the dynamic scans. The correlation value between the two SUVs group was 0.8216, indicating a good positive correlation.

5.7 Discussion:

5.7.1 Standard protocol analysis:

Several attempts have been made to quantify MGM and MBF in various murine models using micro-PET imaging. However, there is still a lack of standard PET imaging protocols to quantify these biomarkers in mice. In this chapter, the concept of compartmental modelling along with micro-PET imaging was used to develop, standardize, and validate imaging protocols in a healthy murine model. It is important to emphasize that these protocols were designed based on the previous investigations that have handled one or multiple challenging aspects in mice PET imaging by applying different experimental conditions. The applied protocols were designed to ensure optimal accuracy and repeatability while maintaining the least methodological complexity.

Our results of MGM and MBF, in adenosine rest and dobutamine groups, were repeatable and comparable to the scans obtained using MRI or electrocardiography imaging (Raheer et al. 2007; Jogiya et al. 2013b; Naresh et al. 2015). In later sections, both MGM and MBF will be discussed separately and with more detail.

Mice are sensitive to changes in the surrounding environmental conditions, it was critical to standardize the imaging protocols to minimize any variation that might originate due to the lack of consistency. Studies showed that mouse metabolism and blood flow are susceptible to any source of stress thus, this was minimized by allowing one week for mice to rest following delivery (Fueger et al. 2006; Prior 2017; McDougald et al. 2020). The scanning protocols were designed to align with our project animal license, which only allowed only one non-recovery imaging session per mouse, thus scanning over multiple days was not possible. This led to the idea of performing three scans in a row considering the half-life of the radiotracers and any other injected drugs and the duration of their effects.

The scanning began with standardizing the general animal handling variables including, temperature, fasting and anesthesia. Fasting for one hour is recommended to increase the uptake of the glucose. The use of anesthesia was essential to scan the mouse, but it might introduce another source of variation or errors if adjusted differently in each scan (Hildebrandt et al. 2008). Previous studies demonstrated an improvement in ^{18}F -FDG uptake in fasted and warm mice (Fueger et al. 2006; Hildebrandt et al. 2008). Consequently, on the day of the scanning, each mouse was warmed and fasted (before one hour and extra half an hour during the scan before FDG injection) to ensure maximum uptake of the ^{18}F -FDG. In addition, the choice of anesthesia has a significant impact on the

metabolism and perfusion of the mice myocardium (Hildebrandt et al. 2008). In our protocols, the anesthetic agent given was isoflurane at 1-2% v/v, which should minimally alter MBF.(Kober et al. 2005).

Importantly, mice could only handle a limited injected volume, thus, increasing the total injected volume might interfere with the body hemostasis of the mouse (Kuntner et al. 2009; Thackeray et al. 2015). (Lindsey et al. 2018). Therefore, two cannulation routes were prepared, including the IV route to inject the radiotracers and the IP route to inject the pharmacological stressing agent.

One tissue compartmental (1TC) model was the best fit with the mechanism of ammonia uptake. Ideally, the application of 1TC model should have been formally tested, as it may vary between species and experimental set-up. In our case, we have tested this model using our standardized imaging protocol settings before applying it in all our mice and then compared the MBF results with the literature which revealed a comparable result of MBF in mice with other MBF results produced by the MRI and microspheres. It is the simplest model, which consists of two-compartments, namely blood and cardiac compartments (Choi et al. 1999). The metabolite percentage in ammonia extraction was reported to be negligible by several studies in the early duration of the dynamic scan (Choi et al. 1999). Importantly, for the IF measurements, which were derived based on our dynamic images, LVBP VOI were created from placing a VOI in the LV blood pool region, and the LVBP VOI was convoluted with the PSF of the scanner as well as corrected for PVE and spill-in using the RV VOI (Huang et al. 2019). Notably, this approach was verified by several previous studies and showed similar results when also using the inferior vena cava region to correct for PVE and spill-in activity within the same scan and mouse (Fang and Muzic 2008; Huang et al. 2019). The VOI of the myocardium was over the LV region, and it's the largest chamber of the heart. In our 1TC model, the MBF over the whole LV is assumed to be uniform (Chang et al. 2020). However, in our data analysis, there was slight variation within the different LV regions generated, but this was expected due to the small size of the mouse heart and the limited SR of the system that generates spillover and PVE. Consequently, the images were reconstructed using the iterative reconstruction method while applying attenuation and scatter corrections to maintain maximum SR.

PMOD was the software of choice, and it allows a variety of compartmental modelling options. For our ammonia scans, two models were used, including 1TC (DeGrado) and 2TC models, to quantify MBF and ammonia trapping, respectively. The main difference between the two models was the timing from which the LV VOIs were extracted. The 1TC (DeGrado) model only considers the first 2-3 minutes for the ammonia perfusion estimation, while the other 2TC model considers the last

15-20 minutes of the dynamic scan duration. The DeGrado model was applied to avoid the metabolite build-up, though Choi and his co-worker (Choi et al. 1999) reported negligible metabolite amounts in ammonia clinical studies. No previous literature was found regarding measuring the metabolite percentage interference during ammonia scan in mice; thus, 4 minutes was the best option to accurately represent the MBF.

The MBF values during dobutamine stress were higher than the rest ones as expected. Visual interpretation and comparison between the two scans within each mouse also confirm a rise in the radioactivity concentration in the heart, considering sufficient time were allowed between the two scans to allow for ammonia to decay. However, no increase in MBF values was reported in our scans following the administration of adenosine.

For ^{18}F -FDG scans, the scans were 40 minutes duration because it has been reported by several investigations that FDG reaches the equilibrium state within 40 minutes (Cussó et al. 2014; Fischer et al. 2021b). Since FDG can be metabolically trapped or not trapped, the 2TC model was applied. Note that the compartment does not mean a physical entity; however, it describes the state of the radiotracer (Bertoldo et al. 2014).

5.7.2 MBF quantification:

A comprehensive understanding of the influence of genes, proteins and different metabolic pathways is a crucial aspect that explains the close connection between cellular level processes and the health state of the organ of interest and the whole animal body (Krueger et al. 2013). This integrated understanding, for example, of how genes work or how metabolic pathways might reflect the general health state and disease conditions, can be achieved through the assessment of many physiological biomarkers, one of which is MBF (Krueger et al. 2013). Animal models have been used extensively to generate structural and physiological information about normal or pathological conditions that obtainable in humans to facilitate the correlation of research findings between clinical and preclinical studies. Importantly, the evaluation of new treatments for CVDs can also benefit from the ability to monitor changes in biomarkers through scanning small animals repeatedly and non-invasively (Krueger et al. 2013).

The myocardial blood flow is an important physiological biomarker because any reduction in its value may precede disease onset (Krueger et al. 2013). There were several validation studies to assess MBF in mice using microspheres, open chest Doppler perfusion imaging, MRI, and echocardiography (Kober et al. 2005; Makowski et al. 2010; Krueger et al. 2013; Phoon and Turnbull 2016). All the previous modalities do not provide absolute quantification of MBF; however, micro-PET imaging

allows quantitatively assessment MBF in mice through compartmental modelling (Sharp et al. 2005; Herrero et al. 2006). In addition, the various image acquisition options in micro-PET imaging also provide an evaluation of temporal changes of the physiological biomarker of interest, which can predict disease onset or assess the response to a new therapy (Herrero et al. 2006).

Several PET perfusion tracers, such as ^{15}O -water, ^{82}Rb , ^{11}C -acetate and ^{13}N - NH_3 , are used in conjunction with well-validated compartment models (Choi et al. 1999; Morris et al. 2004). In this research, ^{13}N - NH_3 was used to measure quantitatively MBF in rest and stress conditions using Mediso micro-PET/CT scanner and compartmental modelling. Indeed, this chapter has mainly focused on developing PET imaging methodologies in mice for CVS assessment, a better understanding of substrate metabolism and MBF, and their baseline values in case of different physiological states. To achieve this, previous cardiac PET methodologies that were used in clinical and preclinical research were reviewed to apply the optimal choice in mice.

^{13}N - NH_3 is a PET perfusion radiotracer used to assess regional blood flow in tissue in clinical and research studies. Following the injection, ^{13}N - NH_3 , in its nonionic form, diffuses freely through the cell membrane with a high extraction fraction (about 80%-90%) and a diffusion rate that is proportion to myocardial tissue blood flow, as explained in detail by previous studies (Walsh et al. 1977; Krivokapich et al. 1982; Ziessman et al. 2014). Therefore, it is one of the optimal radiotracers for the accurate representation of MBF (Krivokapich et al. 1982; Ziessman et al. 2014; Nkepan et al. 2019). After extraction, its cellular localization is not entirely explained, but previous evidence suggested that it converted to an ionic ammonium ion, which is a relatively impermeable cation to the cell membrane (Walsh et al. 1977). Therefore, ammonium does not diffuse back to the blood pool and become metabolically trapped, simplifying the compartment model. The backflow to the blood compartment could be assumed small or negligible (Krivokapich et al. 1982; Nkepan et al. 2019). The ammonium ion (NH_4^+) is involved in many metabolic pathways in various body organs such as the heart, liver, and kidneys (Walsh et al. 1977; Krivokapich et al. 1982). In muscle, as in the case of the heart, NH_4^+ plays a role in glutamine synthesis and is converted to glutamate, which is then transported via the bloodstream to the liver for further metabolism and excretion; thus, high liver uptake is something expected and was reported in later images of our scans (Walsh et al. 1977; Krivokapich et al. 1982; Nkepan et al. 2019). Consequently, only the first 5 minutes of the dynamic scan were used in our blood flow measurement, although the scan duration was 20 minutes. PMOD software, using the kinetic tool, allows the users to choose the dynamic duration for the generated TAC of the myocardium.

It is evident from our data in the table 5.2 that the measurements of MBF at rest and dobutamine stress, assessed by Mediso micro-PET using $^{13}\text{N-NH}_3$ in mice, is accurate and repeatable with good correlation with other obtainable data from microspheres and MRI imaging (Raheer et al. 2007; Jogiya et al. 2013b; Naresh et al. 2015). The imaging was performed using an isoflurane concentration of less than 2% to prevent the rise in MBF reported by Kober et al. (Kober et al. 2005) when raising the isoflurane concentration to 2% or more. In fact, most anesthetic agents are known to trigger slight coronary vasodilation if their concentration is not maintained carefully, but to a lesser extent when compared to the vasodilator dobutamine (Croteau et al. 2004). Clearly, our PET imaging cannot be performed without the use of anesthesia; thus, their influence cannot be avoided but can be controlled by the anesthetic type and its concentration.

At rest, MBF values ranged 4.11-7.99 ml/g/min with a significant increase reaching 10.71 – 15.78 ml/g/min following bolus IP injection of dobutamine as a pharmacological stress agent (Kober et al. 2005). The IP route was mainly used to avoid injecting intravenously large volumes that interfere with the hemodynamics of the animal (Kober et al. 2005). In addition, our rest and stress imaging protocol indicated that the vasodilation of the coronary arteries, which was initiated by dobutamine, can be identified by micro-PET in mice. Dobutamine is an inotropic agent that activates the β_1 -adrenergic receptors agonist, which subsequently raises the HR and the intensity of contraction (Croteau et al. 2004; Croteau et al. 2014). Generally, it has been demonstrated that the pharmacological stress agent, such as dobutamine, is valuable for detecting and assessing the severity of the ischemic event and monitoring response to treatment intervention under different blood flow rates (Rust et al. 2006). The recorded differences between rest and stress $^{13}\text{N-NH}_3$ scans using dobutamine were statistically significant, with a p-value of 0.0001, revealing that our imaging protocol could detect temporal differences in the blood flow.

On the other hand, we didn't report any effect of adenosine to induce a hyperemic response in the myocardium, and this was also reported previously by Kalkan et al. (Kalkan et al. 2010), but MBF values during both rest and stress scans were repeatable. Even though adenosine is known to control the CBF and has vasodilatory effects in most vessels among mammalian species, we haven't reported increase in the MBF (Berne 1963; Mubagwa et al. 1996; Jackson et al. 2018). Importantly, we have recorded a decrease in the HR following the infusion of adenosine which was consistent with several studies that indicated its influence on slowing the heart rhythm and decreasing blood pressure (Zhao et al. 1997; Fromonot et al. 2016; Jackson et al. 2018).

Importantly, the MBF measurement in mice is not a simple process in the way that it requires careful management to sources of variability and errors. As described previously, several challenges were associated with mice imaging with respect to the imaging system, radiotracer of choice, the applied imaging protocol, reconstruction, and compartmental modelling.

To begin with, MBF measurement requires high temporal and spatial resolution to generate images and subsequent TACs that genuinely represent the arterial input function, cardiac extraction, and uptake of the radiotracer. Moreover, the detection of MBF changes under two physical conditions requires a high temporal resolution of the PET scanner, which was achieved using a Mediso scanner with a temporal resolution of 1.2 ns.

The fast heart rate and the small size of the mice LV were other challenges that were tackled to the best of our ability and knowledge. As reported by the Mediso scanner manufacturer, the SR with the iterative reconstruction method is 0.7 mm. However, the type of the injected radiotracer also affects the SR level because each tracer has its own positron range that adds more blurring to the images. To evaluate the SR for the used tracers, we assessed the scanner performance and calculated the RCs in different rod sizes using ^{18}F -FDG and ^{13}N - NH_3 . Although the two radiotracers have a different half-life, the timing of image acquisition in the performance assessment test was the same for both radiotracers to be consistent with NEMA standard evaluation, which uses ^{18}F -FDG as a reference radiotracer. The ^{18}F -FDG images produce good SR images, but in the case of ^{13}N - NH_3 , the images had relatively lower SR, which was expected as we didn't consider the half-life. Consequently, ^{13}N - NH_3 images can be significantly improved by injecting a higher dose. This was done by injecting a higher ammonia dose-ranging 30 ± 2 MBq to compensate for the loss in counts and improve the image quality. After scan completion, the images were reconstructed with IR for maximum possible resolution as recommended by the Mediso manufacturer and applied all the corrections, including attenuation and scatter corrections.

The compartmental modelling first requires the knowledge of IF to calculate the kinetic rate constant as in figures 5.5-5.8. Several studies have described the type of compartment models that can be applied when using ammonia (Kuhle et al. 1992; Muzik et al. 1993; Choi et al. 1999). Even though each applied compartment model tackles different problems related to ^{13}N - NH_3 and PET systems, all agree with a basic model configuration consisting of two compartments (Muzik et al. 1993; Choi et al. 1999). Compartment one is the blood plasma compartment or IF, which represents ammonia concentration in the arterial blood, while compartment two reflects the cardiac compartment through which ammonia is freely diffusible, as illustrated in figure 5.7 (Muzik et al. 1993; Choi et al. 1999).

Other ^{13}N -ammonia compartment models configurations involve a third compartment that describes the metabolically bound ammonia in the form of ^{13}N -glutamine within the cardiac tissue.

Several lines of evidence have justified that 1TC model for MBF quantification in which the data are derived from the first few minutes of the dynamic scan while disregarding the rest of the dynamic duration (Choi et al. 1993; Muzik et al. 1993; Choi et al. 1999; Carli et al. 2000). In fact, by only considering the first few minutes to measure MBF, the metabolite percentage and its correction can be neglected, as suggested by many studies (Choi et al. 1993; Choi et al. 1999). In addition, Croteau et al. (Croteau et al. 2004) demonstrated that both metabolites and the cardiac to blood spillover occurs in the later dynamic frame thus they have a minor effect on our MBF values which were derived from the first 5 minutes of our applied model (1TC) model.

Describing the kinetics of ammonia in the DeGrado (1TC) model can be done mathematically using first-order differential equations in which rate constants are used to describe the tracer kinetics between compartments as in figure 5.7 and equation.1. In 1TC, which is the case in the DeGrado model, the rate constants K_1 (mL/min/g) reflect the MBF; in contrast, K_2 (min^{-1}) represents the MBF/V in which V is the volume distribution of ammonia in free space (Choi et al. 1999).

5.7.3 MGM quantification:

This section aimed to assess the Mediso micro-PET scanner's ability and the concepts of compartmental modelling of ^{18}F -FDG to quantify MGM to generate baseline quantitative and repeatable data among healthy mice. In addition, the myocardial glucose uptake was assessed using SUV and was compared to the ^{13}N -ammonia uptake values in the next section.

Our MGM results in the table 5.3 produced from healthy mice using ^{18}F -FDG demonstrated the ability to generate repeatable and quantitative glucose metabolism results by integrating the Mediso micro-scanner with the 2TC model. Notably, data were comparable to results reported in mice by Wu and his colleagues using the ^{18}F -FDG and 2TC model (Wu et al. 2007). Furthermore, both uptake images produced from ^{18}F -FDG, and ^{13}N -ammonia were strongly correlated ($r= 0.8264$), indicating the ability to use the uptake images generated from the SUV method as other methods to validate the compartmental modelling techniques, especially when comparing treatment within different animal groups.

The myocardial metabolic pathways are highly flexible and complicated and they can use all types of energy substrates, mainly FAs and glucose, for energy production that is important for cell function and contractility (Simões et al. 2004). Moreover, recent investigation reported an increase in the glycolytic flux to cope with the higher energy need during pathological events such as hypertrophy or

heart failure (Schönekeess et al. 1995; Depré et al. 1998; Simões et al. 2004). In addition, stimulation of the glycolysis process appears to play a protective role during acute ischemic events and myocardial infarction (Vanoverschelde et al. 1994; Kudej et al. 2002). These previous findings justify the importance of exploring the MGM of the heart besides its direct importance in developing new therapeutic interventions (Simões et al. 2004).

Therefore, it is widely accepted that MGM quantification can be used as a biomarker to reflect myocardial viability and function. The assessment of myocardial viability with PET imaging includes the measurement of MBF and metabolic activity by using two radiotracers. Consequently, PET imaging protocols usually involve injecting ^{18}F -FDG for MGM evaluation as well as flow tracers to detect myocardial infarction or irreversible defect. Accurate differentiation between viable (reversible) and nonviable (irreversible) myocardium has crucial diagnostic value regarding the decision of surgical intervention or assessing the severity of CADs and LV dysfunction.

Importantly, it has been demonstrated by previous papers that the uptake of the FDG is significantly affected by many factors, including type of anaesthesia, dietary state, and ambient temperature, as previously discussed. Fueger et al. (Fueger et al. 2006) had reported an increase in ^{18}F -FDG when mice were kept fast and warm and anaesthetized using isoflurane concentration between 1-2%. Therefore, these technical parameters were applied in which mice were kept fasted (1 hour) and warmed (1 hour) with isoflurane concentration in the recommended range. These parameters were standardized in all the scanning processes to eliminate any source of variability induced by technical factors.

5.8 Conclusion:

The results of this chapter confirm the accuracy and repeatability of non-invasive measurements of MGM and MBF in mice with ^{18}F -FDG and ^{13}N - NH_3 , using micro-PET imaging and quantification methods, including compartmental modelling and SUV. The compartmental modelling method is a comprehensive method for describing physiological functions, but it is methodologically and mathematically more complicated certainly in mouse imaging. In contrast, SUV analyses are simple to implement; however, they might not provide a profound insight into physiological biomarkers. Both quantification methods have been applied and showed a good correlation between the two radiotracers results with the ability of compartmental modelling to measure quantitatively regional MBF and glucose. The applied imaging protocols were based on previous clinical and preclinical investigations in which choices were made to produce as much information as possible with minimum complexity and the

simplest possible assumptions. Additionally, our findings indicate that, among the different compartment models available in PMOD software, our pilot studies results indicated that preference should be given to two-tissue compartment and Degrado models for MGM and MBF measurements, respectively. Our data were also accurate when compared to the MGM and MBF, produced either by other imaging modalities or different imaging protocols.

In conclusion, Our Mediso micro-PET/CT scanner is able to evaluate the murine cardiac function through MBF and MGM in which the data were accurate and repeatable. Importantly, we have successfully developed baseline imaging protocols that could be applied to different disease models or conditions to evaluate therapeutic strategies for treating different CVDs. In next chapter, these developed protocols will be further validated using HLI model.

Chapter 6:

The ability of the Micro-PET/CT system to detect metabolic and blood flow changes in the HLI model

6.1 Introduction:

Peripheral arterial diseases (PADs) are one of the main causes of morbidity and mortality in the world (Niiyama et al. 2009; Campia et al. 2019; Zemaitis et al. 2022). They are characterized by a decrease in the arterial perfusion in the lower extremity (Niiyama et al. 2009; Campia et al. 2019; Zemaitis et al. 2022). The decrease in blood perfusion is mostly caused by atherosclerotic plaque formation which narrows the arterial lumen wall leading to a reduction in the blood supply or ischemia (Zemaitis et al. 2022). However, there are other causes of PADs which could be blood vessel inflammation, injury, radiation exposure, or any other CVDs. PADs have a group of risk factors such as obesity, high blood pressure, DM and increasing age (Zemaitis et al. 2022). Diagnosing PADs has had a great clinical impact as it is often considered to be a marker for the onset of atherosclerosis. There are different treatment choices available for PADs, which, depending on the severity of the disease, might include a change in lifestyle or pharmacological, endovascular or surgical interventions.

The murine model with induced hindlimb ischemia (HLI) has been used widely to test new approaches to therapies, such as therapeutic angiogenesis, stem cell therapy or gene therapy. The induction of HLI in mice often involves the ligation of the femoral or iliac arteries, both of which have easy surgical access with a low mortality rate (Niiyama et al. 2009). There are a variety of modalities available for assessing the blood flow in HLI and monitoring the recovery process following treatment (Kochi et al. 2013). Moreover, the assessment of HLI is usually performed using a combination of imaging modalities and molecular and histological tests, each of which has its own advantages and disadvantages (Orbay et al. ; Paek et al. 2002; Niiyama et al. 2009).

CVDs have a major impact on both the heart and vascular components, thus studying vessel growth mechanisms and their potential repair could be a fundamental aspect in testing the efficiency of treatment (Niiyama et al. 2009; Tsatralis et al. 2016). The growth of new blood vessels involves

vasculogenesis, angiogenesis and arteriogenesis (Swift et al. 1999; Dikici et al. 2020). Both angiogenesis and arteriogenesis are vital mechanisms that respond to pathological conditions for adaptation and regeneration purposes of the infected tissue (Dikici et al. 2020).

In clinical settings, the HLI could be assessed by Doppler ultrasonography, contrast angiography, and various molecular imaging techniques (Orbay et al. ; Paek et al. 2002; Hoinoiu et al. 2019). In preclinical studies, the HLI is often evaluated using laser Doppler perfusion imaging (Orbay et al. ; Peñuelas et al. 2007; Niiyama et al. 2009). Doppler imaging is only able to measure blood flow superficially, thus it could be a reliable tool in assessing subtle changes in blood flow (Gill 1985), however, it remains an inadequate tool for the estimation of changes in blood flow or for monitoring an angiogenesis process (Niu et al. 2019). Both high resolution MRI imaging and nuclear imaging could be a promising tool for an in-vivo assessment of the perfusion in a tissue or organ (Englund and Langham 2020). MRI imaging provides a good spatial resolution including the morphological and functional representation of the peripheral arteries without the need of radiation; but it is an expensive option (Englund and Langham 2020). On the other hand, nuclear medicine techniques such as SPECT and PET imaging are noninvasive imaging modalities that could be used to detect ischemic events, abnormal changes in blood flow at a molecular level in an early stage (Orbay et al. ; Hoinoiu et al. 2019). The great development in the spatial resolution of the small PET/CT scanner has helped in providing more reliable and accurate in-vivo studies of small animal imaging with different diseased models, resulting in an easier translation of experimental trials between different species.

Accordingly, in this chapter, we aim to evaluate the ability of our Mediso micro-PET/CT scanner to assess blood flow and detect changes following HLI induction.

6.2 Objectives:

- Assess the ability of our micro-PET/CT scanner to detect blood flow changes following surgical HLI.
- Compare our PET results with both the Doppler imaging and histological data.

6.3 Materials and methods:

All procedures are approved by the British Home Office and Bristol University (Project License PPL 30/2911) using the Care and Use of Laboratory Animals Guide (The Institute of Laboratory Animal Resources, 1996). The surgical operations were carried out in Bristol Medical School, Translational Health Sciences (Bristol Heart Institute), University of Bristol (UOB).

6.3.1 The animals:

Four healthy male mice C57BL/6 aged about 8 weeks (body weight 20–30 g), were obtained from Charles River which is one of the main Cardiff and Bristol university suppliers. The option of using healthy mice for the induced HL model was an appropriate choice as it created a baseline study without any ageing or pathological conditions which would have added other degrees of complexity to this study.

6.3.2 Animal preparation and surgical HLI induction:

The surgical HLI induction was performed by one of the research group members in Bristol university and not by the researcher who had only observed the surgical procedures. Prior to each HL surgery, the heating pad was set to 37 °C and a nose cone tube was connected to an isoflurane vaporizer to ensure a continuous flow of anaesthetic gas. On the other side of the operation room, there was another anaesthesia system including an oxygen cylinder, induction box, scavenger, isoflurane liquid and vaporizer. Each mouse was placed in the induction box with an oxygen flow of 1 L/min and isoflurane percentage of 1 - 2%. Before being transferred to the surgical bench, each mouse was tested to ensure it was anesthetized completely. It was then moved to the Doppler imaging panel for a blood flow assessment prior to surgery. The mouse was finally moved to the surgical bench, applying ophthalmic lubricant to both eyes to prevent dryness. Isoflurane was set to be between 1.5-3% and hair was removed from the left leg using hair removal cream.

6.3.2.1 Induction procedures:

An initial incision was made in the abdomen moving downwards to the center of the medial left thigh using fine scissors and a scalpel. A retractor was inserted and pulled out to expose the ligation site. For the acute HL induction, a transaction was performed for the left proximal femoral artery using a 7 – 0 thread suture under the artery and then the artery was ligated. After that, a second transection and ligation were performed 1mm distally from the proximal point of the left femoral artery. The incision was closed later using interrupted 5 - 0 vicryl sutures. Finally, a post-surgery Doppler imaging was performed on Day 0, Day 3, and Day 7.

As advised by the UOB National Veterinary Services (NVS), the four mice were housed individually to avoid them fighting following HL surgery and not due to toe checking requirements. Thus, they were placed separately in four normal cages with an environment of a 12-hour light-dark cycle and daily monitoring of temperature and humidity. They were supplied with water and food. In addition

to that, their appearance, clinical signs, unprovoked behaviour, and behaviour responses to external stimuli were all monitored daily after IHL surgery.

6.3.3 The doppler imaging:

The doppler imaging was performed by one of the research group members in Bristol university and not by the researcher who had only observed the doppler imaging procedures. The mice were positioned in dorsal decubitus, anaesthetised with 4% isoflurane induction dose which was then reduced to 1.5-2% maintenance dose and oxygen with 1L/min. During doppler imaging, the mice were maintained at 36°C temperature to prevent hypothermia. The mice were shaved prior to ligation procedure. The doppler acquisition required 5 minutes under anaesthesia per each mouse. We allowed 10 minutes following induction dose of anaesthesia to avoid unstable body temperature which might affect the blood flow readings.

Doppler was performed using the moorLDI2 laser Doppler blood flow imager (Moor Instruments, Millwey Rise Industrial Estate, Weycroft Ave, UK). The laser source was moorLDI2-VR; 633nm wavelength, 1.2mm beam using the high resolution of 0.05 mm/pixel and scan speed of 4ms/pixel. The Doppler imaging is based on the principle of the doppler effect, in which the laser interacts with red blood cells and is translated as coloured dots in the computerized image with a chromatic scale ranging from blue to red which represent poor and good blood flow respectively and expressed in Volts. The blood flow values were calculated from the generated image through drawing ROIs in the hindlimb region and then the mean of the signal in the ROI was measured.

After completing the Doppler imaging on Day 7, mice were transferred to Cardiff university for PET/CT imaging.

6.3.4 The micro-PET/CT scanner:

The Mediso Nano-Scan 122S small-bore PET/CT imaging system manufactured by the Mediso medical imaging system, Budapest, Hungary. All the scanner specifications are described in the methodology chapter.

6.3.5 Radiotracers:

In this chapter, two radiotracers were used, ^{18}F and ^{13}N , to quantify glucose uptake and blood flow (MBF) respectively in both legs.

6.3.6 PET/CT imaging protocol:

The four mice were transferred to the animal facility in Cardiff university within one week after surgery. PET/CT imaging was carried out a week to prevent discomfort or any stress conditions for the animals. The scanning and termination procedures were carried out over two days (two mice per

day) with the same imaging protocols and considerations standardised in chapter five. The imaging scans include 10-minute $^{13}\text{N-NH}_3$ rest scan, 10-minute dobutamine $^{13}\text{N-NH}_3$ stress scan, 40 minutes $^{18}\text{F-FDG}$ scan and then termination of the mouse. The total PET/CT scanning time for each mouse was approximately 35-45 minutes.

6.3.7 Culling, tissue collection and histological analysis:

The mice were then culled with an euthatal injection via the IV cannula and death was confirmed by cervical dislocation or onset of rigor mortis prior to the dissection process. Muscle collection was carried out to investigate arterial supply and necrotic events in the HLI leg and to compare them to the healthy leg. Thus, following termination, the mice were dissected in order to collect the muscles, including the gracilis and adductor muscles, from each leg. The dissected muscles were then dropped and fixed separately in 4% PFA, which is a fixative compound that fixes tissue by cross-linking proteins. The muscle samples were kept at laboratory temperature (around 20° C) in the PFA solution for 24 hours which was then replaced with normal PBS and kept at 4° C (in the fridge) for further histological analysis. Immunohistochemistry staining was performed to quantify the capillary and arteriole density in each muscle tissue using isolectin GS-IB4 (IB4, I21414, Life Technologies, USA) and specific antibody anti- α -smooth muscle actin (α SMA; C6198, Sigma, UK) as explained in the methodology chapter. Following staining, the sections were analysed using optical or fluorescence microscopy (Zeiss Axio observer microscope, Cat # 1026044910, Germany). The staining with green colour (488 emission) lectin binding representing the capillaries, and red (Cy3 emission) α SMA staining identifying the arteries. All fields were saved in TIF (Tagged image file) format in an external hard drive-in order to be analysed with Image J software as explained in the methodology chapter.

6.3.8 PET image reconstruction and analysis software:

PET images were reconstructed with Mediso's Nucline NanoScan reconstruction software (v 3.04.010.0000) using the Tera-Tomo 3D reconstruction algorithm with four iterations and six subsets, on 0.4 mm isotropic 3D voxel grids and an energy-window of 400-600 KeV. Next, the images were imported to PMOD to carry out quantitative analysis. The analysis was divided into three sections which include:

- The measurement of the blood flow in both legs during rest and stress conditions, and the data were compared to confirm the state of stress using the $^{13}\text{N-NH}_3$ scans and 1TC model.
- The blood flow data was compared in the normal and ligated legs.
- The glucose uptake was measured in both legs using the $^{18}\text{F-FDG}$ and SUV tool.

- PET data was directly compared with both the Doppler imaging and histological data through performing the correlation test and calculating the correlation factor (Pearson r coefficient).

6.3.9 Statistical analysis:

Statistical analyses were conducted using GraphPad Prism (version 9.4.0, USA), through which data were represented with their individual values, mean and STD. After testing for normality, comparisons were generated using Student's *t*-test. Differences were considered significant when $p < 0.05$. To assess the relation between the parameters produced with different imaging or tests, the correlation Pearson coefficient (*r*) was used in which values between 0.5-1 reflects good positive correlation.

6.4 Results:

6.4.1 Doppler imaging results:

The surgical ligation of the HL was completed for all mice with no adverse effects. Laser Doppler imaging was performed for all mice prior and post-surgery, including day 0, day 3 and day 7. The blood flow values for both legs in all mice were illustrated in table 6.1, including the blood flow ratio between the two legs. In Figure 6.1, the pre-surgery images for both legs, showed a good blood flow with red colour. After ligation, there was significant decrease in the blood flow in the ligated (L) leg compared to the normal (N) leg as in table 6.1 and figure 6.1. In figure 6.2, there was a significant decrease in blood flow of the ligated leg at day 7 compared to the normal one with $p < 0.005$.

6.4.2 PET Results:

The table 6.3 shows the rest and stress blood flow values measured in both hindlimb using $^{13}\text{N-NH}_3$ and 1TC model in Pmod. There was a significant decrease in the blood flow between the ligated leg compared to normal leg with $p < 0.0001$ as in figure 6.2, which confirm the state of ligation. In addition, there was a statistical difference between rest and stress scan in the normal legs which confirmed the effect of the pharmacological stress agent as in figure 6.3. However, there was no considerable increase in the blood flow in the ligated leg as in figure 6.4.

Furthermore, semi quantification of the SUVs in both legs was performed using $^{18}\text{F-FDG}$ scans after averaging the dynamic scan to generate a static image. The SUVs for both legs are illustrated in table 6.4. A comparison between the blood flow (at rest) and the calculated glucose uptake in both legs revealed the presence of good correlation between the blood flow ($^{13}\text{N-NH}_3$) and the glucose uptake ($^{18}\text{F-FDG}$) in both normal and ligated legs with correlation Pearson coefficient $r = 0.93$ and 0.67 respectively as in figure 6.5-6.6.

Mouse ID	Time of the doppler imaging	Left leg Flow velocity (ligated leg) ml/min	Right leg Flow velocity (normal leg) ml/min	Blood flow ratio (Lf leg/Rt leg)
AA01	Pre-surgery Day 0	1435.8	1292.2	1.111
	Post-surgery Day 0	123.4	2146.2	0.057
	Post-surgery Day 3	218.6	1754.9	0.124
	Post-surgery Day 7	156.4	1228.1	0.127
AA02	Pre-surgery Day 0	1098.8	949.4	1.157
	Post-surgery Day 0	68.8	2046.9	0.034
	Post-surgery Day 3	219.2	986.5	0.222
	Post-surgery Day 7	401.8	2069.4	0.194
AA03	Pre-surgery Day 0	763.4	828.9	0.9210
	Post-surgery Day 0	101	1718.8	0.059
	Post-surgery Day 3	180.6	1271.1	0.142
	Post-surgery Day 7	259.7	1016	0.255
AA04	Pre-surgery Day 0	1264.5	1551.8	0.815
	Post-surgery Day 0	100.9	2726.7	0.037
	Post-surgery Day 3	220.2	1102.7	0.199
	Post-surgery Day 7	297.4	1067.3	0.278

Table 6.1: The blood flow and blood flow ratio for both legs in all mice pre- and post-surgery at Day 0, 3, and 7. The flow in the left leg was reduced following surgical ligation.

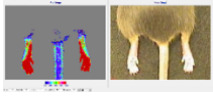
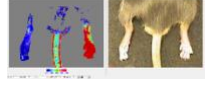

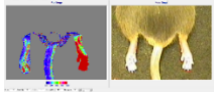
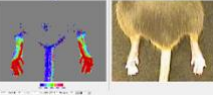
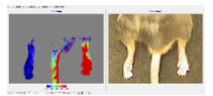
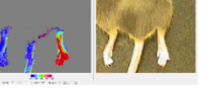


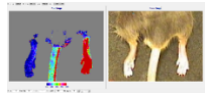


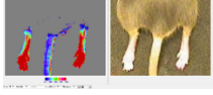
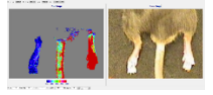


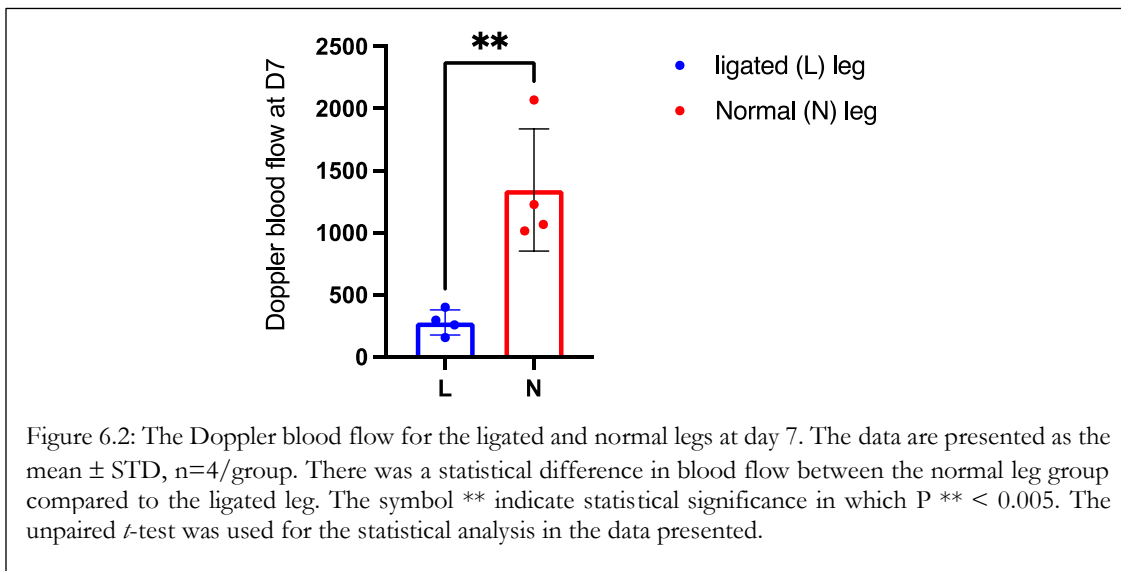
Mouse ID	Pre-surgery	D0	D3	D7
AA01	 Both normal	 L vs N	 L vs N	 L vs N
AA02	 Both normal	 L vs N	 L vs N	 L vs N
AA03	 Both normal	 L vs N	 L vs N	 L vs N
AA04	 Both normal	 L vs N	 L vs N	 L vs N

Figure 6.1: Demonstration of Doppler repeated scans for the four mice during Day 0,3 and 7. Perfusion signal which appeared in red colour represents good blood flow, while the blue colour represents the poor blood flow. The mouse is placed in dorsal recumbency. It visible that the ligated (L) leg in all mice had significant decrease in the blood flow following ligation at D0. The normal (N) leg showed good blood flow perfusion with red colour in all mice.



Mice ID	Physical condition	Blood flow	Blood flow
		(ml/min/g) Lf Leg Ligated leg	(ml/min/g) Rt Leg Normal leg
AA01	Rest state	0.26	4.01
AA02		0.35	4.34
AA03		0.43	4.9
AA04		0.45	5.9
AA01	Stress state	0.32	9.5
AA02		0.06	10.1
AA03		0.90	12.88
AA04		0.51	13.7

Table 6.2: The blood flow values (ml/min/g) for both legs using $^{13}\text{N-NH}_3$ and ITC.

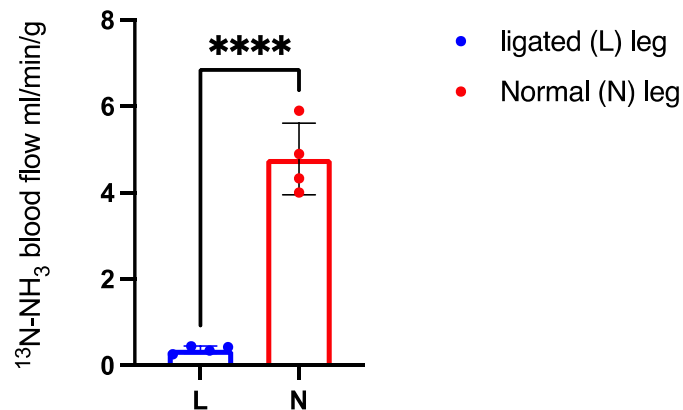


Figure 6.3: The $^{13}\text{N-NH}_3$ resting blood flow values (ml/min/g) for the ligated (L) and normal (N) leg. The data are presented as the mean \pm STD, $n=4$ /group. There was a statistical difference in blood flow between the normal leg group compared to the ligated leg. The symbol **** indicate statistical significance in which $P^{**} < 0.0001$. The unpaired t -test was used for the statistical analysis in the data presented.

Mice ID	SUVs using FDG scan	
	Rt normal Leg	Lf ligated Leg
AA01	28	12
AA02	26	17
AA03	31	14
AA04	36	19

Table 6.3: The calculated SUVs for both legs using $^{18}\text{F-FDG}$ scans.

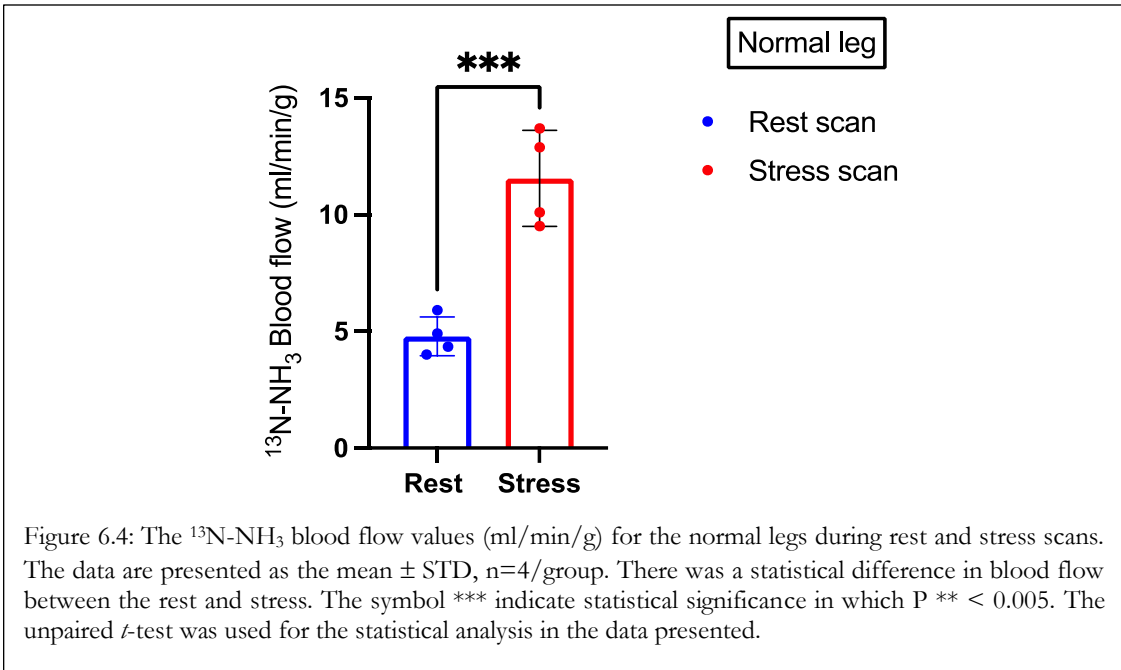


Figure 6.4: The $^{13}\text{N-NH}_3$ blood flow values (ml/min/g) for the normal legs during rest and stress scans. The data are presented as the mean \pm STD, n=4/group. There was a statistical difference in blood flow between the rest and stress. The symbol *** indicate statistical significance in which $P < 0.005$. The unpaired *t*-test was used for the statistical analysis in the data presented.

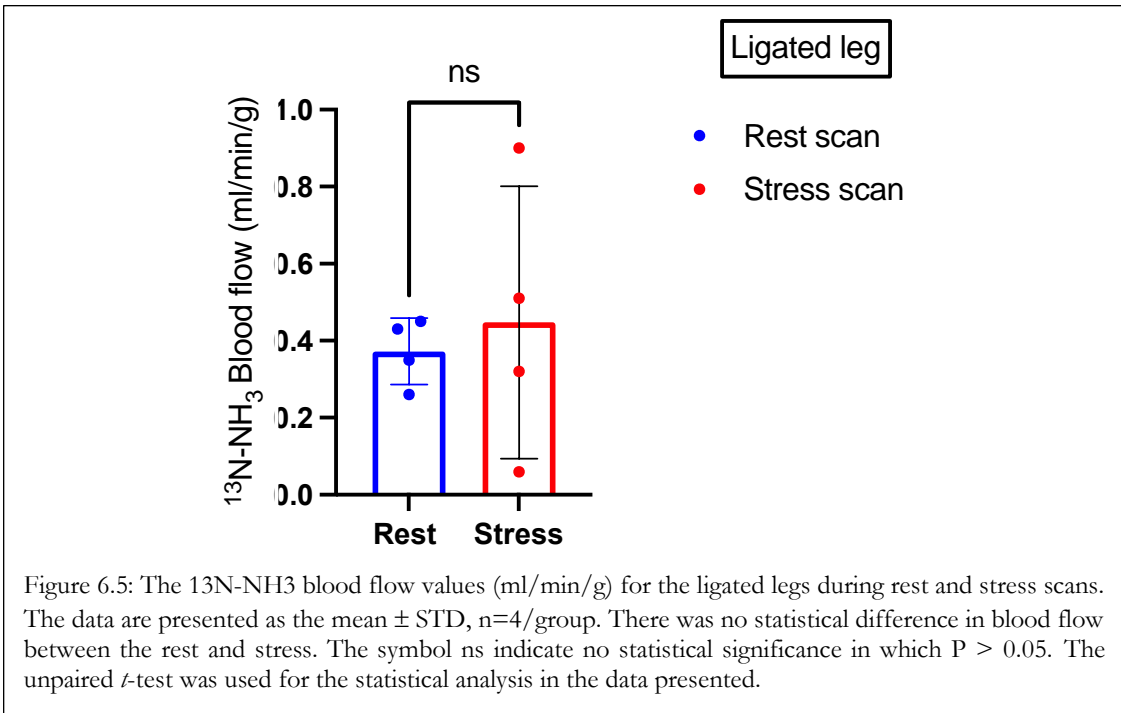
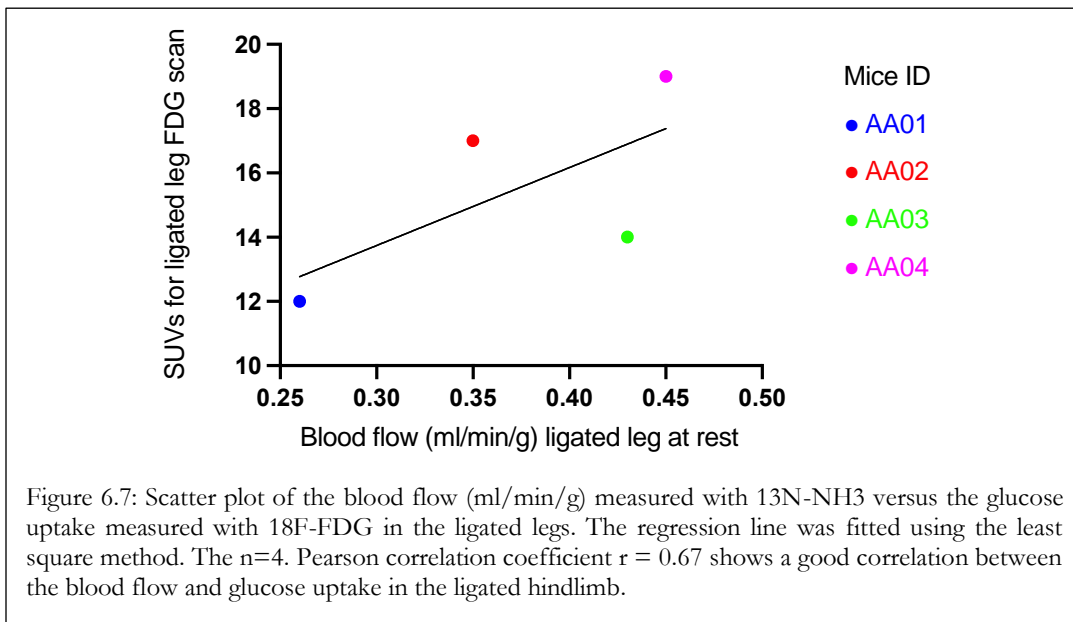
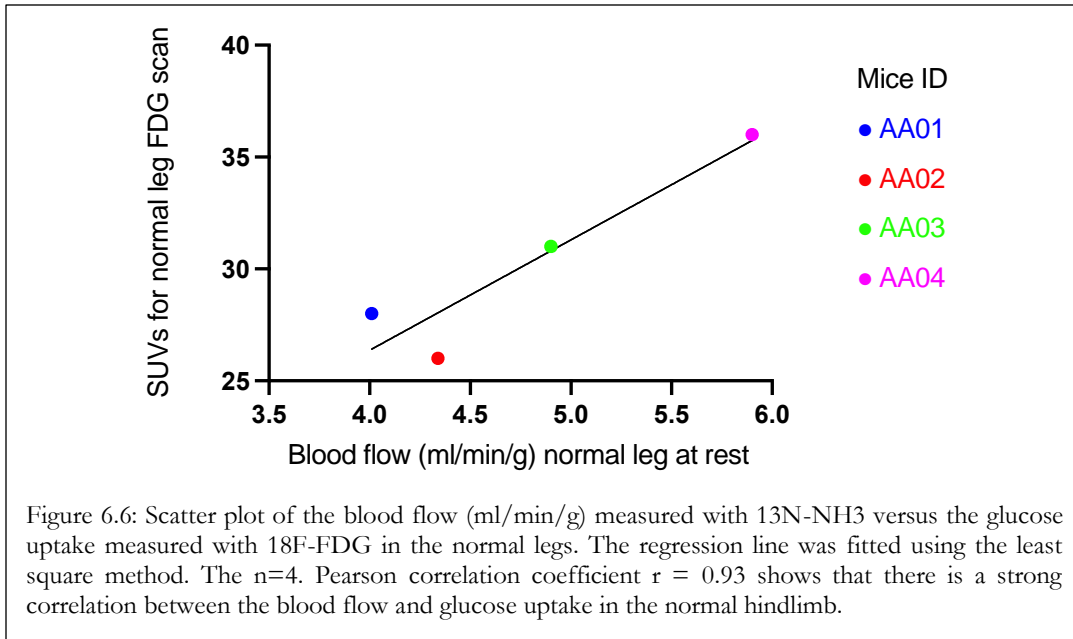


Figure 6.5: The $^{13}\text{N-NH}_3$ blood flow values (ml/min/g) for the ligated legs during rest and stress scans. The data are presented as the mean \pm STD, n=4/group. There was no statistical difference in blood flow between the rest and stress. The symbol ns indicate no statistical significance in which $P > 0.05$. The unpaired *t*-test was used for the statistical analysis in the data presented.



6.4.3 Capillary and artery density results:

Immunohistochemical staining revealed that capillary and artery numbers were significantly higher in normal legs compared to ligated legs as in table 6.5 and figure 6.7- 6.8. Images of capillary and artery density staining are illustrated figure 6.9.

Mice ID	Capillary density n/mm ²		Arterial density n/mm ²	
	Rt Leg	Lf Leg (ligated leg)	Rt Leg	Lf Leg (ligated leg)
AA01	87	49	17	7
AA02	86	52	19	8
AA03	93	67	21	11
AA04	95	69	23	9

Table 6.4: The Capillary and artery density in (n/mm²) in both the normal and ligated legs.

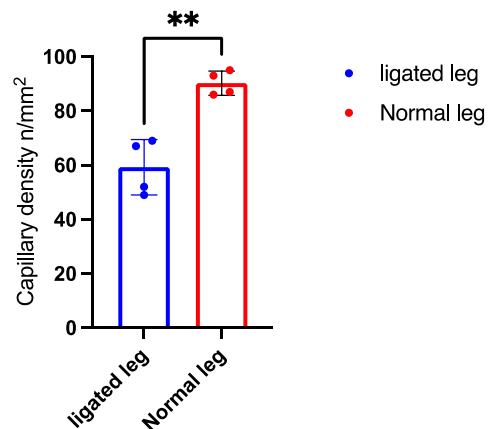


Figure 6.8: The capillary density (n/mm²) in both the normal and ligated legs. The data are presented as mean \pm STD, n=4. The capillary density in normal legs was statistically higher than the ligated legs. The symbol * represents significant difference with p values $** < 0.005$. The unpaired *t*-test was used for the statistical analysis in the data presented.

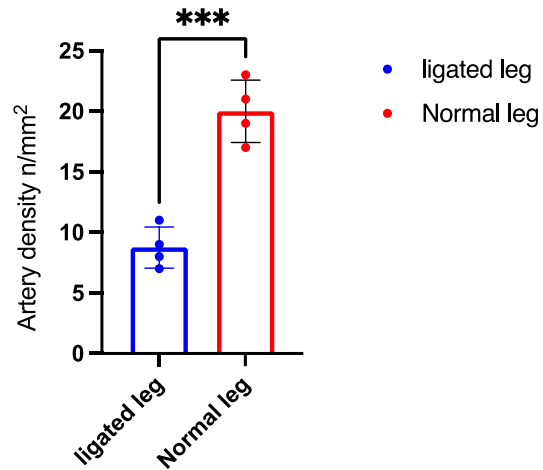


Figure 6.9: The artery density (n/mm²) in the normal and the ligated legs. The data are presented as mean \pm STD, n=4. The artery density in normal legs was statistically higher than the ligated legs. The symbol *** represents significant difference with p values $** < 0.0005$. The unpaired *t*-test was used for the statistical analysis in the data presented.

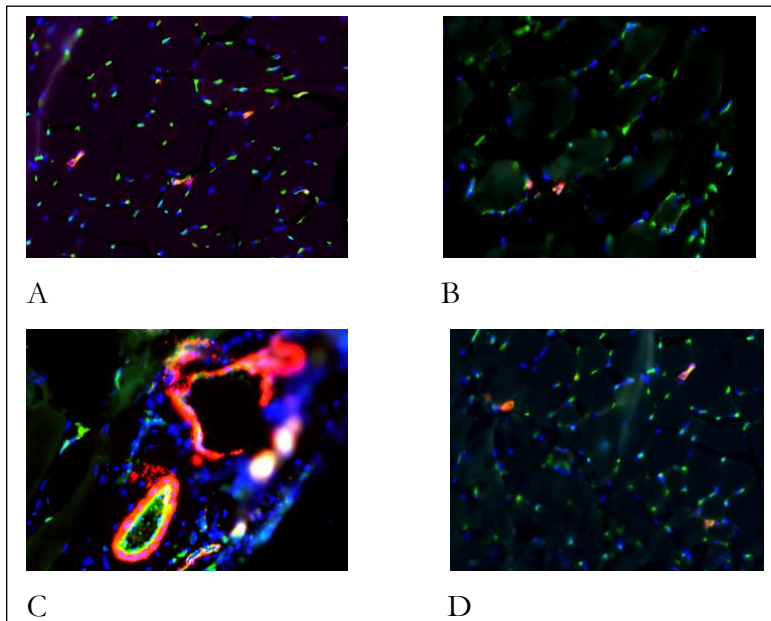


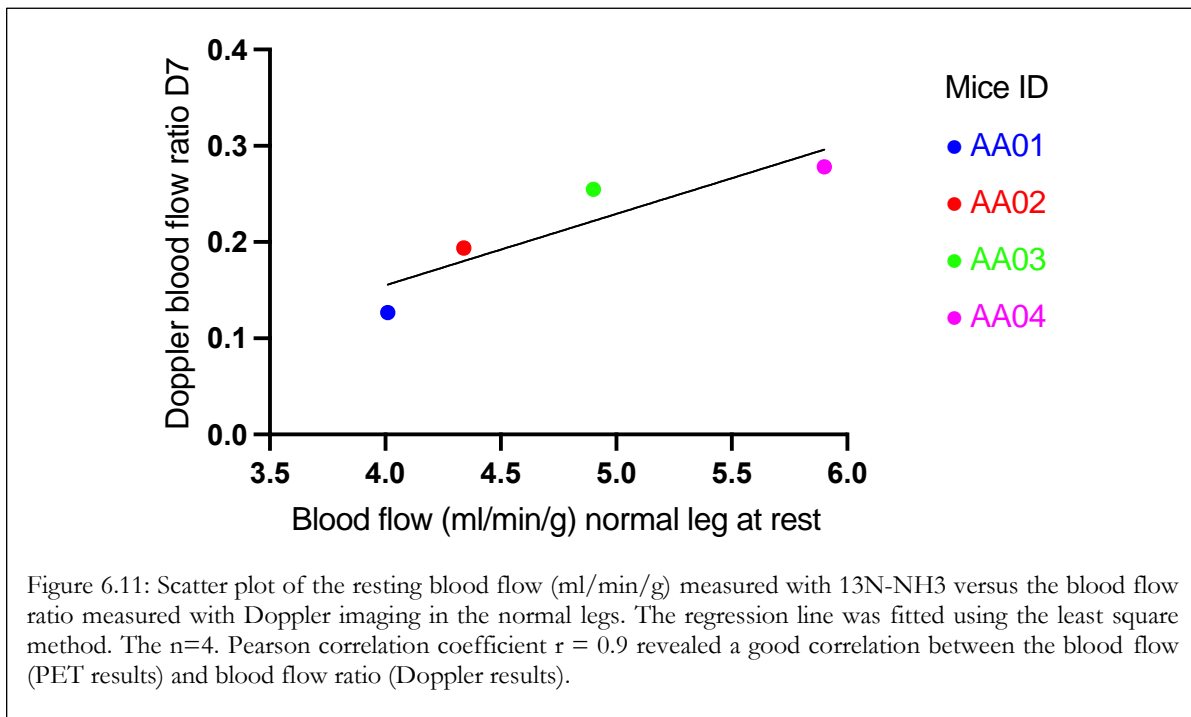
Figure 6.10: Representative images of ischemic hindlimb samples after immunostaining with green colour (488 emission) lectin binding representing the capillaries, and red (Cy3 emission) α SMA staining identifying the arteries. Nuclei counterstained with DAPI (blue). A, B Quantitative analysis of the capillaries in normal and ligated legs respectively. C, D α -SMA-positive artery staining in normal and ligated legs respectively.

6.4.4 Comparison of PET results with the Doppler imaging and histology:

The correlation was assessed between the resting blood flow (ml/min/g) measured by $^{13}\text{N-NH}_3$ for both legs with both the Doppler imaging blood flow ratio as well as the histological results. The correlation was based on calculating Pearson correlation coefficient r , in which the values between 0.5 and 1 reflect a strong positive correlation (Mukaka 2012; Schober et al. 2018).

There was a good correlation between the PET blood flow in normal leg and the blood flow ratio measured by the doppler imaging at day 7 (as the most recent results generated by doppler) with correlation $r= 0.9$ as in figures 6.10-6.11.

Furthermore, there was a strong positive correlation between the resting blood flow measured by PET scans and the capillary density calculated by the immunohistochemistry staining with $r= 0.91$ and 0.94 in the normal and the ligated legs respectively as in figure 6.12-6.13. Similarly, there was a strong correlation between the blood flow at rest and artery density in both normal and ligated legs with $r= 0.97$ and 0.81 respectively as in figure 6.14-6.15.



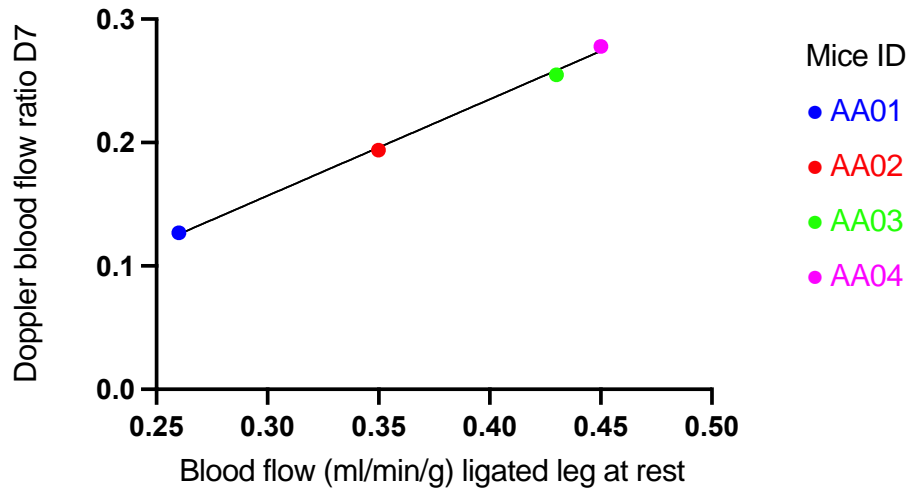


Figure 6.12: Scatter plot of the resting blood flow (ml/min/g) measured with $^{13}\text{N-NH}_3$ versus the blood flow ratio measured with Doppler imaging in the ligated legs. The regression line was fitted using the least square method. The $n=4$. Pearson correlation coefficient $r = 0.99$ revealed a good positive correlation between the blood flow (PET results) and blood flow ratio (Doppler results).

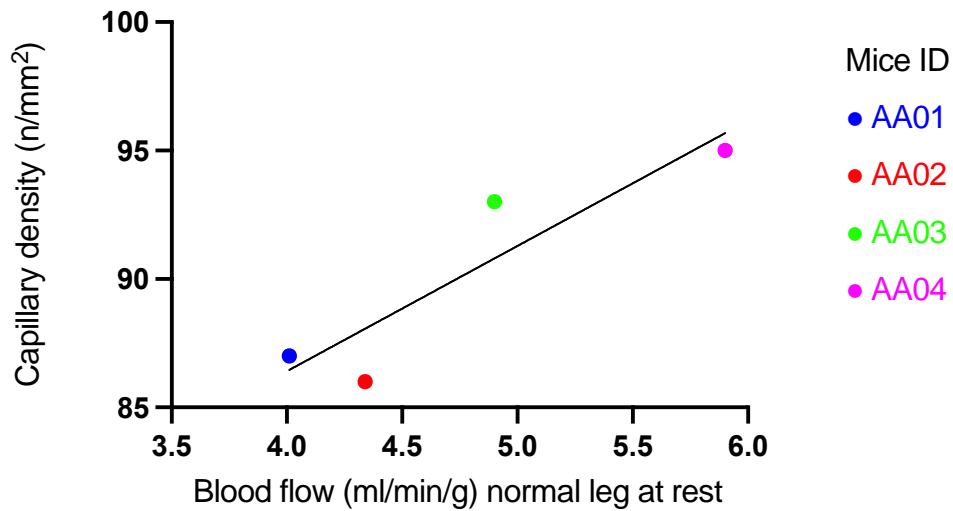


Figure 6.13: Scatter plot of the resting blood flow (ml/min/g) measured with $^{13}\text{N-NH}_3$ versus the capillary density (n/mm²) in the normal legs. The regression line was fitted using the least square method. The $n=4$. Pearson correlation coefficient $r = 0.91$ revealed a good correlation between the blood flow (PET results) and capillary density (histological results).

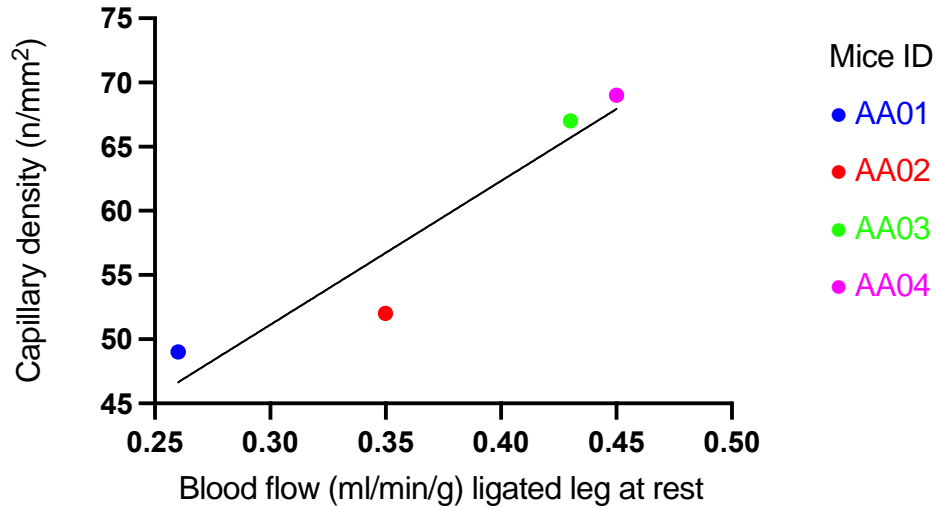


Figure 6.14: Scatter plot of the resting blood flow (ml/min/g) measured with $^{13}\text{N-NH}_3$ versus the capillary density (n/mm^2) in the ligated legs. The regression line was fitted using the least square method. The $n=4$. Pearson correlation coefficient $r = 0.94$ revealed a good correlation between the blood flow (PET results) and capillary density (histological results).

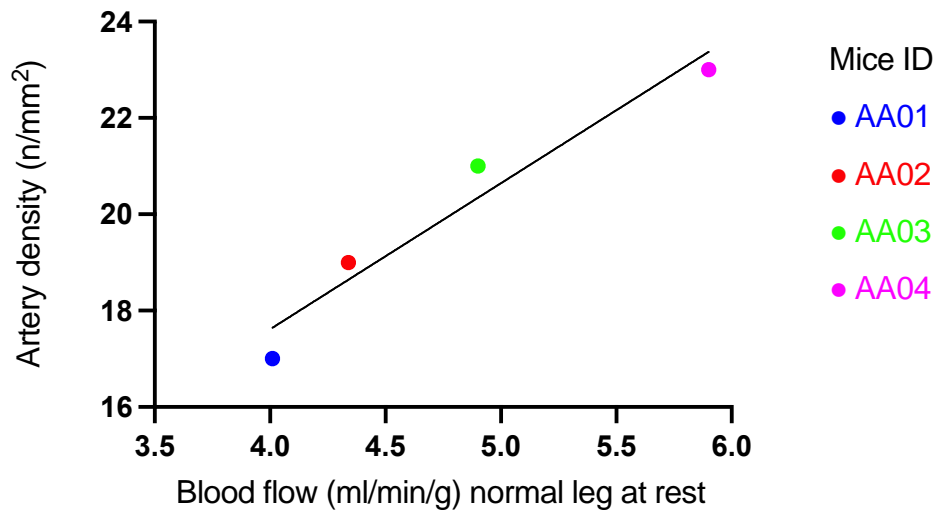
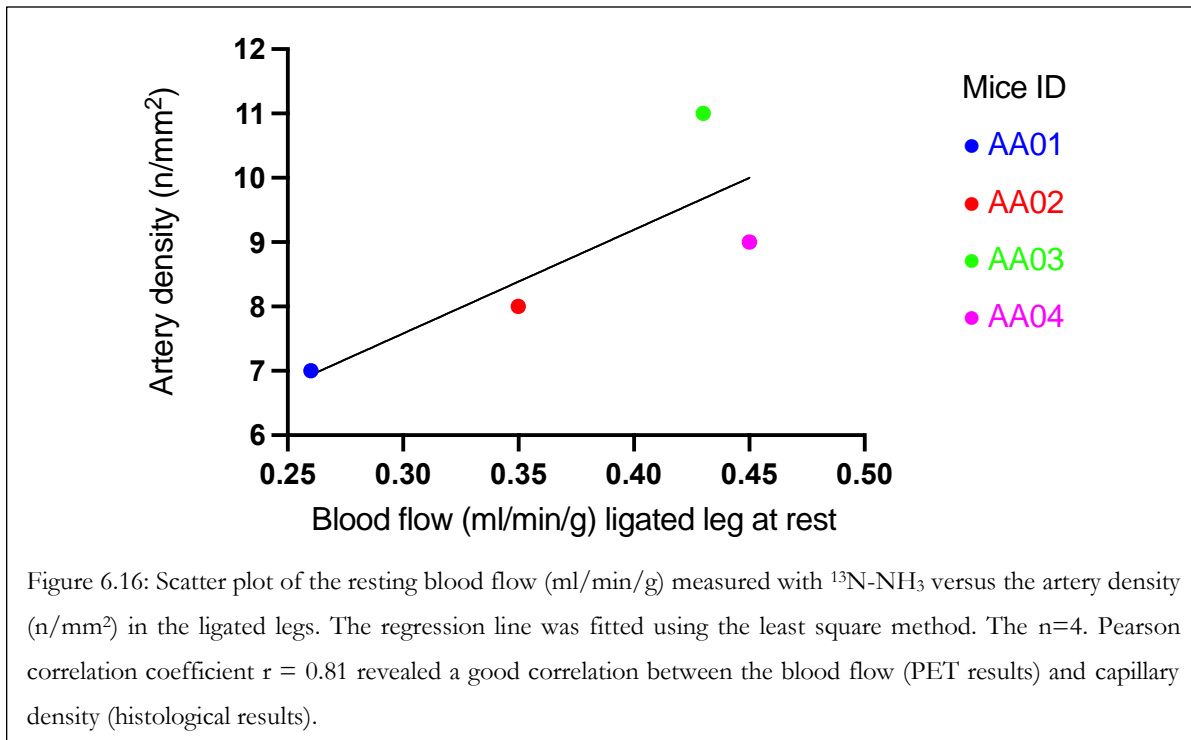


Figure 6.15: Scatter plot of the resting blood flow (ml/min/g) measured with $^{13}\text{N-NH}_3$ versus the artery density (n/mm^2) in the normal legs. The regression line was fitted using the least square method. The $n=4$. Pearson correlation coefficient $r = 0.97$ revealed a good correlation between the blood flow (PET results) and capillary density (histological results).



6.5 Discussion:

Murine models have been used extensively to assess the efficiency of therapy which resulted in the development of various animal models. Among them, the HLI model which is used to study PADs through simple surgical steps with low death rate. Measuring the blood flow in murine HLI is frequently performed using Doppler imaging which is non-invasive technique that allows the evaluation of superficial blood flow in mice. However, it cannot measure absolute perfusion values, such as mL/min/g, which is essential to evaluate angiogenesis and new vessels formation in response to therapy. Rather, its blood flow readings are expressed in arbitrary perfusion units (PU). Molecular imaging modalities, such as PET, have been used to detect alteration in the extremity blood circulation which might provide early and sensitive insight of ischemic defects at a molecular level (Dobrucki and Sinusas 2007; Cavalcanti Filho et al. 2011).

¹³N-NH₃ has been widely used in PET imaging as a perfusion agent that allows the assessment of regional MBF in both rest and stress heart conditions. In contrast, attempts to quantify the blood flow in skeletal muscle have rarely been reported particularly in murine model due to the associated challenge such as scanner resolution and animal preparation. In this chapter, our goal was to test the ability of our micro-PET/CT scanner to detect changes in the blood flow following surgical ligation of the mouse using ¹³N-NH₃ as the perfusion tracer and compartmental modelling tool.

Our $^{13}\text{N-NH}_3$ quantification successfully detected the reduction in the blood flow values in the ligated leg. The blood flow values were significantly higher in the normal leg compared to the ligated leg, confirming the poor blood supply following surgical ligation. Additionally, we detected a significant increase in the blood flow in the normal legs compared to its baseline values during the stress scan. This is likely due to the vasodilation process stimulated by the administration of pharmacological stress agent. In contrast, the blood flow values in the ligated legs were similar to their baseline values due to the ischemic defect in which the muscle fail to raise the blood flow in response to the pharmacological agent (Orbay et al. 2013; Hoinoiu et al. 2019).

With regards to the glucose uptake values, we have reported a significant decrease of the glucose uptake in the ligated leg compared to the normal legs. Under normal condition, the skeletal muscle, such as the hindlimb, extract it oxygen supply from the blood vessels (Rivas et al. 1976). Since the metabolisim in muscle is mainly aerobic and the anaerobic metabolism is limited during ischemia, the metabolic change in the muscle depends on adequate blood supply (Rivas et al. 1976). Subsequently, the poor blood supply in ligation could be the cause of the reduction in the glucose uptake. In fact, this might explain the strong correlation between the blood flow and the glucose uptake results.

Furthermore, we next sought to assess the correlation between our PET results and the Doppler imaging and histological data. It is important to emphasise that proper judgment of the feasibility and the accuracy of any imaging technique could be accomplished through performing a combination of other histological and functional tests. Consequently, we have assessed the relation between PET blood flow results and both the Doppler and vascular density results. The blood flow ratio values measured in doppler imaging were in strongly correlated with PET flow results suggesting that PET imaging can detect the flow defect as the case in Doppler imaging but in absolute value.

Traditional assessment of ischemia and angiogenesis in murine model involve the use of invasive technique which include animal termination and tissue collection, which subsequently limits serial examination of the physiological process in living animals (Orbay et al. 2013). We have assessed the correlation between PET and histological results and there was a strong correlation between of the PET blood flow and vascular density results. The vascular density in the ligated legs reduced dramatically compared with the normal legs. It has been reported that the reduction in the microvasculature density, or vascular density, may contribute to the decrease in the blood flow and that is possibly the cause of the strong correlation found between the PET and vascular density results (Landers-Ramos and Prior 2018). Several studied have recorded the reduction in vascular density following ligation process, which was aligned with our vascular density results in which both the

capillary and artery density were significantly reduced in the ligated leg (Peñuelas et al. 2007; Hoinoiu et al. 2019; Tang and Kim 2021).

6.6 Conclusion:

In this chapter, we have shown that the Mediso-micro-PET/CT scanner can detect the changes in the blood flow and glucose metabolism following induced HLI in mice using N^{13} - NH_3 and F^{18} -FDG respectively. Our developed imaging protocols were applied for the quantitative assessment of blood flow in the ischemic hindlimb murine model. An advantage of using PET is it allows measuring blood perfusion in an absolute value ml/min/g (Orbay et al. 2013). The resulted biomarkers, that frequently are used to evaluate cardiac function, were applicable to be used in the murine hindlimb using our developed imaging protocols and PET quantitative tools. Importantly, the use of the traditional blood flow evaluation techniques, namely Doppler imaging, and histological analysis, were in good agreement with our PET results.

In conclusion, we demonstrated that our micro-PETCT scanner can be used as a feasible tool in detecting blood flow and glucose uptake changes in disease model, such as HLI, in which the results were validated successfully with other measurement tests. Therefore, micro-PT/CT may permit of the evaluation of disease progresses and therapeutic intervention to be translated directly to humans. In the next chapter, we will use our imaging protocols to evaluate the therapeutic effect of LAV-BPIFB4 gene in protecting from cardiomyopathy in diabetic model.

Chapter 7:

The therapeutic effect of longevity-associated variant (LAV)-BPIFB4 gene therapy on Diabetes mellitus (DM) murine models

7.1 Introduction:

DM is a group of metabolic disorders that is characterized by an abnormal rise in blood sugar resulting either from the inability of the body to produce enough insulin or not responding normally to it (D. 1979; Mellitus and World Health 1980). DM is difficult to classify, but the most common classifications include two types, T1D and T2D, as previously mentioned in the introduction chapter (Group 1979; Mellitus and World Health 1980).

T1D is an autoimmune disease in which the immune system attacks and destroys the pancreatic beta cells that produce insulin (Group 1979; Mellitus and World Health 1980). It occurs mainly among children and the young population, whereas T2D is more common in older people (Group 1979; Mellitus and World Health 1980). T2D occurs when the body's cells lose their ability to respond to insulin ("insulin resistance") and is often associated with obesity (Group 1979; Mellitus and World Health 1980). DM is one of the risk factors for CVDs, especially vascular diseases, through its impact on initiating or accelerating atherosclerosis (Kolakalapudi and Omar 2015; Oikonomou et al. 2018).

Generally, DM induces microvascular and macrovascular changes in the majority of the body's organs. These changes include endothelial dysfunction, aortic stiffness, arterial stenosis and diabetic nephropathy (Kampoli et al. 2009). The effects of DM on the CVS, including the mechanisms that lead to vascular dysfunction and CVDs, has gained great interest from the medical communities. We will only briefly discuss the effects of DM on the endothelium because of its adverse outcomes and complications that could lead to PADs, CADs or MI.

The endothelium is the inner most layer of the vasculature (Kampoli et al. 2009; Aaronson et al. 2020). It consists of a monolayer of cells that acts as a barrier between the circulating blood and body tissues (Kampoli et al. 2009; Aaronson et al. 2020). Endothelium dysfunction results in abnormalities such as changes in the vasomotor ability of the vessel, increased production of inflammatory cytokines

and chemokines, and changes in platelet activity and coagulation (Kampoli et al. 2009; Aaronson et al. 2020). These may ultimately lead to changes in vasoconstriction, inflammation, and thrombosis (Kampoli et al. 2009; Aaronson et al. 2020).

In the case of DM, the endothelium has an increased probability of plaque formation due to a variety of factors that include hyperglycaemia, insulin resistance and increased free fatty acids in the blood (Kampoli et al. 2009; Aaronson et al. 2020). These factors might affect the endothelium, causing oxidative stress and endothelial dysfunction (Kampoli et al. 2009; Aaronson et al. 2020). Abnormal vasodilation in DM is a result of the reduction in nitric oxide (NO) production (Navab et al. 1996; Kampoli et al. 2009; Aaronson et al. 2020). NO is antioxidant, anti-inflammatory and anti-coagulant gaseous molecule that is associated with the maintenance of vascular vasodilation and blood pressure (Kampoli et al. 2009; Aaronson et al. 2020). It plays a significant role in regulating the functions of the CVS since any malformation in its production or availability might induce hypertension, angiogenesis disorders and atherosclerosis (Moncada and Higgs 2006; Pacher et al. 2007; Vanhoutte et al. 2009). Importantly, NO synthesizes through nitric oxide synthase (eNOS) which is a vital protective enzyme for vascular functions and the CVS (Dossena et al. 2020). Following NO production, it diffuses into the smooth muscle cell layer of the vasculature and induces the secretion of an enzyme called soluble guanylate cyclase (sGC) which activates the transformation of guanosine triphosphate (GTP) into cyclic guanosine monophosphate (cGMP) (Zhao et al. 2015; Hofmann 2020). In fact, cGMP is a messenger regulator molecule that modulates various mechanisms such as vasodilation, glycogenolysis, retinal phototransduction, calcium homeostasis, ion channel conductance and cellular apoptosis (Zhao et al. 2015; Hofmann 2020). Once synthesized, cGMP stimulates protein kinase G (PKG enzyme) that boosts many phosphorylation processes within the cell, decreases calcium levels as well as promoting vascular relaxation (Wolfertstetter et al. 2013; Zhao et al. 2015; Hofmann 2020).

A genetic study among LLIs reported a gene variant that improved the NO production which subsequently reduced endothelium dysfunction and boosted the vascular reparative process that is often impaired in DM (Villa et al. 2015c). This gene is the longevity associated gene variant (LAV) of the bactericidal/permeability-increasing fold-containing family B member 4 (BPIFB4), a four-missense single-nucleotide polymorphism haplotype allele, or LAV-BPIFB4 (Villa et al. 2015b; Faulkner et al. 2020). BPIFB4 belongs to a group of proteins that appear to be involved in innate immunity, many antimicrobial activities, cholesterol handling and the release of surfactant proteins with anti-infection and immunomodulatory properties (Villa et al. 2015c; Spinelli et al. 2017; Dang et al. 2020; Faulkner et al. 2020). Villa et al. (Villa et al. 2015b) noted that BPIFB4 is reduced in aged

mice and forcing the expression of LAV-BPIFB4 prevented endothelial dysfunction which is one of the common hallmarks of ageing. They also found that LAV-BPIFB4 enhanced angiogenesis and wound healing in murine HLI models following femoral artery ligation.

Other studies showed that LAV-BPIFB4 stimulated proteostasis and adaptive stress responses which is known to be the key elements for enhancing cell survival (Nisoli et al. 2005; Vilchez et al. 2014). Many investigations, which have been carried out to justify these remarkable therapeutic effects, demonstrated that LAV-BPIFB4 is more effectively phosphorylated and stimulated by protein kinase C alpha and protein kinase R-like endoplasmic reticulum kinase, triggers and increases calcium mobilisation, recruits heat shock protein 90 and stimulates endothelial NO synthase eNOS signalling pathways (Villa et al. 2015a; Spinelli et al. 2017; Villa et al. 2018; Malavolta et al. 2019). The eNOS is one of the three isoform enzymes responsible for synthesizing NO which is responsible for regulating vasodilation and blood flow through sGC in the vascular smooth muscle and monitoring O₂ consumption of the mitochondria (Kukreja and Xi 2007; Chen et al. 2008). In addition, studies showed that the presence of the LAV- BPIFB4 gene, is associated with a lower incidence of ischemia, hypertension, and atherosclerosis (Villa et al. 2015a; Spinelli et al. 2017; Malavolta et al. 2019; Di Pardo et al. 2020; Faulkner et al. 2020). In our previous work (Dang et al. 2020), we revealed that the LAV-BPIFB4 gene activates the expression of stromal derived factor-1 (SDF-1) in CD14+CD16+ intermediate monocytes. SDF-1 is a chemokine that belongs to a large family of secreted proteins involved in cell signalling through cell surface G protein-couple chemokine receptors (Valenzuela-Fernández et al. 2002; Hughes and Nibbs 2018). Their major function is to regulate all protective and destructive inflammatory and immune responses through inducing cell migration, mostly leukocytes (Valenzuela-Fernández et al. 2002; Hughes and Nibbs 2018). Moreover, their receptors on white blood cells also regulate the biology of many non-leukocytic cell types (Hughes and Nibbs 2018). Therefore, they play a significant role in the development of the immune system and homeostasis (Valenzuela-Fernández et al. 2002; Hughes and Nibbs 2018). Much evidence has reported that the chemokine receptor CXCR4 and its sole ligand stromal cell-derived factor-1 (SDF-1) (also called CXCL12) regulates the CVS and neural growth, and the homeostasis of hematopoietic lineages, modulates lymphocyte trafficking (the process in which lymphocytes and phagocytic cells adhere and migrate across the endothelium of the vasculature into an organ or the region of inflammation) (Nagasawa et al. 1996; Aiuti et al. 1997; Ma et al. 1998; Tachibana et al. 1998; Zou et al. 1998; Peled et al. 1999). In fact, SDF-1 and CXCR4 have constitutive (their genes are transcribed constantly) and large expression in the body tissues (Shirozu et al. 1995; Nagasawa et al. 1996). Additionally, several studies reported

that SDF-1/CXCR4 pairs participate in the pathogenesis of inflammatory and infectious processes through inducing platelet aggregation (platelets adhere to each other in the region of vascular injury) and subsequent development of atherosclerosis (Bleul et al. 1996; Feng et al. 1996).

When gathering the above evidence, LAV-BPIFB4 gene therapy might be a novel treatment for fighting CVDs and age-related cardiovascular pathology. Therefore, in this chapter we will evaluate the ability of the LAV-BPIFB4 gene to prevent the progression of T2D using murine models through the assessment of cardiac function. The cardiac function was evaluated through the quantification of myocardial glucose uptake and metabolism using the SUV and compartmental modelling methods respectively.

7.2 Objective:

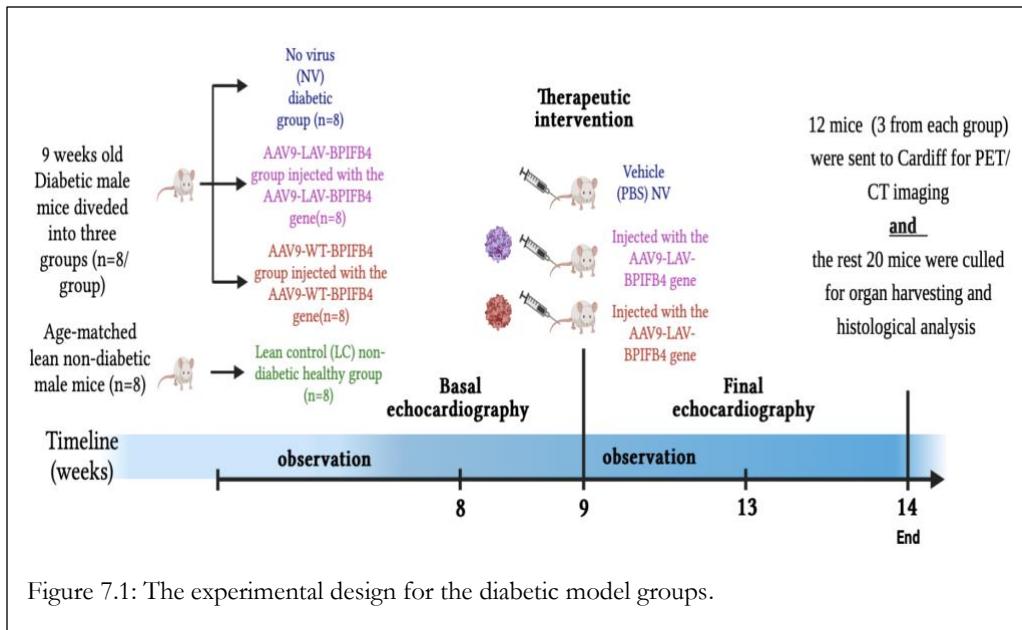
The main objective of the experiments described in this chapter was to determine whether the LAV-BPIFB4 gene treatment has a therapeutic effect on a murine model of diabetes. This was done through:

1. Quantifying myocardial glucose uptake (through the SUVs) and metabolism (MGM through compartmental modelling) in four groups of mice (1 experimental group, 3 control groups: further details included in the method section).
2. Assessing any differences in either the SUVs or MGM between the experimental group and the control groups.
3. Comparing our PET data with the echocardiography and relevant histological data that were produced from the same groups of mice. Please note that the echocardiography and histological analysis in this chapter were carried out by other members of the research group.

7.3 Material and Methods:

7.3.1 Study design:

Some of the data in this chapter has been published (Dang et al. 2020). The experimental design of this study can be seen in figure 7.1. Echocardiography scan results for the mice that underwent PET/CT imaging have been included in this chapter to enable a direct comparison with the PET scan results. The mice that were not sent to Cardiff underwent a histological assessment after the echocardiography (i.e., at the same timepoint as the PET/CT scans), as a further comparator to assess the potential therapeutic effect of the LAV variant on the diabetic models.



7.3.2 Animal groups:

All animal experiments and imaging procedures in this research were approved by the British Home Office (Project License PPL 30/3373), at the University of Bristol and conducted according to the Care and Use of Laboratory Animals (The Institute of Laboratory Animal Resources, 1996).

Twenty-four nine-week-old male C57BLKS/J-Lepr^{db}/Lepr^{db}/Dock7+[db/db] mice (Envigo, Bicester, Oxfordshire, UK) and eight age-matched lean non-diabetic mice [C57BLKS/J-Lepr^{db}/Lepr^{WT} Dock7+ (wt/db), Envigo] received a base line echocardiogram (at week 8) before entering the study. One week later, when all the DbDb mice were fully diabetic (glycosuria tests), the mice were anaesthetised using isoflurane and given a single injection via the tail vein of vehicle (PBS), AAV9-LAV-BPIFB4 or AAV9-WT-BPIFB4 (100 μ L at 1×10^{12} GC/mL) as can be seen in figure 7.1. Therefore, the mice were divided into four groups (8 mice each):

1. No virus (NV) control group.
2. AAV9-WT-BPIFB4 control group.
3. AAV9-LAV-BPIFB4 experimental group.
4. Lean non-diabetic (Dblean) control group.

One month after the gene delivery (when the mice were 13 weeks old), the mice underwent a final echocardiography and then the mice (n=3/group) were randomly chosen to be sent from Bristol University to PETIC in Cardiff university to undergo PET/CT imaging under terminal anaesthesia. The remaining animals (n=5/group) underwent histological assessment in Bristol.

7.3.3 Micro PET/CT scanner:

The specifications for the Mediso Nano-Scan 122S small-bore PET/CT imaging system manufactured by the Mediso medical imaging system, Budapest, Hungary have been outlined in the methodology chapter.

7.3.4 The used radiotracers:

^{18}F -FDG was used to assess the glucose uptake and metabolism through the SUVs and MGM. It was not possible to use ^{13}N -ammonia in these mice, as the manufacture and supply logistics had not been finalized. In any case, the aim of this study was to assess glucose uptake and metabolism in these diabetic mice, and to compare the results of the echocardiography and PET/CT in the same animals.

7.3.5 Animal preparation:

Following the echocardiography, the mice were examined by the Bristol university veterinarian (National veterinarian services NVS) prior to their transfer to Cardiff. The scanning procedures were started after waiting for at least 5 days following the transfer to avoid mice distress. Each mouse was fasted for one hour and then warmed up to 37°C for 5 minutes (for better vein cannulation) before being anaesthetised with 2-3% isoflurane in O_2 (1L/min). An IP injection of 100 μl of Iohexol CT contrast agent (647 mg/ml) was given to the mouse just before injecting ^{18}F -FDG to help distinguish between the kidneys and the liver in the CT images.

Next, the mouse was transferred to a pre-warmed imaging scanner bed which was supplied with a small tooth bar (attached to a nose cone) and a pad, in order to position the mouse, maintain anaesthesia ($\sim 1.5\text{-}2\%$ isoflurane in O_2), and measure the heart rate.

7.3.6 Animal PET/CT imaging:

A 16 second CT scout scan was acquired for accurate mouse positioning followed by an ^{18}F -FDG injection via the lateral tail vein route (~ 20 MBq in 0.1 ml). A 60-minute whole body dynamic PET scan was initiated immediately following the injection. This was followed by a 2.5-minute whole body CT scan (480 projections in a semi-circular method, one rotation, 50 kVP, 300 ms exposure time, 1-4 binning and a maximum FOV was used). The CT scan was used to calculate attenuation correction. The co-registration process of images was automatically applied to allow a better visualisation of structural and functional information from the CT and PET respectively.

7.3.7 Reconstruction of PET images:

All PET scans were acquired in list mode acquisition, and images were reconstructed using Mediso's proprietary Teratomo-3D reconstruction algorithm with a voxel size of 400 μm using Nucline software. The FDG scans were reconstructed with a frame set of 6x10 sec, 4x60 sec, 1x300

sec, 5x600 sec (total duration 1 hour). The difference in reconstruction frameset was due to the different in the injection time. CT scans were reconstructed using a 250 μm voxel size, and sinograms produced using the 2-D filtered back-projection method. Attenuation (CT based) and scatter corrections, as well as normalization, were applied to the reconstructed images. Following the reconstruction, all images were exported to PMOD software for SUV and MGM quantifications using data analysis and kinetic modelling tools. Importantly, PET images were corrected for dead time, scatter, and radiation decay.

7.3.8 Data analysis:

As described previously, PMOD was the software of choice for all image analysis due to its sophisticated ability of performing all quantification methods in PET imaging. In this chapter, cardiac analysis was carried out using the heart SUVs and compartmental modelling (for MGM calculation).

7.3.9 SUV measurements:

Standard uptake value (SUV) is the simplest semi-quantification PET method that is applied using static PET images (Turkheimer et al. 2014). It is performed routinely for clinical and preclinical studies because it can generate an approximate metabolic uptake of the radiotracer in the region of interest (Turkheimer et al. 2014). However, it is only applicable to irreversibly binding radiotracers, such as $^{13}\text{N-NH}_3$ and FDG (Boellaard 2009).

Since SUV measurements can be only generated for static PET images, the dynamic FDG scan was averaged for the duration of the final 30 minutes (which is the time that FDG reached the equilibrium as previously explained), and the regions of interest (ROIs) were delineated over the myocardium using the manual delineation tool. Following this, the SUV, which is independent of the dimension of the object, was calculated through the following the formula in equations 2.5-2.6, and it has no unit.

7.3.10 Myocardial glucose metabolism (MGM) measurements:

The MGM for the four groups was assessed using FDG scans and a 2TC model that was explained previously.

7.3.11 Echocardiography:

The echocardiography was performed by two Bristol-based members in our research group. A depilatory cream was used on the chest prior to scanning. The Vevo 3100 echocardiography system (Fujifilm VisualSonics Inc, Toronto, Canada) was used with a MX400 transducer to measure cardiac dimensional and functional parameters such as SV, EF%, fractional shortening (FS%) and CO (Katare et al. 2010; Katare et al. 2011; Dang et al. 2020). The results were obtained from the 13-week

echocardiography using the parasternal long-axis (PLAX View) and short-axis views placed at the papillary muscle level in M-mode imaging. The mice were anaesthetized using isoflurane at 2.5% in air, then the proportion of isoflurane was altered to maintain the heart rate at 450 bpm (\pm 25 bpm). The procedure lasted for about 1 hour.

7.3.12 Histological analysis:

The tissue harvest and histological examinations were performed on the mice that had not undergone PET/CT by other members of the research group (based in Bristol), and not by the researcher. This data has been included as a comparator for the PET/CT study. After fixation in PFA and cryopreservation in sucrose, the hearts were embedded in OCT and the cryosections were cut. Capillary density was assessed after staining with isolectin IB4 and an antibody specific for α -SMA staining to identify capillaries and arteries, respectively. The sections were examined using fluorescence microscopy (Zeiss Axio observer microscope, 20 X magnification). Photomicrographs were taken and image analyses were performed using the image J software. The total number of the capillary and arteriole (at <10 μ m, 10-50 μ m and >50 μ m) were identified in at least 20 fields. Final data were expressed as the number of capillary or arteriole per mm^2 .

7.4 Statistics:

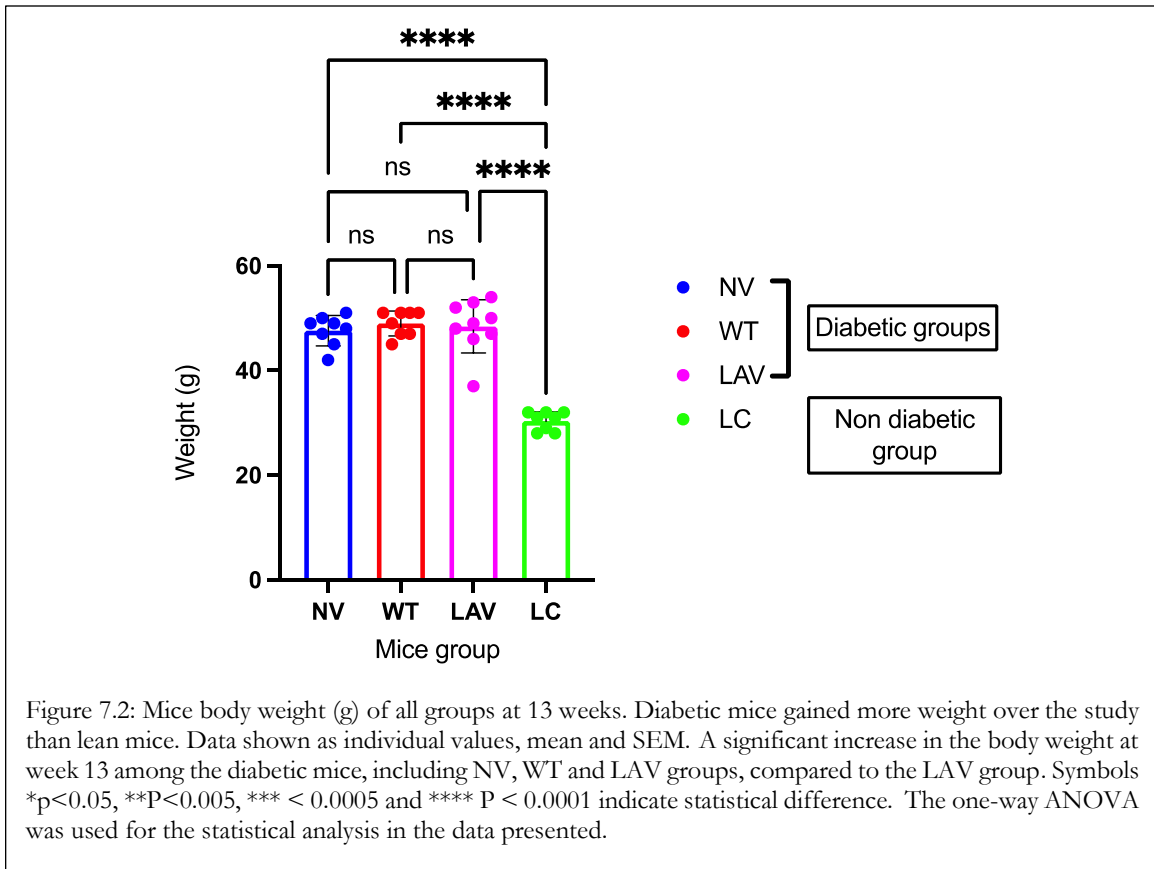
Statistical analysis was performed using GraphPad Prism (version 9.3.0). Data are shown as individual values and/or mean with \pm standard error of the mean. Comparisons were made using the student's *t*-test and one- or two-way analysis of variance (ANOVA), as appropriate. The Brown-Forsythe test was used to determine equal variance between groups. Post-hoc analysis of ANOVA included Tukey and Welch tests, as appropriate. A P value of less than 0.05 was considered to be statistically significant.

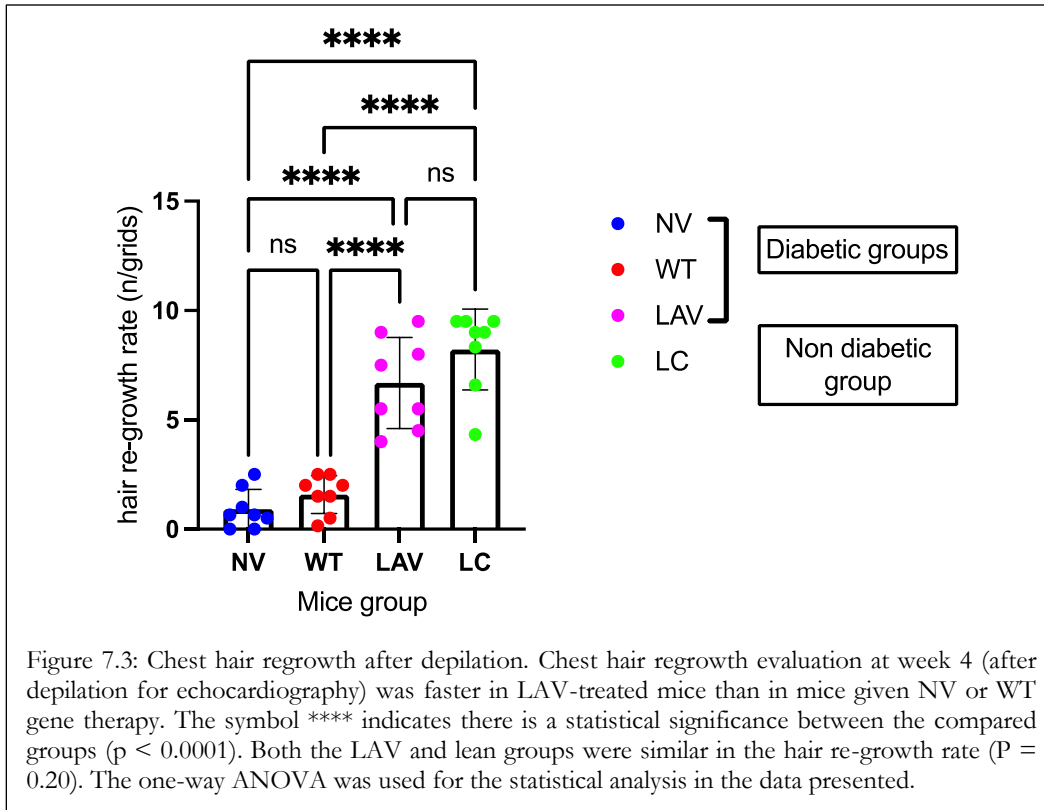
7.5 Results:

All mice were given the tail vein injections (virus or control) and underwent echocardiography without complications. As expected, the diabetic mice had gained a considerable amount of weight by the end of the experiment at week 13 (figure 7.2, appendices A.1-A.4). The mice underwent hair removal (with depilatory cream) prior to the echocardiography. A serendipitous observation identified differences in hair regrowth, with the diabetic mice having impaired regrowth compared with the non-diabetic animals (figure 7.3, Appendix B.1). Interestingly, when evaluating the appearance of all the groups (8 mice/group), including both the harvested and the PET/CT scanned mice, there was a significant increase in the hair re-growth rate within the AAV9-LAV-BPIFB4 treated group compared

with the other diabetic groups ($p < 0.0001$), while both the LAV and lean groups showed a similar hair re-growth trend ($p = 0.20$).

During PET/CT imaging, all mice recorded stable and normal heart rates (HR) (with little fluctuation), with a value of approximately 463-509 beats/min as reported previously in literature and under isoflurane anesthesia (Doevendans et al. 1998; Low et al. 2016). This is slightly elevated compared with the HR maintained in the mice during echocardiography.



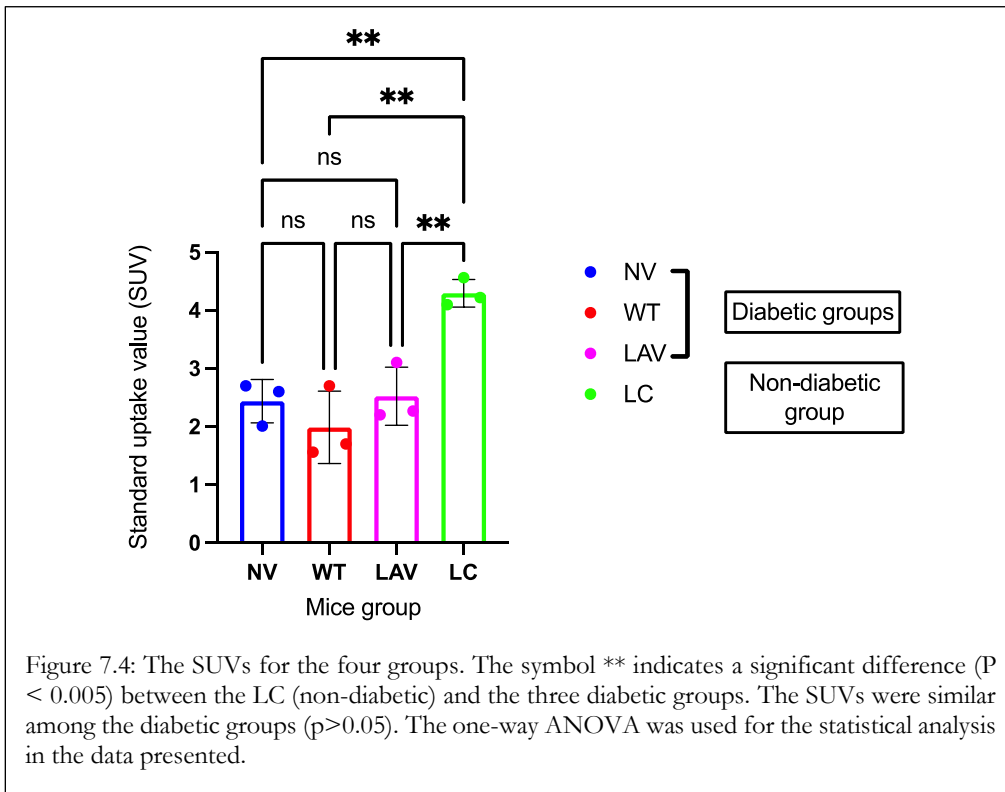


7.5.1 SUV measurements:

We investigated whether a single intravenous injection of the AAV9-LAV-BPIFB4 gene could promote glucose uptake, using the ^{18}F -FDG images and the semi-quantitative assessment (represented by SUVs). As previously explained, the SUV is a general index that represents the radiotracer uptake within a ROI or volume of interest (VOI). The uptake of the radiotracer was measured by averaging the final 30 min of the 60 min ^{18}F -FDG scan for each individual mouse. Table 7.1 illustrates the SUVs of the four groups. As shown in figure 7.4, the healthy LC group reported the highest SUVs compared to the other three groups with $p < 0.005$, suggesting a significant difference between its values and the SUVs of the three diabetic groups. Generally, the SUV results (figure 7.4) suggested a reduction in the ^{18}F -FDG uptake among diabetic groups compared with the uptake in lean mice (LC). No significant differences were found between the three diabetic groups, as illustrated in figure 7.4, possibly because of the low numbers of animals involved. Consequently, we cannot say that the gene treatment of mice with the AAV9-LAV gene improved the glucose uptake in the LAV group.

Model	Mice group	Mouse ID	SUVs for the ¹⁸ F-FDG scan
Diabetic mice	NV	PA85	2.7
		PA86	2.6
		PA87	2.01
	WT	PA91	2.7
		PA92	1.56
		PA93	1.7
	LAV	PA88	3.1
		PA89	2.2
		PA90	2.27
Non-diabetic mice	Lean	PA94	4.1
		PA95	5.56
		PA96	4.22

Table 7.1: The SUVs for all the groups. There was a significant difference between the lean group (non-diabetic) and the diabetic groups (P<0.005).



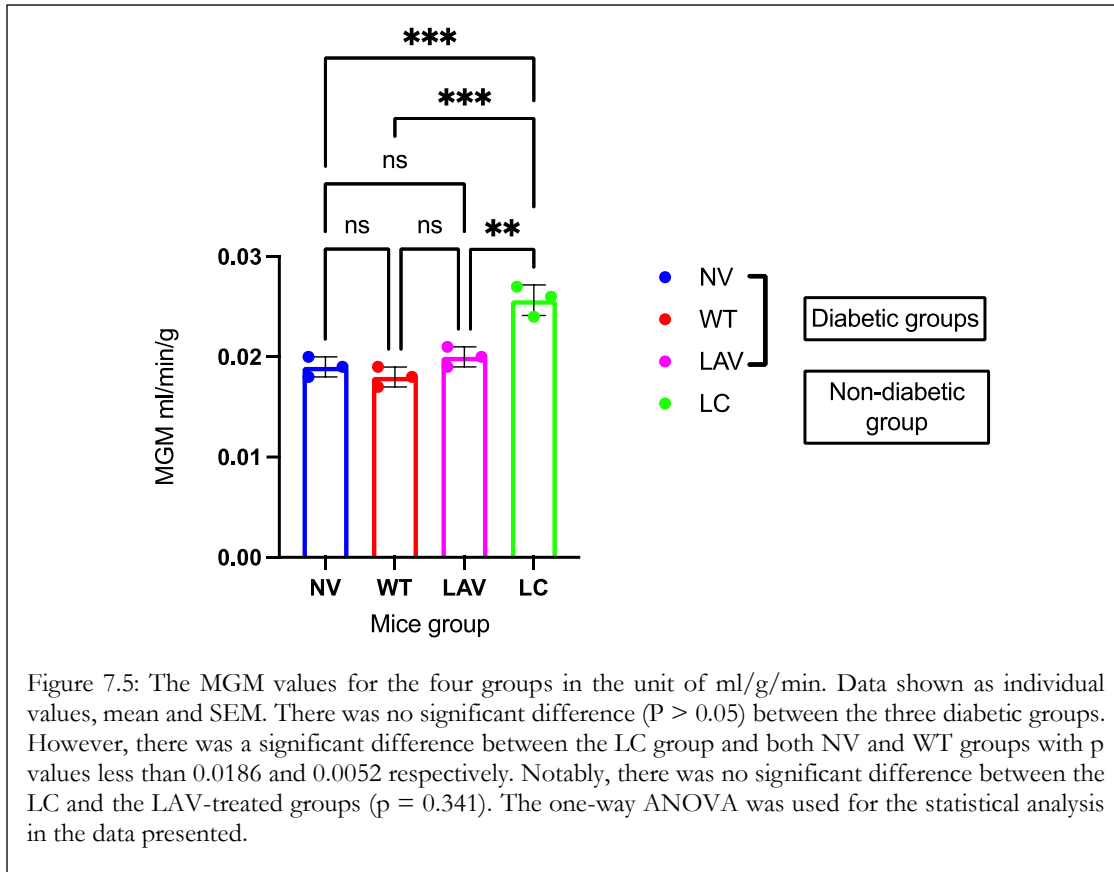
7.5.2 MGM measurements through compartmental modelling:

To further understand and investigate the impact of the single intravenous injection of the AAV9-LAV gene on glucose uptake and metabolism among diabetic mice, the data were fitted into a two-tissue compartment model as explained previously. The compartmental modelling was used to assess the rates of ^{18}F -FDG phosphorylation through the myocardial glucose metabolism (MGM) or K_{FDG} (Cochran et al. 2017).

The MGM or K_{FDG} (in the unit of ml/g/min) of the four groups can be seen in table 7.2. Data from each group were tested for normal distribution using the Shapiro-Wilks test and the p values were greater than 0.8301 suggesting normal distribution. Thus, the two-way ANOVA was carried out between the four groups to test the statistical difference between them. From these table 7.2 and figure 7.5, it is apparent that the treatment with the AAV9-LAV-BPIFB4 gene did not significantly increase the MGM in the LAV group compared to the other two diabetic groups (NV&WT). In addition, it can be seen from this graph that the LC group had significantly higher MGM values, as expected when compared to NV and WT groups with *P < 0.005.

Model	Mice group	Mouse ID	MGM or K_{FDG} in the unit of ml/min/g
Diabetic mice	NV	PA85	0.018
		PA86	0.021
		PA87	0.019
	WT	PA91	0.017
		PA92	0.019
		PA93	0.018
	LAV	PA88	0.021
		PA89	0.020
		PA90	0.019
Non-diabetic mice	LC	PA94	0.026
		PA95	0.027
		PA96	0.024

Table 7.2: The MGM values for all the groups in the unit of ml/g/min. There was a significant difference between the lean group (non-diabetic) and the diabetic groups (P values were <0.005).



7.5.3 Echocardiography:

Echocardiography was used to characterize the role of LAV in functional studies. Many different parameters can be obtained using echocardiography, but we have chosen to focus on cardiac output (CO) and left ventricular ejection fraction (LVEF) as better comparators with our PET/CT results (table 7.3-7.4). Table 7.3 provides the mean HR, EF%, CO and LV mass for all mice (mice for PET/CT that were also used in histological studies). The CO and LVEF% was significantly higher in the lean control group (non-diabetic) compared to the diabetic groups (Figure 7.6-7.7), while both parameters were similar in the three diabetic groups. However, when adding the echocardiography data for the harvested mice, we observed a statistical difference between the diabetic groups as can be seen in table 7.4 and figures 7.8-7.9. The larger sample size in the echocardiography data, when including both the scanned and harvested mice, revealed a statistical difference between the LAV group compared to the other diabetic groups for both functional parameters (the CO and LVEF%) as in figures (7.8-7.9).

	Mice Group	Mice ID	HR	Ejection fraction%	Cardiac output (ml/min)	LV mass (mg)
Diabetic mice	NV	PA85	433.930993	62.610172	15.699646	84.700259
		PA86	448.109538	76.474949	15.435991	112.939812
		PA87	443.008768	78.466467	14.437056	107.968245
	WT	PA91	458.160993	65.119227	17.72038	89.149981
		PA92	449.929698	75.477833	14.963909	84.155673
		PA93	449.648712	79.685441	12.86803	72.544914
	LAV	PA85	459.550024	82.426317	15.557526	80.780513
		PA86	456.780333	71.790507	17.320126	79.4936
		PA87	455.62411	84.847426	18.160426	88.577606
Non-diabetic mice	LC	PA94	460.358056	97.444579	21.224636	122.979011
		PA95	459.110473	98.506749	22.24266	152.688008
		PA96	459.256897	97.664174	21.874793	99.85695

Table 7.3: Echocardiography (at week 13) for all mice groups that were scanned with PET/CT scanner.

Parameter	Age (weeks)	NV	WT	LAV	LC
HR (beats/min)	8	431 ± 7	439 ± 6	430 ± 8	453 ± 5
	13	448 ± 8	449 ± 4	446 ± 4	464 ± 5
LVEF%	8	74.9 ± 1.4	76.3 ± 2.0	75.4 ± 1.1	78.0 ± 0.7
	13	70.8 ± 0.9	70.5 ± 1.5	76.3 ± 0.9	77.3 ± 2.1
CO (mL/min)	8	19.9 ± 0.7	18.6 ± 0.8	17.8 ± 0.7	20.1 ± 0.8
	13	19.5 ± 0.7	17.7 ± 1.0	21.9 ± 0.7	19.9 ± 0.8
LV Mass (mg)	8	117 ± 9	111 ± 7	116 ± 4	138 ± 13
	13	132 ± 9	133 ± 11	148 ± 11	145 ± 12

Table 7.4: The echocardiography results for all mice in the four groups. The healthy LC group was significantly higher in all the parameters compared to the diabetic groups at 13 weeks. Importantly, there was a statistical difference between the LAV group vs. the other two diabetic in terms of LVEF%, CO and LV mass at 13 weeks.

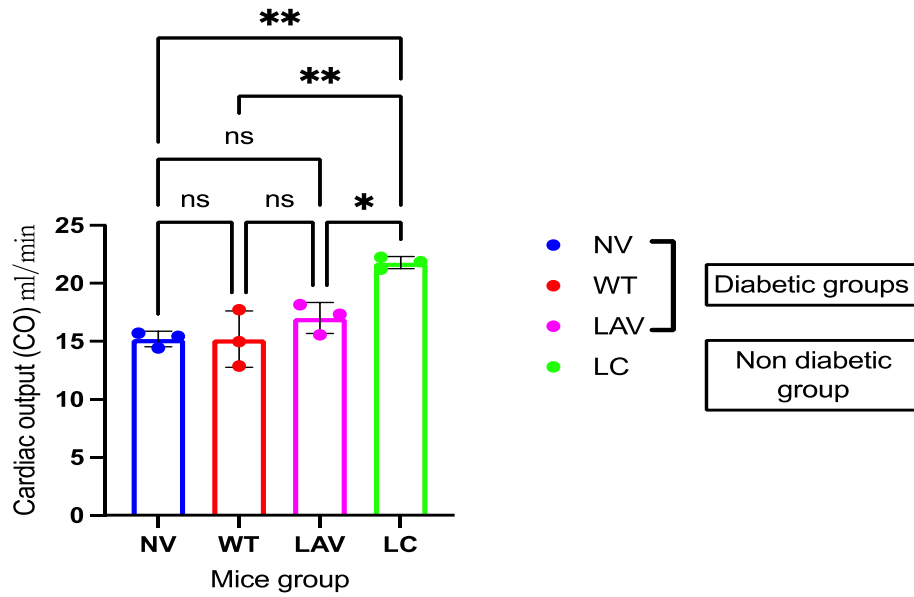


Figure 7.6: The CO (ml/min) measured by the echocardiography (at week 13) for the PET/CT scanned mice groups. Data shown as individual values, mean and SEM. There was no statistical difference between the diabetic groups in which $p > 0.05$. However, the CO was significantly higher in the LC (non-diabetic) group compared to the diabetic groups. Symbols $*p < 0.05$, $**P < 0.005$ indicate statistical difference. The one-way ANOVA was used for the statistical analysis in the data presented.

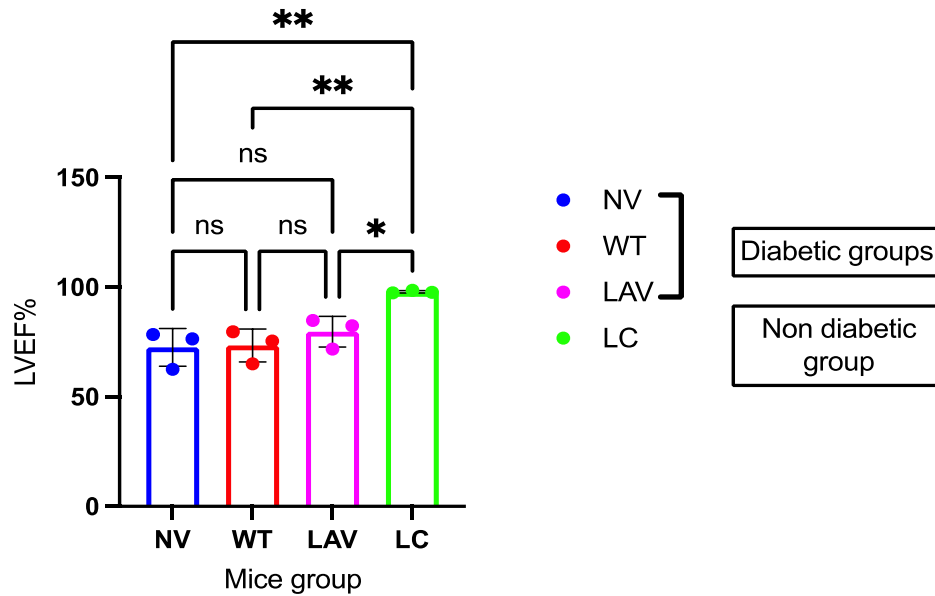


Figure 7.7: The LVEF% measured by the echocardiography (at week 13) for the PET/CT scanned mice groups. Data shown as individual values, mean and SEM. There was no statistical difference between the diabetic groups in which $p > 0.05$. However, the LVEF% was significantly higher in the LC (non-diabetic) group compared to the diabetic groups. Symbols $*p < 0.05$, $**P < 0.005$ indicate statistical difference. The one-way ANOVA was used for the statistical analysis in the data presented.

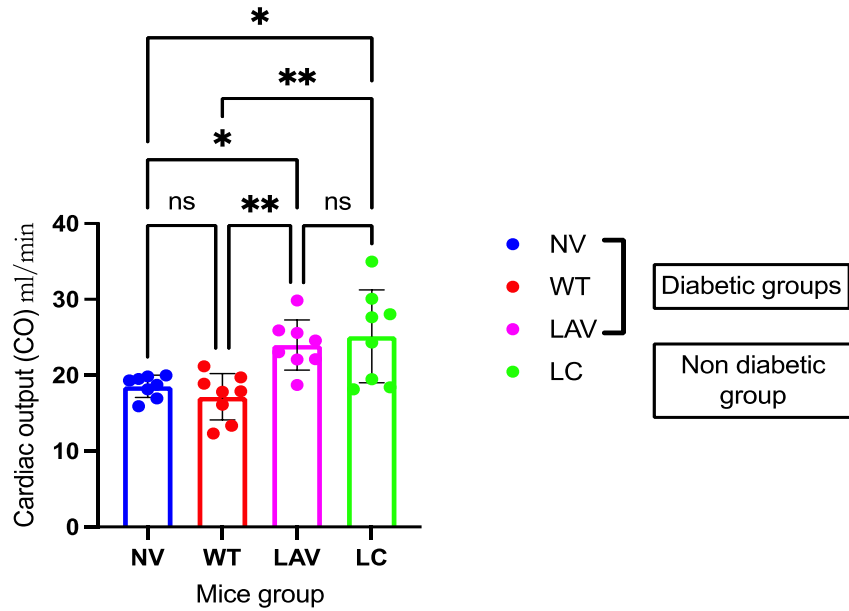


Figure 7.8: The echocardiography CO (ml/min) for all mice groups (at week13) including the scanned and harvested ones (n=8/group). There was a statistical difference between the LC compared to the WT and NV (diabetic groups). The CO values of the LAV group were statistically higher than the other diabetic groups (WT and NV). Symbols * $p < 0.05$, ** $P < 0.005$ indicate statistical difference. The one-way ANOVA was used for the statistical analysis in the data presented.

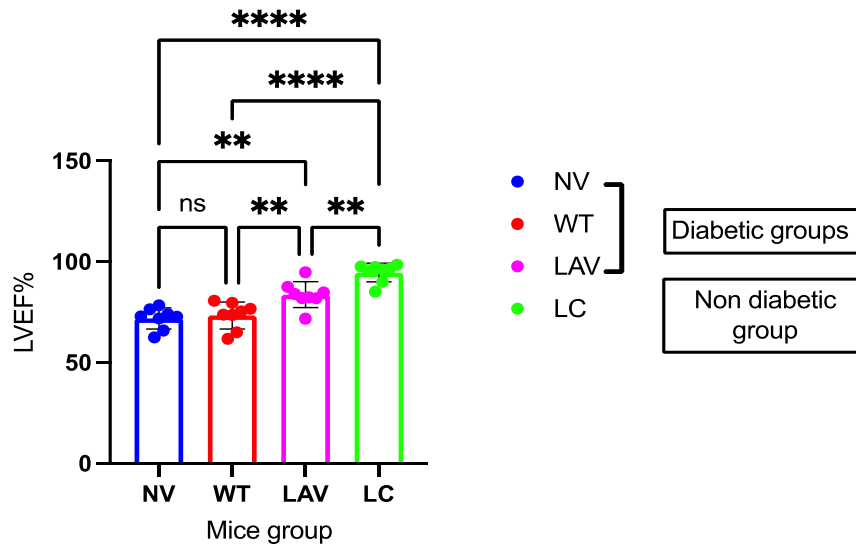


Figure 7.9: The echocardiography LVEF% for all mice groups (at week 13) including the scanned and harvested ones (n=8/group). There was a statistical difference between the LC compared to the diabetic groups. The LVEF% values for the LAV group were statistically higher than the WT and NV (diabetic) groups. Symbols * $p < 0.05$, ** $P < 0.005$, *** < 0.0005 and **** $P < 0.0001$ indicate statistical difference. The one-way ANOVA was used for the statistical analysis in the data presented.

7.5.4 Histological data:

The results of capillary and arteriole density measurements are presented in table 7.5 and figures 7.10 and 7.11. The LAV group has a significant increase in the capillary and artery density compared with the other diabetic groups including NV and WT as in figures 7.10 and 7.11. In addition, the LC group exhibited the highest capillary density and artery density, as expected, when compared to the NV and WT groups.

	Mice Group	Mice ID	Capillary density (number/mm ²)	Artery density (number/mm ²)
Diabetic mice	NV	PA21	118.9	55.1
		PA22	133.1	46.8
		PA24	118.1	35.5
		PA26	153.0	65.2
		PA15	136.4	57.2
		PA16	140.5	29.9
		PA40	171.9	34.7
	WT	PA7	139.8	34.0
		PA8	147.4	51.4
		PA9	144.8	63.8
		PA10	156.0	52.0
		PA11	140.3	66.4
		PA12	143.6	37.7
	LAV	PA27	144.2	31.2
		PA17	176.3	50.7
		PA18	179.8	67.7
		PA19	155.6	64.3
PA20		174.7	49.7	
PA32		207	87.9	
PA37		180.3	72.5	
Non-diabetic mice	LC	PA42	194.4	78.9
		PA52	173.4	95
		PA53	186.2	95.1
		PA58	240.8	90.7
		PA59	222.8	81.1
		PA60	241.8	79.4
		PA62	237.6	85.3
PA63	195.8	76.1		

Table 7.5: The capillary and artery density of all the harvested mice groups.

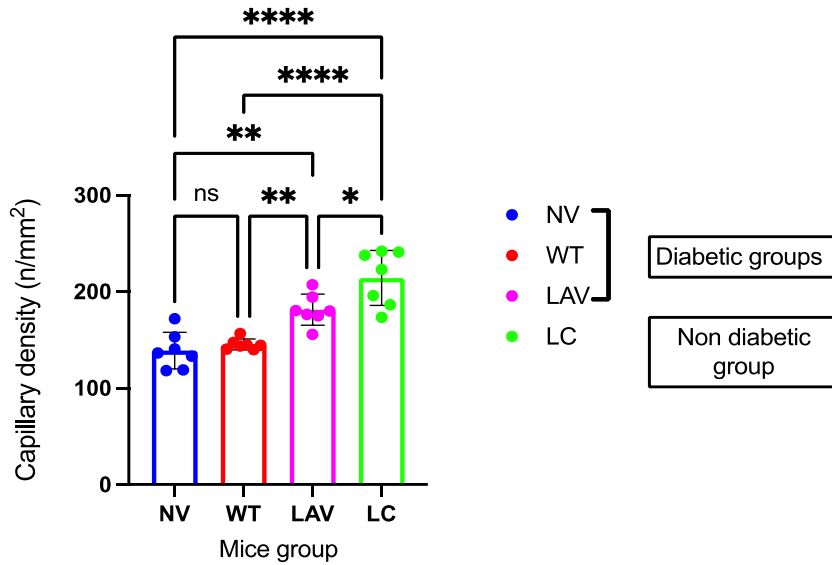


Figure 7.10: The Capillary density (unit of n/mm^2) in the four groups. There was a significant difference between the LC (non-diabetic) and the three diabetic groups. In addition, there was also a significant increase in the capillary density in the LAV group compared to the other diabetic ones. Symbols $*p < 0.05$, $**P < 0.005$, $*** < 0.0005$ and $**** P < 0.0001$ indicate statistical difference. The one-way ANOVA was used for the statistical analysis in the data presented.

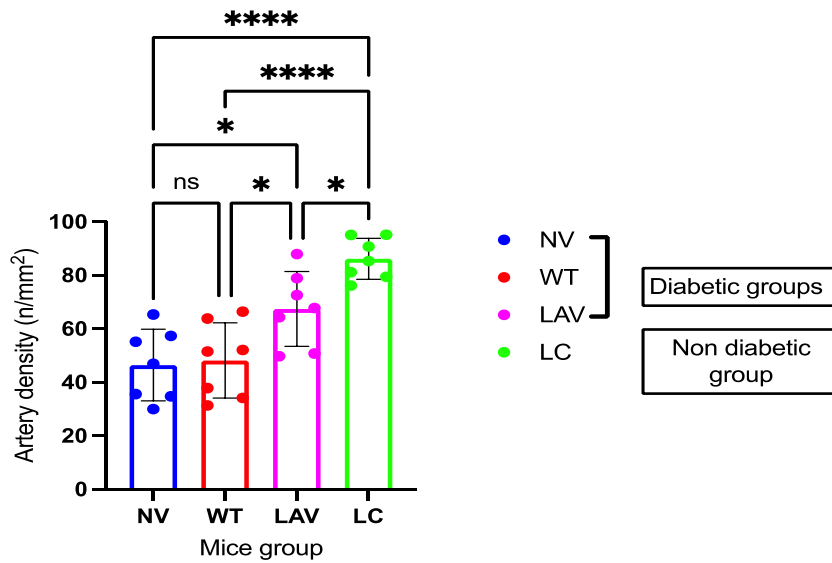
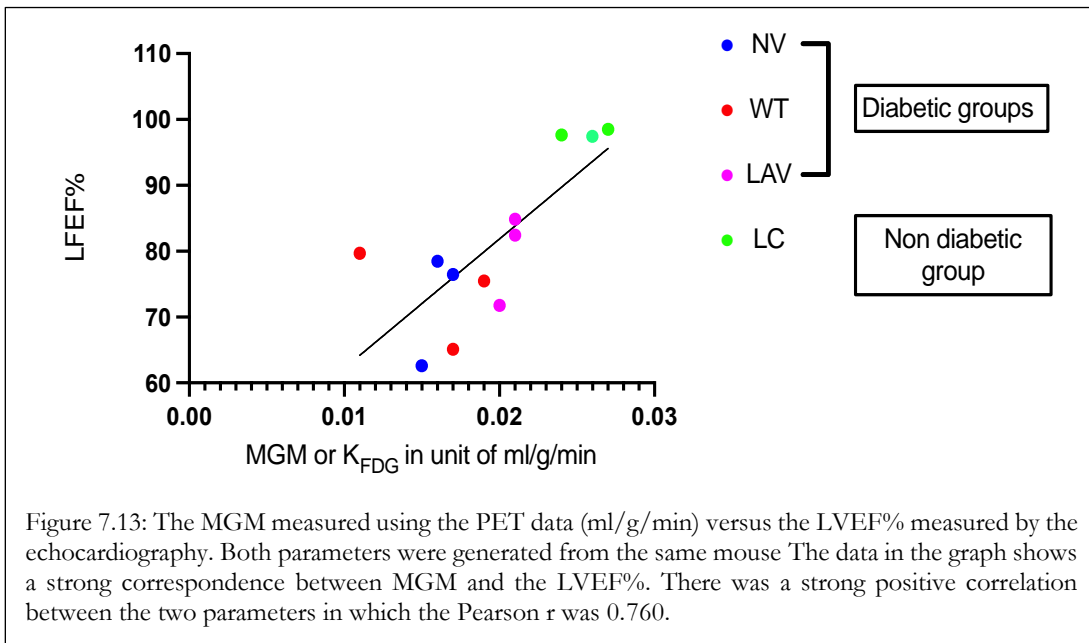
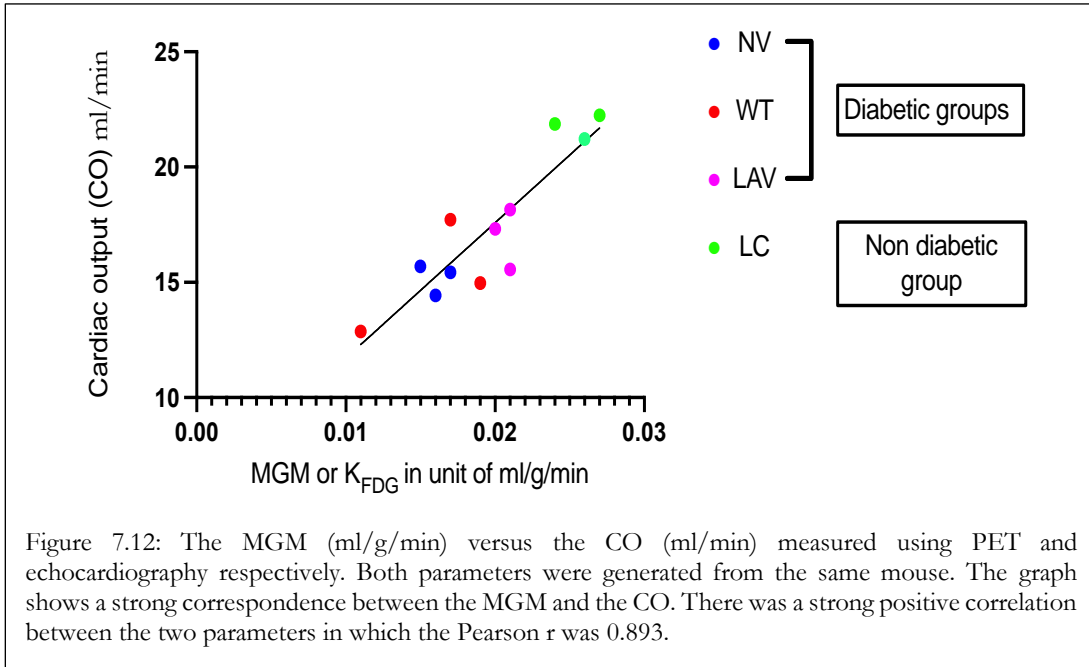


Figure 7.11: The artery density (unit of n/mm^2) in the four groups. There was a significant difference between the LC (non-diabetic) and the three diabetic groups. In addition, there was also a significant increase in the artery density in the LAV group compared to the other diabetic ones. Symbols $*p < 0.05$, $**P < 0.005$, $*** < 0.0005$ and $**** P < 0.0001$ indicate statistical difference. The one-way ANOVA was used for the statistical analysis in the data presented.

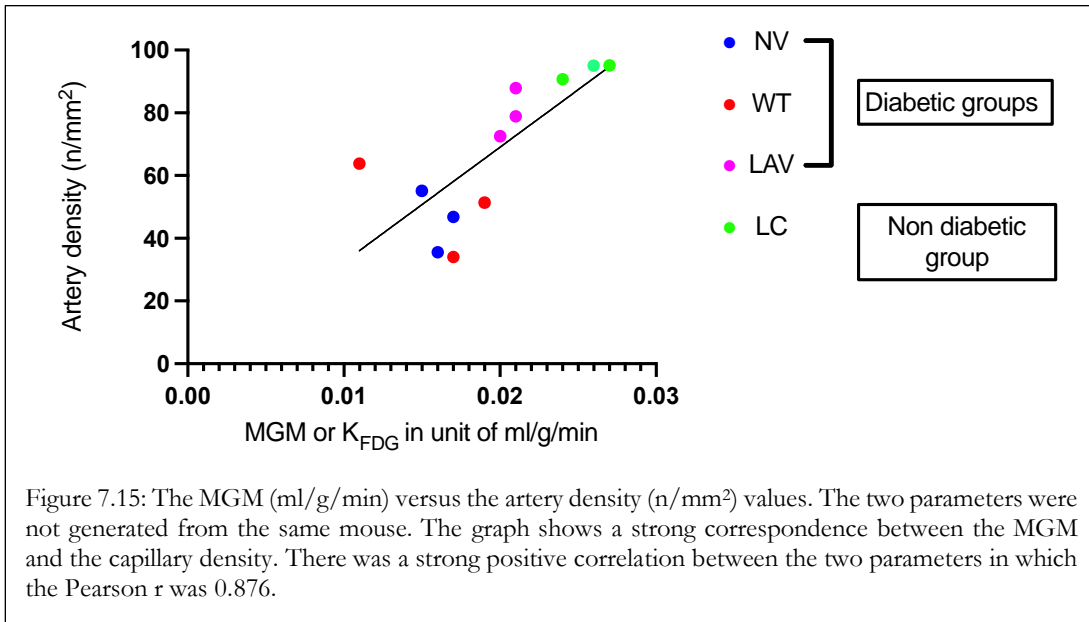
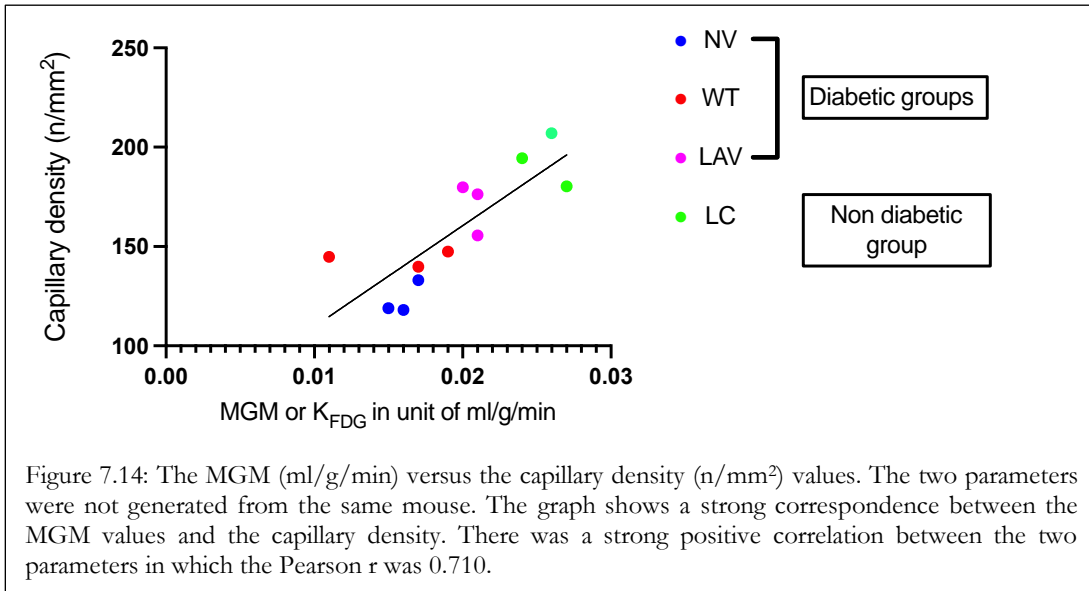
7.5.5 PET comparison with echocardiography:

There was a strong positive correlation between our MGM results (as a full quantitative tool) and the echocardiography functional parameters, including CO and LVEF%. Both the PET and echocardiography data were measured using the same mouse. The correlation Pearson r was 0.893 between the MGM and CO, while it was 0.760 between MGM and LVEF% as in figures 7.12-7.13.



7.5.6 PET comparison with the histology data:

The capillary and artery density data were compared to the MGM PET results although the histological data were not generated from the same mouse. There was a strong positive correlation between our MGM results and the capillary and artery density as in figures 7.14-7.15. The correlation Pearson r was 0.710 between the MGM and the capillary density, while it was 0.876 between MGM and the artery density.



7.6 Discussions:

DM is a complex metabolic disorder that results from an imbalance in the level of circulating glucose caused by an abnormality in the secretion of insulin (as in T1D) or its absorption (T2D) (Tsalamandris et al. 2019). In fact, persistent hyperglycaemia (high blood glucose) in DM might lead to many pathophysiological changes because it can promote oxidative stress resulting in an abnormal level of reactive oxygen species (ROS) that inhibits Ca^{+2} mobilisation and activates proapoptotic signals (Galicia-Garcia et al. 2020). Moreover, hyperglycaemia could boost the formation of advanced glycation end-products (AGEs) and finally, may alter gene expressions or cause organ failure (Giri et al. 2018; Tsalamandris et al. 2019; Galicia-Garcia et al. 2020). Importantly, there is a well-established relation between DM, as a metabolic disorder and inflammatory disorders (Giri et al. 2018; Tsalamandris et al. 2019). Therefore, many investigations have focused on using diabetic models while suppressing or enhancing various inflammatory pathways and monitoring their effects on the disease progression (Wendt et al. 2002; Alexandraki et al. 2006; Rajesh et al. 2010; Tabas and Glass 2013; Wada and Makino 2013; Wang et al. 2016b).

A genetic study reported that the presence of the LAV-BPIFB4 gene under a homozygous genetic model is related to the extreme age of LLIs (Villa et al. 2015a; Spinelli et al. 2017; Villa et al. 2018; Faulkner et al. 2020). The authors hypothesised that this gene variant could play a protective role against disease and ageing processes, possibly due to its ability to enhance endothelial vasorelaxation and revascularisation through increasing eNOS activation, and stimulating a stress response by upregulating the heat shock proteins, proteostasis (protein homeostasis), and protein synthesis (Villa et al. 2015a; Puca et al. 2020; Ciaglia et al. 2022).

In this study we sought to explore whether LAV-BPIFB4 gene therapy can inhibit the early development of cardiomyopathy in T2D murine models, and how LAV may exert any positive effect. The PET/CT arm of the study was an arm of a larger study which we published in 2020 (Dang et al. etc). Glucose uptake and metabolism can be used as biomarkers for cardiac function which we chose to evaluate through the measurement of SUVs and MGM, respectively. We then compared the SUVs and MGM generated from the LV region of the dynamic PET scans with echocardiography and vascular density measurements of the LV.

We found a decreased FDG uptake (SUV assessments) and increased subcutaneous fat in all animals in the diabetic groups. This, plus the glucosuria measurements, confirmed the state of T2D in these mice (Thorn et al. 2013; Ko et al. 2017). We similarly found that MGM (representing glucose

metabolism and phosphorylation) was lower in the diabetic animals than the lean animals. The LAV group values were similar to other diabetic groups, suggesting that AAV9-LAV-BPIFB4 gene therapy does not promote glucose uptake (SUVs) and metabolism (MGM). These results were consistent with our work (Dang et al. 2020) in which the plasma glucose level values were similar among the diabetic groups including the LAV treated one (Dang et al. 2020). Importantly, we have not measured the plasma glucose levels before PET scanning. Before discussing possible explanations for these findings, it is important to reiterate that T2D has a complicated pathological basis that is linked with multiple metabolic or signalling pathway disorders.

A possible explanation might be not having allowed enough time for the LAV-BPIFB4 gene therapy to produce the potential therapeutic effect that can raise the SUVs and MGM in the treated group. This is unlikely, however, as the timeframe was sufficient for us to observe the benefits of the LAV therapy in the echocardiography, histological and molecular biology measurements as represented previously (Dang et al. 2020)). Shoghi et al. (Shoghi et al. 2008) performed PET imaging on Zucker fatty rats and found that metabolic alterations, such as glucose uptake and metabolism, were apparent only at the later stages of diabetes. It is possible that extending the time of our study in DbDb mice may have allowed us to observe changes in SUV and MGM. Our PET/CT scanning was performed at week 14, which might be considered as neither early nor late stage T2D.

Although the LAV-BPIFB4 gene therapy did not cause changes in glucose uptake and metabolism in its treated mice, we noted increased hair regrowth in the LAV-treated mice compared with the other diabetic mice. This observation may be explained by previous findings by our collaborators, which included upregulation in eNOS activity and increased production of NO resulting in increased vasorelaxation (Villa et al. 2015a; Spinelli et al. 2017; Malavolta et al. 2019). Hair loss in diabetes is thought to be caused by many factors including inflammation and a reduction in NO availability (Cotsarelis and Millar 2001; Sasaki et al. 2018). While NO is associated with changes in innate immunity, it also contributes to vascular relaxation and may act in promoting hair growth by increasing blood flow in the hair root (Cotsarelis and Millar 2001; Clark et al. 2010; Lombardo and Lamattina 2012; Jampa-Ngern et al. 2017). Accordingly, the higher rate of hair re-growth in the LAV-BPIFB4 treated mice may be due to the upregulation of eNOS activity and the subsequent rise in NO caused by the LAV-BPIFB4 gene. Importantly, we demonstrated that the LAV gene induced the SDF-1/CXCR4 duo signalling pathways (Dang et al. 2020). A subset of haematopoietic cells, which is part of the pro-angiogenic bone marrow (BM) cells, offers vascular support as well as endothelial progenitor cells (EPCs) which could differentiate into vascular cells during certain conditions

(Valenzuela-Fernández et al. 2002; Ratajczak et al. 2006; Petit et al. 2007). Recent studies indicated that the SDF-1/CXCR4 duo play a crucial role in recruiting CXCR4+ BM cells towards the neo-angiogenic niches, and subsequently, in enhancing the vascularisation process (Valenzuela-Fernández et al. 2002; Ratajczak et al. 2006; Petit et al. 2007). In fact, this is a likely explanation for the increased capillary and artery density that we recorded in the LAV-treated group, which will be addressed in the next sections.

The echocardiography data (at week 13) for the twelve mice that were scanned using PET/CT imaging revealed a reduction in the echocardiography parameters in the diabetic groups compared to the LC group. This was reported previously in diabetic mice due to the possible effect of diabetes in inducing LV dysfunction (Hamdani et al. 2014). When comparing the echocardiography data of the diabetic mice, we found no significant difference among them in terms of EF%, CO and LV mass (despite a trend to improvements in the LAV-treated group), and these results were comparable to our PET data. However, it is likely that these findings are because of the small number of animals in each group. When data from the remaining animals were added, LAV-treatment was found to be beneficial, resulting in increased end systole, end diastole, SV, and CO, leading to a considerable improvement in their EF% values as can be observed in figures 7.8-7.9. Indeed, many parameters were similar to those found in the lean (control) animals. The improvement in the cardiac performance, represented by the CO and LVEF%, are most likely due to the ability of the LAV gene to induce both eNOS signalling as well as the SDF-1/CXCR4 signalling pathways. As addressed earlier in this chapter, the eNOS enzyme is one of the NOS enzymes responsible for synthesising NO molecules, which is known to cause vasodilation and increase blood flow (Zhao et al. 2015; Spinelli et al. 2017; Dossena et al. 2020). The SDF-1/CXCR4 signalling also has been linked with improved vascularisation and angiogenesis, possibly through increasing the expression of MyHC- α protein and reducing myocardial fibrosis (Dang et al. 2020). We reported an increased level of circulating SDF-1 in the LAV treated mice as well as an increased expression of MyHC- α , which is a contractile protein important for the restoration of the endothelium (Korte et al. 2005; Dang et al. 2020). A study using diabetic murine models, reported a downregulation of MyHC- α protein among them (Rundell et al. 2004).

In our histological analysis, we reported an increase in the capillary and artery density (figures 7.10-7.11) which was expected due to the above discussed reasons including the induction of the SDF-1/CXCR4 duo that induced the expression of MyHC- α and enhanced vascularisation and angiogenesis.

One last thing to mention is the reason behind having an improved contractile function, represented by the CO and LFEF%, but having similar MGM values among the four groups. As previously outlined, fatty acid oxidation is the primary energy source in normal myocardium, followed by glucose and lactate (Taegtmeyer et al. 1980). In diabetic myocardium, the contribution of glucose to the total myocardial energy supply is reduced due to insulin resistance, leading to an increased reliance on fatty acids as the main energy source (Saddik and Lopaschuk 1994). Indeed, glucose only contributes to a part of the total ATP synthesis by the oxidative metabolism (Kolwicz et al. 2013). Interestingly, a study using a transgenic mouse, which was deficient in an insulin independent glucose transporter (GLUT1), reported a rise in glucose uptake and glycolysis without a change in the cardiac output values (Luptak et al. 2007). Their results might explain the reason behind having a rise in the CO without observing an alteration in the glucose uptake and metabolism.

Gathering these results can explain the strong correlation that we measured between our PET data and both the echocardiography and histological data.

7.7 Conclusion:

Small PET/CT imaging allows the quantification of the metabolic state of the heart; thus, it provides a unique platform to evaluate novel therapeutic attempts that can possibly be translated clinically. In this chapter, we used micro-PET/CT with ¹⁸F-FDG to quantify myocardial glucose uptake and metabolism in T2D murine models. Our work was a part of larger study (Dang et al. 2020) in which we did not detect changes in glucose uptake and metabolism within the LAV-BPIFB4 treated mice. We performed a direct comparison between PET data and echocardiography results at week 13, and found that they were comparable, with no significant changes in EF%, CO and LV mass between the four groups. However, this lack of effect for LAV-treatment is likely to be due to the small number of animals in each group. When data from all the animals were included, a significant improvement in EF%, CO, and LV mass in the LAV-BPIFB4 group with respect to the other diabetic ones as our previously published work (Dang et al. 2020). Our histological analysis showed interesting findings, in which the LAV group had a significant increase in capillary density with respect to the control diabetic groups.

The present results are significant in two major respects, including the echocardiography of all mice as well as the histological analysis. Overall, those findings demonstrated that LAV-BPIFB4 gene therapy enhances the cardiac function allowing the myocardium to withstand diabetes-induced stress through improving its systolic performance and contractility.

In conclusion, the LAV-BPIFB4 gene enhanced capillary density which resulted in an increase in vascularisation, angiogenesis, blood flow and ultimately, a significant improvement in the cardiac performance. In the next chapter, we will investigate the effect of LAV-BPIFB4 gene in ageing mice.

Chapter 8:

The therapeutic effect of longevity-associated variant (LAV)-BPIFB4 gene therapy on ageing model

8.1 Introduction:

8.1.1 Aging and Cellular Senescence:

Ageing is a biological phenomenon that is characterized by progressive deterioration in the tissues and organs of the body, resulting in a general decline in physiological homeostasis (the capability of the body to maintain vital physiological parameters such as blood pressure and blood glucose) and death (Balcombe and Sinclair 2001; Melzer et al. 2020). Common hallmarks of ageing, which occur at molecular and cellular levels, include hair loss, loss of skin elasticity, muscle weakness, decrease in immune competence, and increased susceptibility to many common diseases such as CVDs, osteoarthritis, T2D and Alzheimer's disease (Balcombe and Sinclair 2001; Melzer et al. 2020).

Senescent cells have a reduction in replicative capacity due to telomere attrition (Balcombe and Sinclair 2001). They also undergo morphological and organelle alterations, such as cell and mitochondrial enlargement, increased ROS and oxidative stress, and changes to the cytoskeleton (Hwang et al., 2009; Zhang et al., 2007). While cellular senescence occurs in all cells, tissues, and organs (Hwang et al. 2009), CVDs poses the greatest burden on older adults (Balcombe and Sinclair 2001). With age, the CVS exhibits several structural and functional alterations in the myocardium and the vascular components (Ferrari et al. 2003).

The aged myocardium can be quite anatomically and physiologically different from young animals (Khan et al. 2001). These changes include a reduction in the total number of cardiomyocytes, increased LV wall thickness, endothelial cell dysfunction, arterial stiffening and fibrosis, all of which can lead to a higher risk of MI and heart failure (Gerstenblith et al. 1977; Anversa et al. 1990; Anversa et al. 1994; Lakhan and Harle 2008). With age, there are often considerable decreases in the LV diastolic filling, myocardial oxygen consumption and coronary blood flow (Lakatta et al. 1975; Schulman 1999;

Fajemiroye et al. 2018). These age-related changes are responsible for the generalized decline the physical condition among the aged individuals.

CVS ageing in healthy mice is similar to that found in humans (Dai and Rabinovitch 2009), and their short lifespan makes them a good model to study ageing. A mouse at the age of 24 months is approximately equivalent to a human in the seventh decade as illustrated in figure 8.1 (Dutta and Sengupta 2016). The echocardiography of C57Bl/6 24 months aged mice revealed a significant increase in LV mass index, and a reduction in both the fractional shortening (FS) and the diastolic function (Dai and Rabinovitch 2009). The same study also reported that the aged mice suffered from cardiac hypertrophy, significant decline in the oxygen consumption, less exercise capability and a considerable reduction in the cardiac performance and output.

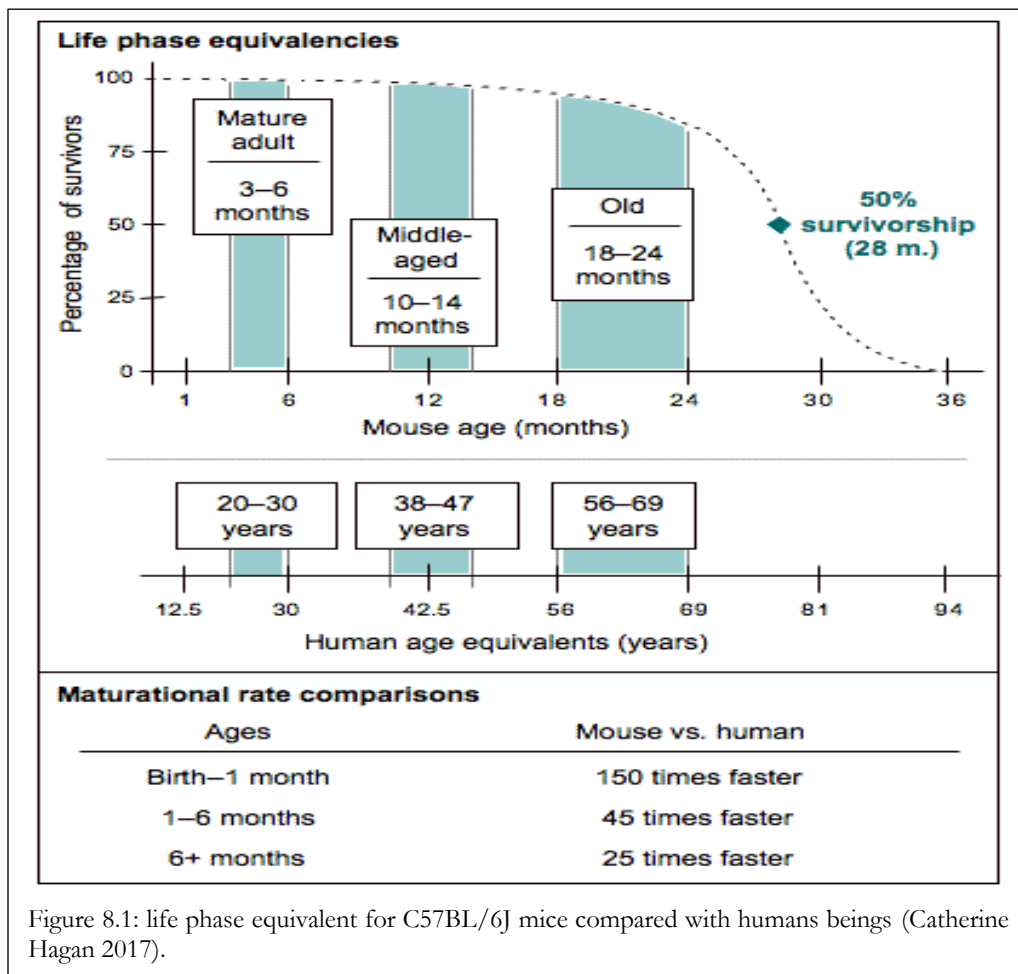


Figure 8.1: life phase equivalent for C57BL/6J mice compared with humans beings (Catherine Hagan 2017).

Recent research aims to improve health and disease prevention through anti-ageing using gene therapy. This therapeutic approach is a promising field in preventing or treating chronic or polygenic diseases that is linked with age. Recent study in elderly mice showed that LAV-BPIFB4 gene therapy increases endothelial vasorelaxation and revascularization through potentiating eNOS activity and enhancing NO production thus delaying ageing (Malavolta et al. 2019). This findings was further supported by other investigations where the authors reported that the high level of BPIFB4 isoforms in LLIs serum stimulated adaptive stress responses and proteostasis, which are two vital aspects linked with exceptional longevity, the maintenance of the stem cells, and the improved survival of the organism (Vilchez et al. 2014; Villa et al. 2015a).

In the previous chapters we reported that while the LAV variant didn't induce glucose metabolic changes in T2D model, but it increased the LV capillary density, accelerated hair growth, and reduced endothelial dysfunction via unknown mechanisms (Dang et al. 2020).

In this chapter we will investigate the therapeutic effect of LAV therapy on ageing through measuring its impact on the MBF, during rest and stress conditions, and MGM using $^{13}\text{N-NH}_3$ and $^{18}\text{F-FDG}$ respectively. Additionally, we will also examine the short- and long-term effect of LAV gene therapy in aging. Finally, a direct comparison between the PET results and the echocardiography and capillary data will be performed.

8.2 Objective:

1. Evaluate the effect of the LAV-BPIFB4 gene on MBF and MGM with respect to three control groups.
2. Assess the short and long effects of the LAV-BPIFB4 therapy, using MBF.
3. Compare the data from our PET/CT scans with histological and high-performance echocardiography results.

8.3 Materials and Methods:

8.3.1 Study design:

All procedures conformed to the guidelines of British Home Office and Bristol University (Project License PPL 30/3373) and The Care and Use of Laboratory Animals Guide (The Institute of Laboratory Animal Resources, 1996). The first cohort of mice were included in the '*early treatment*' experiments and consisted of 42 14-month-old C57BL/6 female mice and 12 14-month-old male mice (12 female and 3 male mice per group) as in figure 8.2. These mice were followed up for 4 months. Forty 18-month-old C57BL/6 female mice were used in the '*late treatment*' experiments (10

mice/group), and these mice were followed up for 1 month as in figure 8.3. Twelve female mice from each experiment were transferred to PETIC at the end of each study for PET/CT scanning and harvest of tissues (figures 8.2- 8.3).

In the early treatment group (figure 8.2), all mice underwent baseline echocardiography on arrival (ie at the age of 14 months). One week later, AAV or control solution was injected via the tail vein. Mice were assessed at least weekly for health and clinical signs. Four months after the gene therapy, the mice underwent echocardiography assessment, and the cohort of 12 mice (n=3 per group) transferred to PETIC to be scanned using micro-PET/CT and tissue harvest (for later capillary and artery density assessment).

Similarly, the late treatment group (figure 8.3) had a baseline echocardiography at age of 18 months. One week later, they were injected intravenously with the virus or control solutions. One month later the mice were assessed using echocardiography and then 12 mice transferred to PETIC for scanning and tissue harvest.

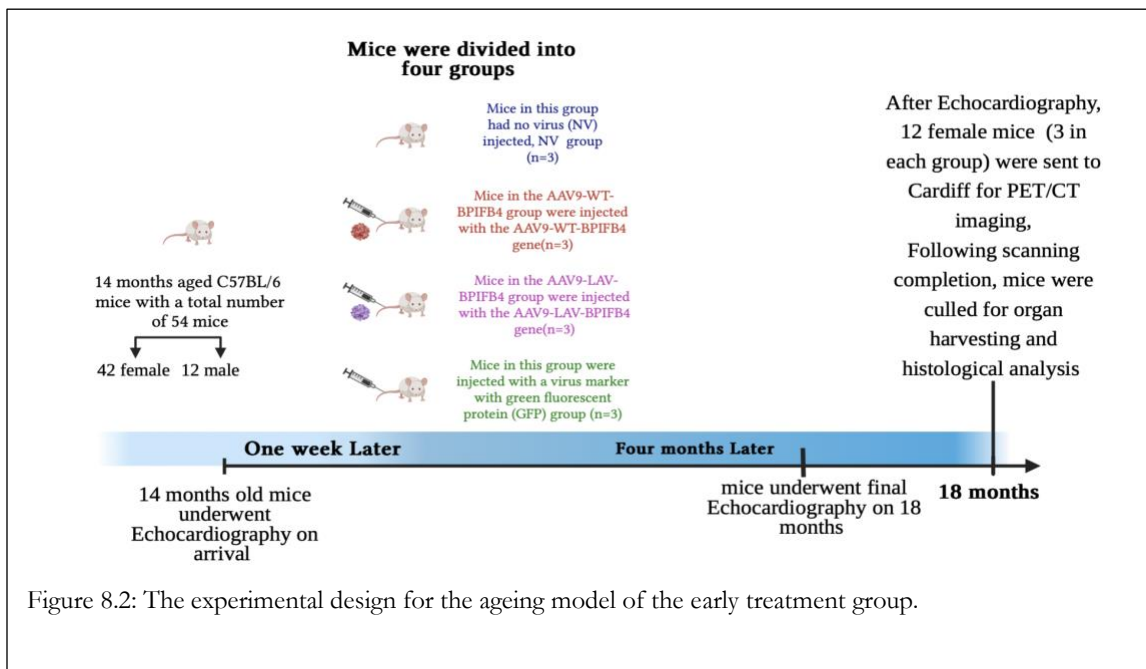
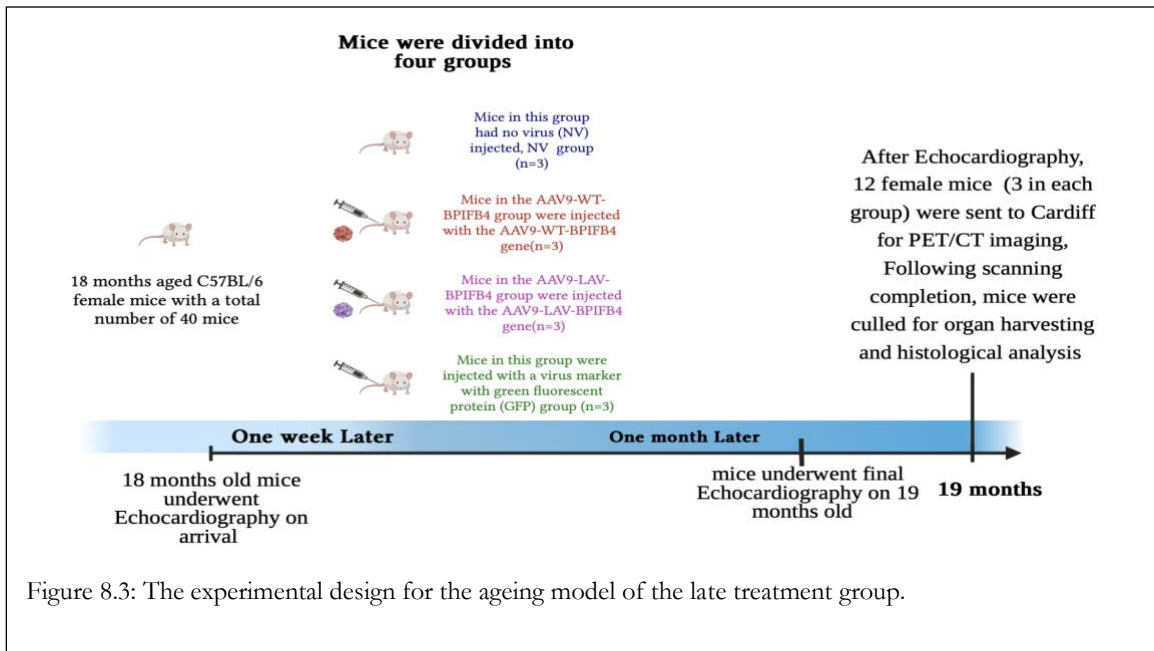


Figure 8.2: The experimental design for the ageing model of the early treatment group.



8.3.2 Animal groups:

As mentioned above, mice (Envigo, Bicester, Oxfordshire, UK) were divided into two groups, the early and late treatment groups, both of which were divided further into 4 groups (3mice/ group). The four groups were first anesthetized (with isoflurane 1.5-2%) and injected intravenously with either:

1. Control group: No virus (NV).
2. Control group: Wild-type isoform (WT) of the gene BPIFB4 or WT-BPIFB4.
3. Control group: A virus marker with green fluorescent protein (GFP) group.
4. Experimental group: Longevity-associated variant (LAV) of the gene BPIFB4 (LAV-BPIFB4).

8.3.3 Micro PET/CT Scanner:

The Mediso Nano-Scan 122S small-bore PET/CT imaging system manufactured by the Mediso medical imaging system, Budapest, Hungary. All the scanner specifications have been previously mentioned in the methodology chapter.

8.3.4 The used radiotracers:

$^{13}\text{N-NH}_3$ and $^{18}\text{F-FDG}$ was used to quantify the MBF and MGM respectively.

8.3.5 Animal preparation, scanning and tissue harvesting:

The previously validated imaging protocol sets were applied in this chapter. Mice were allowed to rest for one week following transfer from Bristol group, to avoid distress that could affect the quantification of the PET results. They were housed in normal cages with an environment of a 12-hour light-dark cycle. Cages were monitored on daily basis for temperature, humidity, water, and food supply. Furthermore, Weekly checks were also carried out in terms of appearance, weight and other signs that may originate due to their age.

From one week after transfer, PET/CT imaging was carried out for each mouse (with a maximum of 3 mice on each day). The scanning and termination procedures were performed in one day with the same imaging protocols and considerations explained in chapter 6.

On the scanning day, each mouse was fasted for one hour and warmed up to 37C° (inside a warming box for 5 minutes) for better visualization and cannulation process of the tail vein. After that, it was anesthetized using 3-5% of isoflurane and then transferred to a pre-warmed imaging scanner bed which was supplied with a small tooth bar (attached to a nose cone) and a pad to maintain both anaesthesia (using ~1.5-2% isoflurane of O₂ (1L/min) nose tube) and heart rate measurement respectively. Next, the mouse was cannulated in two different areas including IV and IP routes for the injection of the radiotracers and the pharmacological stress agent (dobutamine) respectively. Each mouse had three scans in total including a 10-minute ¹³N-NH₃ rest scan, a 10-minute ¹³N-NH₃ stress scan, 40-minute ¹⁸F-FDG and a CT scan. As our purpose in this chapter was only to measure the MBF only and not its metabolic trapping, the scanning duration of the ¹³N-NH₃ was reduced to 10 minutes dynamic scan. The total PET/CT scanning time for each mouse was approximately 35-45 minutes which was comparable to the scanning duration of the echocardiography (approximately one hour).

8.3.5.1 ¹³N-NH₃ rest scan:

During the image acquisition of each mouse, ¹³N-NH₃ (30-100 MBq in 20-60 ul) was injected through an IV cannula. Following the injection, a 10-minute dynamic PET scan was performed. The actual acquisition started a few seconds prior to the administration of ¹³N-NH₃ to catch all the myocardial flow process.

8.3.5.2 ¹³N-NH₃ stress scan:

Ten minutes later, the stress scan was initiated (without moving the animal) by IP injection of the dobutamine as a pharmacological stress stimulus (2.5 ug/kg in 50 ul). A 5-minute period was allowed in order for the cardiac stress event to occur before initiating the stress scan. When the heart rate

increased to about 600 bpm (measured by ECG pads placed on the paws), a second dose of $^{13}\text{N-NH}_3$ (30-100 MBq in 20-60 ul) was injected intravenously. Image acquisition was also initiated a few seconds prior to the radiotracer injection by applying the same image acquisition process as in the rest scan.

8.3.5.3 CT scan:

Following the $^{13}\text{N-NH}_3$ stress scan, a whole-body CT scan with a duration of 5 minutes (480 projections, 2 rotations, 50 Kev) was performed to calculate attenuation corrections as well as allowing the co-registration of images which in turn give a better visualisation of the structural and functional information from the CT and PET respectively.

8.3.5.4 $^{18}\text{F-FDG}$ scan:

Following the ammonia scans, an injection of ~ 20 MBq of $^{18}\text{F-FDG} \approx 20$ ul was administered via the same iv cannula line, and a 40-minute whole-body dynamic PET scan acquired immediately.

8.3.5.5 Mice termination, tissue collection and histological analysis:

Following scanning completion and while the mouse was under anaesthesia, 0.1-1 mL of blood was taken directly from the heart using an EDTA-coated syringe with 23-gauge needle (the syringe was kept in ice before blood withdrawal) via cardiac puncture technique. Death was confirmed by tissue harvest.

After determination of heart weight and dimension, the heart was cut into pieces (a top 2/3 section, and a lower third section). The top section of the heart, right kidney, aorta, chest skin, and the right adrenal gland were all drop-fixed in 4% PFA at RT for 24 h. The PFA was then replaced by PBS and the samples kept at 4°C.

The lower part of the heart was divided into LV (2 pieces) and RV and these, along with chest skin, left kidney, liver, plasma, left adrenal gland and urine, were flash-frozen in liquid nitrogen and kept in -80°C for later use.

8.3.6 Image Reconstruction for the PET/CT scans:

All PET scans were acquired in list mode acquisition and images were reconstructed with the same voxel size of 400 μm using interview fusion software. The frame sets of both rest and stress scans were as follow: 35 frames (12x5 secs; 18x30 secs, with a whole duration of 10 minutes).

CT scans were reconstructed with a 250 μm voxel size and the sinograms were produced using 2-dimensional filtered back projection method. Attenuation (CT based) and scatter corrections as well as normalization were applied to the reconstructed images. Following the reconstruction, all images were exported to PMOD software for data analysis using the kinetic modelling tool.

8.3.7 Medical Image analysis software for PET/CT scans:

PMOD was the software of choice for the MBF quantification using the kinetic modelling tool. The measurements of MBF in both rest and stress were carried out using $^{13}\text{N-NH}_3$ dynamic scans and 1TC model. The MGM quantification were performed using the FDG scans and 2TC model.

8.3.8 Echocardiography:

The echocardiography results were added to this chapter to explore the impact of LAV gene on the cardiac contractility and output in the aged mice groups and during early and late treatment (Dang et al. 2020). The procedures in this section were carried out by one of members in our research group. As described in the previous chapter, we used a Vevo3100 echocardiography system (Fujifilm VisualSonics Inc, Toronto, Canada) and MX550D transducer to measure a number of cardiac dimensional and functional parameters (Katare et al. 2010; Katare et al. 2011). During the experiment, each mouse was anesthetized using isoflurane starting with 2.5% and then this percentage was adjusted as appropriate to keep the heart rate close to 450 bpm. The echocardiography procedure generally lasted for about one hour.

8.3.9 Histological analysis:

I performed the histological analyses reported in this chapter. We wished to explore the effect of LAV therapy on capillary and arterial density in aged mice. Capillary and arterial density were assessed using sections of myocardium after immunohistochemistry staining, as described in the methodology chapter.

Sections were stained with isolectin GS-IB4 (IB4, I21414, Life Technologies, USA) and anti- α -smooth muscle actin (α SMA; C6198, Sigma, UK) to identify capillaries and arteries, respectively. Following successful staining, the sections were photographed using optical fluorescence microscopy (Zeiss Axio observer microscope, Cat # 1026044910, Germany). Next, the number of vessels were assessed with the aid of Image J software (Fiji version 2.5.0, USA). The total number of capillaries (IB4) (represented by the green colour) and mature arterioles (α SMA; represented by the red colour) were identified in at least 20 fields (20 X magnification). Final data were generated as the number of capillaries or arteries per mm^2 .

8.3.10 Statistical analysis:

Statistical analyses were carried out using GraphPad Prism (version 9.4.0, USA), through which data were represented with their individual values, mean and STD. After testing for normality, comparisons were generated using 1- or 2-way analysis of variance (ANOVA), as appropriate.

Moreover, the means of the four treated groups with respect to one variable were compared using 1-way ANOVAs, whereas 2-way ANOVA tests were used to examine the effect of gene treatment in the four groups with respect to two different variables (the response to the gene therapy at different time points). Differences were considered significant when $P < 0.05$.

8.4 Results:

The rest/stress myocardial perfusion imaging was performed successfully for most of the mice using $^{13}\text{N-NH}_3$ without complications. However, I experienced a cannula break in four mice during the stress. Importantly, during the MGM analysis of the FDG scans, we observed significant changes in the myocardium dimensions which was important issue will be investigated in future work. Therefore, the MGM analysis was excluded for future investigations. The overall PET/CT imaging time was approximately 35 to 45 minutes.

8.4.1 Rest perfusion imaging:

$^{13}\text{N-NH}_3$ was injected intravenously via the tail vein and the MBF values at rest for the early and late treatment groups are presented in tables 8.1. Interestingly, the LAV groups in both the early and late treatment experiments scored the highest resting MBF with a mean value of 5.058 ml/min/g, which was statistically different from the other control groups, as in figure 8.4.

The MBF values in the control groups were similar in both early and late treatments, as in figure 8.5. In contrast, the late treated LAV group had higher rest MBF values compared to the early treated group, suggesting that its therapeutic effect might diminish over time, as in figure 8.5.

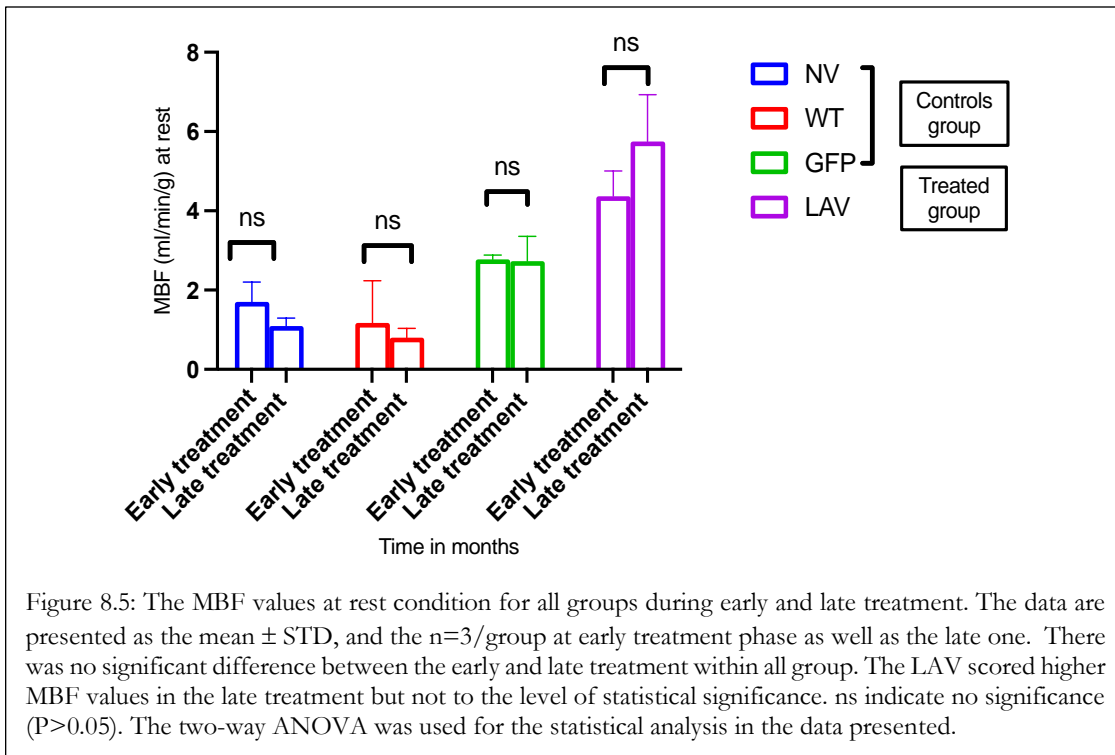
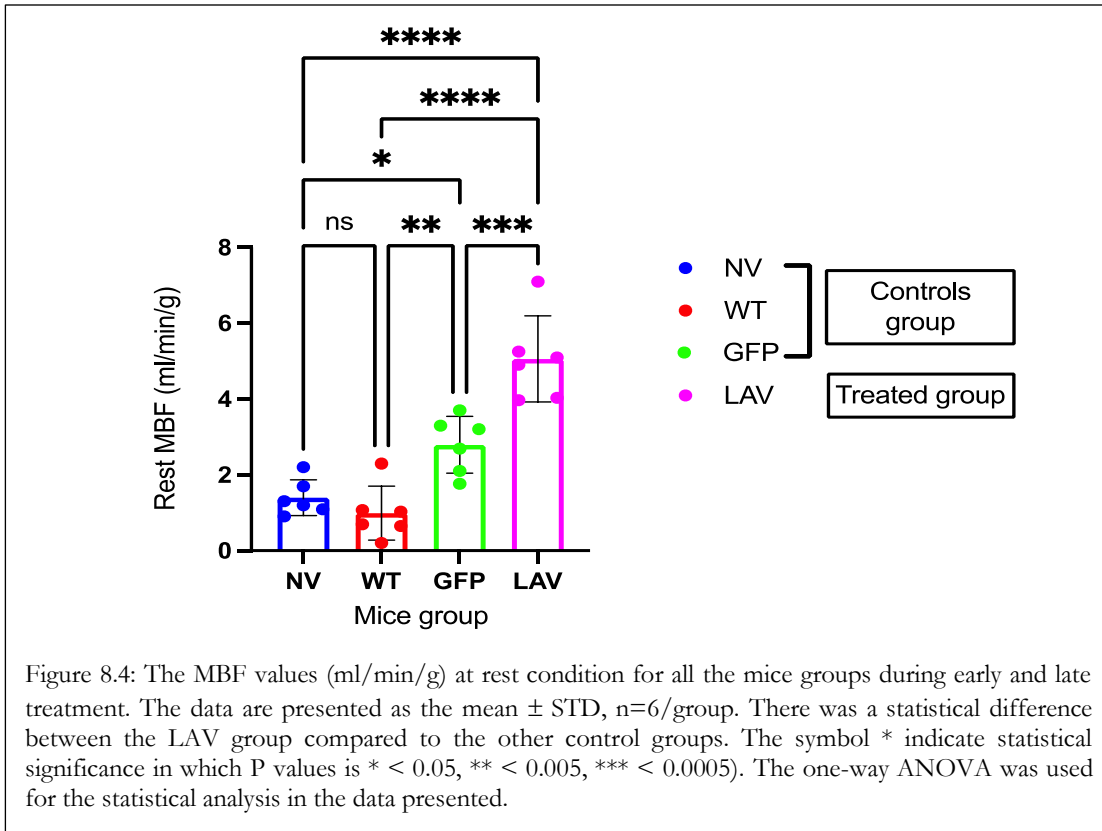
8.4.2 Stress perfusion imaging:

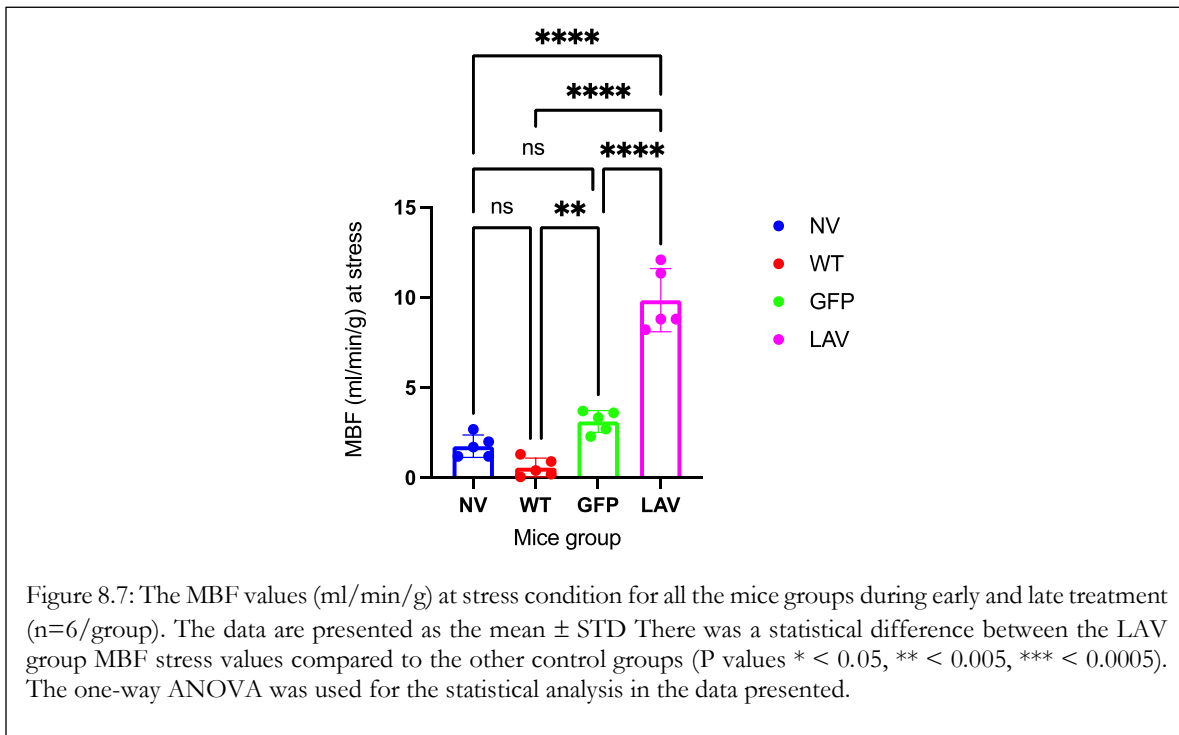
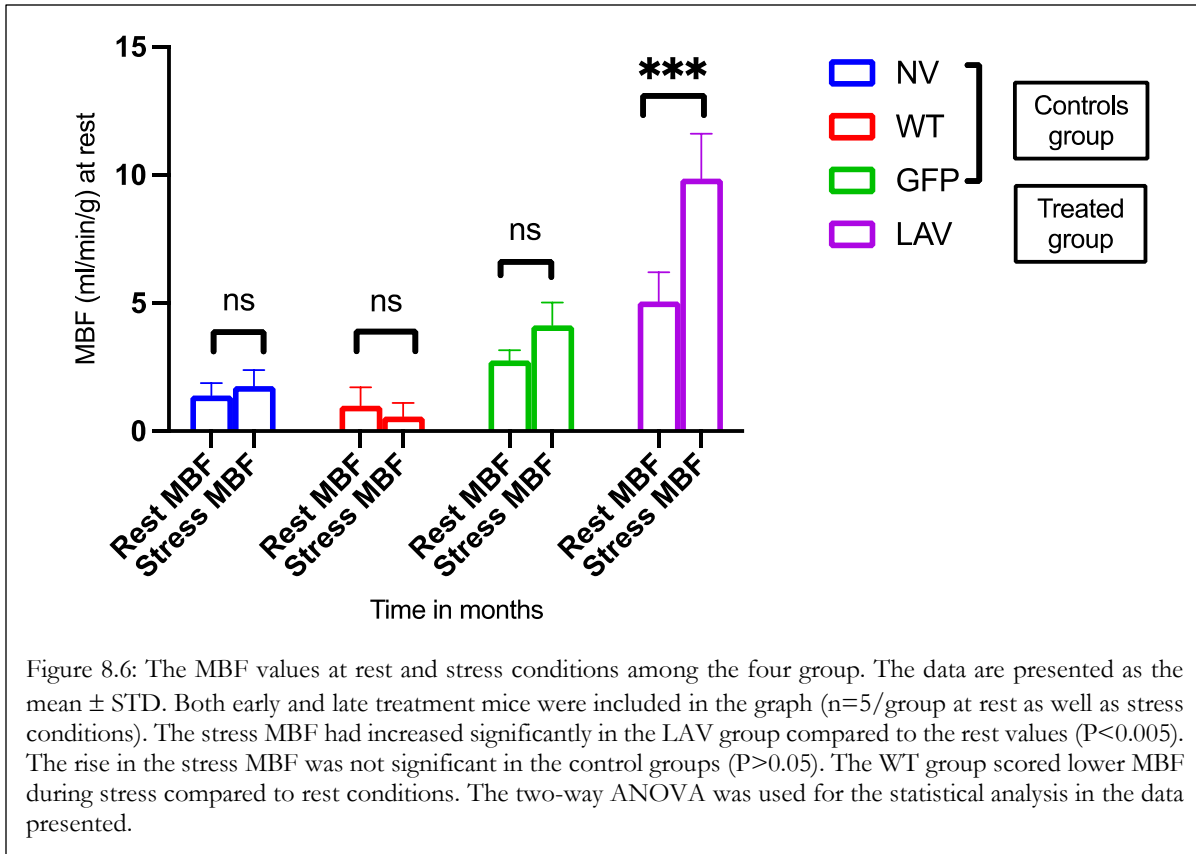
Although the stressor (dobutamine IP injection) resulted in an increased HR in all mice, we did not observe a corresponding increase in the MBF values in the NV, GFP or WT (table 8.1 and figure 8.6): in some mice, the injection of dobutamine lowered the MBF. In contrast, the MBF stress values for LAV were significantly higher than its values at rest condition ($p < 0.005$).

The LAV groups had the highest MBF values under stress conditions, which was significantly different from the stress MBF in the control groups ($P < 0.005$; figure 8.7).

Mice group	Longevity group	Mouse ID	Resting MBF in ml/min/g	HR (BPM) at rest	Stress MBF in ml/min/g	HR (BPM) at stress	CFR	CO ml/min
NV	Early treatment	PA 134	1.7	118-460	1.2	575-590	0.5	15.44
		PA 135	2.2	450-496	1.7	580-600	0.7	13.31
		PA 136	1.2	387-400	-	458-500	-	15.02
	Late treatment	PA 214	1.09	270-340	1.2	390-420	1.10	14.23
		PA 215	1.3	211-323	2.01	390-450	1.5	13.9
		PA 216	0.9	240-260	2.69	470-500	2.9	13.8
WT	Early treatment	PA 149	0.2	118-460	-	480-500	-	12.60
		PA 150	2.3	450-496	0.4	500-580	0.17	15.06
		PA 153	1.03	387-400	0.2	290-313	0.19	14.22
	Late treatment	PA 225	1.07	270-340	0.06	70-181	0.05	11.6
		PA 226	0.65	211-323	1.3	101-147	2	10.6
		PA 228	0.7	240-260	0.9	80-120	1.28	14.06
GFP	Early treatment	PA139	2.69	225-307	2.7	433-630	1.3	14.35
		PA140	2.89	300-400	2.3	574-670	2.04	14.52
		PA142	2.76	380-504	-	570-600	-	14.89
	Late treatment	PA219	3.1	225-312	3.34	380-410	0.90	14.46
		PA222	2.01	198-230	3.6	440-580	1.75	10.8
		PA223	3.08	338-350	3.7	460-500	1.12	10.24
LAV	Early treatment	PA144	3.97	336-506	8.8	559-670	2.21	18.15
		PA146	4.03	331-450	8.22	500-620	2.03	17.5
		PA148	5.1	516-530	-	150-230	-	19.68
	Late treatment	PA229	7.1	289-344	12.1	380-410	1.70	16.76
		PA230	4.9	387-392	11.36	411-570	2.31	17.37
		PA231	5.25	318-326	8.8	350-578	1.67	16.6

Table 8.1: The MBF values (ml/min/g) under the rest and stress conditions during early and late treatment phases along with their recorded HR, CFR, CO. The CO (measured by the echocardiography in ml/min) were recorded for each mouse. The CFR values (MBF at stress/MBF at rest) were calculated for all groups. The Pearson correlation coefficient (r) measured between the MBF at rest and the CO was 0.713 indicating a strong positive relation between them.





8.4.3 Echocardiography results:

The LVEF% values were similar within the control groups at the early and late treatment phases, as in table 8.2 and figures 8.8-8.10. However, the LAV group scored a significantly higher LVEF% value in the late treatment compared to the early treatment as in figure 8.10. Additionally, there were no significant differences in the LAV LVEF% compared to the other control groups at early treatment, as in figure 8.8. However, the LAV-treated mice scored a significantly higher LVEF% compared to the control groups at late treatment group, as in figure 8.9.

The CO values (ml/min) were significantly higher in the LAV group compared to the NV, WT and GFP in the other control groups at early and late treatments, as in table 8.2 and figures 8.11-8.12 (with p values of $**<0.05$). There were no significant changes in the CO between the early and the late treatment phases within each group as in figure 8.13.

8.4.4 Capillary and artery density results:

Immunohistochemical staining revealed that the capillary and artery numbers were significantly increased in the LAV-group mice compared to the other control groups at both early and late treatments, as in table 8.3 and figures 8.14-8.16.

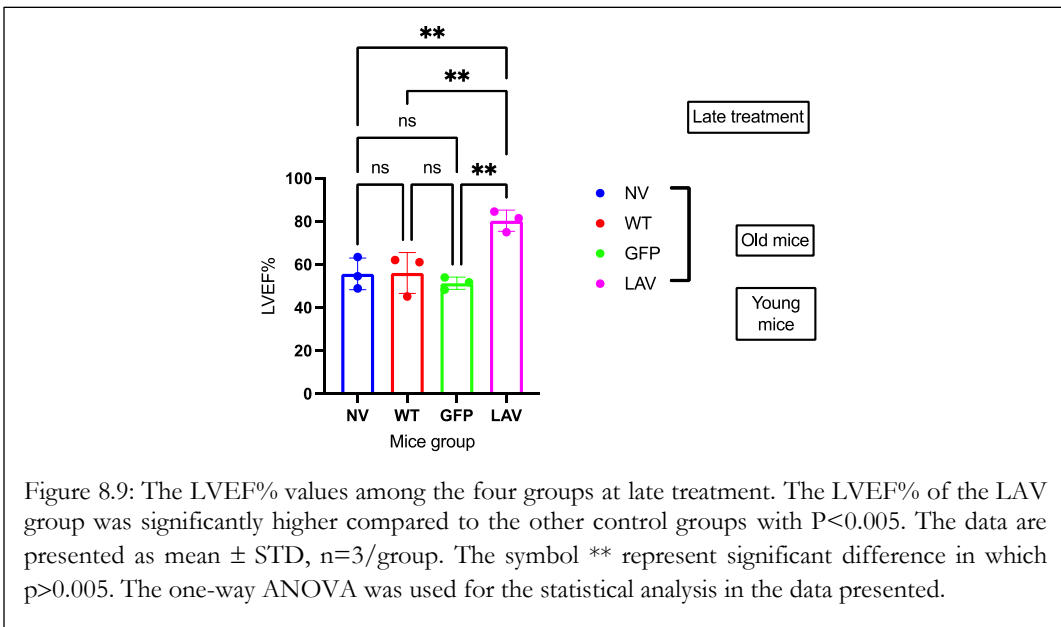
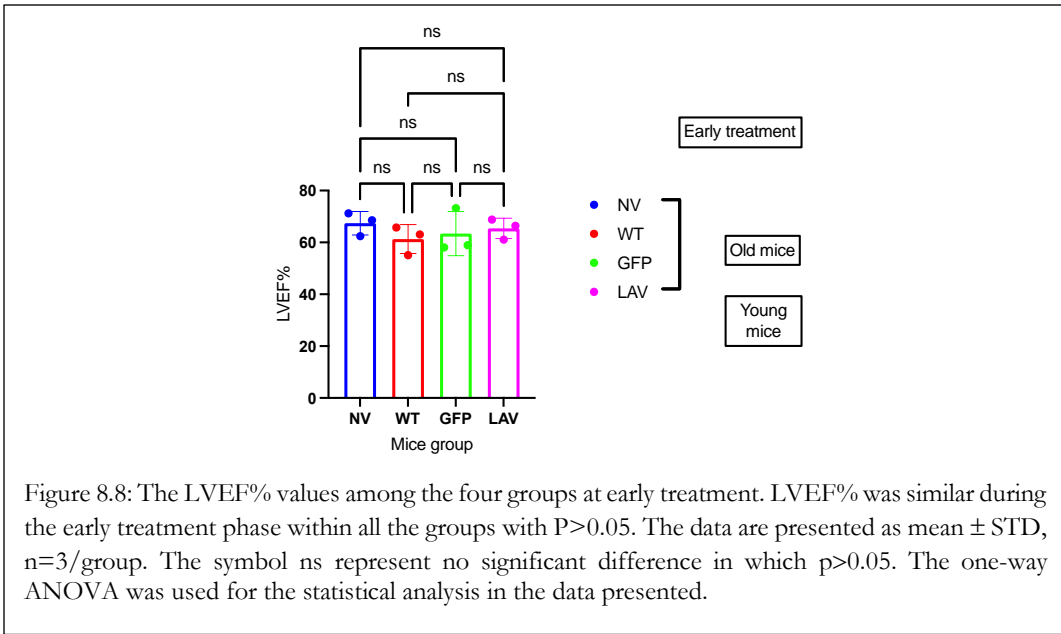
8.4.5 Comparison of the PET results with the echocardiography and histological data:

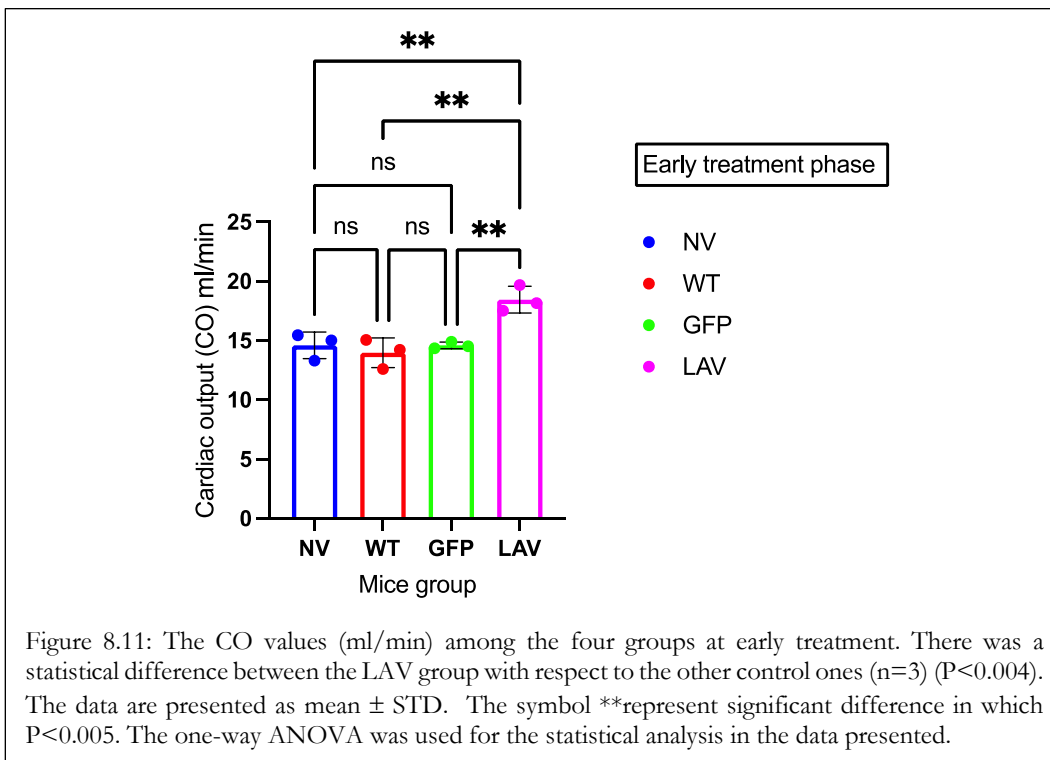
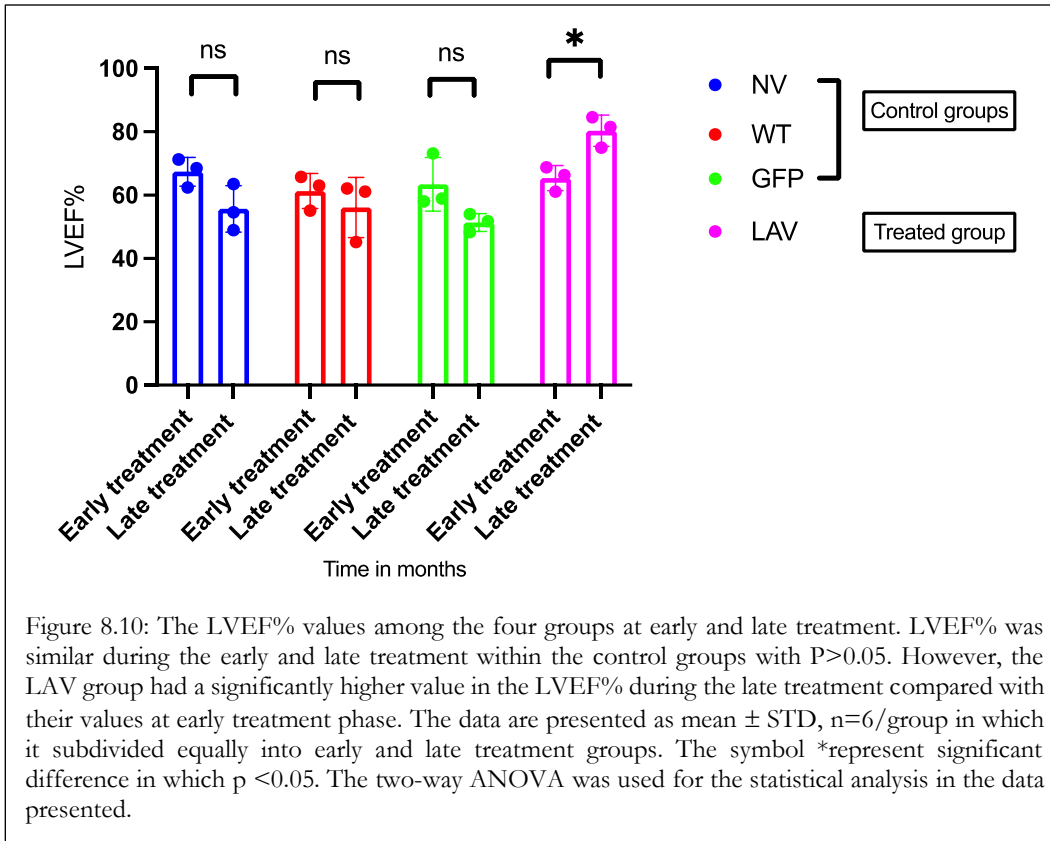
We compared the resting MBF in all the aged mice at early and late treatments with the resting MBF values of the healthy young mice measured in Chapter 5, as in figure 8.18. There was a significant reduction of the MBF in the aged control groups (NV, WT and GFP) compared to the MBF of the healthy young mice ($p<0.0001$). In contrast, the LAV-treated aged mice showed no statistical difference compared with healthy young ones ($p>0.05$).

Furthermore, the correlation was assessed between the resting MBF PET results with both the echocardiography and histological results. The correlation was based on calculating the Pearson correlation coefficient r , in which the values between 0.5 and 1 reflect a strong positive correlation (Mukaka 2012; Schober et al. 2018). There was a strong positive correlation between the MBF values (at rest condition) and the CO during both the early and late treatment phases with the correlation coefficient $r = 0.713$, as in figure 8.19. The comparison of the MBF at rest with the capillary density revealed a strong positive correlation between them with $r = 0.818$ (figure 8.20). Finally, there was also a strong positive correlation between the CO and the capillary density with $r = 0.683$, as in figure 8.21.

Treated group	Longevity group	Mouse ID	LVEF%	CO ml/min
NV	Early treatment	PA 134	68.57	15.44
		PA 135	62.45	13.31
		PA 136	71.25	15.02
	Late treatment	PA 214	54.59	12.5
		PA 215	48.97	13.9
		PA 216	63.56	13
WT	Early treatment	PA 149	65.79	12.60
		PA 150	55.12	15.06
		PA 153	63.08	14.22
	Late treatment	PA 225	62.10	11.6
		PA 226	45.19	10.6
		PA 228	61.13	14.06
GFP	Early treatment	PA139	58.99	14.35
		PA140	58.07	14.52
		PA142	73.24	14.89
	Late treatment	PA219	48.36	14.46
		PA222	51.76	10.8
		PA223	54.00	10.24
LAV	Early treatment	PA144	68.8	18.15
		PA146	61.09	17.5
		PA148	66.41	19.68
	Late treatment	PA229	84.62	16.76
		PA230	81.56	17.37
		PA231	75.02	16.6

Table 8.2: The echocardiography measurements for all the groups at early and late treatment.





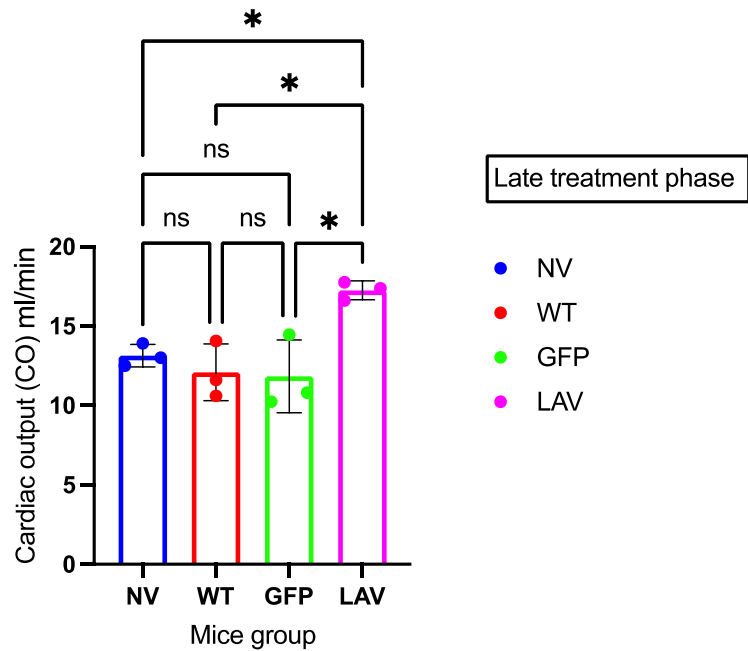


Figure 8.12: The CO values (ml/min) among the four groups at late treatment. There was a statistical difference between the LAV group with respect to the other control ones (n=3) (P<0.004). The data are presented as mean \pm STD. The symbol *represent significant difference in which P<0.05. The one-way ANOVA was used for the statistical analysis in the data presented.

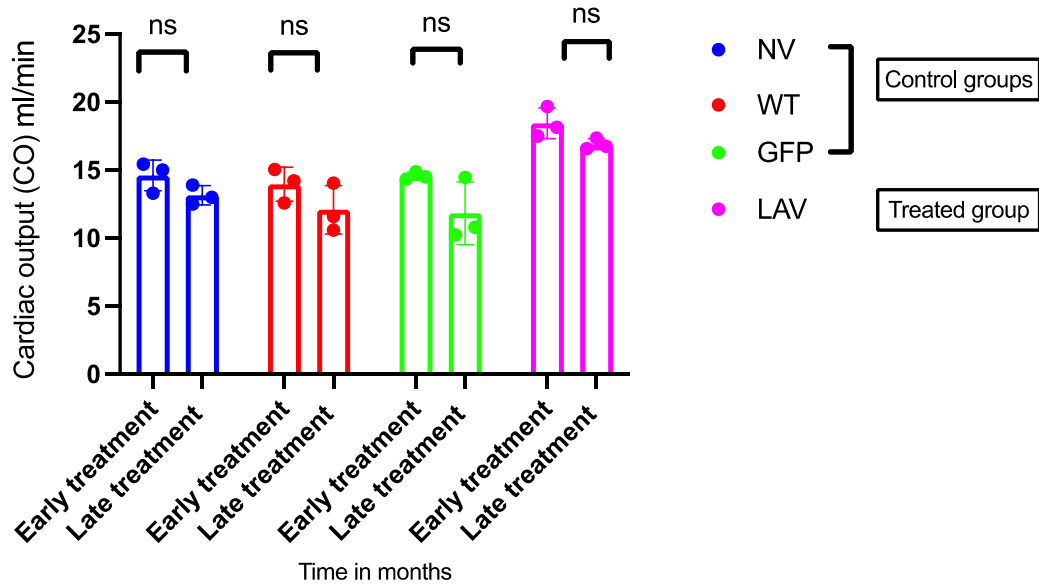


Figure 8.13: The CO values (ml/min) at early and late treatment phases within each group. The data are presented as mean \pm STD, n=3/treatment phase/group. There was no statistical difference between the early and late treatment across all the groups. The symbol (ns) represents no significant difference in which P>0.05. The two-way ANOVA was used for the statistical analysis in the data presented.

Treated group	Longevity group	Mouse ID	Mean number of capillaries (#/mm ²)	Mean number of Arterioles (#/mm ²)
NV	Early treatment	PA 134	7534	69.7
		PA 135	8311	66.65
		PA 136	7175	57.78
	Late treatment	PA 214	7430	106.74
		PA 215	8400.3	125.35
		PA 216	9005.9	73.81
WT	Early treatment	PA 149	8434	67.5
		PA 150	7834	86.5
		PA 153	7987	90.02
	Late treatment	PA 225	7501	93.74
		PA 226	8429	134.25
		PA 228	8525	131.80
GFP	Early treatment	PA139	8910	63.44
		PA140	7630	88.54
		PA142	8053	47.83
	Late treatment	PA219	8165	69.86
		PA222	8255	65.56
		PA223	6971	93.21
LAV	Early treatment	PA144	9285	116.32
		PA146	11475	98.54
		PA148	12042	124.71
	Late treatment	PA229	14546	257
		PA230	13565	194.5
		PA231	14153	210.3

Table 8.3: The capillary and artery density (#/mm²) for all the groups at early and late treatment.

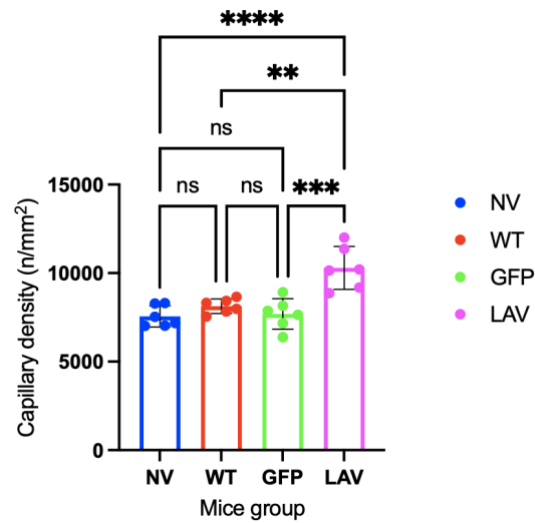


Figure 8.14: Comparison of the capillary density (n/mm^2) for all groups at early treatment. The data are presented as mean \pm STD, $n=6$ /group. The capillary density in the LAV group was statistically higher than the other control groups. The symbol * represents significant difference with p values * < 0.05 , ** < 0.005 , *** < 0.0005 . The one-way ANOVA was used for the statistical analysis in the data presented.

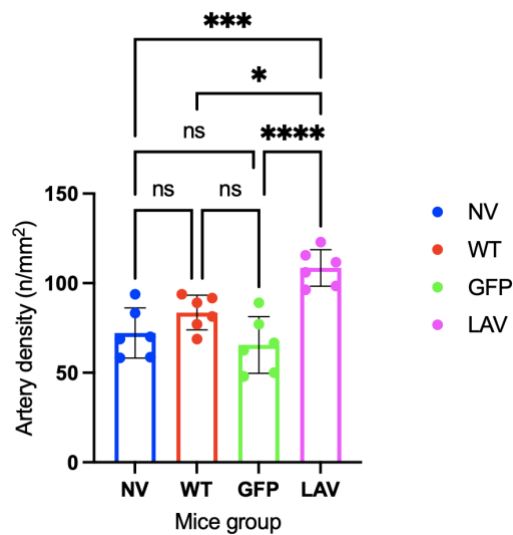
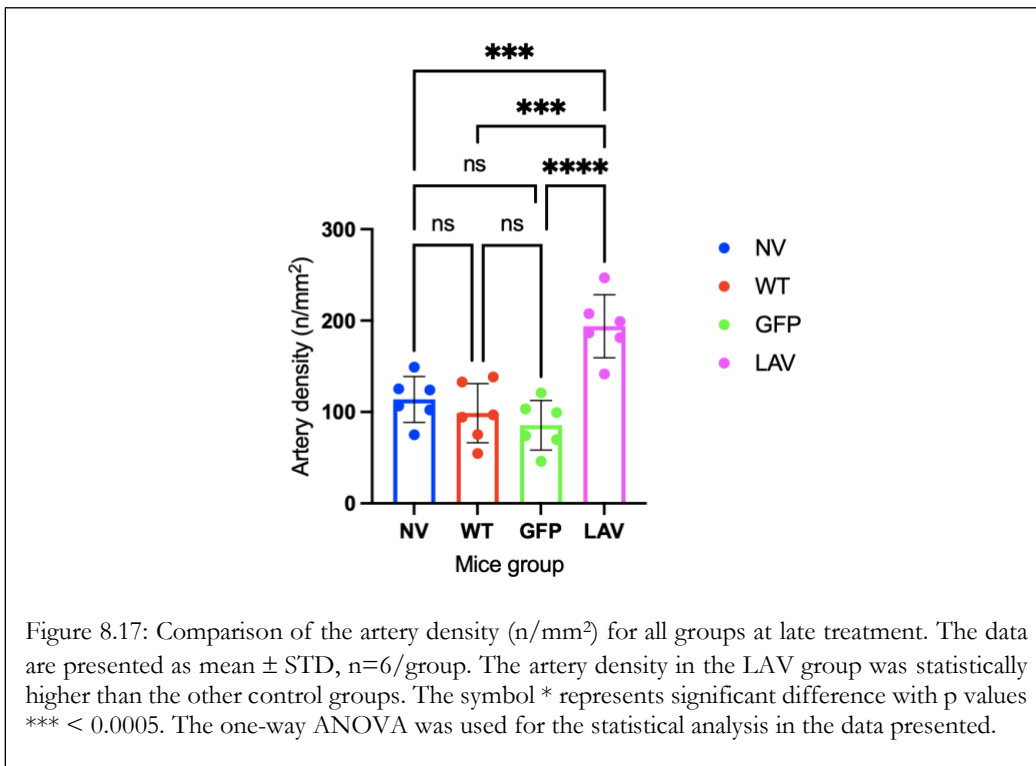
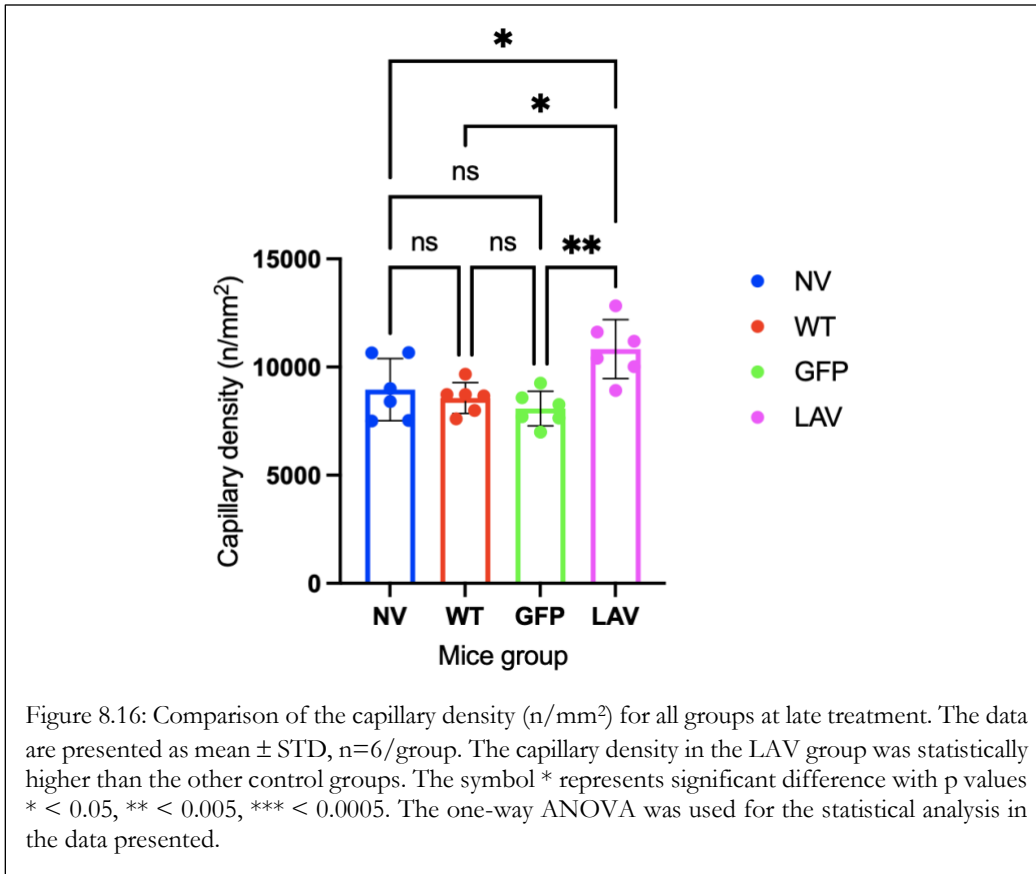


Figure 8.15: Comparison of the artery density (n/mm^2) for all groups at early treatment. The data are presented as mean \pm STD, $n=6$ /group. The artery density in the LAV group was statistically higher than the other control groups. The symbol * represents significant difference with p values * < 0.05 , ** < 0.005 , *** < 0.0005 , **** < 0.0001 . The one-way ANOVA was used for the statistical analysis in the data presented.



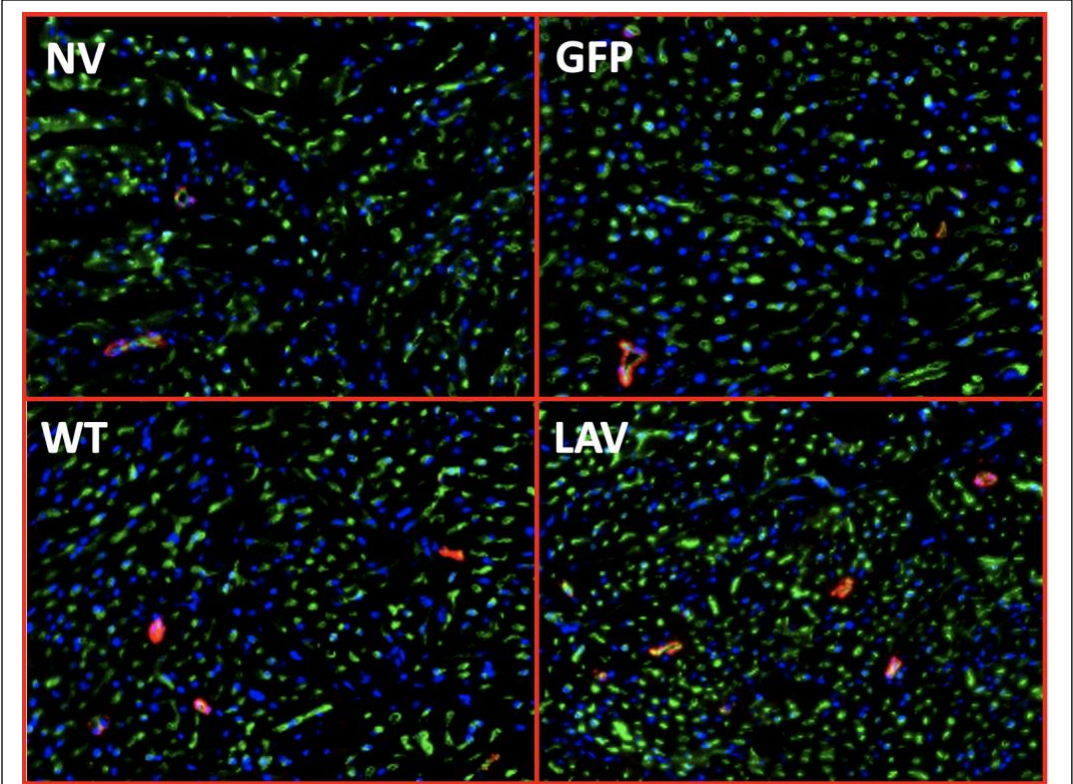


Figure 8.18: Representative images of isolectin B4 (green) positive endothelial cells (representing the capillary density) and α -smooth muscle actin (red) positive smooth muscle cells (representing the artery density), with nuclei identified by DAPI (blue). There was a significant increase in the capillary and artery density in the LAV group compared to the other control groups at both early and late treatment.

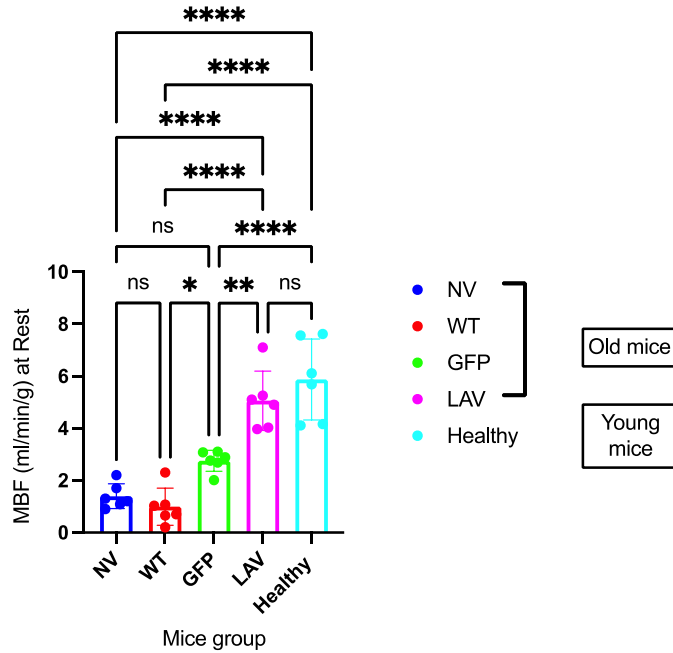


Figure 8.19: Comparison of the rest MBF values (ml/min/g) for all the aged mice groups during early and late treatment and the rest MBF values of the healthy young mice. The data are presented as the mean \pm STD, n=6/group. There was a significant increase in the MBF values in the healthy mice compared to the control groups including NV and WT (p value < 0.005). The LAV group showed similar rest MBF compared to healthy young group with no statistical difference (ns). The symbol * indicate statistical significance in which P values is * < 0.05, ** < 0.005, *** < 0.0005 and ****<0.0001). The one-way ANOVA was used for the statistical analysis in the data presented.

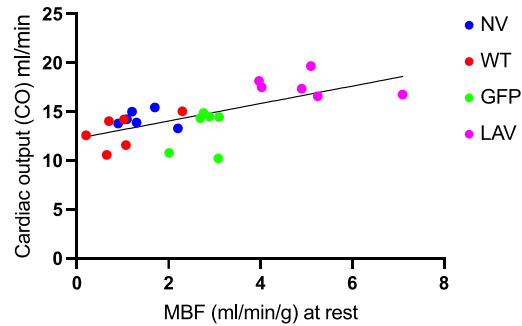


Figure 8.20: Scatter plot of the CO (ml/min) as a function of the MBF (ml/min/g). The regression line was fitted using the least square method. The n=6/group. Pearson coefficient $r = 0.713$ shows that there is a strong correlation between the CO and the MBF.

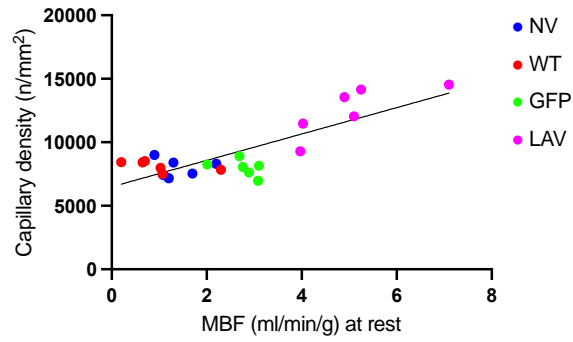


Figure 8.21: Scatter plot of the capillary density (n/mm^2) as a function of the MBF ($ml/min/g$). The regression line was fitted using the least square method. The $n=6/group$ and Pearson coefficient $r = 0.818$ shows the existence of positive significant correlation between the capillary density and the MBF.

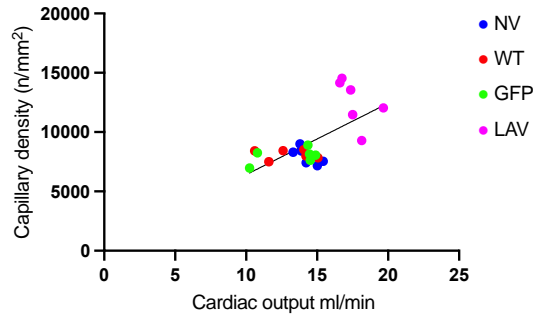


Figure 8.22: Scatter plot of the capillary density (n/mm^2) as a function of the CO (ml/min). The regression line was fitted using the least square method. The $n=6/group$ and Pearson coefficient $r = 0.683$ shows the existence of positive significant correlation between the capillary density and the CO.

8.5 Discussion:

The young myocardium is capable of renewal and repair; however, the extent of the ability to regenerate positively correlates with the lifespan of the animal (Maier et al. 2004; Hosoda et al. 2011). The recent study by Villa et al. (Villa et al. 2015a) among LLIs revealed a high level of BPIFB4 proteins that might be associated with longevity and a lower incidence rate of CVDs among them. In our work (Dang et al. 2020), we showed that the LAV-BPIFB4 gene 216 variant exerted therapeutic effects in diabetic mice through improving the cardiac systolic and diastolic ventricular function. In this chapter, we wished to assess the effects of the LAV-BPIFB4 gene on older mice and whether its influence might diminish over time. Therefore, the mice were divided into two groups which included the early treatment (gene delivery followed by evaluation after 4 months) and late treatment in which the evaluation was performed one month after the gene delivery. The evaluation was performed through quantifying the MBF at rest and under stress conditions using our micro-PET/CT scanner and correlating the data with the echocardiography and histological analyses.

Our data indicated that the LAV-BPIFB4 gene raised the MBF significantly compared to the other control groups during both the rest and stress conditions. Notably, its effect showed a higher trend in the late treatment group compared to the early one but not to a significant level, which might indicate that its benefits might be reduced over time.

To begin with, MBF is a key parameter in CVDs, particularly in ischemia, and is often measured at rest and stress conditions (Gould et al. 1990). During stress, the heart systolic performance should increase to match the body global demand for oxygen and other metabolic needs, unless there is a narrowing in the coronary circulation as the case in many CADs (Vleeming et al. 2018; Guerraty et al. 2020). Therefore, assessing the myocardium under induced stress has been used widely as a diagnostic technique for identifying ischemic defects in CADs as well as assessing the impact of experimental therapies aimed to treat CVDs as the case in our research (Gould et al. 1990; Guerraty et al. 2020). In addition, through stress MBF measurement, the coronary flow reserve (CFR) (flow at stress/flow at rest) can be calculated to be used as a physiological index in evaluating the extent of coronary microvascular dysfunction (Dal Lin et al. 2015). The reduction in resting MBF and CFR is known to be linked with abnormal vasodilation, increased vasoconstriction, or changes in the coronary microvasculature which are all common hallmarks in ageing (Dal Lin et al. 2015; Sinha et al. 2021). A previous study assessed the resting cardiac flow velocity in aged male C57Bl/6 mice using Doppler imaging. They reported a decrease in resting MBF and CFR at later stages of their lifespan which

might be due to abnormal endothelial or microvasculature changes (Hartley et al. 2010). Their findings agreed with our results in which there was a significant reduction in the MBF at rest among the control groups when compared to the resting MBF of the healthy young group measured previously ($p < 0.0001$). However, our LAV group (at early and late treatment phases) showed similar MBF values compared to the healthy young mice during rest and stress conditions with no significant difference suggesting an improvement in the MBF. This improvement might be due to an enhancement in vasodilation or changes in the coronary microvasculature (Dal Lin et al. 2015; Sinha et al. 2021). The coronary microvasculature consists of capillaries (which are responsible for transporting oxygen and metabolites to cardiomyocytes) and arterioles (that are responsible for coronary vasoconstriction and vasodilation in response to stimuli) (Dal Lin et al. 2015; Sinha et al. 2021). Accordingly, improvement in the myocardial microvasculature density, or vascular density, may contribute to the increase in the MBF (Landers-Ramos and Prior 2018). Indeed, the LAV group scored significantly higher capillary and arteriole density values compared to the other control groups and this is possibly the reason behind the observed rise in their MBF. These findings were also validated through the strong correlation that we observed between the MBF and capillary and arteriole density.

Furthermore, the increase in the vascular density is known to be linked with multiple cardiac regenerative mechanisms that aim to restore tissue architecture, particular in case of injury and wound healing, through the activation of sequential processes involved in cellular proliferation, differentiation, and new blood vessel formation such as angiogenesis and revascularisation. In our work (Dang et al. 2020), we showed that the LAV group has a high circulating SDF-1, i.e. chemokines, that appears to recruit cardiac and bone marrow derived stem cells and activate myocardial vasculogenesis and angiogenesis based on paracrine manner (Abbott et al. 2004; Hiasa et al. 2004; Elmadbouh et al. 2007). Villa et al. (Villa et al. 2015a) reported that the SDF-1/CXCR4 might be involved in the ability of the LAV gene to stimulate M2 macrophage polarization using an atherosclerotic model. Therefore, there is a possibility that the LAV gene acted through inducing the SDF-1/CXCR4 signaling pathways, angiogenesis, and new blood formation, which subsequently increased the vascular density and MBF.

Another possible explanation for the rise in MBF during the short- and long-term treatment of the LAV group might be due to the stimulation of the eNOS pathways which resulted in a rise in NO, vasodilation and enhanced blood flow (Dossena et al. 2020). Evidence suggested that impaired angiogenesis in old mice might be due to endothelial dysfunction that may lead to a decreased expression of a vascular endothelial growth factor (VEGF) as well as the reduction in the eNOS

signalling pathways (Swift et al. 1999; Westvik et al. 2009). Our collaborators also showed the link between endothelial dysfunction and the decreased eNOS activity that occurred due to the downregulation of BPIFB4 protein in old mice (Villa et al. 2015b). The eNOS is vital for neovascularisation as well as the bioavailability of NO which is reported to enhance vasodilation and increase blood flow (Mees et al. 2007; Villa et al. 2015b). Accordingly, the increased activity of the eNOS signalling might be one of the causes of enhanced vascular density and MBF in the LAV treated mice.

In our echocardiography data, our LVEF% values were similar across the control groups at the early and late treatment phases. It is well known that ageing causes a generalized degeneration of the cardiac structure and performance, and thus, aged individuals are expected to have a higher rate of arterial stiffness, hypertension, stroke or MI compared to healthy young individuals (Puntmann et al. 2012; AlGhatrif et al. 2013; Chia et al. 2014). Zhang et al. (Zhang et al. 2021) showed that ageing causes impairment in the cardiac diastolic function, but not the systolic functional measures (including fractional shortening, FS and LVEF%), among aged female mice. Additionally, ageing is known to not significantly alter the LVEF% (Leibowitz and Gilon 2012). In our results, we observed a similarity in the LVEF% values across the control groups during both the early and late treatments. In contrast, although the LAV group showed similar values of LVEF% at early treatment compared to the other control groups, there was a significant increase in its LVEF% values compared to the control groups at the late treatment phase, which might suggest that its effects might decrease over time.

Moreover, we also observed a significant increase in the CO values (measured by the echocardiography) in the LAV groups compared with the control groups at both the early and late treatments, suggesting that the therapeutic effects of the LAV-BPIFB4 is continuing to occur even after a long period of time (about 4 months). An improved blood supply to the myocardium (as we found in the LAV group) may result in an improvement in its pumping capability and thus a greater CO. Additionally, the senescent mouse heart appeared to have significant decrease in its contractile ability and thus a reduction in its efficiency to pump the blood (lower CO) (Yang et al. 1999). Noda et al. (Noda et al. 2020) reported age-related contractile dysfunction in aged C57BL/6 mice that might be due to mitochondrial impairment. Another study reported that the dysregulation of the motor and structural proteins, such as decreased myosin expression, could contribute to the contractile dysfunction in old mice (Fanjul et al. 2020). In our previous work, we reported that the LAV-BPIFB4 gene increased the MyHC- α expression in the cardiomyocytes which improved the endothelial function and enhanced vascular eNOS phosphorylation in the diabetic mice model (Dang et al. 2020).

The enhancement in the expression of MyHC- α , which could be due to induced SDF-1/CXCR4 signaling pathways as reported by others (Tang et al. 2009; Chiriac et al. 2010), is likely to be behind the improvement in cardiac performance and thus the observed rise in the CO values among the LAV group (in the early and late treatments) (Nakao et al. 1997; Korte et al. 2005; Lv et al. 2011).

What is more, a previous study demonstrated that the LAV-BPIFB4 gene transfer could be a factor in improving cardiac function and contractility, primarily through boosting multiple mitochondrial-related pathways (Faulkner et al. 2020). Consequently, this might be one of the therapeutic pathways in which the LAV gene exerts its effect in improving cardiac function through enhancing contractility, CO and LVEF% among LAV treated mice.

In addition, the enhanced CO among the LAV group could be attributed to the increase in their capillary and artery density as revealed by our histological results. Microvasculature plays a fundamental role in oxygen and nutrient delivery to the cardiac muscle, particularly during exercise or when under stress (Gliemann 2016). Therefore, an increase in capillary and artery density, which represents the microvasculature, will result in an increase in the exchange surface area between the muscle and blood. As a consequence, this will also decrease the distance required for oxygen diffusion, all of which will result in an improved MBF (Gliemann 2016). The rise in the MBF, due to the increase in vascular density, leads to a higher oxygen supply to the myocardium, enhances its contractile performance and improves the CO, which we reported in our LAV treated mice (Gliemann 2016). This could explain the strong correlation found between MBF values compared to both the vascular density and the CO.

Taken together, our study in this chapter confirms the beneficial effects of the LAV gene that may be involved in several cardiac reparative mechanisms through stimulating SDF-1/CXCR4 and eNOS signalling pathways, several mitochondrial-related pathways, and many other unknown pathways. The stimulation of these pathways among LAV-treated mice is likely to be responsible for the increase in vascular density, MBF and CFR, which all could improve cardiac performance and CO. Our results also indicate that the effect of the LAV-BPIFB4 treatment might persist for several months, but its effect may be diminished with time.

8.6 Conclusion:

The measurement of MBF using $^{13}\text{N-NH}_3$ and PET quantification tools can provide vital information regarding cardiac function following treatment intervention. The purpose of the current study was to determine the beneficial effect of the LAV-BPIFB4 gene on old mice at various times of

intervention. The micro-PET/CT scanner and compartmental modelling were used to investigate its beneficial impact through quantifying the MBF during rest and stress conditions at different points on the timeline. Our PET/CT results were also compared and correlated to the vascular density and echocardiography data.

We demonstrated that the LAV-BPIFB4 improved cardiac function and contractility, enhanced cell survival and proliferation, decreased inflammatory response, and improved cellular communication, angiogenesis, vascularisation, and molecular regulation and proliferation of the cell cycle, all of which subsequently maintains the repair of the heart and its regenerative ability (Spinelli et al. 2017; Malavolta et al. 2019; Dang et al. 2020; Ciaglia et al. 2022). The beneficial effects of the LAV gene could be due to the stimulation of SDF-1/CXCR4 and eNOS signalling, several mitochondrial-related pathways and many other unknown pathways and mechanisms.

In conclusion, LAV-BPIFB4 gene delivery can attenuate the deteriorative impact of age on the CVS through the activation of many reparative mechanisms, but its effects may be reduced over time.

Chapter 9:

Final Discussion:

PET imaging using small animal models has been used widely as a powerful tool in assessing the efficiency of therapeutic interventions, standardizing, or refining imaging protocols, and validating new radiotracers to be used clinically (Cherry and Gambhir 2001; Slomka et al. 2014). Indeed, the strength of PET imaging is that it allows the semi or absolute quantification of various biological biomarkers such as cardiac metabolism, blood flow to different organs, receptor binding or gene expression (Inubushi et al. 2004; Turkheimer et al. 2014).

The primary objective of this research project was to assess the feasibility of using the Mediso micro-PET imaging to evaluate murine cardiac function. This evaluation was performed through the quantification of vital physiological biomarkers, namely MGM and MBF. Micro-PET/CT imaging and quantification was used to examine the effectiveness of LAV-BPIFB4 gene therapy on cardiac function. In order to do this, we first had to test the performance of the micro-PET scanner, and then develop and standardize imaging protocols to assess the accuracy and repeatability of our PET data. Further validation of the feasibility of our micro-PET was achieved by combining different assessment tools including echocardiography and histological tests. An early experiment was to assess whether we could detect changes in the FDG uptake and blood flow following induced HLI. Following the successful completion of these experiments, evaluation of LAV-BPIFB4 gene therapy was carried out on murine models of diabetes and ageing.

In order to do these assessments, we first needed to test the accuracy of our Mediso micro-PET/CT scanner. We did this through evaluating its physical performance in terms of the overall image quality when using ^{18}F and ^{13}N . The evaluation of the performance was carried out according to the NEMA NU 4 – 2008 standard and the manufacturer guidelines which recommended performing the IQ test before quantitative studies for any used radiotracers (Daube-Witherspoon et al. 2002; Cañadas et al. 2011). In line with these NEMA and manufacturer recommendations, the IQ performance was carried out for every radiotracer before carrying out PET quantitative analysis. This test covers most of the important physical factors that are dependent on the radiotracer choice, such as SR and count rate. The IQ test enables measuring the RCs% which is defined as the ability of the PET system to recover radioactivity concentration at different object sizes (Srinivas et al. 2009; Disselhorst et al. 2010; Teuho et al. 2020). The measurements of the RCs reflect the level of SR

particularly in using different radiotracers that have different positron ranges. Generally, a low RCs% reflects a poor resolution and a higher PVE (Srinivas et al. 2009; Disselhorst et al. 2010; Kim et al. 2021).

The RCs of ^{18}F were within the NEMA acceptable ranges, reflecting the good SR of the produced images. The ^{13}N RCs were lower than those of ^{18}F , but this was expected considering that we did not increase the scanning time to compensate for the loss in counting statistics. This issue could be minimised through increasing the imaging time or the injected dose of ^{13}N , and thus, improving both the RCs and the SR (Choi et al. 1999; Maddahi and Packard 2014). Another important factor that contributes to the SR and the accurate quantification of the PET images is the partial volume effects (PVEs) which result from the false estimation of regional radioactivity due to spill-out and spill-in of the radioactivity from the neighbouring regions. Our study on both radiotracers shows that all SOR values were in the required NEMA range.

We have shown that our Mediso 122S small-bore PET/CT scanner offers appropriate levels of sensitivity and SR for small animal imaging when using either ^{18}F -FDG and ^{13}N - NH_3 . However, we wished to further improve ^{13}N - NH_3 image quality by altering aspects of the scanning protocol, including scan duration and the amount of the injected dose. Therefore, we have increased the ^{13}N - NH_3 injected dose to compensate for the loss in counting statistics due to its short half-life.

The next aim of this research was to assess the accuracy and repeatability of our micro-PET system in quantifying MGM and MBF in healthy control mice using ^{18}F -FDG and ^{13}N - NH_3 respectively. Both MGM and MBF are used as biomarkers that may reflect some aspects of cardiac function, hence, they are often quantified to assess response to treatments (Schelbert et al. 1981; Khorsand et al. 2005; Medical Advisory 2005; Ziadi and Beanlands 2010; Prior 2017). In Chapter 5, we developed a set of imaging protocols that could produce as much information as possible with minimum mathematical complexity and the simplest possible assumptions. These imaging protocols were design based on previous clinical and preclinical investigations, and then they were tested for their accuracy and repeatability.

Our imaging protocols were designed to fit with our project animal license which currently only allows non-recovery procedures. Each mouse underwent three scans followed by termination on the same day. This experimental design was designed to take advantage of the short (10 minute) half-life of ^{13}N - NH_3 . The scanning protocols started with fasting the mouse for approximately one hour to enable maximal FDG uptake. The mouse was transferred to a prewarmed bed (to avoid hypothermia (Lee et al. 2005; Cates et al. 2014)). Anesthesia was induced using low-concentration isoflurane (1.5-

2%) in oxygen, in order to prevent the dramatic increase of the MBF under higher isoflurane concentration that was observed by Kober et al. (Kober et al. 2005). Cannula placement was performed via two routes, IV and IP, for the injection of the radiotracer and dobutamine respectively. We decided to use two different routes to avoid injecting large volumes that may interfere with the haemostasis of the mouse (Kuntner et al. 2009; Thackeray et al. 2015; Lindsey et al. 2018). As previously reported, administration of dobutamine via the IV or IP routes had no difference in both cases (Puhl et al. 2016). A resting ammonia dynamic scan (duration of 10 minutes) was performed following IV injection. After a 10-minute gap to allow the ammonia to decay, the dobutamine was injected via the IP route. Five minutes later, the second dose of ammonia for the stress test was injected (Puhl et al. 2016) and the stress scan performed for 10 minutes. A further 10-minute gap was allowed for the ammonia to decay, and the FDG was injected, and the scan was initiated. Finally, the CT scan was acquired, and the animal was terminated. To ensure maximum SR, all dynamic PET images were reconstructed using a 3D OSEM. Both 1TC and 2TC models were used for the quantification of MBF and MGM respectively. The choice of models was conditioned to the mechanism of the radiotracer uptake (Choi et al. 1999). Importantly, the IF measurements were derived from the dynamic images in which a VOI were placed over the LV blood pool region (Huang et al. 2019). The LVBP VOI was convoluted with the PSF that was calculated by the scanner manufacturer. In fact, this technique was applied and validated by previous investigations, and they reported similar results with regards to IDIF derivation (Fang and Muzic 2008; Huang et al. 2019). The myocardium VOI was derived from the LV region.

Our MBF results, during rest and dobutamine stress, were repeatable and comparable to the MBF measured previously in mice (of the same strain) using an intraventricular injection of microspheres, MRI, and echocardiography (Raheer et al. 2007; Jogiya et al. 2013b; Krueger et al. 2013; Naresh et al. 2015). In addition, our MGM results were accurate, repeatable, and consistent with previous MGM values measured in mice under a similar protocol (including animal fasting, anesthetic agent type and concentration) (Wu et al. 2007; Cochran et al. 2017).

We then tested the ability of our micro-PET scanner to detect changes in blood flow and glucose metabolism following the induction of HLI in healthy mice, using $^{13}\text{N-NH}_3$ and $^{18}\text{F-FDG}$. Both blood flow and glucose metabolism measurements were significantly reduced in the ligated leg compared to the normal one, as expected. Next, the blood flow and glucose metabolism results were compared with doppler imaging to assess blood flow, and for changes in vascular density (using histological analyses). There was a strong correlation between the blood flow assessed by our micro-PET/CT

scanner and doppler imaging, validating our PET protocols. In our histological analyses, we found a considerable reduction in capillary and arteriole density in the muscle of the ligated leg of each mouse. As the case with doppler imaging, our histological data strongly correlated with our PET-derived blood flow results. These results demonstrate the capability of our micro-PET/CT system to detect changes in blood flow and metabolism after surgical ischemia. Importantly, our results confirm that $^{13}\text{N-NH}_3$, a flow radiotracer, allows the quantification of hindlimb perfusion in murine models following induced hindlimb ischemia and the data were strongly correlated across different imaging or assessment techniques. Therefore, both $^{13}\text{N-NH}_3$ and $^{18}\text{F-FDG}$ quantitative imaging can be used as an effective imaging modality to evaluate treatment through quantifying blood flow and glucose metabolism respectively.

We then used PET imaging to examine the therapeutic efficiency of the LAV- BPIFB4 gene in animal models of diabetes and ageing. These animals had already undergone hair removal for echocardiography imaging. Hair loss has long been associated with diabetes and has been attributed to stress (cortisol levels) and changes to the circulatory and immune systems (Sasaki et al. 2018; Singh et al. 2018). In the experiments on the diabetic mice, we noted a considerable increase in the hair re-growth rate among the LAV-treated mice compared with control mice (NV and WT groups). This observation suggests that LAV treatment may stimulate signaling pathways related to hair re-growth processes. An alternative hypothesis is that LAV therapy results in improved blood flow, and this may be by a number of possible routes. The role of NO in modulating blood flow is well known (Moncada 1991; Nakanishi et al. 1992; Partovian et al. 2005; Raheer et al. 2007). LAV-BPIFB4 gene therapy is known to increase eNOS phosphorylation and translocation, and increases the release of NO in the in endothelial cells (Villa et al. 2015b). LAV can also improve blood flow by other routes. LAV-treatment of eNOS knockout mice still have improved vasodilation even though eNOS was not present. This was probably via endothelium-derived hyperpolarising factor (EDHF) mediated pathways in smaller blood vessels, thus improving tissue blood flow (Garland et al. 2011; Spinelli et al. 2017). Yet another alternative is that LAV exerts its positive effect on hair growth by improving local blood flow by angiogenesis. We have demonstrated this as an increased density of arteries (aged animals only) and capillaries.

Furthermore, our calculated SUVs and MGM values, which represent myocardial glucose uptake and metabolism respectively, showed a significant reduction within the diabetic groups compared to the lean control (non-diabetic) group, with the MGM in LAV-treated group not as severe as in the control diabetic groups (NV and WT groups). The echocardiography data for our scanned mice at 13

weeks was similar and revealed no statistical difference in CO, LVEF%, or LV mass among the diabetic groups. The lean control showed a considerable increase in both the CO and LVEF%, compared to the diabetic groups. However, this lack of effect is due to the small number of animals in these experiments. When the data obtained from the remaining animals given each treatment (the animals that remained in Bristol), LAV-treatment resulted in significantly different echocardiography characteristics. CO and LVEF% were significantly higher in the LAV group compared with the diabetic NV and WT groups and approached that found in the lean mice. The histological analysis of capillary and arteriole density revealed a significant decrease in two of the diabetic groups, namely the NV and WT groups, compared to the lean control group, and a remarkable increase in both capillary and arteriole density in the LAV-treated group. The capillary density and the MGM values were strongly correlated in the lean control group.

The reduction in the FDG uptake and metabolism, represented by the SUVs and MGM values, by the heart in all the diabetic groups (NV, WT and LAV) confirmed the state of T2D which is known to have a decrease in insulin-stimulated glucose uptake because of the general reduction in the endogenous insulin (Thorn et al. 2013; Ko et al. 2017). Although our LAV-treated group exhibited a higher value with respect to the other diabetic groups, this group did not reveal a significant change in the glucose metabolic rate. Additionally, the further analysis performed by our groups, also recorded no difference in the plasma glucose level among the LAV treated group (Dang et al. 2020). Another possible explanation might be that we did not allow the model to be sufficiently advanced to detect changes in the MGM following the LAV gene treatment. Previously, researchers performed micro-PET imaging and quantification of glucose uptake and metabolism in Zucker fatty rats. They found that changes in glucose uptake and metabolism occurred only at a late stage of the T2D model (Shoghi et al. 2008). We performed PET/CT scanning on our mice when they were 14 weeks old (ie not in an advanced diabetic state). There is a possibility that through extending the time of the study or commencing LAV-treatment at a later age, we might detect MGM changes.

Using echocardiography, we identified a reduction in the CO and LVEF among the two control diabetic groups compared to the treated group. We have observed that hearts from mice treated with LAV-therapy had a considerable increase in the expression of MyHC- α protein when compared to the diabetic groups (Dang et al. 2020). The MyHC- α is a protein involved in the contractile function of the myocardium and a previous study reported its downregulation in diabetic mice (Lv et al. 2011). Therefore, the increase in its expression within the LAV mice may justify the improved systolic performance among these mice (Rundell et al. 2004; Villa et al. 2015b; Dang et al. 2020). The improved

CO and LVEF in the LAV group are likely to be related to the increase in capillary and artery density. The coronary microvasculature consists of arterioles and capillaries both of which have their own function. The arterioles are responsible for resistance in coronary vessels, and they dilate according to the changes in myocardial demand for oxygen (Sinha et al. 2021). The capillary bed transfers the oxygen and substrates to the cardiomyocytes. Therefore, increasing the capillary and arteriole density will increase the oxygen supply and improve the CO. Our collaborators have reported that the SDF-1/CXCR4 is involved in LAV-BPIFB4 stimulated macrophage polarization in atherosclerosis (Puca et al. 2020), and we have found that LAV-treatment in diabetic animals is also at least partially exerted via the SDF-1/CXCR4 axis (Dang et al). SDF-1 is a chemokine that is involved in the activation of many physiological processes such as foetal development and organ haemostasis (Ratajczak et al. 2006). SDF-1 and its receptor CXCR4 play a key role in embryonic vasculogenesis through modulating haematopoietic stem cell (HSCs) trafficking and proper engraftment (Ara et al. 2005; Ratajczak et al. 2006). In addition, multiple studies have demonstrated that the increased expression of the SDF-1/CXCR4 duo in injured tissue strongly related to the new blood vessel formation through angiogenesis (Tachibana et al. 1998; Peled et al. 1999; Ara et al. 2005; Ratajczak et al. 2006). In our related work, we had higher levels of circulating SDF-1 in the LAV treated mice group (Dang et al. 2020). Therefore, there is a possibility that the SDF-1 is involved in the therapeutic effect of the LAV gene through its role in preventing contractile dysfunction, increasing the expression of MyHC- α , and decreasing myocardial fibrosis (Petit et al. 2007)

Even though CO reflects myocardial metabolism as well as coronary circulation, we did not detect changes in MGM (glucose metabolism) in the diabetic animals, which might be due to not allowing enough time to observe changes (Vincent 2008). One reason is based on the results from our RNAseq study on the diabetic mice (Faulkner et al 2020). In this study we found that hearts from LAV-treated diabetic mice had altered mitochondrial metabolism with LAV-treatment resulting in elevated genes and proteins associated with FA metabolism, ketone synthesis, ATP synthesis and acetyl-CoA/TCA cycle progression. This suggestion that glucose metabolism is just one component of myocardial metabolism that has been proposed previously (Kolwicz et al. 2013). A study conducted in transgenic mice engineered to have an overexpression of insulin-independent glucose transporter (GLUT1), denoted a substantial rise in glucose uptake and glycolysis with no change in the normal contractile function (Luptak et al. 2007). This finding also suggests that CO is regulated by multiple metabolic pathways and changes in its value may not directly be as a result of an alteration in the glucose metabolism. This may explain why the LAV-treated group had similar MGM values with respect to

other diabetic mice but experienced a significant increase in their systolic performance represented by the improvement in the LFEV% and CO. Due to the therapeutic effect of the LAV gene that was observed in the diabetic model, we continued to investigate its influence in an ageing model.

In our ageing experiments we reported a substantial increase in the MBF values within the LAV-treated group, during rest and induced stress, compared to the control groups, in both early and late treatments, resulting in an improvement in the CFR in the LAV group. Moreover, the increase in MBF, following pharmacological stress agent administration, was statistically significant in the LAV group in comparison with the control groups. In the stress scan, the other diabetic groups, including NV and WT, didn't have a significant rise in MBF. As in the results using the diabetic model, the echocardiography results indicated a significant improvement in the CO and LVEF% among the LAV group with respect to the other control groups. Importantly, and consistent with our previous findings in the diabetic model, we reported an increase in capillary and arteriole density in the LAV group in contrast to the other control groups. There was a strong positive relation between the MBF values at rest (in late and early treatments) and both CO and LVEF results measured by the echocardiography.

MBF and CFR quantifications are thought to be prognostic biomarkers in many CVDs (Herzog et al. 2009; Fukushima et al. 2011; Farhad et al. 2013; Valenta et al. 2013; Nesterov et al. 2014) and are thought to be a good representation of coronary microvascular function (Guerraty et al. 2020). In clinical studies, a low CFR has been associated with various pathological and physical conditions including CADs, diabetes, obesity and ageing (Chow et al. 2014; Murthy et al. 2014; Shah et al. 2016; Guerraty et al. 2020). We reported a decrease in the MBF values (in rest and stress) in our control groups, including NV, WT and GFP in early and late treatments, in contrast to our MBF values that we measured in healthy young mice previously in Chapter 5, but consistent with a previous study which also used aged C57BL/6J mice (Rammos et al. 2016). The LAV-treated group showed a considerable increase in MBF during rest and stress and in the early and late treatment stages, suggesting the beneficial effect of the LAV-BPIFB4 gene. It is likely that the observed increase in the MBF values within the LAV group was due to the significant increase in the capillary and arteriole density which was also the case in our diabetic LAV-treated mice.

Many CADs are thought to be due to structural changes in the microvascular structure and endothelium dysfunction (Sinha et al. 2021). The microvascular changes might be caused by microvascular obstruction, due to narrowing in the capillaries and arterioles wall, and capillary rarefaction (Mosseri et al. 1986; Sinha et al. 2021), but we did not observe any changes in arteriole diameter in our mice (data from aged studies submitted for publication). These microvascular changes

can occur with endothelial dysfunction and can result in impaired vasodilation, reduced vasoconstriction in response to a stimulus, and a reduction in the CFR (Mosseri et al. 1986; Taqueti and Di Carli 2018; Sinha et al. 2021). We outlined previously that the LAV-BPIFB4 gene treatment resulted in increased expression of SDF-1/CXCR4, which has been linked to the improvement in angiogenesis and vasculogenesis following injury. It is possible that activation of the SDF-1/CXCR4 signalling pathways resulted in the increased MyHC- α expression as reported earlier (Dang et al. 2020).

Age is often associated with endothelial dysfunction and a reduction in NO bioavailability (Villa et al. 2015b). Our collaborators found that LAV-treatment resulted in increased the phosphorylation of eNOS in circulating mononuclear cells (Villa et al. 2015b; Spinelli et al. 2017). The increased eNOS phosphorylation might increase the production of NO which plays a major role in the endothelial function through regulating the vascular tone by inducing vasorelaxation, decreasing oxidative stress, stimulating anti-apoptosis and anti-inflammatory functions, angiogenesis activation and the regulation of blood flow (Karbach et al. 2014; Villa et al. 2015b; Spinelli et al. 2017; Sinha et al. 2021). There is a possibility the increase in eNOS activity noted in the LAV group could be the reason of enhancing the MBF (Villa et al. 2015b; Spinelli et al. 2017; Dang et al. 2020).

The MBF and CFR values in the LAV group during the late treatment trial are higher than those in the early treatment experiments. It is possible that LAV-treatment may be more effective in older animals or that a single injection of the LAV-AAV loses efficacy with time, but this is a consideration open for further investigation (Dang et al. 2020).

There was a strong positive relation between the MBF values at rest in the late and early treatments and the CO results, which could be because the increase in the MBF led to a sufficient oxygen supply to the myocardium and thus an enhancement in its pumping performance and contractile ability (Gliemann 2016; Sinha et al. 2021).

To sum up, our studies have shown that ^{18}F -FDG and ^{13}N -NH₃ can be used to assess aspects of cardiac function in mice with our Mediso nanoscan 122S PET/CT scanner in both diabetic and ageing models. We have also demonstrated that ^{13}N -NH₃ imaging can be used to assess the therapeutic effect of the LAV-BPIFB4 gene which has been shown to improve cardiac performance, reduce capillary rarefaction fibrosis and endothelial dysfunction, and enhance MBF possibly through increasing SDF-1/CXCR4 and eNOS signalling pathways, as well as other unknown mechanisms to be investigated.

Chapter 10:

Conclusion, limitations, and future work:

10.1 Summary and conclusion:

There is a paucity of literature using small PET/CT imaging in mice to assess cardiac function, resulting in a lack of standardized imaging protocols. This is due to many challenges associated with resolution, animal handling, tracer availability, preparation, and access to the scanner. In this research, we successfully revealed the robustness of micro-PET CT scanner in evaluating cardiac function across different murine models. Additionally, we developed imaging protocol sets through which cardiac function could be assessed in terms of MBF and glucose metabolism. Our Mediso micro-PET/CT scanner produced accurate and repeatable results that were congruent with the histological analysis, echocardiography and doppler imaging. The feasibility of these developed protocols has enabled us to extend our work to investigate the therapeutic effect of the LAV gene in diabetic and ageing models. In our study, we also demonstrated that LAV-BPIFB4 therapy increased the MBF and CFR, increased the capillary and arteriole density, decreased endothelial dysfunction, and enhanced the cardiac contractility performance through mechanisms that might be involved in increasing SDF-1 and eNOS signalling pathways and other unknown ones.

In conclusion, we demonstrated the accuracy and repeatability of our Mediso micro-PET/CT scanner as a powerful tool in evaluating cardiac function in mice through the absolute quantification of MBF and MGM using the concept of compartmental modelling. A noteworthy outcome was the feasibility of our micro-PET/CT scanner in making it possible to assess the therapeutic effect of LAV-BPIFB4 gene therapy in diabetic and ageing models. Our results confirmed that the LAV-BPIFB4 gene exerted its beneficial effects through increasing capillary and arteriole density that subsequently resulted in an improvement in the blood flow and contractile performance of the myocardium and these benefits lasted for several months following treatment intervention.

10.2 Novelty of the research:

The novelty of the research can be outlined as follows:

- Demonstrating the ability of the Micro PET/CT scanner in assessing cardiac function in murine models using PET quantitative techniques.
- Standardising PET imaging protocols in murine models for the evaluation of cardiac function through absolute quantification using compartmental modelling and two radiotracers including $^{13}\text{N-NH}_3$ and $^{18}\text{F-FDG}$.
- This study is the first to evaluate the effects of LAV-BPIFB4 gene therapy using a Mediso micro-PET/CT scanner and compartmental modelling that provided absolute quantification of MBF and MGM.

10.3 Research limitations:

Micro PET/CT imaging suffers from multiple challenges associated with the use of short-lived radiotracers which require an on-site cyclotron and coordination with the production team in terms of the time to prepare the radiotracer, the animal cannulation process, and access to the scanner room. In our research, one of the major limitations against smooth imaging processes was due to the cyclotron being located in a different building (about 8-10 minutes delivery time).

Another limitation was calculating the IF, which is a crucial aspect in compartmental modelling. It requires a series of blood withdrawals and tissue specimens to derive the arterial IF and then correlate it with our ammonia flow results. However, this was not possible, and the IF was derived from the image, which was previously validated by several researchers. Although PMOD can extract all heart segments for regional myocardial analysis, the resolution of the scanner might not cope with the small size of each myocardial region.

This research was designed to help in developing a computational cardiac model of the mouse, however this was not possible due to the Covid pandemic which delayed the imaging analysis process and the ability to stay in contact with the assigned supervisors in Bath university. All this delay resulted in a lack of the time necessary to carry out this goal.

10.4 Future work:

Additional experiments might be needed to assess the physical performance of our micro-PET/CT scanner with $^{13}\text{N-NH}_3$. Indeed, NEMA only provided a standard acceptable limit for the preclinical scanner resolution using $^{18}\text{F-FDG}$ and according to our knowledge, no previous work has been conducted to set standard IQ test values for ammonia in a small PET/CT scanner. It would be useful to test the performance of the micro-PET scanner by performing an IQ performance test using different radiotracers considering their physical half-life and positron range differences which are important factors in designing imaging protocols.

Interestingly, our quantitative MBF data, that we measured using $^{13}\text{N-NH}_3$, was of interest to the Pmod developers who we met at the Pmod training course in Switzerland in September 2019. They showed interest in using our $^{13}\text{N-NH}_3$ data for MBF quantification in murine models for the purpose of developing their analysis software. This was agreed but unfortunately, this process has been attenuated by the Covid pandemic crisis. One of our future goals is to contact them again for future collaboration in developing imaging protocols that may play a role in drug development.

Another important goal is the further refinement of our developed imaging protocols to investigate the influence of imaging duration on the produced quantitative data in murine models. In fact, we had problems with changes in the heart dimension in the $^{18}\text{F-FDG}$ scans of the aged mice which might be related to scan duration or the injected pharmacological stress drug. Repeating the protocols, while changing some of the technical variables such as scan duration, might identify the cause behind these results.

One of the aims of this research was to use quantitative gated data in developing computational mice models but due to the limitation addressed above, this was not the case. Therefore, performing gated micro-PET/CT scans to produce functional parameters, such as LVEF%, and then comparing the values with echocardiography values will be an interesting aspect to investigate.

Finally, our collaborators in Bristol university aim to further evaluate the LAV-BPIFB4 gene therapeutic effect by monitoring its effect when it is administrated orally in old mice models.

Appendices:

10.1 Appendix A: The gain in body weight (in gram) for all the diabetic groups at week 6,8,9 and 13.

Group Name: NV (diabetic injected with vehicle)				
Mouse ID	Weight in grams (g)			
	Week 6	Week 8	Week 9	Week 13
PA30	29	38	37	48
PA31	30	37	36	49
PA40	30	41	36	45
PA41	34	41	40	49
PA45	32	38	37	42
PA46	32	39	38	47
PA50	26	37	34	51
PA51	37	35	32	50
Mean	31.25	38.25	36.25	47.63

Table A.1: The gain in the body weight (in gram) for the NV group at week 6,8,9 and 13.

Group Name: LC (healthy mice)				
Mouse ID	Weight in grams			
	Week 6	Week 8	Week 9	Week 13
PA52	34	28	25	32
PA53	23	26	25	32
PA54	22	24	24	28
PA55	24	26	26	32
PA56	22	24	24	28
PA57	25	27	26	31
PA58	24	27	27	31
PA59	23	24	24	29
Mean	24.63	25.75	25.13	30.38

Table A.2: The gain in the body weight (in gram) for the LC group at week 6,8,9 and 13.

Group Name: WT (diabetic injected with AAV9-WT-BPIFB4)				
Mouse ID	Weight in grams			
	Week 6	Week 8	Week 9	Week 13
PA27	30	38	36	45
PA28	30	38	37	51
PA29	26	34	33	47
PA35	30	36	36	51
PA36	29	35	35	47
PA47	28	36	34	51
PA48	30	38	36	51
PA49	29	36	33	49
Mean	29.00	36.38	35.00	49.00

Table A.3: The gain in the body weight (in gram) for the WT group at week 6,8,9 and 13.

Group Name: LAV (diabetic injected with AAV9-LAV-BPIFB4)				
Mouse ID	Weight in grams			
	Week 6	Week 8	Week 9	Week 13
PA32	33	36	36	52
PA33	33	39	39	37
PA34	33	40	35	53
PA37	33	41	38	54
PA38	34	39	39	49
PA39	36	41	40	50
PA42	30	38	35	48
PA43	32	38	36	46
PA44	33	40	38	47
Mean	33.00	39.11	37.33	48.44

Table A.4: The gain in the body weight (in gram) for the LAV group at week 6,8,9 and 13.

10.2 Appendix B: The chest hair regrowth (# of grids) in all the diabetic groups.

Group	Mouse ID	DOB	Hair removal date	Week 1	Week 2	Week 3	Week 4
				later	later	later	later
				Chest hairiness (# of grids)	Chest hairiness (# of grids)	Chest hairiness (# of grids)	Chest hairiness (# of grids)
NV control	PA85	18/01/2017	13/03/2017	0	2	2	2.5
NV control	PA86	18/01/2017	13/03/2017	0	0	0	0.5
NV control	PA87	18/01/2017	13/03/2017	0	0	0	0
LAV virus	PA88	18/01/2017	13/03/2017	0	0	2	2
LAV virus	PA89	18/01/2017	13/03/2017	0	1	1	3.5
LAV virus	PA90	18/01/2017	13/03/2017	0	2.5	3	4
WT virus	PA91	18/01/2017	13/03/2017	0	0	2	2.5
WT virus	PA92	18/01/2017	13/03/2017	0	0.5	1	2
WT virus	PA93	18/01/2017	13/03/2017	0.5	1	1.5	1.5
lean control	PA94	18/01/2017	13/03/2017	1	4	7	7
lean control	PA95	18/01/2017	13/03/2017	3	7	9	9.5
lean control	PA96	18/01/2017	13/03/2017	9	9	9	9.5

Table B.1: The chest hair regrowth (# of grids) in the diabetic groups.

10.3 Appendix C: Image demonstration for the $^{13}\text{N-NH}_3$ dynamic scans at rest and stress for all the ageing groups during the early and late treatments.

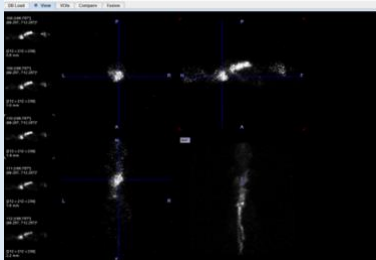
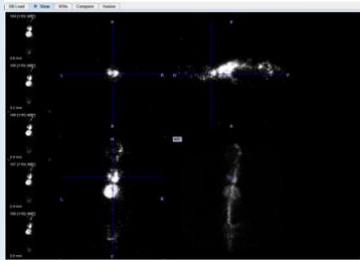
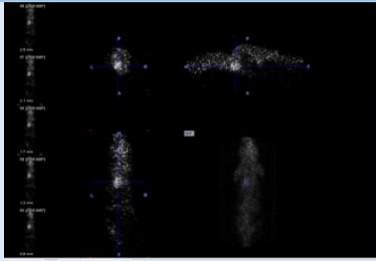
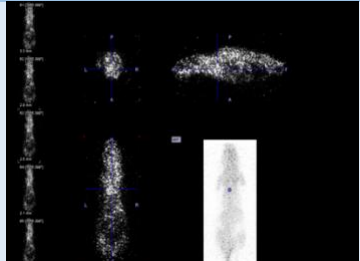
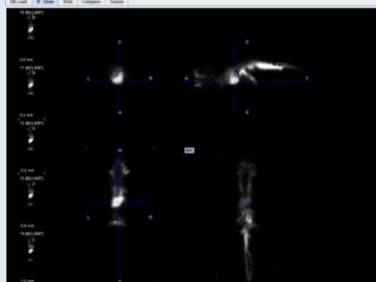
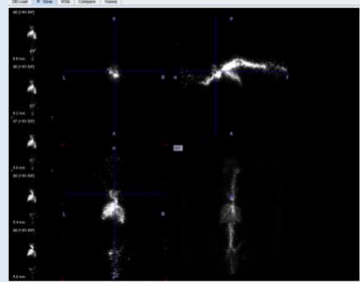
Mice Group	Treatment phase		Rest scan	Stress scan
NV	Early treatment	PA134		
		PA135		
		PA136		

Table C.1: Image demonstration for the $^{13}\text{N-NH}_3$ dynamic scans at rest and stress for the NV group at early treatment phase.


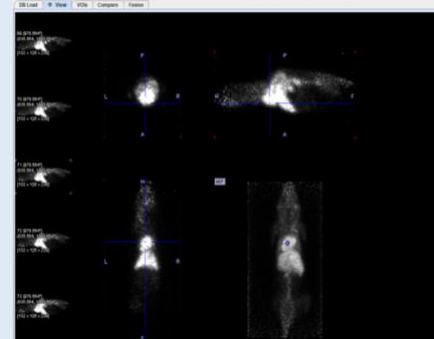
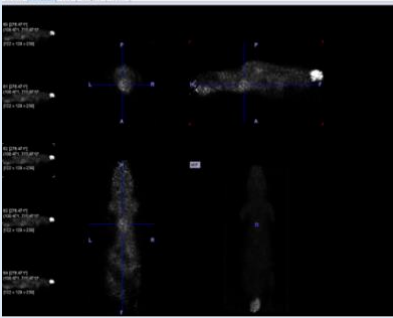
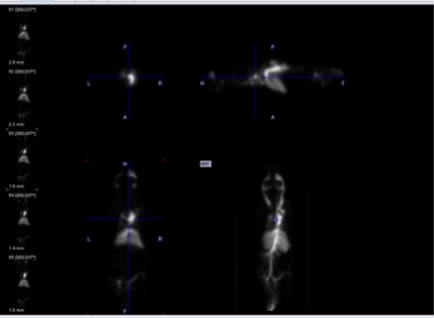
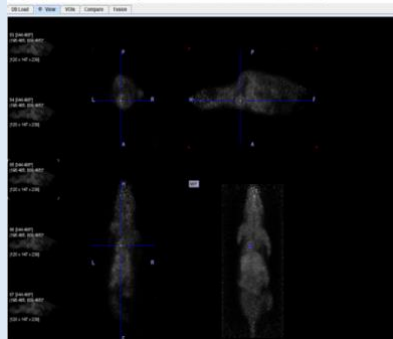
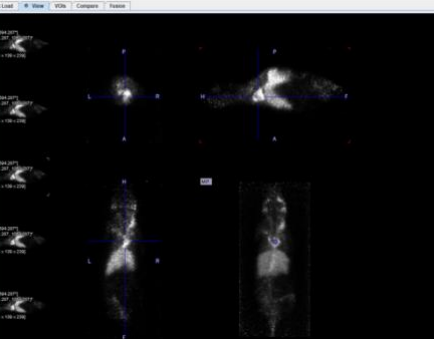
Mice Group	Treatment phase		Rest scan	Stress scan
NV	Late treatment	PA214		
		PA215		
		PA216		

Table C.2: Image demonstration for the $^{13}\text{N-NH}_3$ dynamic scans at rest and stress for the NV group at late treatment phase.

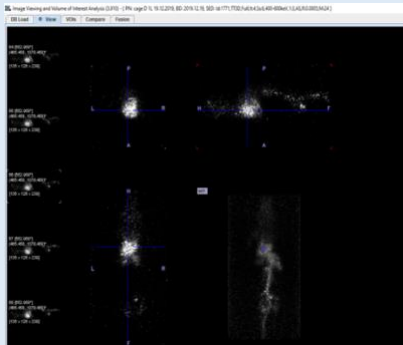
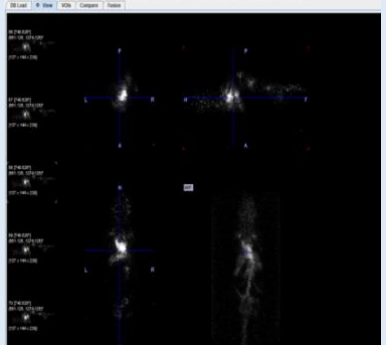
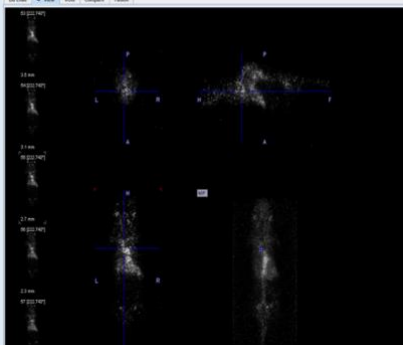
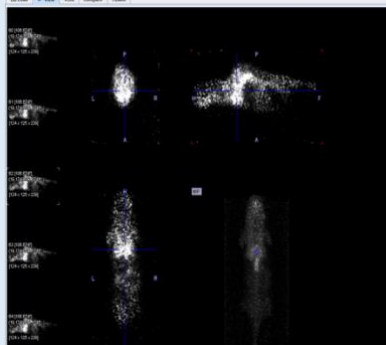
Mice Group	Treatment phase		Rest scan	Stress scan
WT	Early treatment	PA150		
		PA153		

Table C.3: Image demonstration for the $^{15}\text{N-NH}_3$ dynamic scans at rest and stress for the WT group at early treatment phase.

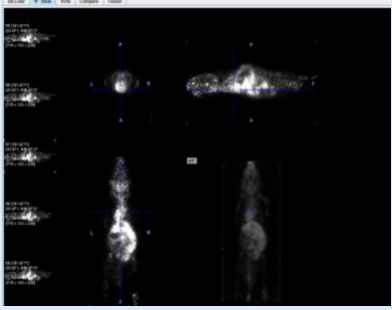
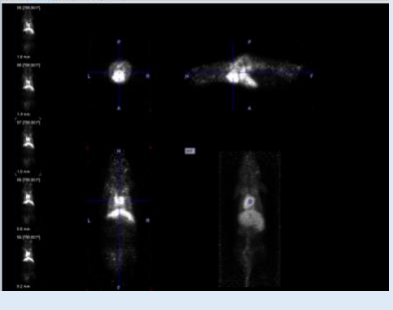
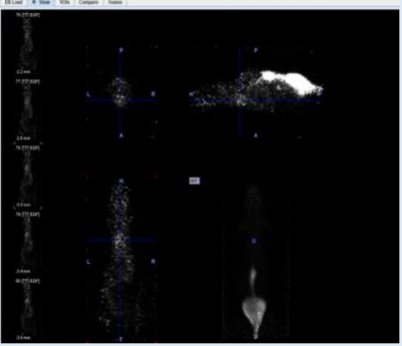
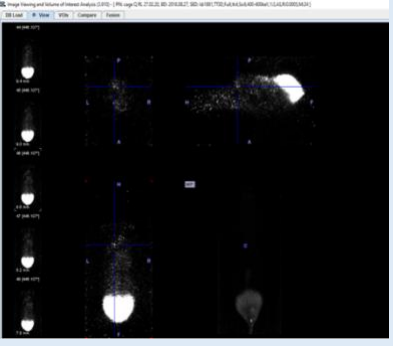
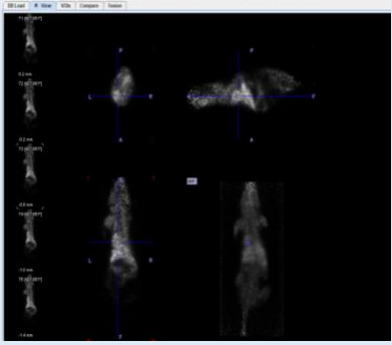
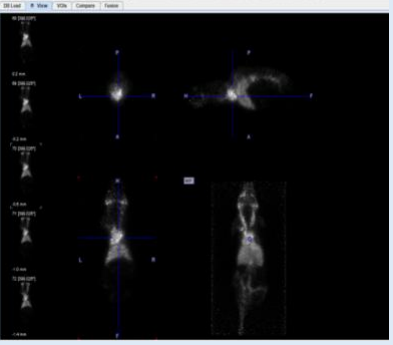
Mice Group	Treatment phase		Rest scan	Stress scan
WT	Late treatment	PA225		
		PA226		
		PA228		

Table C.4: Image demonstration for the $^{13}\text{N-NH}_3$ dynamic scans at rest and stress for the WT group at late treatment phase.

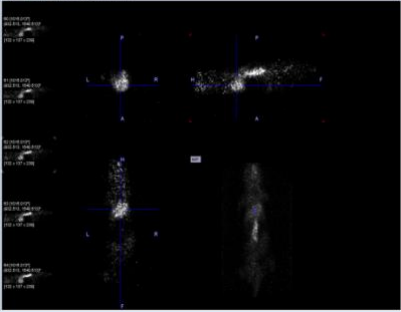
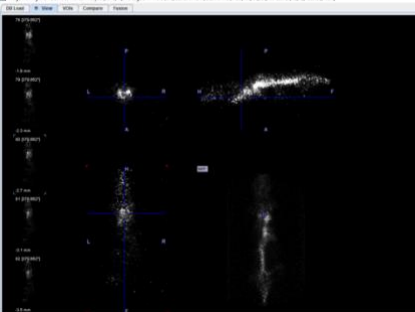
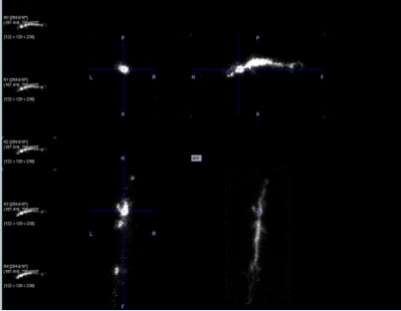
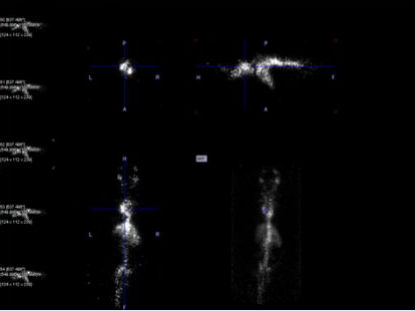
Mice Group	Treatment phase		Rest scan	Stress scan
GFP	Early treatment	PA139		
		PA140		

Table C.5: Image demonstration for the ¹³N-NH₃ dynamic scans at rest and stress for the GFP group at early treatment phase.



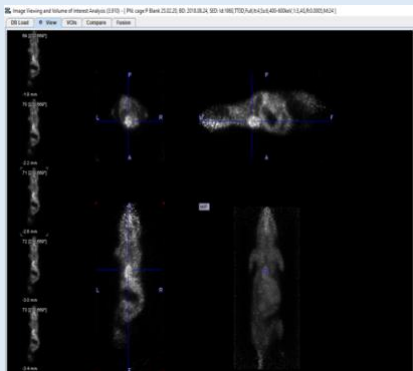
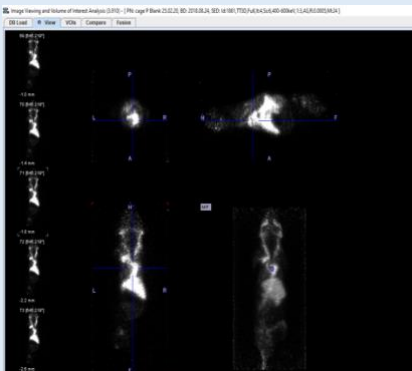
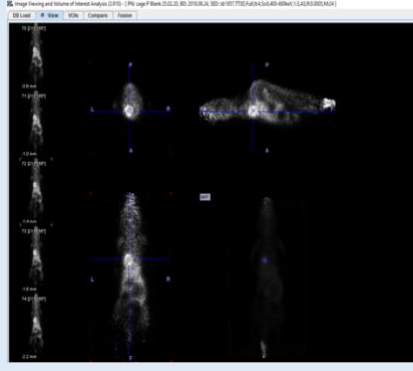
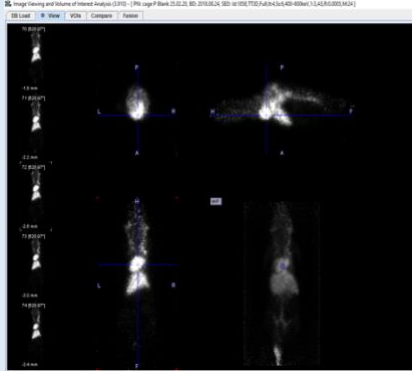
Mice Group	Treatment phase		Rest scan	Stress scan
GFP	Late treatment	PA219		
		PA222		
		PA223		

Table C.6: Image demonstration for the $^{13}\text{N-NH}_3$ dynamic scans at rest and stress for the GFP group at late treatment phase.

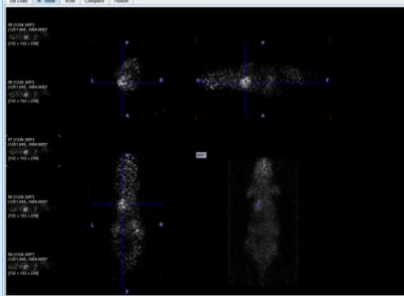
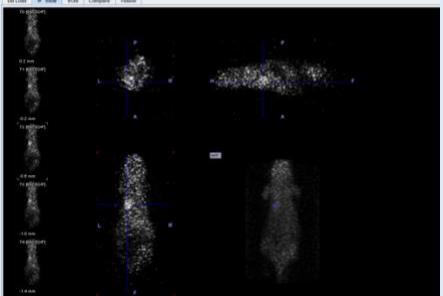
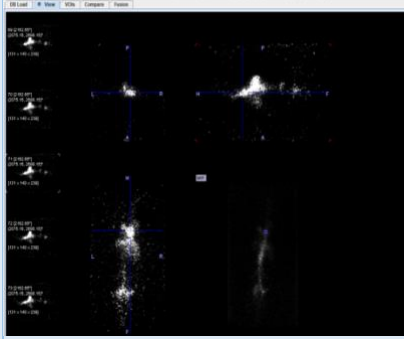
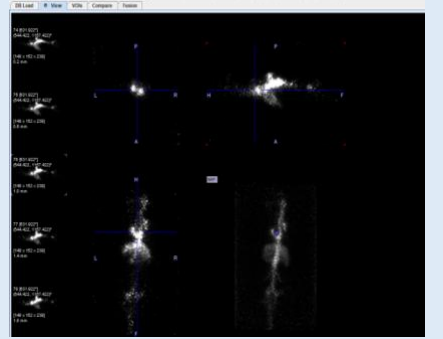
Mice Group	Treatment phase		Rest scan	Stress scan
LAV	Early treatment	PA144		
		PA146		

Table C.7: Image demonstration for the $^{13}\text{N-NH}_3$ dynamic scans at rest and stress for the LAV group at early treatment phase.

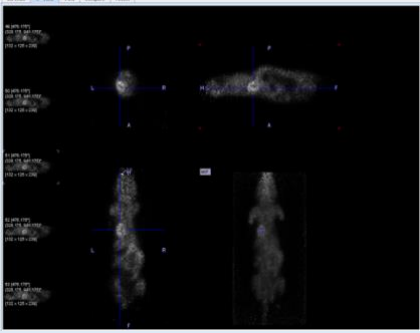
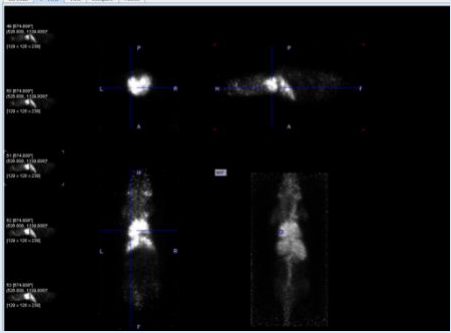
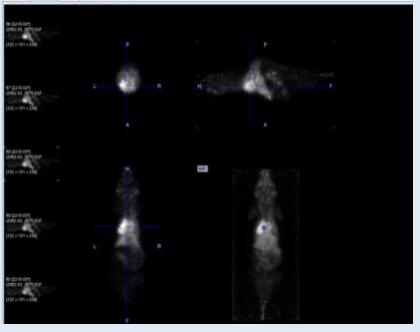
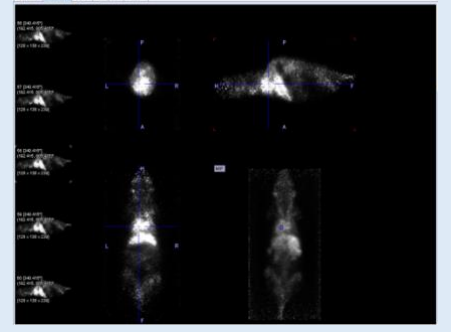
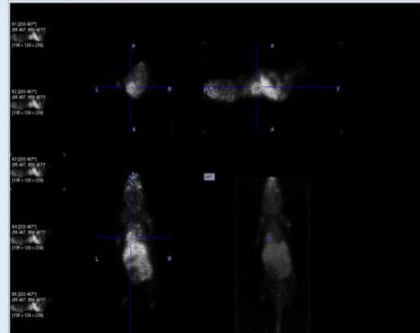
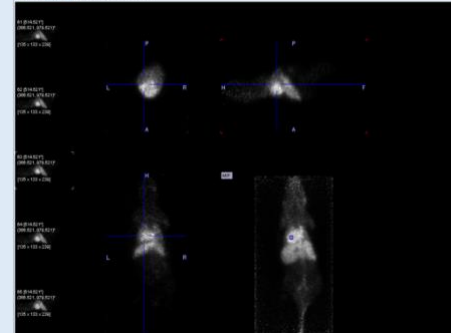
Mice Group	Treatment phase		Rest scan	Stress scan
LAV	Late treatment	PA229		
		PA230		
		PA231		

Table C.8: Image demonstration for the $^{13}\text{N-NH}_3$ dynamic scans at rest and stress for the LAV group at late treatment phase.

10.4 Appendix D:

10.4.1 Publications:

1. Dang, Z. et al. 2020. Transfer of a human gene variant associated with exceptional longevity improves cardiac function in obese type 2 diabetic mice through induction of the SDF-1/CXCR4 signalling pathway.

10.4.2 Expected to be published:

1. LAV-BPIFB4 rejuvenates human heart pericytes and improves aged cardiac function and vascularization.

Corresponding Author(s):

Dr. Paolo Madeddu

Contributing Author(s):

Monica Cattaneo, Antonio Paolo Beltrami, Anita Thomas, Gaia Spinetti, Valeria Alvino, Elisa Avolio, Claudia Veneziano, Irene Giulia Rolle, Sandro Sponga, Elena Sangalli, Anna Maciag, Fabrizio Dal Piaz, Carmine Vecchione, Aishah Alenezi, Stephen Paisey, Annibale Alessandro Puca.

10.4.3 Presentation:

1. 5th of October 2018- Wales Research and diagnostic Imaging Center PETIC, University Hospital of Wales UHW, Cardiff, UK, “Quantitative Analysis in cardiac PET Imaging”.
2. 25th of October 2019- PETIC Research Roadshow Autumn 2019, Wales Research and diagnostic Imaging Center PETIC, University Hospital of Wales UHW, Cardiff, UK, “Quantitative Analysis in cardiac PET Imaging”.

10.4.4 Poster:

1. 16th of April 2021, The 35th student-led Cardiff Medical and Dental School Research Symposium, University Hospital of Wales UHW, Cardiff, UK, “Quantitative Analysis in cardiac PET Imaging”.
2. 6th -8th of September 2021-British Society of Cardiovascular Research BSCR Autumn Meeting and Early Career Symposium 2021, “Quantitative cardiac micro-PET/CT Imaging to evaluate murine cardiac function”, Bristol Medical school, University of Bristol. Online (Zoom) & Gather.Town.

References:

- Aaronson, P. I., Ward, J. P. and Connolly, M. J. 2020. *The cardiovascular system at a glance*. John Wiley & Sons.
- Abbott, J. D., Huang, Y., Liu, D., Hickey, R., Krause, D. S. and Giordano, F. J. 2004. Stromal cell-derived factor-1alpha plays a critical role in stem cell recruitment to the heart after myocardial infarction but is not sufficient to induce homing in the absence of injury. *Circulation* 110(21), pp. 3300-3305. doi: 10.1161/01.Cir.0000147780.30124.Cf
- Adams, M. C., Turkington, T. G., Wilson, J. M. and Wong, T. Z. 2010. A systematic review of the factors affecting accuracy of SUV measurements. *American Journal of Roentgenology*. American Roentgen Ray Society.
- Adeshara, K. A., Diwan, A. G. and Tupe, R. S. 2016. Diabetes and Complications: Cellular Signaling Pathways, Current Understanding and Targeted Therapies. *Curr Drug Targets* 17(11), pp. 1309-1328. doi: 10.2174/1389450117666151209124007
- Aiuti, A., Webb, I. J., Bleul, C., Springer, T. and Gutierrez-Ramos, J. C. 1997. The chemokine SDF-1 is a chemoattractant for human CD34+ hematopoietic progenitor cells and provides a new mechanism to explain the mobilization of CD34+ progenitors to peripheral blood. *J Exp Med* 185(1), pp. 111-120. doi: 10.1084/jem.185.1.111
- Alberti, K. G. and Zimmet, P. Z. 1998. Definition, diagnosis and classification of diabetes mellitus and its complications. Part 1: diagnosis and classification of diabetes mellitus provisional report of a WHO consultation. *Diabet Med* 15(7), pp. 539-553. doi: 10.1002/(sici)1096-9136(199807)15:7<539::Aid-dia668>3.0.Co;2-s
- Alexandraki, K., Piperi, C., Kalofoutis, C., Singh, J., Alaveras, A. and Kalofoutis, A. 2006. Inflammatory process in type 2 diabetes: The role of cytokines. *Annals of the New York Academy of Sciences* 1084(1), pp. 89-117.
- AlGhatrif, M. et al. 2013. Longitudinal trajectories of arterial stiffness and the role of blood pressure: the Baltimore Longitudinal Study of Aging. *Hypertension* 62(5), pp. 934-941. doi: 10.1161/hypertensionaha.113.01445
- Anderson, R. H., Spicer, D. E., Hlavacek, A. M., Cook, A. C., Backer, C. L. and Wilcox, B. R. 2013. *Wilcox's surgical anatomy of the heart*. Fourth edition. ed. Cambridge: Cambridge University Press.
- Anjan, V., Pryma, D., Zamani, P., Guerraty, M. and Dubroff, J. 2015. *mYocArdiAl Blood floW reserve: A BiomArker for Adverse cArdionAsculAr outcomes?*
- Anversa, P., Li, P., Sonnenblick, E. H. and Olivetti, G. 1994. Effects of aging on quantitative structural properties of coronary vasculature and microvasculature in rats. *Am J Physiol* 267(3 Pt 2), pp. H1062-1073. doi: 10.1152/ajpheart.1994.267.3.H1062

- Anversa, P., Palackal, T., Sonnenblick, E. H., Olivetti, G., Meggs, L. G. and Capasso, J. M. 1990. Myocyte cell loss and myocyte cellular hyperplasia in the hypertrophied aging rat heart. *Circ Res* 67(4), pp. 871-885. doi: 10.1161/01.res.67.4.871
- Ara, T., Tokoyoda, K., Okamoto, R., Koni, P. A. and Nagasawa, T. 2005. The role of CXCL12 in the organ-specific process of artery formation. *Blood* 105(8), pp. 3155-3161.
- Association, N. E. M. 2008. Performance measurements of small animal positron emission tomographs NEMA Standards Publication NU 4-2008. *Rosslyn, VA: NEMA* 23,
- Balcombe, N. R. and Sinclair, A. 2001. Ageing: definitions, mechanisms and the magnitude of the problem. *Baillière's best practice & research. Clinical gastroenterology* 15(6), pp. 835-849. doi: 10.1053/bega.2001.0244
- Basu, D. and Kulkarni, R. 2014. Overview of blood components and their preparation. *Indian journal of anaesthesia* 58(5), pp. 529-537. doi: 10.4103/0019-5049.144647
- Basu, S., Kwee, T. C., Surti, S., Akin, E. A., Yoo, D. and Alavi, A. 2011. Fundamentals of PET and PET/CT imaging. *Annals of the New York Academy of Sciences* 1228(1), pp. 1-18.
- Bateman, T. M. 2012. Advantages and disadvantages of PET and SPECT in a busy clinical practice. *Journal of Nuclear Cardiology* 19(1), pp. 3-11.
- Beekman, F. and van der Have, F. 2007. The pinhole: gateway to ultra-high-resolution three-dimensional radionuclide imaging. *European Journal of Nuclear Medicine and Molecular Imaging* 34(2), pp. 151-161. doi: 10.1007/s00259-006-0248-6
- Berenson, G. S., Srinivasan, S. R. and 2005. Cardiovascular risk factors in youth with implications for aging: The Bogalusa Heart Study.
- Berne, R. M. 1963. Cardiac nucleotides in hypoxia: possible role in regulation of coronary blood flow. *Am J Physiol* 204, pp. 317-322. doi: 10.1152/ajplegacy.1963.204.2.317
- Bertoldo, A., Rizzo, G. and Veronese, M. 2014. Deriving physiological information from PET images: From SUV to compartmental modelling. *Clinical and Translational Imaging*. Springer-Verlag Italia s.r.l.
- BioRender. 2017. *BioRender ICONS & TEMPLATES*. BioRender. Available at: <https://biorender.com/features/> [Accessed.
- Bleul, C. C., Farzan, M., Choe, H., Parolin, C., Clark-Lewis, I., Sodroski, J. and Springer, T. A. 1996. The lymphocyte chemoattractant SDF-1 is a ligand for LESTR/fusin and blocks HIV-1 entry. *Nature* 382(6594), pp. 829-833. doi: 10.1038/382829a0
- Boellaard, R. 2009. Standards for PET image acquisition and quantitative data analysis. *Journal of Nuclear Medicine*.

Bulcha, J. T., Wang, Y., Ma, H., Tai, P. W. L. and Gao, G. 2021. Viral vector platforms within the gene therapy landscape. *Signal Transduction and Targeted Therapy*. Springer Nature.

Buonincontri, G., Methner, C., Carpenter, T. A., Hawkes, R. C., Sawiak, S. J. and Krieg, T. 2013. MRI and PET in mouse models of myocardial infarction. *Journal of visualized experiments : JoVE* (82), pp. e50806-e50806. doi: 10.3791/50806

Büscher, K. et al. 2010. Isochronous Assessment of Cardiac Metabolism and Function in Mice Using Hybrid PET/MRI. *Journal of Nuclear Medicine* 51(8), p. 1277. doi: 10.2967/jnumed.110.076448

Campia, U., Gerhard-Herman, M., Piazza, G. and Goldhaber, S. Z. 2019. Peripheral Artery Disease: Past, Present, and Future. *Am J Med* 132(10), pp. 1133-1141. doi: 10.1016/j.amjmed.2019.04.043

Cañadas, M., Embid, M., Lage, E., Desco, M., Vaquero, J. J., Member, S. and Pérez, J. M. 2011. NEMA NU 4-2008 Performance Measurements of Two Commercial Small-Animal PET Scanners. *Science* 58(1), pp. 58-65.

Carli, M. F. D., Prcevski, P., Singh, T. P., Janisse, J., Ager, J., Muzik, O. and Heide, R. V. 2000. *Myocardial Blood Flow, Function, and Metabolism in Repetitive Stunning*.

Carter, L. M. et al. 2020. The Impact of Positron Range on PET Resolution, Evaluated with Phantoms and PHITS Monte Carlo Simulations for Conventional and Non-conventional Radionuclides. *Molecular Imaging and Biology* 22(1), pp. 73-84. doi: 10.1007/s11307-019-01337-2

Cates, C. C., McCabe, J. G., Lawson, G. W. and Couto, M. A. 2014. Core body temperature as adjunct to endpoint determination in murine median lethal dose testing of rattlesnake venom. *Comp Med* 64(6), pp. 440-447.

Catherine Hagan, D. V. M., Ph.D.,. 2017. *WHEN ARE MICE CONSIDERED OLD?* The Jackson Laboratory. Available at: <https://www.jax.org/news-and-insights/jax-blog/2017/november/when-are-mice-considered-old> [Accessed: September 2019].

Cavalcanti Filho, J. L. G., Lima, R. d. S. L., Neto, L. d. S. M., Bittencourt, L. K., Domingues, R. C. and da Fonseca, L. M. B. 2011. PET/CT and vascular disease: current concepts. *European journal of radiology* 80(1), pp. 60-67.

Cerqueira, M. D. et al. 2002. Standardized Myocardial Segmentation and Nomenclature for Tomographic Imaging of the Heart. *Circulation* 105(4), pp. 539-542. doi: doi:10.1161/hc0402.102975

Champion, C. and Le Loirec, C. 2007. Positron follow-up in liquid water: II. Spatial and energetic study for the most important radioisotopes used in PET. *Phys Med Biol* 52(22), pp. 6605-6625. doi: 10.1088/0031-9155/52/22/004

Chan, S. Y., White, K. and Loscalzo, J. 2012. Deciphering the molecular basis of human cardiovascular disease through network biology. *Curr Opin Cardiol* 27(3), pp. 202-209. doi: 10.1097/HCO.0b013e3283515b31

- Chang, C. Y. et al. 2020. Simplified quantification of ¹³N-ammonia PET myocardial blood flow: A comparative study with the standard compartment model to facilitate clinical use. *Journal of Nuclear Cardiology* 27(3), pp. 819-828. doi: 10.1007/s12350-018-1450-1
- Chen, K., Pittman, R. N. and Popel, A. S. 2008. Nitric oxide in the vasculature: where does it come from and where does it go? A quantitative perspective. *Antioxid Redox Signal* 10(7), pp. 1185-1198. doi: 10.1089/ars.2007.1959
- Chen, S., Hu, P., Gu, Y., Yu, H. and Shi, H. 2020. Performance characteristics of the digital uMI550 PET/CT system according to the NEMA NU2-2018 standard. *EJNMMI Physics* 7(1), doi: 10.1186/s40658-020-00315-w
- Cherry, S., Sorenson, J. and Phelps, M. 2012. *Physics in Nuclear Medicine*.
- Cherry, S. R. and Gambhir, S. S. 2001. Use of Positron Emission Tomography in Animal Research. *ILAR Journal* 42(3), pp. 219-232. doi: 10.1093/ilar.42.3.219
- Chia, E. M., Hsieh, C. H., Boyd, A., Pham, P., Vidaic, J., Leung, D. and Thomas, L. 2014. Effects of age and gender on right ventricular systolic and diastolic function using two-dimensional speckle-tracking strain. *J Am Soc Echocardiogr* 27(10), pp. 1079-1086.e1071. doi: 10.1016/j.echo.2014.06.007
- Chien, K. R. 2004. *Molecular basis of cardiovascular disease : a companion to Braunwald's Heart disease*. Place of publication not identified: Saunders.
- Chiriac, A., Terzic, A., Park, S., Ikeda, Y., Faustino, R. and Nelson, T. J. 2010. SDF-1-enhanced cardiogenesis requires CXCR4 induction in pluripotent stem cells. *J Cardiovasc Transl Res* 3(6), pp. 674-682. doi: 10.1007/s12265-010-9219-1
- Choi, Y. et al. 1999. Quantification of myocardial blood flow using ¹³N-ammonia and PET: Comparison of tracer models. *Journal of Nuclear Medicine* 40(6), pp. 1045-1055.
- Choi, Y. et al. 1993. A simplified method for quantification of myocardial blood flow using nitrogen-13-ammonia and dynamic PET. *Journal of Nuclear Medicine* 34(3), pp. 488-497.
- Chow, B. J. et al. 2014. Prognostic value of PET myocardial perfusion imaging in obese patients. *JACC Cardiovasc Imaging* 7(3), pp. 278-287. doi: 10.1016/j.jcmg.2013.12.008
- Ciaglia, E. et al. 2022. Transfer of the longevity-associated variant of BPIFB4 gene rejuvenates immune system and vasculature by a reduction of CD38+ macrophages and NAD+ decline. *Cell Death & Disease* 13(1), p. 86. doi: 10.1038/s41419-022-04535-z
- Cicone, F. et al. 2017. Cardiac Radionuclide Imaging in Rodents: A Review of Methods, Results, and Factors at Play. *Front Med (Lausanne)* 4, p. 35. doi: 10.3389/fmed.2017.00035
- Clark, G. et al. 2010. Both the stimulation and inhibition of root hair growth induced by extracellular nucleotides in Arabidopsis are mediated by nitric oxide and reactive oxygen species. *Plant Mol Biol* 74(4-5), pp. 423-435. doi: 10.1007/s11103-010-9683-7

- Clemmensen, A. E., Ghotbi, A. A., Bodholdt, R. P., Hag, A. M. F., Hasbak, P., Ripa, R. S. and Kjaer, A. 2017. Perfusion imaging using rubidium-82 ((82)Rb) PET in rats with myocardial infarction: First small animal cardiac (82)Rb-PET. *J Nucl Cardiol* 24(2), pp. 750-752. doi: 10.1007/s12350-016-0564-6
- Cochran, B. J. et al. 2017. Determining Glucose Metabolism Kinetics Using 18F-FDG Micro-PET/CT. *Journal of visualized experiments : JoVE* (123), p. 55184. doi: 10.3791/55184
- Cotsarelis, G. and Millar, S. E. 2001. Towards a molecular understanding of hair loss and its treatment. *Trends in Molecular Medicine* 7(7), pp. 293-301. doi: [https://doi.org/10.1016/S1471-4914\(01\)02027-5](https://doi.org/10.1016/S1471-4914(01)02027-5)
- Crock, H. V. 1996. *Atlas of vascular anatomy of the skeleton and spinal cord*. London: Martin Dunitz.
- Croteau, E., Bénard, F., Cadorette, J., Gauthier, M.-E., Aliaga, A., Bentourkia, M. h. and Lecomte, R. 2003. Quantitative gated PET for the assessment of left ventricular function in small animals. *Journal of nuclear medicine : official publication, Society of Nuclear Medicine* 44(10), pp. 1655-1661.
- Croteau, E., Bénard, F., hamed, B., Rousseau, J., Paquette, M. and Lecomte, R. 2004. *Quantitative Myocardial Perfusion and Coronary Reserve in Rats with 13 N-Ammonia and Small Animal PET: Impact of Anesthesia and Pharmacologic Stress Agents*. Available at: <http://jnm.snmjournals.org/content/45/11/1924.full.pdf>
<https://jnm.snmjournals.org/content/jnumed/45/11/1924.full.pdf>
- Croteau, E. et al. 2014. β 2-adrenergic stress evaluation of coronary endothelial-dependent vasodilator function in mice using 11 C-acetate micro-PET imaging of myocardial blood flow and oxidative metabolism. doi: 10.1186/s13550-014-0068-9
- Cussó, L., Vaquero, J. J., Bacharach, S. and Desco, M. 2014. Comparison of methods to reduce myocardial 18F-FDG uptake in mice: calcium channel blockers versus high-fat diets. *PLoS One* 9(9), p. e107999. doi: 10.1371/journal.pone.0107999
- D., N. D. 1979. Classification and diagnosis of diabetes mellitus and other categories of glucose intolerance. National Diabetes Data Group. *Diabetes* 28(12), pp. 1039-1057. doi: 10.2337/diab.28.12.1039
- Dai, D.-F. and Rabinovitch, P. S. 2009. Cardiac aging in mice and humans: the role of mitochondrial oxidative stress. *Trends in cardiovascular medicine* 19(7), pp. 213-220. doi: 10.1016/j.tcm.2009.12.004
- Dal Lin, C., Tona, F. and Osto, E. 2015. Coronary Microvascular Function and Beyond: The Crosstalk between Hormones, Cytokines, and Neurotransmitters. *Int J Endocrinol* 2015, p. 312848. doi: 10.1155/2015/312848
- Dang, Z. et al. 2020. Transfer of a human gene variant associated with exceptional longevity improves cardiac function in obese type 2 diabetic mice through induction of the SDF-1/CXCR4 signalling pathway.

- Daube-Witherspoon, M. E. et al. 2002. *PET Performance Measurements Using the NEMA NU 2-2001 Standard*. Available at: www.nema.org
- Deelen, J. et al. 2019. A meta-analysis of genome-wide association studies identifies multiple longevity genes. *Nat Commun* 10(1), p. 3669. doi: 10.1038/s41467-019-11558-2
- DeGrado, T. R. et al. 1996. Estimation of myocardial blood flow for longitudinal studies with ^{13}N -labeled ammonia and positron emission tomography. *Journal of Nuclear Cardiology* 3(6 PART I), pp. 494-507. doi: 10.1016/s1071-3581(96)90059-8
- DeGrado, T. R., Turkington, T. G., Williams, J. J., Stearns, C. W., Hoffman, J. M. and Coleman, R. E. 1994. Performance characteristics of a whole-body PET scanner. *Journal of Nuclear Medicine* 35(8), pp. 1398-1406.
- Denayer, T., Stöhr, T. and Van Roy, M. 2014. Animal models in translational medicine: Validation and prediction. *New Horizons in Translational Medicine* 2(1), pp. 5-11. doi: <https://doi.org/10.1016/j.nhtm.2014.08.001>
- Depré, C., Rider, M. H. and Hue, L. 1998. Mechanisms of control of heart glycolysis. *Eur J Biochem* 258(2), pp. 277-290. doi: 10.1046/j.1432-1327.1998.2580277.x
- Depre, C., Vanoverschelde, J.-L. J. and Taegtmeyer, H. 1999. *Glucose for the Heart Regulation of Glucose Metabolism in Normoxic Heart*. Available at: <http://www.circulationaha.org>
- Dewey, M. et al. 2020. Clinical quantitative cardiac imaging for the assessment of myocardial ischaemia. *Nature Reviews Cardiology* 17(7), pp. 427-450. doi: 10.1038/s41569-020-0341-8
- Di Carli, M. F., Dorbala, S., Meserve, J., El Fakhri, G., Sitek, A. and Moore, S. C. 2007. Clinical myocardial perfusion PET/CT. *Journal of Nuclear Medicine* 48(5), pp. 783-793. doi: 10.2967/jnumed.106.032789
- Di Pardo, A. et al. 2020. The longevity-associated variant of BPIFB4 improves a CXCR4-mediated striatum–microglia crosstalk preventing disease progression in a mouse model of Huntington’s disease. *Cell Death and Disease* 11(7), doi: 10.1038/s41419-020-02754-w
- Dikici, S., Claeysens, F. and MacNeil, S. 2020. Bioengineering vascular networks to study angiogenesis and vascularization of physiologically relevant tissue models in vitro. *ACS Biomaterials Science & Engineering* 6(6), pp. 3513-3528.
- Disselhorst, J. A. et al. 2010. Image-quality assessment for several positron emitters using the NEMA NU 4-2008 standards in the Siemens Inveon small-animal PET scanner. *J Nucl Med* 51(4), pp. 610-617. doi: 10.2967/jnumed.109.068858
- Dobrucki, L. W. and Sinusas, A. J. 2007. Imaging of angiogenesis. *Cardiac PET and PET/CT Imaging*, pp. 394-411.
- Doevendans, P. A. et al. 1998. Cardiovascular phenotyping in mice.

- Dossena, M. et al. 2020. New insights for BPIFB4 in cardiovascular therapy.
- Dunet, V., Klein, R., Allenbach, G., Renaud, J., deKemp, R. A. and Prior, J. O. 2016. Myocardial blood flow quantification by Rb-82 cardiac PET/CT: A detailed reproducibility study between two semi-automatic analysis programs. *Journal of Nuclear Cardiology* 23(3), pp. 499-510. doi: 10.1007/s12350-015-0151-2
- Dutta, S. and Sengupta, P. 2016. Men and mice: Relating their ages. *Life Sci* 152, pp. 244-248. doi: 10.1016/j.lfs.2015.10.025
- Elmadbouh, I., Haider, H., Jiang, S., Idris, N. M., Lu, G. and Ashraf, M. 2007. Ex vivo delivered stromal cell-derived factor-1alpha promotes stem cell homing and induces angiomyogenesis in the infarcted myocardium. *J Mol Cell Cardiol* 42(4), pp. 792-803. doi: 10.1016/j.yjmcc.2007.02.001
- Emini Veseli, B., Perrotta, P., De Meyer, G. R. A., Roth, L., Van der Donckt, C., Martinet, W. and De Meyer, G. R. Y. 2017. Animal models of atherosclerosis. *Eur J Pharmacol* 816, pp. 3-13. doi: 10.1016/j.ejphar.2017.05.010
- Englund, E. K. and Langham, M. C. 2020. Quantitative and Dynamic MRI Measures of Peripheral Vascular Function. *Front Physiol* 11, p. 120. doi: 10.3389/fphys.2020.00120
- Erikson, G. A. et al. 2016. Whole-Genome Sequencing of a Healthy Aging Cohort. *Cell* 165(4), pp. 1002-1011. doi: 10.1016/j.cell.2016.03.022
- Erlandsson, K., Dickson, J., Arridge, S., Atkinson, D., Ourselin, S. and Hutton, B. F. 2016. MR Imaging-Guided Partial Volume Correction of PET Data in PET/MR Imaging. *PET Clin* 11(2), pp. 161-177. doi: 10.1016/j.cpet.2015.09.002
- Fajemiroye, J. O. et al. 2018. Aging-Induced Biological Changes and Cardiovascular Diseases.
- Fang, Y. H. and Muzic, R. F., Jr. 2008. Spillover and partial-volume correction for image-derived input functions for small-animal 18F-FDG PET studies. *J Nucl Med* 49(4), pp. 606-614. doi: 10.2967/jnumed.107.047613
- Fanjul, V. et al. 2020. Identification of common cardiometabolic alterations and deregulated pathways in mouse and pig models of aging. *Aging Cell* 19(9), p. e13203. doi: 10.1111/accel.13203
- Farhad, H., Dunet, V., Bachelard, K., Allenbach, G., Kaufmann, P. A. and Prior, J. O. 2013. Added prognostic value of myocardial blood flow quantitation in rubidium-82 positron emission tomography imaging. *Eur Heart J Cardiovasc Imaging* 14(12), pp. 1203-1210. doi: 10.1093/ehjci/jet068
- Faulkner, A. et al. 2020. Multi-Omics Analysis of Diabetic Heart Disease in the db/db Model Reveals Potential Targets for Treatment by a Longevity-Associated Gene.

- Feng, Y., Broder, C. C., Kennedy, P. E. and Berger, E. A. 1996. HIV-1 entry cofactor: functional cDNA cloning of a seven-transmembrane, G protein-coupled receptor. *Science* 272(5263), pp. 872-877.
- Ferrari, A. U., Radaelli, A. and Centola, M. 2003. Physiology of Aging Invited Review: Aging and the cardiovascular system. *J Appl Physiol* 95, pp. 2591-2597.
- Fischer, M. et al. 2021a. Cardiac 18F-FDG Positron Emission Tomography: An Accurate Tool to Monitor In vivo Metabolic and Functional Alterations in Murine Myocardial Infarction. *Front Cardiovasc Med* 8, p. 656742. doi: 10.3389/fcvm.2021.656742
- Fischer, M. et al. 2021b. Comparison of metabolic and functional parameters using cardiac 18F-FDG-PET in early to mid-adulthood male and female mice. *EJNMMI Research* 11(1), p. 7. doi: 10.1186/s13550-021-00748-z
- Flora, G. D. and Nayak, M. K. 2019. A Brief Review of Cardiovascular Diseases, Associated Risk Factors and Current Treatment Regimes. *Curr Pharm Des* 25(38), pp. 4063-4084. doi: 10.2174/1381612825666190925163827
- Force, A. P. E. T. S. T. 2008. NEMA Standards Publication NU 4 – 2008 Performance Measurements of Small Animal Positron Emission Tomographs. *Nema*, pp. 23-23.
- Fromonot, J. et al. 2016. Hyperoxia Improves Hemodynamic Status During Head-up Tilt Testing in Healthy Volunteers: A Randomized Study. *Medicine (Baltimore)* 95(8), p. e2876. doi: 10.1097/md.0000000000002876
- Fueger, B. J. et al. 2006. Impact of Animal Handling on the Results of ¹⁸F-FDG PET Studies in Mice. *Journal of Nuclear Medicine* 47(6), p. 999.
- FUJIFILM VisualSonics designs. 1999. *Your Best Tool For Mouse Echocardiography*. FUJIFILM VisualSonics design and manufacture. Available at: <https://www.visualsonics.com/application/preclinical/cardiology> [Accessed: 11 June 2022].
- Fukushima, K., Javadi, M. S., Higuchi, T., Lautamäki, R., Merrill, J., Nekolla, S. G. and Bengel, F. M. 2011. Prediction of short-term cardiovascular events using quantification of global myocardial flow reserve in patients referred for clinical 82Rb PET perfusion imaging. *J Nucl Med* 52(5), pp. 726-732. doi: 10.2967/jnumed.110.081828
- Galicia-Garcia, U. et al. 2020. Pathophysiology of Type 2 Diabetes Mellitus. *Int J Mol Sci* 21(17), doi: 10.3390/ijms21176275
- Gallagher, M. and Rapp, P. R. 1997. The use of animal models to study the effects of aging on cognition. *Annual review of psychology* 48(1), pp. 339-370.
- Gargiulo, S. et al. 2012. PET/CT Imaging in Mouse Models of Myocardial Ischemia. *Journal of Biomedicine and Biotechnology* 2012, p. 541872. doi: 10.1155/2012/541872

- Garland, C. J., Hiley, C. R. and Dora, K. A. 2011. EDHF: spreading the influence of the endothelium. *British journal of pharmacology* 164(3), pp. 839-852. doi: 10.1111/j.1476-5381.2010.01148.x
- Gehling, A. M. et al. 2018. Evaluation of Volume of Intramuscular Injection into the Caudal Thigh Muscles of Female and Male BALB/c Mice (*Mus musculus*). *J Am Assoc Lab Anim Sci* 57(1), pp. 35-43.
- Gerstenblith, G., Frederiksen, J., Yin, F. C., Fortuin, N. J., Lakatta, E. G. and Weisfeldt, M. L. 1977. Echocardiographic assessment of a normal adult aging population. *Circulation* 56(2), pp. 273-278. doi: 10.1161/01.cir.56.2.273
- Gewirtz, H. and Dilsizian, V. 2017. Myocardial viability: survival mechanisms and molecular imaging targets in acute and chronic ischemia. *Circulation Research*. Lippincott Williams and Wilkins.
- Gill, R. W. 1985. Measurement of blood flow by ultrasound: Accuracy and sources of error. *Ultrasound in Medicine & Biology* 11(4), pp. 625-641. doi: [https://doi.org/10.1016/0301-5629\(85\)90035-3](https://doi.org/10.1016/0301-5629(85)90035-3)
- Giri, B., Dey, S., Das, T., Sarkar, M., Banerjee, J. and Dash, S. K. 2018. Chronic hyperglycemia mediated physiological alteration and metabolic distortion leads to organ dysfunction, infection, cancer progression and other pathophysiological consequences: An update on glucose toxicity. *Biomed Pharmacother* 107, pp. 306-328. doi: 10.1016/j.biopha.2018.07.157
- Gliemann, L. 2016. Training for skeletal muscle capillarization: a Janus-faced role of exercise intensity? *Eur J Appl Physiol* 116(8), pp. 1443-1444. doi: 10.1007/s00421-016-3419-6
- Goertzen, A. L. et al. 2012. NEMA NU 4-2008 comparison of preclinical PET imaging systems. *J Nucl Med* 53(8), pp. 1300-1309. doi: 10.2967/jnumed.111.099382
- Gontijo, R. M. G., Ferreira, A. V., Silva, J. B. and Mamede, M. 2017. *IMAGE QUALITY ASSESMENT USING NEMA NU 4/2008 STANDARDS IN SMALL ANIMAL PET SCANNER*.
- Gotlieb, A. I. 2018. Molecular basis of cardiovascular disease. In: Coleman, W. and Tsongalis, G. eds. *Molecular Pathology The Molecular Basis of Human Disease*. London: Elsevier.
- Gotlieb, A. I. 2020. Molecular basis of cardiovascular disease. *Essential Concepts in Molecular Pathology*. Elsevier, pp. 209-227.
- Gould, K. L., Kirkeeide, R. L. and Buchi, M. 1990. Coronary flow reserve as a physiologic measure of stenosis severity. *J Am Coll Cardiol* 15(2), pp. 459-474. doi: 10.1016/s0735-1097(10)80078-6
- Greco, A. et al. 2012. Reproducibility and accuracy of non-invasive measurement of infarct size in mice with high-resolution PET/CT. *Journal of Nuclear Cardiology* 19(3), pp. 492-499. doi: 10.1007/s12350-012-9538-5

Group, N. D. D. 1979. Classification and Diagnosis of Diabetes Mellitus and Other Categories of Glucose Intolerance. *Diabetes* 28(12), pp. 1039-1057. doi: 10.2337/diab.28.12.1039

Guerraty, M. A. et al. 2020. The role of resting myocardial blood flow and myocardial blood flow reserve as a predictor of major adverse cardiovascular outcomes. *PLoS One* 15(2), p. e0228931. doi: 10.1371/journal.pone.0228931

Guieu, R., Deharo, J.-C., Maille, B., Crotti, L., Torresani, E., Brignole, M. and Parati, G. 2020. Adenosine and the Cardiovascular System: The Good and the Bad. *Journal of clinical medicine* 9(5), p. 1366. doi: 10.3390/jcm9051366

Hallen, P., Schug, D., Weissler, B., Gebhardt, P., Salomon, A., Kiessling, F. and Schulz, V. 2018. PET performance evaluation of the small-animal Hyperion II(D) PET/MRI insert based on the NEMA NU-4 standard. *Biomed Phys Eng Express* 4(6), p. 065027. doi: 10.1088/2057-1976/aae6c2

Hamdani, N. et al. 2014. Left ventricular diastolic dysfunction and myocardial stiffness in diabetic mice is attenuated by inhibition of dipeptidyl peptidase 4. *Cardiovascular Research* 104(3), pp. 423-431. doi: 10.1093/cvr/cvu223

Hartley, C. J., Reddy, A. K., Madala, S., Michael, L. H., Entman, M. L. and Taffet, G. E. 2007. Effects of Isoflurane on Coronary Blood Flow Velocity in Young, Old and ApoE^{-/-} Mice Measured by Doppler Ultrasound. *Ultrasound in Medicine and Biology* 33(4), pp. 512-521. doi: 10.1016/j.ultrasmedbio.2006.11.002

Hartley, C. J., Reddy, A. K., Michael, L. H., Entman, M. L., Chintalagattu, V., Khakoo, A. Y. and Taffet, G. E. 2010. Coronary flow reserve in mice: effects of age, coronary disease, and vascular loading. *Annu Int Conf IEEE Eng Med Biol Soc* 2010, pp. 3780-3783. doi: 10.1109/iembs.2010.5627571

He, X. et al. 2019. Image-Derived Input Functions for Quantification of A(1) Adenosine Receptors Availability in Mice Brains Using PET and [(18)F]CPFPX. *Front Physiol* 10, p. 1617. doi: 10.3389/fphys.2019.01617

Herrero, P., Kim, J., Sharp, T. L., Engelbach, J. A., Lewis, J. S., Gropler, R. J. and Welch, M. J. 2006. Assessment of myocardial blood flow using 15O-water and 1-11C-acetate in rats with small-animal PET. *J Nucl Med* 47(3), pp. 477-485.

Herzog, B. A. et al. 2009. Long-term prognostic value of 13N-ammonia myocardial perfusion positron emission tomography added value of coronary flow reserve. *J Am Coll Cardiol* 54(2), pp. 150-156. doi: 10.1016/j.jacc.2009.02.069

Hiasa, K. et al. 2004. Gene transfer of stromal cell-derived factor-1alpha enhances ischemic vasculogenesis and angiogenesis via vascular endothelial growth factor/endothelial nitric oxide synthase-related pathway: next-generation chemokine therapy for therapeutic neovascularization. *Circulation* 109(20), pp. 2454-2461. doi: 10.1161/01.Cir.0000128213.96779.61

Higuchi, T. et al. 2007. Characterization of normal and infarcted rat myocardium using a combination of small-animal PET and clinical MRI. *J Nucl Med* 48(2), pp. 288-294.

- Hildebrandt, I. J., Su, H. and Weber, W. A. 2008. Anesthesia and other considerations for in vivo imaging of small animals. *Ilar j* 49(1), pp. 17-26. doi: 10.1093/ilar.49.1.17
- Hoffman, E. J., Huang, S. C. and Phelps, M. E. 1979. Quantitation in positron emission computed tomography: 1. Effect of object size. *J Comput Assist Tomogr* 3(3), pp. 299-308. doi: 10.1097/00004728-197906000-00001
- Hofmann, F. 2020. The cGMP system: components and function. *Biol Chem* 401(4), pp. 447-469. doi: 10.1515/hsz-2019-0386
- Hoinoiu, B. et al. 2019. Chronic Hindlimb Ischemia Assessment; Quantitative Evaluation Using Laser Doppler in a Rodent Model of Surgically Induced Peripheral Arterial Occlusion. *Diagnostics (Basel)* 9(4), doi: 10.3390/diagnostics9040139
- Hoskins, P. R. 1990. Measurement of arterial blood flow by Doppler ultrasound. *Clin Phys Physiol Meas* 11(1), pp. 1-26. doi: 10.1088/0143-0815/11/1/001
- Hosoda, T., Rota, M., Kajstura, J., Leri, A. and Anversa, P. 2011. Role of stem cells in cardiovascular biology. *J Thromb Haemost* 9 Suppl 1(0 1), pp. 151-161. doi: 10.1111/j.1538-7836.2011.04363.x
- Huang, Q., Massey, J. C., Mińczuk, K., Li, J. and Kundu, B. K. 2019. Non-invasive determination of blood input function to compute rate of myocardial glucose uptake from dynamic FDG PET images of rat heart in vivo: comparative study between the inferior vena cava and the left ventricular blood pool with spill over and partial volume corrections. *Physics in Medicine & Biology* 64(16), p. 165010. doi: 10.1088/1361-6560/ab3238
- Hue, L., Beauloye, C. and Bertrand, L. 2016. Principles in the Regulation of Cardiac Metabolism. *The Scientist's Guide to Cardiac Metabolism*. pp. 57-71.
- Hughes, C. E. and Nibbs, R. J. B. 2018. A guide to chemokines and their receptors. *Febs j* 285(16), pp. 2944-2971. doi: 10.1111/febs.14466
- Hwang, E. S., , Yoon, G., , Kang, H. T. and 2009. A comparative analysis of the cell biology of senescence and aging.
- Inubushi, M. et al. 2004. Nitrogen-13 ammonia cardiac positron emission tomography in mice: effects of clonidine-induced changes in cardiac work on myocardial perfusion. *Eur J Nucl Med Mol Imaging* 31(1), pp. 110-116. doi: 10.1007/s00259-003-1328-5
- J, C. et al. 1993. Regional blood flow, oxidative metabolism, and glucose utilization in patients with recent myocardial infarction. *Circulation* 88(3), pp. 884-895.
- Jackson, E. K., Gillespie, D. G., Mi, Z. and Cheng, D. 2018. Adenosine Receptors Influence Hypertension in Dahl Salt-Sensitive Rats: Dependence on Receptor Subtype, Salt Diet, and Sex. *Hypertension* 72(2), pp. 511-521. doi: 10.1161/hypertensionaha.117.10765

- Jampa-Ngern, S., Viravaidya-Pasuwat, K., Suvanasuthi, S. and Khantachawana, A. 2017. Effect of laser diode light irradiation on growth capability of human hair follicle dermal papilla cells. *Annu Int Conf IEEE Eng Med Biol Soc* 2017, pp. 3592-3595. doi: 10.1109/embc.2017.8037634
- Jan, M.-L., Ni, Y.-C., Chen, K.-W., Liang, H.-C., Chuang, K.-S. and Fu, Y.-K. 2006. A combined micro-PET/CT scanner for small animal imaging. *Nuclear Instruments and Methods in Physics Research Section A: Accelerators, Spectrometers, Detectors and Associated Equipment* 569(2), pp. 314-318. doi: <https://doi.org/10.1016/j.nima.2006.08.106>
- Jia, G., Hill, M. A. and Sowers, J. R. 2018. Diabetic Cardiomyopathy: An Update of Mechanisms Contributing to This Clinical Entity. *Circulation Research* 122(4), pp. 624-638. doi: 10.1161/CIRCRESAHA.117.311586
- Jogiya, R. et al. 2013a. Hyperemic stress myocardial perfusion cardiovascular magnetic resonance in mice at 3 Tesla: Initial experience and validation against microspheres.
- Jogiya, R. et al. 2013b. Hyperemic stress myocardial perfusion cardiovascular magnetic resonance in mice at 3 Tesla: initial experience and validation against microspheres. *J Cardiovasc Magn Reson* 15(1), p. 62. doi: 10.1186/1532-429x-15-62
- Johnson, S. G. and Peters, S. 2010. Advances in Pharmacologic Stress Agents: Focus on Regadenoson. *J Nucl Med Technol* 38, pp. 163-171. doi: 10.2967/jnmt.109.065581
- Jones, C. M. et al. 2014. Measurement science in the circulatory system. *Cell Mol Bioeng* 7(1), pp. 1-14. doi: 10.1007/s12195-013-0317-4
- Juarez-Orozco, L. E., Monroy-Gonzalez, A., Prakken, N. H. J., Noordzij, W., Knuuti, J., deKemp, R. A. and Slart, R. H. J. A. 2019. Phase analysis of gated PET in the evaluation of mechanical ventricular synchrony: A narrative overview. *Journal of Nuclear Cardiology*. Springer.
- Kalkan, S., Hocaoglu, N., Arici, A. A., Oransay, K., Ergor, G. and Tuncok, Y. 2010. Effects of adenosine receptor antagonists on survival in amitriptyline-poisoned mice. *Drug Chem Toxicol* 33(3), pp. 233-237. doi: 10.3109/01480540903130690
- Kalogeris, T., Baines, C. P., Krenz, M. and Korthuis, R. J. 2016. Ischemia/Reperfusion. *Comprehensive Physiology* 7(1), pp. 113-170. doi: 10.1002/cphy.c160006
- Kampoli, A.-M., Tousoulis, D., Marinou, K., Siasos, G. and Stefanadis, C. 2009. Vascular effects of diabetes mellitus. *Vascular disease prevention* 6(1),
- Kapoor, V., McCook, B. M. and Torok, F. S. 2004. An introduction to PET-CT imaging. *Radiographics* 24(2), pp. 523-543.
- Karbach, S., Wenzel, P., Waisman, A., Munzel, T. and Daiber, A. 2014. eNOS uncoupling in cardiovascular diseases--the role of oxidative stress and inflammation. *Curr Pharm Des* 20(22), pp. 3579-3594. doi: 10.2174/13816128113196660748

- Katara, R. et al. 2011. Intravenous gene therapy with PIM-1 via a cardiotropic viral vector halts the progression of diabetic cardiomyopathy through promotion of prosurvival signaling. *Circ Res* 108(10), pp. 1238-1251. doi: 10.1161/circresaha.110.239111
- Katara, R. G., Caporali, A., Oikawa, A., Meloni, M., Emanuelli, C. and Madeddu, P. 2010. Vitamin B1 analog benfotiamine prevents diabetes-induced diastolic dysfunction and heart failure through Akt/Pim-1-mediated survival pathway. *Circ Heart Fail* 3(2), pp. 294-305. doi: 10.1161/circheartfailure.109.903450
- Kaufmann, P. A. and Camici, P. G. 2005. Myocardial blood flow measurement by PET: technical aspects and clinical applications. *J Nucl Med* 46(1), pp. 75-88.
- Keating, M. T. and Sanguinetti, M. C. 1996. Molecular Genetic Insights Into Cardiovascular Disease. *Science (American Association for the Advancement of Science)* 272(5262), pp. 681-685. doi: 10.1126/science.272.5262.681
- Khalil. 2017. *Small Animal micro-PET imaging: an overview INTRODUCTION*.
- Khan, A. S. et al. 2001. Growth hormone increases regional coronary blood flow and capillary density in aged rats.
- Khorsand, A. et al. 2005. Gated cardiac ¹³N-NH₃ PET for assessment of left ventricular volumes, mass, and ejection fraction: comparison with electrocardiography-gated ¹⁸F-FDG PET. *J Nucl Med* 46(12), pp. 2009-2013.
- Khurana, R., , Martin, J. F., , Zachary, I. and 2001. Gene therapy for cardiovascular disease: A case for cautious optimism.
- Kim, H.-S., Lee, B.-i. and Ahn, J.-S. 2021. Assessment of MicroPET Image Quality Based on Reconstruction Methods and Post-Filtering. *Applied Sciences* 11, p. 8707. doi: 10.3390/app11188707
- Kinahan, P. E. and Fletcher, J. W. 2010. PET/CT Standardized Uptake Value (SUVs) in Clinical Practice and Assessing Response to Therapy. *Seminars in Ultrasound, CT and MRI* 31(6), pp. 496-505. doi: 10.1053/j.sult.2010.10.001.PET/CT
- King, M. A., Pretorius, P. H., Farncombe, T. and Beekman, F. J. 2002. Introduction to the physics of molecular imaging with radioactive tracers in small animals. *J Cell Biochem Suppl* 39, pp. 221-230. doi: 10.1002/jcb.10447
- Kishore, S. P. et al. 2018. Modernizing the World Health Organization List of Essential Medicines for Preventing and Controlling Cardiovascular Diseases. *Journal of the American College of Cardiology* 71(5), pp. 564-574. doi: <https://doi.org/10.1016/j.jacc.2017.11.056>
- Knaapen, P. et al. 2010. Cardiac PET-CT: advanced hybrid imaging for the detection of coronary artery disease. *Neth Heart J* 18(2), pp. 90-98. doi: 10.1007/bf03091744

- Ko, K.-Y., Wu, Y.-W., Liu, C.-W., Cheng, M.-F., Yen, R.-F. and Yang, W.-S. 2017. Longitudinal evaluation of myocardial glucose metabolism and contractile function in obese type 2 diabetic db/db mice using small-animal dynamic (18)F-FDG PET and echocardiography. *Oncotarget* 8(50), pp. 87795-87808. doi: 10.18632/oncotarget.21202
- Kober, F., Iltis, I., Cozzone, P. J. and Bernard, M. 2005. Myocardial blood flow mapping in mice using high-resolution spin labeling magnetic resonance imaging: influence of ketamine/xylazine and isoflurane anesthesia. *Magn Reson Med* 53(3), pp. 601-606. doi: 10.1002/mrm.20373
- Kochi, T., Imai, Y., Takeda, A., Watanabe, Y., Mori, S., Tachi, M. and Kodama, T. 2013. Characterization of the arterial anatomy of the murine hindlimb: Functional role in the design and understanding of ischemia models. *PLoS One* 8(12), doi: 10.1371/journal.pone.0084047
- Kolakalapudi, P. and Omar, B. 2015. *Diabetes Mellitus and the Cardiovascular System*.
- Kolwicz, S. C. 2018. An “Exercise” in Cardiac Metabolism. *Frontiers in Cardiovascular Medicine* 5(June), doi: 10.3389/fcvm.2018.00066
- Kolwicz, S. C., Jr., Purohit, S. and Tian, R. 2013. Cardiac metabolism and its interactions with contraction, growth, and survival of cardiomyocytes. *Circ Res* 113(5), pp. 603-616. doi: 10.1161/CIRCRESAHA.113.302095
- Kolwicz, S. C., Jr. and Tian, R. 2011. Glucose metabolism and cardiac hypertrophy. *Cardiovasc Res* 90(2), pp. 194-201. doi: 10.1093/cvr/cvr071
- Korte, F. S., Herron, T. J., Rovetto, M. J. and McDonald, K. S. 2005. Power output is linearly related to MyHC content in rat skinned myocytes and isolated working hearts. *Am J Physiol Heart Circ Physiol* 289(2), pp. H801-812. doi: 10.1152/ajpheart.01227.2004
- Kreissl, M. C. et al. 2011. Influence of dietary state and insulin on myocardial, skeletal muscle and brain [18F]-fluorodeoxyglucose kinetics in mice. *EJNMMI Research* 1(1), p. 8. doi: 10.1186/2191-219X-1-8
- Kreissl, M. C. et al. 2006. Noninvasive Measurement of Cardiovascular Function in Mice with High-Temporal-Resolution Small-Animal PET. *Journal of Nuclear Medicine* 47(6), p. 974.
- Krivokapich, J., Huang, S. C., Phelps, M. E., MacDonald, N. S. and Shine, K. I. 1982. Dependence of ¹³NH₃ myocardial extraction and clearance on flow and metabolism. *American Journal of Physiology-Heart and Circulatory Physiology* 242(4), pp. H536-H542. doi: 10.1152/ajpheart.1982.242.4.H536
- Krueger, M. A., Huke, S. S. and Glenny, R. W. 2013. Visualizing Regional Myocardial Blood Flow in the Mouse. *Circulation Research* 112(9), pp. e88-e97. doi: doi:10.1161/CIRCRESAHA.113.301162
- Kudej, R. K., White, L. T., Kudej, A. B., Vatner, S. F. and Lewandowski, E. D. 2002. Brief increase in carbohydrate oxidation after reperfusion reverses myocardial stunning in conscious pigs. *Circulation* 106(22), pp. 2836-2841. doi: 10.1161/01.cir.0000039326.87475.98

- Kudo, T. et al. 2002. Noninvasive measurement of myocardial activity concentrations and perfusion defect sizes in rats with a new small-animal positron emission tomograph. *Circulation* 106(1), pp. 118-123. doi: 10.1161/01.cir.0000020221.28996.78
- Kuhle, W. G. et al. 1992. Quantification of regional myocardial blood flow using ¹³N-ammonia and reoriented dynamic positron emission tomographic imaging. *Circulation* 86(3), pp. 1004-1017. doi: 10.1161/01.CIR.86.3.1004
- Kukreja, R. C. and Xi, L. 2007. eNOS phosphorylation: a pivotal molecular switch in vasodilation and cardioprotection? *J Mol Cell Cardiol* 42(2), pp. 280-282. doi: 10.1016/j.yjmcc.2006.10.011
- Kundu, B. K., Zhong, M., Sen, S., Davogustto, G., Keller, S. R. and Taegtmeyer, H. 2015. Remodeling of glucose metabolism precedes pressure overload-induced left ventricular hypertrophy: Review of a hypothesis. *Cardiology (Switzerland)* 130(4), pp. 211-220. doi: 10.1159/000369782
- Kuntner, C. et al. 2009. Limitations of small animal PET imaging with [¹⁸F]FDDNP and FDG for quantitative studies in a transgenic mouse model of alzheimer's disease. *Molecular Imaging and Biology* 11(4), pp. 236-240. doi: 10.1007/s11307-009-0198-z
- Laforest, R. et al. 2005. Measurement of input functions in rodents: challenges and solutions. *Nuclear Medicine and Biology* 32(7), pp. 679-685. doi: <https://doi.org/10.1016/j.nucmedbio.2005.06.012>
- Lakatta, E. G., Gerstenblith, G., Angell, C. S., Shock, N. W. and Weisfeldt, M. L. 1975. Diminished inotropic response of aged myocardium to catecholamines. *Circulation Research* 36(2), pp. 262-269. doi: 10.1161/01.RES.36.2.262
- Lakhan, S. E. and Harle, L. 2008. Cardiac fibrosis in the elderly, normotensive athlete: case report and review of the literature. *Diagnostic Pathology* 3(1), p. 12. doi: 10.1186/1746-1596-3-12
- Lamoureux, M. et al. 2012. Uniformity and repeatability of normal resting myocardial blood flow in rats using [¹³N]-ammonia and small animal PET. *Nucl Med Commun* 33(9), pp. 917-925. doi: 10.1097/MNM.0b013e328355d8bc
- Landers-Ramos, R. Q. and Prior, S. J. 2018. The Microvasculature and Skeletal Muscle Health in Aging. *Exerc Sport Sci Rev* 46(3), pp. 172-179. doi: 10.1249/jes.0000000000000151
- Layland, J., Carrick, D., Lee, M., Oldroyd, K. and Berry, C. 2014. Adenosine: Physiology, Pharmacology, and Clinical Applications. *JACC: Cardiovascular Interventions* 7(6), pp. 581-591. doi: <https://doi.org/10.1016/j.jcin.2014.02.009>
- Lee, K. H., Ko, B. H., Paik, J. Y., Jung, K. H., Choe, Y. S., Choi, Y. and Kim, B. T. 2005. Effects of anesthetic agents and fasting duration on ¹⁸F-FDG biodistribution and insulin levels in tumor-bearing mice. *J Nucl Med* 46(9), pp. 1531-1536.
- Lee, Y., Fluckey, J. D., Chakraborty, S. and Muthuchamy, M. 2017. Hyperglycemia- and hyperinsulinemia-induced insulin resistance causes alterations in cellular bioenergetics and activation

- of inflammatory signaling in lymphatic muscle. *Faseb j* 31(7), pp. 2744-2759. doi: 10.1096/fj.201600887R
- Leibowitz, D. and Gilon, D. 2012. Echocardiography and the Aging Heart. *Current Cardiovascular Imaging Reports* 5(6), pp. 501-506. doi: 10.1007/s12410-012-9164-2
- Levi, M. and Coronel, R. 1997. *Gene Therapy in the Cardiovascular System*. Available at: <http://cardiovascres.oxfordjournals.org/>
- Lewellen, T. K. 2008. Recent developments in PET detector technology. *Physics in Medicine and Biology*.
- Libby, P. et al. 2019. Atherosclerosis. *Nat Rev Dis Primers* 5(1), p. 56. doi: 10.1038/s41572-019-0106-z
- Liberale, L. and Camici, G. G. 2020. Longevity-associated variant BPIFB4 gene transfer to recapitulate healthy ageing in patients at risk: Is the future around the corner? *European Heart Journal*. Oxford University Press.
- Lin, K., Lloyd-Jones, D. M., Li, D. and Carr, J. C. 2014. Quantitative imaging biomarkers for the evaluation of cardiovascular complications in type 2 diabetes mellitus. *J Diabetes Complications* 28(2), pp. 234-242. doi: 10.1016/j.jdiacomp.2013.09.008
- Lindsey, M. L. et al. 2018. Guidelines for measuring cardiac physiology in mice.
- Liu, A. and Gotlieb, A. 2010. Molecular Basis of Cardiovascular Disease. *Essential Concepts in Molecular Pathology*, pp. 161-173. doi: 10.1016/B978-0-12-374418-0.00014-1
- Liu, X. and Laforest, R. 2009. Quantitative small animal PET imaging with nonconventional nuclides. *Nucl Med Biol* 36(5), doi: 10.1016/j.nucmedbio.2009.01.019
- Lombardo, M. C. and Lamattina, L. 2012. Nitric oxide is essential for vesicle formation and trafficking in Arabidopsis root hair growth. *J Exp Bot* 63(13), pp. 4875-4885. doi: 10.1093/jxb/ers166
- Low, L. A., Bauer, L. C. and Klaunberg, B. A. 2016. Comparing the Effects of Isoflurane and Alpha Chloralose upon Mouse Physiology. *PLoS One* 11(5), p. e0154936. doi: 10.1371/journal.pone.0154936
- Luptak, I., Yan, J., Cui, L., Jain, M., Liao, R. and Tian, R. 2007. Long-term effects of increased glucose entry on mouse hearts during normal aging and ischemic stress. *Circulation* 116(8), pp. 901-909. doi: 10.1161/circulationaha.107.691253
- Lv, H. et al. 2011. Impaired thymic tolerance to α -myosin directs autoimmunity to the heart in mice and humans. *J Clin Invest* 121(4), pp. 1561-1573. doi: 10.1172/jci44583
- Ma, Q. et al. 1998. Impaired B-lymphopoiesis, myelopoiesis, and derailed cerebellar neuron migration in CXCR4- and SDF-1-deficient mice. *Proc Natl Acad Sci U S A* 95(16), pp. 9448-9453. doi: 10.1073/pnas.95.16.9448

- Maddahi, J. and Packard, R. R. S. 2014. Cardiac PET perfusion tracers: current status and future directions. *Seminars in Nuclear Medicine* 44(5), pp. 333-343. doi: 10.1053/j.semnuclmed.2014.06.011
- Maier, B. et al. 2004. Modulation of mammalian life span by the short isoform of p53. *Genes Dev* 18(3), pp. 306-319. doi: 10.1101/gad.1162404
- Makowski, M. et al. 2010. First-pass contrast-enhanced myocardial perfusion MRI in mice on a 3-T clinical MR scanner. *Magnetic Resonance in Medicine* 64(6), pp. 1592-1598. doi: 10.1002/mrm.22470
- Malavolta, M. et al. 2019. LAV-BPIFB4 associates with reduced frailty in humans and its transfer prevents frailty progression in old mice. *Aging* 11(16), pp. 6555-6568. doi: 10.18632/aging.102209
- Manabe, O. et al. 2018. Radiopharmaceutical tracers for cardiac imaging. *Journal of Nuclear Cardiology* 25(4), pp. 1204-1236. doi: 10.1007/s12350-017-1131-5
- Manapragada, P. P., Andrikopoulou, E., Bajaj, N. and Bhambhani, P. 2021. PET cardiac imaging (perfusion, viability, sarcoidosis, and infection). *Radiologic Clinics* 59(5), pp. 835-852.
- Maqbool, M., Dar, M. A., Gani, I. and Mir, S. A. 2019. Animal models in diabetes mellitus: an overview. *Journal of Drug Delivery and Therapeutics* 9(1-s), pp. 472-475.
- Massey, J. C., Seshadri, V., Paul, S., Mińczuk, K., Molinos, C., Li, J. and Kundu, B. K. 2021. Model Corrected Blood Input Function to Compute Cerebral FDG Uptake Rates From Dynamic Total-Body PET Images of Rats in vivo. *Frontiers in Medicine* 8(238), doi: 10.3389/fmed.2021.618645
- Mawlawi, O. et al. 2004. Performance characteristics of a newly developed PET/CT scanner using NEMA standards in 2D and 3D modes. *Journal of nuclear medicine : official publication, Society of Nuclear Medicine* 45(10), pp. 1734-1742.
- Mawlawi, O. and Townsend, D. W. Multimodality imaging: an update on PET/CT technology. doi: 10.1007/s00259-008-1016-6
- McDougald, W. et al. 2020. Standardization of Preclinical PET/CT Imaging to Improve Quantitative Accuracy, Precision, and Reproducibility: A Multicenter Study. *J Nucl Med* 61(3), pp. 461-468. doi: 10.2967/jnumed.119.231308
- McGuinness, M. E. and Talbert, R. L. 1994. Pharmacologic stress testing: experience with dipyridamole, adenosine, and dobutamine. *Am J Hosp Pharm* 51(3), pp. 328-346; quiz 404-325.
- McMurray, F. and Cox, R. D. 2011. Mouse models and type 2 diabetes: Translational opportunities. *Mammalian Genome* 22(7-8), pp. 390-400. doi: 10.1007/s00335-011-9345-3
- Medical Advisory, S. 2005. *Positron emission tomography for the assessment of myocardial viability: an evidence-based analysis*.

- Meechai, T., Tepmongkol, S. and Pluempitiwiriyaewej, C. 2015. Partial-volume effect correction in positron emission tomography brain scan image using super-resolution image reconstruction. *The British journal of radiology* 88(1046), pp. 20140119-20140119. doi: 10.1259/bjr.20140119
- Mees, B. et al. 2007. Endothelial nitric oxide synthase activity is essential for vasodilation during blood flow recovery but not for arteriogenesis. *Arterioscler Thromb Vasc Biol* 27(9), pp. 1926-1933. doi: 10.1161/atvbaha.107.145375
- Meikle, S. R., Kench, P., Kassiou, M. and Banati, R. B. 2005. Small animal SPECT and its place in the matrix of molecular imaging technologies. *Phys Med Biol* 50(22), pp. R45-61. doi: 10.1088/0031-9155/50/22/r01
- Mellitus, W. H. O. E. C. o. D. and World Health, O. 1980. WHO Expert Committee on Diabetes Mellitus [meeting held in Geneva from 25 September to 1 October 1979] : second report. Geneva: World Health Organization.
- Melzer, D., Pilling, L. C. and Ferrucci, L. 2020. The genetics of human ageing. *Nature Reviews Genetics* 21(2), pp. 88-101. doi: 10.1038/s41576-019-0183-6
- Miyashita, K., Takahashi, N., Oka, T., Asakawa, S., Lee, J., Shizukuishi, K. and Inoue, T. 2007. SUV correction for injection errors in FDG-PET examination. *Ann Nucl Med* 21(10), pp. 607-613. doi: 10.1007/s12149-007-0068-1
- Moncada, S. 1991. Nitric oxide: physiology, pathophysiology and pharmacology. *Pharmacol rev* 43, pp. 109-142.
- Moncada, S. and Higgs, E. A. 2006. Nitric Oxide and the Vascular Endothelium. In: Moncada, S. and Higgs, A. eds. *The Vascular Endothelium I*. Berlin, Heidelberg: Springer Berlin Heidelberg, pp. 213-254.
- Morishita, R. 2002. Recent progress in gene therapy for cardiovascular disease. *Circulation Journal* 66(12), pp. 1077-1086. doi: 10.1253/circj.66.1077
- Morris, E. D., Endres, C. J., Schmidt, K. C., Christian, B. T., Muzic, R. F. and Fisher, R. E. 2004. Kinetic Modeling in Positron Emission Tomography. *Emission Tomography: The Fundamentals of PET and SPECT*. pp. 499-540.
- Moses, W. W. 2011. Fundamental Limits of Spatial Resolution in PET. *Nuclear instruments & methods in physics research. Section A, Accelerators, spectrometers, detectors and associated equipment* 648 Supplement 1, pp. S236-S240. doi: 10.1016/j.nima.2010.11.092
- Mosseri, M., Yarom, R., Gotsman, M. and Hasin, Y. 1986. Histologic evidence for small-vessel coronary artery disease in patients with angina pectoris and patent large coronary arteries. *Circulation* 74(5), pp. 964-972.
- Mubagwa, K., Mullane, K. and Flameng, W. 1996. Role of adenosine in the heart and circulation. *Cardiovasc Res* 32(5), pp. 797-813.

- Mukaka, M. M. 2012. Statistics corner: A guide to appropriate use of correlation coefficient in medical research. *Malawi Med J* 24(3), pp. 69-71.
- Muller, D. W. M. 1994. Gene therapy for cardiovascular disease.
- Murthy, V. L. et al. 2014. Effects of sex on coronary microvascular dysfunction and cardiac outcomes. *Circulation* 129(24), pp. 2518-2527. doi: 10.1161/circulationaha.113.008507
- Muzik, O., Beanlands, R. S. B., Hutchins, G. D., Mangner, T. J., Nguyen, N. and Schwaiger, M. 1993. Validation of nitrogen-13-ammonia tracer kinetic model for quantification of myocardial blood flow using PET. *Journal of Nuclear Medicine* 34(1), pp. 83-91.
- Nadig, V., Herrmann, K., Mottaghy, F. M. and Schulz, V. 2022. Hybrid total-body pet scanners—current status and future perspectives. *European Journal of Nuclear Medicine and Molecular Imaging* 49(2), pp. 445-459. doi: 10.1007/s00259-021-05536-4
- Nagasawa, T. et al. 1996. Defects of B-cell lymphopoiesis and bone-marrow myelopoiesis in mice lacking the CXC chemokine PBSF/SDF-1. *Nature* 382(6592), pp. 635-638. doi: 10.1038/382635a0
- Nahrendorf, M. et al. 2006. Multimodal functional cardiac MRI in creatine kinase-deficient mice reveals subtle abnormalities in myocardial perfusion and mechanics. *American Journal of Physiology-Heart and Circulatory Physiology* 290(6), pp. H2516-H2521. doi: 10.1152/ajpheart.01038.2005
- Nakanishi, K., Vinten-Johansen, J., Lefer, D. J., Zhao, Z., Fowler, W. C., 3rd, McGee, D. S. and Johnston, W. E. 1992. Intracoronary L-arginine during reperfusion improves endothelial function and reduces infarct size. *Am J Physiol* 263(6 Pt 2), pp. H1650-1658. doi: 10.1152/ajpheart.1992.263.6.H1650
- Nakao, K., Minobe, W., Roden, R., Bristow, M. R. and Leinwand, L. A. 1997. Myosin heavy chain gene expression in human heart failure. *J Clin Invest* 100(9), pp. 2362-2370. doi: 10.1172/jci119776
- Nappi, C. and El Fakhri, G. 2013. State of the Art in Cardiac Hybrid Technology: PET/MR. *Current Cardiovascular Imaging Reports* 6(4), pp. 338-345. doi: 10.1007/s12410-013-9213-5
- Naresh, N. K., Chen, X., Roy, R. J., Antkowiak, P. F., Annex, B. H. and Epstein, F. H. 2015. Accelerated dual-contrast first-pass perfusion MRI of the mouse heart: Development and application to diet-induced obese mice. *Magnetic Resonance in Medicine* 73(3), pp. 1237-1245. doi: 10.1002/mrm.25238
- Navab, M. et al. 1996. The Yin and Yang of oxidation in the development of the fatty streak. A review based on the 1994 George Lyman Duff Memorial Lecture. *Arterioscler Thromb Vasc Biol* 16(7), pp. 831-842. doi: 10.1161/01.atv.16.7.831
- Nayerossadat, N., Ali, P. and Maedeh, T. 2012. Viral and nonviral delivery systems for gene delivery. *Advanced Biomedical Research* 1(1), pp. 27-27. doi: 10.4103/2277-9175.98152

- Nekolla, S. G., Martinez-Moeller, A. and Saraste, A. 2009. PET and MRI in cardiac imaging: from validation studies to integrated applications. *European Journal of Nuclear Medicine and Molecular Imaging* 36(1), pp. 121-130.
- Nesterov, S. V. et al. 2014. Quantification of myocardial blood flow in absolute terms using (82)Rb PET imaging: the RUBY-10 Study. *JACC Cardiovasc Imaging* 7(11), pp. 1119-1127. doi: 10.1016/j.jcmg.2014.08.003
- Niiyama, H., Huang, N. F., Rollins, M. D. and Cooke, J. P. 2009. Murine Model of Hindlimb Ischemia. *Journal of Visualized Experiments* (23), pp. 1-4. doi: 10.3791/1035
- Nisoli, E. et al. 2005. Calorie Restriction Promotes Mitochondrial Biogenesis by Inducing the Expression of eNOS. *Science (New York, N.Y.)* 310, pp. 314-317. doi: 10.1126/science.1117728
- Niu, J., Ma, J., Guan, X., Zhao, X., Li, P. and Zhang, M. 2019. Correlation Between Doppler Ultrasound Blood Flow Parameters and Angiogenesis and Proliferation Activity in Breast Cancer. *Med Sci Monit* 25, pp. 7035-7041. doi: 10.12659/msm.914395
- Nkepan, G. N. et al. 2019. Production of [13N]ammonia from [13C]methanol on a 7.5 MeV cyclotron using $^{13}\text{C}(p, n)^{13}\text{N}$ reaction: Detection of myocardial infarction in a mouse model. *Applied Radiation and Isotopes* 150, pp. 19-24. doi: <https://doi.org/10.1016/j.apradiso.2019.05.002>
- Noda, S., Sato, S., Fukuda, T., Tada, N. and Hattori, N. 2020. Aging-related motor function and dopaminergic neuronal loss in C57BL/6 mice. *Molecular brain* 13(1), pp. 46-46. doi: 10.1186/s13041-020-00585-6
- Oikonomou, E., Latsios, G., Vogiatzi, G. and Tousoulis, D. 2018. Chapter 1.3 - Atherosclerotic Plaque. In: Tousoulis, D. ed. *Coronary Artery Disease*. Academic Press, pp. 31-41.
- Orbay, H., Hong, H., Zhang, Y. and Cai, W. PET/SPECT imaging of hindlimb ischemia: focusing on angiogenesis and blood flow. doi: 10.1007/s10456-012-9319-4
- Orbay, H., Hong, H., Zhang, Y. and Cai, W. 2013. PET/SPECT imaging of hindlimb ischemia: focusing on angiogenesis and blood flow. *Angiogenesis* 16(2), pp. 279-287. doi: 10.1007/s10456-012-9319-4
- Pacher, P., Beckman, J. S. and Liaudet, L. 2007. Nitric Oxide and Peroxynitrite in Health and Disease. *Physiological Reviews* 87(1), pp. 315-424. doi: 10.1152/physrev.00029.2006
- Padgett, M. E., McCord, T. J., McClung, J. M. and Kontos, C. D. 2016. Methods for acute and subacute murine hindlimb ischemia. *Journal of Visualized Experiments* 2016(112), pp. 1-8. doi: 10.3791/54166
- Paek, R. et al. 2002. Correlation of a simple direct measurement of muscle pO₂ to a clinical ischemia index and histology in a rat model of chronic severe hindlimb ischemia. *Journal of Vascular Surgery* 36(1), pp. 172-179. doi: 10.1067/mva.2002.124361

- Partovian, C. et al. 2005. PKC α activates eNOS and increases arterial blood flow in vivo. *Circ Res* 97(5), pp. 482-487. doi: 10.1161/01.Res.0000179775.04114.45
- Patel, K. K. et al. 2019. Randomized comparison of clinical effectiveness of pharmacologic SPECT and PET MPI in symptomatic CAD patients. *JACC: Cardiovascular Imaging* 12(9), pp. 1821-1831.
- Peled, A. et al. 1999. Dependence of human stem cell engraftment and repopulation of NOD/SCID mice on CXCR4. *Science* 283(5403), pp. 845-848. doi: 10.1126/science.283.5403.845
- Peñuelas, I. et al. 2007. ³N-Ammonia PET as a Measurement of Hindlimb Perfusion in a Mouse Model of Peripheral Artery Occlusive Disease. *J Nucl Med* 48, pp. 1216-1223. doi: 10.2967/jnumed.106.039180
- Petersmann, A. et al. 2019. Definition, classification and diagnosis of diabetes mellitus. *Experimental and Clinical Endocrinology & Diabetes* 127(S 01), pp. S1-S7.
- Petit, I., Jin, D. and Rafii, S. 2007. The SDF-1-CXCR4 signaling pathway: a molecular hub modulating neo-angiogenesis. *Trends Immunol* 28(7), pp. 299-307. doi: 10.1016/j.it.2007.05.007
- Phelps, M. E., Hoffman, E. J., Huang, S.-C. and Ter-Pogossian, M. M. 1975. Effect of Positron Range on Spatial Resolution. *Journal of Nuclear Medicine* 16(7), p. 649.
- Phoon, C. K. L. and Turnbull, D. H. 2016. Cardiovascular Imaging in Mice. *Current protocols in mouse biology* 6(1), pp. 15-38. doi: 10.1002/9780470942390.mo150122
- Pien, H. H., Fischman, A. J., Thrall, J. H. and Sorensen, A. G. 2005. Using imaging biomarkers to accelerate drug development and clinical trials. *Drug Discovery Today* 10(4), pp. 259-266. doi: 10.1016/s1359-6446(04)03334-3
- Podoloff, D. and Stearns, C. W. 2004. *Performance characteristics of a newly developed PET/CT scanner using NEMA standards in 2D and 3D modes.* Available at: <https://www.researchgate.net/publication/8243634>
- Prasad, R., Ratib, O. and Zaidi, H. 2011. NEMA NU-04-based performance characteristics of the LabPET-8™ small animal PET scanner. *Physics in Medicine and Biology* 56(20), pp. 6649-6664. doi: 10.1088/0031-9155/56/20/009
- Prieto, E. et al. 2010. Evaluation of spatial resolution of a PET scanner through the simulation and experimental measurement of the recovery coefficient. *Comput Biol Med* 40(1), pp. 75-80. doi: 10.1016/j.combiomed.2009.11.002
- Prior, M. C. O. 2017. Cardiac Radionuclide Imaging in Rodents: A Review of Methods, Results, and Factors at Play. *Front.* 4, pp. 35-35. doi: 10.3389/fmed.2017.00035
- Puca, A. A. et al. 2020. Single systemic transfer of a human gene associated with exceptional longevity halts the progression of atherosclerosis and inflammation in ApoE knockout mice through a CXCR4-mediated mechanism. *Eur Heart J* 41(26), pp. 2487-2497. doi: 10.1093/eurheartj/ehz459

- Puhl, S. L., Weeks, K. L., Ranieri, A. and Avkiran, M. 2016. Assessing structural and functional responses of murine hearts to acute and sustained β -adrenergic stimulation in vivo. *J Pharmacol Toxicol Methods* 79, pp. 60-71. doi: 10.1016/j.vascn.2016.01.007
- Puntmann, V. O. et al. 2012. Gender-specific differences in myocardial deformation and aortic stiffness at rest and dobutamine stress. *Hypertension* 59(3), pp. 712-718. doi: 10.1161/hypertensionaha.111.183335
- Raher, M. J. et al. 2007. In vivo characterization of murine myocardial perfusion with myocardial contrast echocardiography: Validation and application in nitric oxide synthase 3-deficient mice.
- Rajesh, M. et al. 2010. Cannabidiol attenuates cardiac dysfunction, oxidative stress, fibrosis, and inflammatory and cell death signaling pathways in diabetic cardiomyopathy. *Journal of the American College of Cardiology* 56(25), pp. 2115-2125.
- Ramandika, E. et al. 2020. Effects of aging on coronary flow reserve in patients with no evidence of myocardial perfusion abnormality. Springer Japan.
- Rammos, C. et al. 2016. Impact of dietary nitrate on age-related diastolic dysfunction. *Eur J Heart Fail* 18(6), pp. 599-610. doi: 10.1002/ejhf.535
- Ratajczak, M., Zuba-Surma, E., Kucia, M., Reza, R., Wojakowski, W. and Ratajczak, J. 2006. The pleiotropic effects of the SDF-1–CXCR4 axis in organogenesis, regeneration and tumorigenesis. *Leukemia* 20(11), pp. 1915-1924.
- Rehman, R., Yelamanchili, V. S. and Makaryus, A. N. 2021. Cardiac imaging. *StatPearls [Internet]*,
- Rincon, M. Y., VandenDriessche, T. and Chuah, M. K. 2015. Gene therapy for cardiovascular disease: Advances in vector development, targeting, and delivery for clinical translation. *Cardiovascular Research* 108(1), pp. 4-20. doi: 10.1093/cvr/cvv205
- Rischpler, C., Park, M. J., Fung, G. S., Javadi, M., Tsui, B. M. and Higuchi, T. 2012. Advances in PET myocardial perfusion imaging: F-18 labeled tracers. *Ann Nucl Med* 26(1), pp. 1-6. doi: 10.1007/s12149-011-0552-5
- Rivas, F., Cobb, F. R., Bache, R. J. and Greenfield, J. C. 1976. Relationship between blood flow to ischemic regions and extent of myocardial infarction. Serial measurement of blood flow to ischemic regions in dogs. *Circulation Research* 38(5), pp. 439-447. doi: doi:10.1161/01.RES.38.5.439
- Rodrigues, R. 2016. A Comprehensive Review: The Use of Animal Models in Diabetes Research. *Journal of Analytical & Pharmaceutical Research* 3(6), doi: 10.15406/japlr.2016.03.00071
- Rongen, G. A., Brooks, S. C., Pollard, M. J., Ando, S., Dajani, H. R., Notarius, C. F. and Floras, J. S. 1999. Effect of adenosine on heart rate variability in humans. *Clin Sci (Lond)* 96(6), pp. 597-604.

- Rowland, D. J. and Cherry, S. R. 2008. Small-animal preclinical nuclear medicine instrumentation and methodology. *Semin Nucl Med* 38(3), pp. 209-222. doi: 10.1053/j.semnuclmed.2008.01.004
- Rundell, V. L., Geenen, D. L., Buttrick, P. M. and de Tombe, P. P. 2004. Depressed cardiac tension cost in experimental diabetes is due to altered myosin heavy chain isoform expression. *Am J Physiol Heart Circ Physiol* 287(1), pp. H408-413. doi: 10.1152/ajpheart.00049.2004
- Rust, T. C., DiBella, E. V. R., McGann, C. J., Christian, P. E., Hoffman, J. M. and Kadrmas, D. J. 2006. Rapid dual-injection single-scan ¹³N-ammonia PET for quantification of rest and stress myocardial blood flows. *Physics in Medicine and Biology* 51(20), pp. 5347-5362. doi: 10.1088/0031-9155/51/20/018
- Saddik, M. and Lopaschuk, G. D. 1994. Triacylglycerol turnover in isolated working hearts of acutely diabetic rats. *Can J Physiol Pharmacol* 72(10), pp. 1110-1119. doi: 10.1139/y94-157
- Saha, G. B. 2010. *Physics and Radiobiology of Nuclear Medicine*. Springer New York.
- Şahin, B. and İlğün, G. 2022. Risk factors of deaths related to cardiovascular diseases in World Health Organization (WHO) member countries. *Health Soc Care Community* 30(1), pp. 73-80. doi: 10.1111/hsc.13156
- Santos, A. et al. 2015. Cardiovascular imaging: What have we learned from animal models?
- Saraste, A., Nekolla, S. G. and Schwaiger, M. 2009. Cardiovascular molecular imaging: an overview. *Cardiovasc Res* 83(4), pp. 643-652. doi: 10.1093/cvr/cvp209
- Sasaki, M., Shinozaki, S., Morinaga, H., Kaneki, M., Nishimura, E. and Shimokado, K. 2018. iNOS inhibits hair regeneration in obese diabetic (ob/ob) mice. *Biochemical and biophysical research communications* 501(4), pp. 893-897. doi: <https://doi.org/10.1016/j.bbrc.2018.05.071>
- Sato, K. et al. 2016. Performance evaluation of the small-animal PET scanner ClairvivoPET using NEMA NU 4-2008 Standards. *Phys Med Biol* 61(2), pp. 696-711. doi: 10.1088/0031-9155/61/2/696
- Schelbert, H. R., Phelps, M. E., Huang, S. C., MacDonald, N. S., Hansen, H., Selin, C. and Kuhl, D. E. 1981. N-13 ammonia as an indicator of myocardial blood flow. *Circulation* 63(6 I), pp. 1259-1272. doi: 10.1161/01.CIR.63.6.1259
- Schober, P., Boer, C. and Schwarte, L. A. 2018. Correlation Coefficients: Appropriate Use and Interpretation. *Anesth Analg* 126(5), pp. 1763-1768. doi: 10.1213/ane.0000000000002864
- Schöder, H., Campisi, R., Ohtake, T., Hoh, C. K., Moon, D. H., Czernin, J. and Schelbert, H. R. 1999. Blood flow-metabolism imaging with positron emission tomography in patients with diabetes mellitus for the assessment of reversible left ventricular contractile dysfunction. *Journal of the American College of Cardiology* 33(5), pp. 1328-1337. doi: 10.1016/S0735-1097(99)00010-8

- Schönekeß, B. O., Allard, M. F. and Lopaschuk, G. D. 1995. Propionyl L-carnitine improvement of hypertrophied heart function is accompanied by an increase in carbohydrate oxidation. *Circ Res* 77(4), pp. 726-734. doi: 10.1161/01.res.77.4.726
- Schrepper, A. 2016. Cardiac Metabolism During Development and Aging. *The Scientist's Guide to Cardiac Metabolism*. pp. 73-83.
- Schulman, S. P. 1999. Cardiovascular consequences of the aging process. *Cardiol Clin* 17(1), pp. 35-49, viii. doi: 10.1016/s0733-8651(05)70055-2
- Schulze, P. C., Kennel, P. J., Doenst, T. and Peterson, L. R. 2016. Cardiac Metabolism – The Link to Clinical Practice. *The Scientist's Guide to Cardiac Metabolism*. pp. 191-205.
- Schwarzer, M. and Doenst, T. 2016. Introduction to Cardiac Metabolism. *The Scientist's Guide to Cardiac Metabolism*. pp. 1-5.
- Serhani, M. A., H, T. E. K., Ismail, H. and Nujum Navaz, A. 2020. ECG Monitoring Systems: Review, Architecture, Processes, and Key Challenges. *Sensors (Basel)* 20(6), doi: 10.3390/s20061796
- Shah, M. S. and Brownlee, M. 2016. Molecular and Cellular Mechanisms of Cardiovascular Disorders in Diabetes. *Circ Res* 118(11), pp. 1808-1829. doi: 10.1161/CIRCRESAHA.116.306923
- Shah, N. R. et al. 2016. Prognostic Value of Coronary Flow Reserve in Patients with Dialysis-Dependent ESRD. *J Am Soc Nephrol* 27(6), pp. 1823-1829. doi: 10.1681/asn.2015030301
- Shahhosseini, S. 2011. PET Radiopharmaceuticals. *Iran J Pharm Res* 10(1), pp. 1-2.
- Sharp, T. L., Dence, C. S., Engelbach, J. A., Herrero, P., Gropler, R. J. and Welch, M. J. 2005. Techniques necessary for multiple tracer quantitative small-animal imaging studies. *Nucl Med Biol* 32(8), pp. 875-884. doi: 10.1016/j.nucmedbio.2005.05.010
- Shirozu, M., Nakano, T., Inazawa, J., Tashiro, K., Tada, H., Shinohara, T. and Honjo, T. 1995. Structure and chromosomal localization of the human stromal cell-derived factor 1 (SDF1) gene. *Genomics* 28(3), pp. 495-500. doi: 10.1006/geno.1995.1180
- Shoghi, K. I. et al. 2008. Time course of alterations in myocardial glucose utilization in the Zucker diabetic fatty rat with correlation to gene expression of glucose transporters: a small-animal PET investigation. *J Nucl Med* 49(8), pp. 1320-1327. doi: 10.2967/jnumed.108.051672
- Shrestha, U. and Seo, Y. 2015. Myocardial Blood Flow as a Biomarker. In: Patel, V.B. and Preedy, V.R. eds. *Biomarkers in Cardiovascular Disease*. Dordrecht: Springer Netherlands, pp. 1-20.
- Simões, M. V. et al. 2004. Delayed response of insulin-stimulated fluorine-18 deoxyglucose uptake in glucose transporter-4-null mice hearts. *Journal of the American College of Cardiology* 43(9), pp. 1690-1697. doi: <https://doi.org/10.1016/j.jacc.2003.12.038>

Singh, B., Schoeb, T. R., Bajpai, P., Slominski, A. and Singh, K. K. 2018. Reversing wrinkled skin and hair loss in mice by restoring mitochondrial function. *Cell Death Dis* 9(7), p. 735. doi: 10.1038/s41419-018-0765-9

Sinha, A., Rahman, H. and Perera, D. 2021. Coronary microvascular disease: current concepts of pathophysiology, diagnosis and management. *Cardiovasc Endocrinol Metab* 10(1), pp. 22-30. doi: 10.1097/xce.0000000000000223

Sinnaeve, P., Varenne, O., Collen, D. and Janssens, S. 1999. *Gene therapy in the cardiovascular system: an update*. Available at: www.elsevier.com/locate/cardioreswww.elsevier.nl/locate/cardiores

Slideshare Scribd company. 2006. *Medical imaging*. Slideshare Available at: https://www.slideshare.net/sirrainbow/medical-imaging-summary-1?qid=d5d8f0ec-c446-4840-9299-5e2043e5f684&v=&b=&from_search=3 [Accessed: 10 June 2022].

Slomka, P., Berman, D. S., Alexanderson, E. and Germano, G. 2014. The role of PET quantification in cardiovascular imaging. *Clinical and Translational Imaging*. Springer-Verlag Italia s.r.l.

Smith, N. B. and Webb, A. 2010. *Introduction to Medical Imaging: Physics, Engineering and Clinical Applications*. Cambridge: Cambridge University Press.

Soret, M., Bacharach, S. L. and Buvat, I. 2007. Partial-volume effect in PET tumor imaging. *J Nucl Med* 48(6), pp. 932-945. doi: 10.2967/jnumed.106.035774

Spinelli, C. C. et al. 2017. LAV-BPIFB4 isoform modulates eNOS signalling through Ca²⁺/PKC- α -dependent mechanism. *Cardiovascular Research* 113(7), pp. 795-804. doi: 10.1093/cvr/cvx072

Srinivas, S. M., Dhurairaj, T., Basu, S., Bural, G., Surti, S. and Alavi, A. 2009. A recovery coefficient method for partial volume correction of PET images. *Ann Nucl Med* 23(4), pp. 341-348. doi: 10.1007/s12149-009-0241-9

Stefano, G. B., Challenger, S. and Kream, R. M. 2016. Hyperglycemia-associated alterations in cellular signaling and dysregulated mitochondrial bioenergetics in human metabolic disorders. *Eur J Nutr* 55(8), pp. 2339-2345. doi: 10.1007/s00394-016-1212-2

Stegger, L., Hoffmeier, A.-N., Schäfers, K. P., Hermann, S., Schober, O., Schäfers, M. A. and Theilmeyer, G. 2006. Accurate Noninvasive Measurement of Infarct Size in Mice with High-Resolution PET. *Journal of Nuclear Medicine* 47(11), p. 1837.

Sun, Y. V. et al. 2020. Cardiovascular disease risk and pathophysiology in South Asians: can longitudinal multi-omics shed light? *Wellcome Open Res* 5, p. 255. doi: 10.12688/wellcomeopenres.16336.2

Sunderland, J. J. and Christian, P. E. 2015. Quantitative PET/CT scanner performance characterization based upon the society of nuclear medicine and molecular imaging clinical trials network oncology clinical simulator phantom. *Journal of Nuclear Medicine* 56(1), pp. 145-152. doi: 10.2967/jnumed.114.148056

- Surti, S., Karp, J., Perkins, A., Cardi, C., Daube-Witherspoon, M., Kuhn, A. and Muehllehner, G. 2005. Imaging performance of A-PET: a small animal PET camera. *Medical Imaging, IEEE Transactions on* 24, pp. 844-852. doi: 10.1109/TMI.2005.844078
- Swift, M. E., Kleinman, H. K. and DiPietro, L. A. 1999. Impaired wound repair and delayed angiogenesis in aged mice. *Laboratory investigation; a journal of technical methods and pathology* 79(12), pp. 1479-1487.
- Szymanski, M. K. et al. 2012. Use of gated ¹³N-NH₃ micro-PET to examine left ventricular function in rats. *Nucl Med Biol* 39(5), pp. 724-729. doi: 10.1016/j.nucmedbio.2011.12.009
- Tabas, I. and Glass, C. K. 2013. Anti-inflammatory therapy in chronic disease: challenges and opportunities. *Science* 339(6116), pp. 166-172.
- Tachibana, K. et al. 1998. The chemokine receptor CXCR4 is essential for vascularization of the gastrointestinal tract. *Nature* 393(6685), pp. 591-594. doi: 10.1038/31261
- Taegtmeyer, H., Golfman, L., Sharma, S., Razeghi, P. and van Arsdall, M. 2004. Linking gene expression to function: metabolic flexibility in the normal and diseased heart. *Ann N Y Acad Sci* 1015, pp. 202-213. doi: 10.1196/annals.1302.017
- Taegtmeyer, H., Hems, R. and Krebs, H. A. 1980. Utilization of energy-providing substrates in the isolated working rat heart. *Biochem J* 186(3), pp. 701-711. doi: 10.1042/bj1860701
- Tang, G. L. and Kim, K. J. 2021. Laser Doppler Perfusion Imaging in the Mouse Hindlimb. *J Vis Exp* (170), doi: 10.3791/62012
- Tang, J. et al. 2009. Mesenchymal stem cells over-expressing SDF-1 promote angiogenesis and improve heart function in experimental myocardial infarction in rats. *European Journal of Cardio-Thoracic Surgery* 36(4), pp. 644-650. doi: 10.1016/j.ejcts.2009.04.052
- Taqueti, V. R. and Di Carli, M. F. 2018. Coronary microvascular disease pathogenic mechanisms and therapeutic options: JACC state-of-the-art review. *Journal of the American College of Cardiology* 72(21), pp. 2625-2641.
- Teuho, J. et al. 2020. Evaluation of image quality with four positron emitters and three preclinical PET/CT systems. *EJNMMI Res* 10(1), p. 155. doi: 10.1186/s13550-020-00724-z
- Thackeray, J. T., Bankstahl, J. P. and Bengel, F. M. 2015. Impact of Image-Derived Input Function and Fit Time Intervals on Patlak Quantification of Myocardial Glucose Uptake in Mice. *J Nucl Med* 56(10), pp. 1615-1621. doi: 10.2967/jnumed.115.160820
- Thackeray, J. T. and Bengel, F. M. 2018. Molecular Imaging of Myocardial Inflammation With Positron Emission Tomography Post-Ischemia: A Determinant of Subsequent Remodeling or Recovery. *JACC Cardiovasc Imaging* 11(9), pp. 1340-1355. doi: 10.1016/j.jcmg.2018.05.026

- Thorn, S. L. et al. 2013. Repeatable noninvasive measurement of mouse myocardial glucose uptake with 18F-FDG: evaluation of tracer kinetics in a type 1 diabetes model. *J Nucl Med* 54(9), pp. 1637-1644. doi: 10.2967/jnumed.112.110114
- Toyama, H. et al. 2004. Evaluation of anesthesia effects on [18F]FDG uptake in mouse brain and heart using small animal PET. *Nuclear Medicine and Biology* 31(2), pp. 251-256. doi: [https://doi.org/10.1016/S0969-8051\(03\)00124-0](https://doi.org/10.1016/S0969-8051(03)00124-0)
- Tsalamandris, S. et al. 2019. The Role of Inflammation in Diabetes: Current Concepts and Future Perspectives. *European cardiology* 14(1), pp. 50-59. doi: 10.15420/ecr.2018.33.1
- Tsatralis, T. et al. 2016. Reconstituted high-density lipoproteins promote wound repair and blood flow recovery in response to ischemia in aged mice. *Lipids in Health and Disease* 15(1), pp. 1-12. doi: 10.1186/s12944-016-0322-4
- Turkheimer, F., Veronese, M. and Dunn, J. 2014. *Experimental Design and Practical Data Analysis in Positron Emission Tomography*.
- Tyrankiewicz, U., Skorka, T., Jablonska, M., Petkow-Dimitrow, P. and Chlopicki, S. 2013. Characterization of the cardiac response to a low and high dose of dobutamine in the mouse model of dilated cardiomyopathy by MRI in vivo. *Journal of Magnetic Resonance Imaging* 37(3), pp. 669-677. doi: 10.1002/jmri.23854
- Valenta, I., Dilsizian, V., Quercioli, A., Ruddy, T. D. and Schindler, T. H. 2013. Quantitative PET/CT measures of myocardial flow reserve and atherosclerosis for cardiac risk assessment and predicting adverse patient outcomes. *Curr Cardiol Rep* 15(3), p. 344. doi: 10.1007/s11886-012-0344-0
- Valenzuela-Fernández, A. et al. 2002. Leukocyte elastase negatively regulates Stromal cell-derived factor-1 (SDF-1)/CXCR4 binding and functions by amino-terminal processing of SDF-1 and CXCR4. *J Biol Chem* 277(18), pp. 15677-15689. doi: 10.1074/jbc.M111388200
- Vallet, B., Dupuis, B. and Chopin, C. 1991. [Dobutamine: mechanisms of action and use in acute cardiovascular pathology]. *Ann Cardiol Angeiol (Paris)* 40(6), pp. 397-402.
- Vanhooren, V. and Libert, C. 2013. The mouse as a model organism in aging research: Usefulness, pitfalls and possibilities. *Ageing Research Reviews*.
- Vanhoutte, P. M., Shimokawa, H., Tang, E. H. and Feletou, M. 2009. Endothelial dysfunction and vascular disease. *Acta physiologica* 196(2), pp. 193-222.
- Vanoverschelde, J. L., Janier, M. F., Bakke, J. E., Marshall, D. R. and Bergmann, S. R. 1994. Rate of glycolysis during ischemia determines extent of ischemic injury and functional recovery after reperfusion. *Am J Physiol* 267(5 Pt 2), pp. H1785-1794. doi: 10.1152/ajpheart.1994.267.5.H1785
- Vasan, R. S. 2006. Biomarkers of cardiovascular disease: molecular basis and practical considerations. *Circulation* 113(19), pp. 2335-2362. doi: 10.1161/CIRCULATIONAHA.104.482570

- Vaska, P., Rubins, D. J., Alexoff, D. L. and Schiffer, W. K. 2006. Quantitative Imaging with the Micro-pet Small-Animal Pet Tomograph. pp. 191-218.
- Vassiliou, V. S., Cameron, D., Prasad, S. K. and Gatehouse, P. D. 2018. Magnetic resonance imaging: Physics basics for the cardiologist. *JRSM Cardiovasc Dis* 7, p. 2048004018772237. doi: 10.1177/2048004018772237
- Vasudevan, P. et al. 2020. (18)F-FDG PET-Based Imaging of Myocardial Inflammation Following Acute Myocardial Infarction in a Mouse Model. *Int J Mol Sci* 21(9), doi: 10.3390/ijms21093340
- Vicente, E. et al. 2007a. Influence of random, pile-up and scatter corrections in the quantification properties of small-animal PET scanners. *2007 IEEE Nuclear Science Symposium Conference Record*. pp. 3964-3968. doi: 10.1109/nssmic.2007.4436985
- Vicente, E. et al. eds. 2007b. *Influence of random, pile-up and scatter corrections in the quantification properties of small-animal PET scanners. IEEE Nuclear Science Symposium Conference Record*.
- Vilchez, D., Simic, M. S. and Dillin, A. 2014. Proteostasis and aging of stem cells. *Trends Cell Biol* 24(3), pp. 161-170. doi: 10.1016/j.tcb.2013.09.002
- Villa, F. et al. 2015a. Serum BPIFB4 levels classify health status in long-living individuals.
- Villa, F. et al. 2018. A model of evolutionary selection: The cardiovascular protective function of the longevity associated variant of BPIFB4. *International Journal of Molecular Sciences*. MDPI AG.
- Villa, F. et al. 2015b. Genetic Analysis Reveals a Longevity-Associated Protein Modulating Endothelial Function and Angiogenesis. *Circulation Research* 117(4), pp. 333-345. doi: doi:10.1161/CIRCRESAHA.117.305875
- Villa, F. et al. 2015c. Genetic Analysis Reveals a Longevity-Associated Protein Modulating Endothelial Function and Angiogenesis HHS Public Access. *Circ Res* 117(4), pp. 333-345. doi: 10.1161/CIRCRESAHA.117.305875/-/DC1
- Villanueva, F. S. and Wagner, W. R. 2008. Ultrasound molecular imaging of cardiovascular disease. *Nat Clin Pract Cardiovasc Med* 5 Suppl 2, pp. S26-32. doi: 10.1038/ncpcardio1246
- Vincent, J. L. 2008. Understanding cardiac output. *Crit Care* 12(4), p. 174. doi: 10.1186/cc6975
- Visser, E. P., Disselhorst, J. A., Brom, M., Laverman, P., Gotthardt, M., Oyen, W. J. G. and Boerman, O. C. 2008. Spatial Resolution and Sensitivity of the Inveon Small-Animal PET Scanner. *Journal of Nuclear Medicine* 50(1), pp. 139-147. doi: 10.2967/jnumed.108.055152
- Vleeming, E. J., Lazarenko, S. V., van der Zant, F. M., Pan, X.-B., Declerck, J. M., Wondergem, M. and Knol, R. J. J. 2018. Cardiac Displacement During 13 N-Ammonia Myocardial Perfusion PET/CT: Comparison Between Adenosine- and Regadenoson-Induced Stress. *Journal of Nuclear Medicine Technology* 46(2), pp. 114-122. doi: 10.2967/jnmt.117.199463

- vom Dahl, J. et al. 1993. Myocardial glucose uptake in patients with insulin-dependent diabetes mellitus assessed quantitatively by dynamic positron emission tomography. *Circulation* 88(2), pp. 395-404. doi: 10.1161/01.cir.88.2.395
- Wada, J. and Makino, H. 2013. Inflammation and the pathogenesis of diabetic nephropathy. *Clinical science* 124(3), pp. 139-152.
- Walden, R. and Tomlinson, B. 2011. Cardiovascular Disease. In: Benzie, I.F.F. and Wachtel-Galor, S. eds. *Herbal Medicine: Biomolecular and Clinical Aspects*. Boca Raton (FL): CRC Press/Taylor & Francis Copyright © 2011 by Taylor and Francis Group, LLC.
- Walsh, W. F., Fill, H. R. and Harper, P. V. 1977. Nitrogen-13-labeled ammonia for myocardial imaging. *Seminars in Nuclear Medicine* 7(1), pp. 59-66. doi: [https://doi.org/10.1016/S0001-2998\(77\)80008-1](https://doi.org/10.1016/S0001-2998(77)80008-1)
- Wang, H. et al. 2016a. Global, regional, and national life expectancy, all-cause mortality, and cause-specific mortality for 249 causes of death, 1980–2015: a systematic analysis for the Global Burden of Disease Study 2015. *The Lancet* 388(10053), pp. 1459-1544.
- Wang, J., Balu, N., Canton, G. and Yuan, C. 2010. Imaging biomarkers of cardiovascular disease. *J Magn Reson Imaging* 32(3), pp. 502-515. doi: 10.1002/jmri.22266
- Wang, L. et al. 2016b. Diabetes mellitus stimulates pancreatic cancer growth and epithelial-mesenchymal transition-mediated metastasis via a p38 MAPK pathway. *Oncotarget* 7(25), p. 38539.
- Watabe, H., Ikoma, Y., Kimura, Y., Naganawa, M. and Shidahara, M. 2006. *PET kinetic analysis compartmental model*.
- Weber, S. and Bauer, A. 2004. Small animal PET: Aspects of performance assessment. *European Journal of Nuclear Medicine and Molecular Imaging* 31(11), pp. 1545-1555. doi: 10.1007/s00259-004-1683-x
- Weber, W. A., Ziegler, S. I., Thödtmann, R., Hanauske, A. R. and Schwaiger, M. 1999. Reproducibility of metabolic measurements in malignant tumors using FDG PET. *J Nucl Med* 40(11), pp. 1771-1777.
- Wendt, T., Bucciarelli, L., Qu, W., Lu, Y., Yan, S. F., Stern, D. M. and Schmidt, A. M. 2002. Receptor for advanced glycation endproducts (RAGE) and vascular inflammation: insights into the pathogenesis of macrovascular complications in diabetes. *Current atherosclerosis reports* 4(3), pp. 228-237.
- Werner, C., Doenst, T. and Schwarzer, M. 2016. Chapter 4 - Metabolic Pathways and Cycles. In: Schwarzer, M. and Doenst, T. eds. *The Scientist's Guide to Cardiac Metabolism*. Boston: Academic Press, pp. 39-55.
- Westvik, T. S. et al. 2009. Limb ischemia after iliac ligation in aged mice stimulates angiogenesis without arteriogenesis. Elsevier Inc.
- Wieland, B. et al. 1991. In-target production of [¹³N]ammonia via proton irradiation of dilute aqueous ethanol and acetic acid mixtures. *International Journal of Radiation Applications and Instrumentation. Part A*.

Applied Radiation and Isotopes 42(11), pp. 1095-1098. doi: [https://doi.org/10.1016/0883-2889\(91\)90018-V](https://doi.org/10.1016/0883-2889(91)90018-V)

Wolfertstetter, S., Huettner, J. P. and Schlossmann, J. 2013. cGMP-Dependent Protein Kinase Inhibitors in Health and Disease. *Pharmaceuticals (Basel, Switzerland)* 6(2), pp. 269-286. doi: 10.3390/ph6020269

Wong, W. H. et al. 2012. Engineering and performance (NEMA and animal) of a lower-cost higher-resolution animal PET/CT scanner using photomultiplier-quadrant-sharing detectors. *Journal of Nuclear Medicine* 53(11), doi: 10.2967/jnumed.112.103507

Wu, H.-M. et al. 2007. In Vivo Quantitation of Glucose Metabolism in Mice Using Small-Animal PET and a Microfluidic Device. *Journal of Nuclear Medicine* 48(5), p. 837. doi: 10.2967/jnumed.106.038182

Yamamoto, Y., Silva, R. d., Rhodes, C. G., Iida, H., Lammertsma, A. A., Jones, T. and Maseri, A. 1996. Noninvasive quantification of regional myocardial metabolic rate of oxygen by $^{15}\text{O}_2$ inhalation and positron emission tomography. Experimental validation.

Yang, B., Larson, D. F. and Watson, R. 1999. Age-related left ventricular function in the mouse: analysis based on in vivo pressure-volume relationships. *Am J Physiol* 277(5), pp. H1906-1913. doi: 10.1152/ajpheart.1999.277.5.H1906

Yang, Y., Rendig, S., Siegel, S., Newport, D. F. and Cherry, S. R. 2005. Cardiac PET imaging in mice with simultaneous cardiac and respiratory gating. *Physics in Medicine and Biology* 50(13), pp. 2979-2989. doi: 10.1088/0031-9155/50/13/001

Yang, Y. et al. 2004. Optimization and performance evaluation of the microPET II scanner for in vivo small-animal imaging. *Physics in Medicine and Biology* 49(12), pp. 2527-2545. doi: 10.1088/0031-9155/49/12/005

Yap, J. et al. 2004. *Combined clinical PET/CT and microPET small animal imaging*.

Young, M. E. 2016. Diurnal Variation in Cardiac Metabolism. *The Scientist's Guide to Cardiac Metabolism*. pp. 123-137.

Zemaitis, M. R., Boll, J. M. and Dreyer, M. A. 2022. Peripheral Arterial Disease. *StatPearls*. Treasure Island (FL): StatPearls Publishing
Copyright © 2022, StatPearls Publishing LLC.

Zhang, T. Y., Zhao, B. J., Wang, T. and Wang, J. 2021. Effect of aging and sex on cardiovascular structure and function in wildtype mice assessed with echocardiography. *Sci Rep* 11(1), p. 22800. doi: 10.1038/s41598-021-02196-0

Zhao, Y., Vanhoutte, P. M. and Leung, S. W. 2015. Vascular nitric oxide: Beyond eNOS. *J Pharmacol Sci* 129(2), pp. 83-94. doi: 10.1016/j.jphs.2015.09.002

- Zhao, Z., Francis, C. E. and Ravid, K. 1997. An A3-subtype adenosine receptor is highly expressed in rat vascular smooth muscle cells: its role in attenuating adenosine-induced increase in cAMP. *Microvasc Res* 54(3), pp. 243-252. doi: 10.1006/mvre.1997.2044
- Zhong, M., Alonso, C. E., Taegtmeier, H. and Kundu, B. K. 2013a. Quantitative PET Imaging Detects Early Metabolic Remodeling in a Mouse Model of Pressure-Overload Left Ventricular Hypertrophy In Vivo. *Journal of Nuclear Medicine* 54(4), p. 609. doi: 10.2967/jnumed.112.108092
- Zhong, M., Alonso, C. E., Taegtmeier, H. and Kundu, B. K. 2013b. Quantitative PET imaging detects early metabolic remodeling in a mouse model of pressure-overload left ventricular hypertrophy in vivo. *Journal of Nuclear Medicine* 54(4), pp. 609-615. doi: 10.2967/jnumed.112.108092
- Zhong, M. and Kundu, B. K. 2013. Optimization of a Model Corrected Blood Input Function From Dynamic FDG-PET Images of Small Animal Heart In Vivo. *IEEE Transactions on Nuclear Science* 60(5), pp. 3417-3422. doi: 10.1109/TNS.2013.2269032
- Ziadi, M. C. and Beanlands, R. S. 2010. The clinical utility of assessing myocardial blood flow using positron emission tomography. *J Nucl Cardiol* 17(4), pp. 571-581. doi: 10.1007/s12350-010-9258-7
- Ziessman, H. A., O'Malley, J. P., Thrall, J. H. and Fahey, F. H. 2014. Preface. In: Ziessman, H.A., O'Malley, J.P. and Thrall, J.H. eds. *Nuclear Medicine (Fourth Edition)*. Philadelphia: W.B. Saunders, p. ix.
- Zou, Y. R., Kottmann, A. H., Kuroda, M., Taniuchi, I. and Littman, D. R. 1998. Function of the chemokine receptor CXCR4 in haematopoiesis and in cerebellar development. *Nature* 393(6685), pp. 595-599. doi: 10.1038/31269

List of Abbreviations:

MBF	Myocardial Blood Flow
MGM	Myocardial glucose metabolism
CVDs	cardiovascular diseases
LAV-BPIFB4 gene	bactericidal/permeability-increasing fold-containing- family-B-member-4 longevity associated variant gene
CADs	Coronary Artery Diseases
PADs	Peripheral Artery Diseases
DM	Diabetes Mellitus
CVS	Cardiovascular System
US	Ultrasound Imaging
MRI	Magnetic Resonance Imaging
CT	X-ray Computed Tomography
PET	Positron Emission Tomography imaging
CM	Cardiac Metabolism
MGM	Myocardial Glucose Metabolism
LAV	Longevity Associated Variant
NEMA	National Electrical Manufacturers Association
¹⁸F-FDG	¹⁸Fluorine labelled Fluorodeoxyglucose
¹³N-NH₃	¹³Nitrogen labelled Ammonia
HLI	Hindlimb Ischemia
MI	Myocardial Infarction
RA	Right Atrium
RV	Right Ventricle
LA	Left Atrium
LV	Left Ventricle
CMs	Cardiomyocytes
FBs	Fibroblasts
ECs	Endothelial cells

SMCs	Smooth Muscle Cells
ECM	Extracellular Matrix
FA	Fatty Acid
ECG	Electrocardiogram
FR	Frame Rate
2D	2-Dimensional
3D	3-Dimensional
AC	Attenuation Correction
β^+	Positron
Bq	Becquerel
Ci	Curie
PMTs	Photomultiplier Tubes
PHA	Pulse Height Analysers
ACD	Annihilation Coincidence Detection Window
LOR	Line of Response
TOF	Time of Flight
SC	Scatter Corrections
SNR	Signal to Noise Ratio
NF	Normalization Factors
SUV	Standard Uptake Value
FOV	Field of View
CNR	Contrast to Noise Ratio
FBP	Filtered Back-Projection
DFT	Discrete Fourier Transform
IFT	Inverse Fourier Transform
IR	Iterative Reconstruction Algorithm
OSEM	Ordered Subset Expectation Maximization
RATIO	Tissue Plasma Ratio
PKIN	Pharmacokinetic Modelling
2TC	Two-Tissue Compartment
1TC	One-Tissue Compartment

IDIF	Image-Derived Input Function
CFR	Coronary Flow Reserve
LLIs	Long-Living Individuals
T1D	Type 1 Diabetes
T2D	Type 2 Diabetes
SR	Spatial Resolution
IP	Intraperitoneal
IV	Intravenous
SF	Scatter Fractions
IQ	Image Quality
PR	Positron Range
RC	Recovery Coefficient
SOR	Spill-Over Ratios
PVE	Partial Volume Effect
NO	Nitric Oxide
eNOS	Nitric Oxide Synthase
sGC	Soluble Guanylate Cyclase
GTP	Guanosine Triphosphate
cGMP	Cyclic Guanosine Monophosphate
PKG	Protein Kinase G enzyme
SDF-1	Stromal Derived Factor-1
ROS	Reactive Oxygen Species
BM Cells	Bone Marrow Cells
MyHC-α	Myosin Heavy Chain, α Isoform
CO	Cardiac output
LVEF	Left Ventricular Ejection Fraction
FS%	Fractional Shortening